

Dosimetric verification of radiation therapy including
intensity modulated treatments, using an amorphous-silicon
electronic portal imaging device

by

Krista Joy Chytyk-Praznik

A Thesis submitted to the Faculty of Graduate Studies of
The University of Manitoba
in partial fulfilment of the requirements of the degree of

DOCTOR OF PHILOSOPHY

Department of Physics and Astronomy

University of Manitoba

Winnipeg

Copyright © 2011 Krista Chytyk-Praznik

ACKNOWLEDGEMENTS

I have received funding for my research from numerous sources, including the CancerCare Manitoba Foundation, the Natural Science and Engineering Research Council and the Manitoba Health Research Council. This work could not have been completed without these organizations' financial support.

I would like to thank my advisory committee (Dr. Stephen Pistorius, Dr. Jason Fiege, Dr. Sherif Sherif and Dr. Jim Butler) for their questions, comments and guidance over the years. I also extend my gratitude to my external examiner, Dr. John Schreiner, for his insightful questions and remarks regarding the thesis. Above all, I would like to thank my supervisor, Dr. Boyd McCurdy, for his dedication, understanding, support and leadership throughout my Ph. D. studies.

I am grateful to the numerous radiation therapists that have assisted me in collecting data during patient treatment, as well as the staff physicists and physics assistants who aided me during after-hours data acquisitions and trouble-shooting.

I would also like to sincerely thank my peers and current and past students for their encouragement and friendship – Dr. Jorge Alpuche, Ganiyu Asuni, Heather Champion, Tamar Chighvinadze, Mike Hebb, Jenna King, Peter McCowan, Dave Niven, Dr. Peter Potrebko, Hongyan Sun, Troy Teo, Dr. Eric Van Uytven, Timothy Van Beek and

Niranjan Venugopal. A special thanks is additionally due to Dr. Eric Van Uytven and Timothy Van Beek for their expertise and assistance in the fulfillment of this project.

Most of all, I would like to thank my parents, Maurice and Kathy, and my brother, Cody, for their years of support and faith in me, and my husband, Dane, for his constant encouragement and for always being there for me when I needed him most.

ABSTRACT

Radiation therapy is continuously increasing in complexity due to technological innovation in delivery techniques, necessitating thorough dosimetric verification. Comparing accurately predicted portal dose images to measured images obtained during patient treatment can determine if a particular treatment was delivered correctly. The goal of this thesis was to create a method to predict portal dose images that was versatile and accurate enough to use in a clinical setting. All measured images in this work were obtained with an amorphous silicon electronic portal imaging device (a-Si EPID), but the technique is applicable to any planar imager.

A detailed, physics-motivated fluence model was developed to characterize fluence exiting the linear accelerator head. The model was further refined using results from Monte Carlo simulations and schematics of the linear accelerator. The fluence incident on the EPID was converted to a portal dose image through a superposition of Monte Carlo-generated, monoenergetic dose kernels specific to the a-Si EPID. Predictions of clinical IMRT fields with no patient present agreed with measured portal dose images within 3% and 3 mm.

The dose kernels were applied ignoring the geometrically divergent nature of incident fluence on the EPID. A computational investigation into this parallel dose kernel assumption determined its validity under clinically relevant situations.

Introducing a patient or phantom into the beam required the portal image prediction algorithm to account for patient scatter and attenuation. Primary fluence was calculated by attenuating raylines cast through the patient CT dataset, while scatter fluence was determined through the superposition of pre-calculated scatter fluence kernels. Total dose in the EPID was calculated by convolving the total predicted incident fluence with the EPID-specific dose kernels. The algorithm was tested on water slabs with square fields, agreeing with measurement within 3% and 3 mm. The method was then applied to five prostate and six head-and-neck IMRT treatment courses (~1900 clinical images). Deviations between the predicted and measured images were quantified.

The portal dose image prediction model developed in this thesis work has been shown to be accurate, and it was demonstrated to be able to verify patients' delivered radiation treatments.

TABLE OF CONTENTS

Acknowledgements.....	ii
Abstract.....	iv
List of Tables.....	ix
List of Figures.....	x
List of Copyrighted Material.....	xiii
Contribution to Science.....	xv

CHAPTER ONE: RATIONALE

1.1 Overview of Radiation Therapy.....	1
1.2 Dosimetric Accuracy.....	4
1.3 Radiation Therapy Accidents.....	7
1.4 Dosimetric Verification for Radiation Therapy Treatments.....	9
1.5 Hypothesis.....	9

CHAPTER TWO: INTRODUCTION

2.1 Beam Modeling for Treatment Simulation.....	11
2.2 IMRT Dosimetry Devices.....	27
2.3 Portal Imaging.....	34
2.4 Portal Dosimetry.....	40
2.5 Thesis Summary.....	49

CHAPTER THREE: INVESTIGATION OF TILTED DOSE KERNELS
FOR PORTAL DOSE PREDICTION IN ELECTRONIC PORTAL IMAGERS

3.1 Introduction.....	60
3.2 Methods and Materials.....	64
3.3 Results and Discussion.....	71
3.4 Conclusions.....	79

CHAPTER FOUR: COMPREHENSIVE FLUENCE MODEL FOR
ABSOLUTE PORTAL DOSE IMAGE PREDICTION

4.1 Introduction.....	83
4.2 Methods and Materials.....	87
4.3 Results and Discussion.....	97
4.4 Conclusions.....	111

CHAPTER FIVE: PHYSICS-BASED MODEL FOR PORTAL DOSE
IMAGE PREDICTION DURING TREATMENT

5.1 Introduction.....	115
5.2 Methods and Materials.....	119
5.3 Results and Discussion.....	132
5.4 Conclusions.....	142

CHAPTER SIX: *IN VIVO* DOSIMETRIC VERIFICATION OF INTENSITY-MODULATED RADIATION THERAPY

6.1 Introduction.....147

6.2 Methods and Materials.....150

6.3 Results and Discussion.....155

6.4 Conclusions.....172

CHAPTER SEVEN: SUMMARY AND CONCLUSIONS

7.1 Summary.....176

7.2 Conclusions.....180

7.3 Future Work.....181

CHAPTER EIGHT: APPENDIX

8.1 How To Take Images With an aS1000 EPID.....184

8.2 Monte Carlo Simulation.....185

8.3 Comparison and Evaluation of Dose Distributions.....195

8.4 Model Parameters.....198

8.5 Glossary.....201

8.6 Permissions for Copyrighted Material.....209

LIST OF TABLES

CHAPTER FOUR

4.1 χ -comparison Results of Prostate Open Fields.....	109
4.2 χ -comparison Results of Head and Neck Open Fields.....	109

CHAPTER FIVE

5.1 Fluence Model Updates.....	123
5.2 χ -comparison Results of Prostate IMRT Fields (Slab Phantom).....	139
5.3 χ -comparison Results of Head and Neck IMRT Fields (Slab Phantom).	141

CHAPTER EIGHT

8.1 Chapter 4 Fluence Parameters.....	198
8.2 Chapter 5 Fluence Parameters.....	199

LIST OF FIGURES

CHAPTER ONE

1.1 TCP vs. NTCP.....	5
-----------------------	---

CHAPTER TWO

2.1 Linear Accelerator Head.....	12
2.2 Water Tank Profiles.....	14
2.3 Dual Source Model.....	18
2.4 MLC design.....	22
2.5 Tongue-and-Groove Effect.....	23

CHAPTER THREE

3.1 Parallel vs. Tilted Kernels.....	61
3.2 Set-up for Dose Kernel Generation.....	67
3.3 Rebinning of Cartesian Dose Kernels.....	69
3.4 Dose Kernel Radial Profiles.....	72
3.5 Total Energy with Tilt Angle.....	73
3.6 Comparison of 0° and 14° Kernels.....	74
3.7 Profiles and χ -comparisons of Convolution vs. Superposition.....	76
3.8 χ -comparison Histograms of Clinical Scenario.....	77
3.9 χ -comparison Histograms of Extreme Scenario.....	78

CHAPTER FOUR

4.1 Gaussian and Pearson VII Functions.....	92
4.2 Comprehensive Fluence Model Commissioning.....	95
4.3 Profiles of Extrafocal Source Fluences.....	99
4.4 Extrafocal Fluence from Linac Components.....	100
4.5 Focal and Extrafocal Spectra.....	102
4.6 Measured and Predicted Profiles of Open 20x20 Field.....	106
4.7 Measured and Predicted Profiles of Open 5x5 Field.....	107
4.8 Profiles of Prostate Field.....	110
4.9 Profiles of Head and Neck Field.....	111

CHAPTER FIVE

5.1 Monte Carlo Fluence vs. Algorithm Fluence.....	133
5.2 Plot of Normalization Values.....	135
5.3 Square Fields Delivered to Phantom Slabs.....	136
5.4 Prostate IMRT Field.....	138
5.5 Head and Neck IMRT Field.....	140

CHAPTER SIX

6.1 Image Correction Method.....	153
6.2 Prostate Patient Case Study.....	156
6.3 Prostate Patient Percent Difference with Fraction.....	158
6.4 Summary of Prostate Patients' Agreement.....	161

6.5 Head and Neck Patient Case Study.....	166
6.6 Head and Neck Patient Percent Difference with Fraction.....	167
6.7 Summary of Head and Neck Patients' Agreement.....	169

LIST OF COPYRIGHTED MATERIAL

CHAPTER TWO

Figure 2.3: Dual Source Model.....18

Reprinted from “Sharpe, M.B., Jaffray, D.A., Battista, J.J., and Munro, P., *Extrafocal radiation: a unified approach to the prediction of beam penumbra and output factors for megavoltage x-ray beams*. Med Phys, 1995. **22**(12): p. 2065-74.” (Figure 1), with permission granted by the American Association of Physicists in Medicine (AAPM) on July 19, 2011.

Figure 2.5: Tongue-and-Groove Effect.....23

Adapted figure reprinted from “Seminars in Radiation Oncology, Volume 5, Issue 2, R. Mohan, *Field shaping for three-dimensional conformal radiation therapy and multileaf collimation*, pages 86-99, 1995” (Figure 3), with permission from Elsevier granted on June 30, 2011.

CHAPTER THREE.....60

The entirety of “Investigation of tilted dose kernels for portal dose image prediction in electronic portal images,” Med Phys, 2006. **33**(9): p. 3333-3339, by K. Chytky and B. M. C. McCurdy, with permission from the AAPM granted on April 8, 2011.

CHAPTER FOUR.....83

The entirety of “Comprehensive fluence model for absolute portal dose image prediction,” Med Phys, 2009. **36**(4): p. 1389-98, by K. Chytyk and B. M. C. McCurdy, with permission from the AAPM granted on April 8, 2011.

CONTRIBUTION TO SCIENCE

In this section, a chapter-by-chapter summary of this thesis' contributions to science is presented.

In previous works by other researchers, the assumption of a parallel incident beam for patient dose calculation was examined and found to have a clinically insignificant effect, thus allowing the use of much faster calculation techniques. In this thesis' Chapter Three, the effect of the practice of using parallel dose kernels in portal dose calculation was examined for the first time. Similar to patient dose calculation, it was found that applying the dose kernels in a parallel geometry did not introduce clinically significant error into the EPID dose calculation.

In Chapter Four, a comprehensive fluence model for portal dose image prediction was created. This physics-based method was originally modeled on the Pinnacle Treatment Planning System's (TPS) fluence model. This model was found modified to improve accuracy when determining dose images of square and IMRT fields. This was achieved by adapting the model to use a Gaussian-like extrafocal function (rather than a Gaussian extrafocal function used in the Pinnacle treatment planning system) and a constant extrafocal spectrum (rather than a spectrum that softened off-axis as dictated by the softening of the focal photons). These modifications were driven by results of Monte Carlo simulations of the linac fluence and portal dose image prediction process. The determination of the new parameters were calculated by exploiting Monte Carlo

simulation results. The portal dose image for IMRT fields without a patient or phantom in the beam were then accurately predicted.

In Chapter Five, the fluence model was further developed with the explicit modeling of two effects determined by other researchers (the asymmetric backscatter created by the EPID arm and the optical glare effect) and accounted for according to research by Rowshanfarzad *et al.* (2010) and Kirkby *et al.* (2005). These effects were previously modeled implicitly in the Monte Carlo dose kernel generation. Additional modifications determined by our research group included the use of manufacturer schematics for the MLC design, and Monte Carlo to determine the initial energy fluence profiles. These changes greatly reduced the number of variable parameters in the prediction model, thereby reducing the potential for errors in parameter determination, while simultaneously improving achievable accuracy. Using the manufacturer schematics and accounting for the asymmetry of the backscatter effect improved the accuracy of the algorithm by up to 6% for some fields.

Also in Chapter Five, we further developed the patient scatter model using scatter fluence kernels based on the earlier work of McCurdy and Pistorius (2000, 2001). In the current work, the patient scatter fluence kernels generated using Monte Carlo were recalculated using the latest versions of BEAMnrc and EGSnrc (several significant version upgrades from the EGS4 package used in the earlier work). The “NRC” versions of the EGS code improves on the accuracy of the electron dose deposition calculation. This increase in code accuracy inherently increases the accuracy of the scatter fluence kernels used to

determine the patient scatter incident on the EPID. Employing the energy spectra particular to the linac used during measured image acquisition, as calculated by BEAMnrc, to simulate the patient scatter kernels is also improves accuracy over the spectra determined by Mohan (1985). Importantly, this is the first work combining a calculated fluence model, rather than measured fluences, with a patient scatter model to determine dose delivered to an EPID.

Chapter Six uses the new portal dose image prediction model to predict patient treatment images in order to dosimetrically verify patient IMRT treatments. This is one of the few examples in the literature where patients are followed throughout their entire treatment course. This work is also the first time the developed patient scatter model method was applied to actual patient CT data to verify complex IMRT treatments in a clinical setting.

CHAPTER ONE: RATIONALE

1.1 OVERVIEW OF RADIATION THERAPY

Approximately 60% of all patients diagnosed with cancer will receive radiotherapy as a component of their treatment [1]. The other main methods used to treat cancer are surgery and chemotherapy. A combination of these treatments, as dictated by the diagnosis and the medical condition of the patient, is typically used to attempt to control the tumour without damaging the rest of the body. Surgery and radiation therapy treatments focus on local control of the cancer, while chemotherapy acts systemically to treat disease that may have spread to other areas in the body. The radiation damage inflicted on the malignant cells inhibits their reproduction and controls the tumour. Unfortunately, normal tissues are also harmed by radiation. Therefore, the objective of radiation therapy is to maximize and localize the dose to the tumour to destroy it, while minimizing the dose to the normal tissues to limit complications. The total treatment typically takes place over a period of about five to eight weeks, with a small amount of radiation dose (typically 1.8-2.0 Gy) delivered during each treatment session, or “fraction”.

In order to effectively control the tumour, accurate radiotherapy treatment planning and delivery is required. Prior to the 1970s, patient treatments were planned using external body contours (to obtain the patients’ shape and size) and two-dimensional imaging techniques (planar radiography). The patient was assumed to be composed purely of

homogenous water and charts of isodose distributions measured in water were used to plan the treatment. During the 1970s and 1980s, the development of computed tomography (CT) and magnetic resonance imaging (MRI), aided by advances in computer technology, provided the ability to acquire three-dimensional imaging data sets of individual patients. The CT and MRI data allowed the tumour and organs-at-risk (OARs) to be delineated in three-dimensions, with the MRI data providing better contrast of soft tissues and the CT data providing superior visualization of bony anatomy. Furthermore, the CT data could be converted into an electron density map of the patient, and then used in treatment planning to calculate the dose delivered. Treatments were not simply planned on blocks of homogeneous water anymore, but customized on real patients with individualized body compositions. This marked the start of three-dimensional conformal radiation therapy (3D-CRT), where the treatment beams (typically numbering from two to six) were collimated to the shape of the tumour. This beam collimation shapes the delivered fluence and therefore the delivered dose to the treatment volume – limiting the dose to the normal tissues to create a “conformal” dose distribution surrounding the target (tumour). Hence, the descriptive name of ‘3D conformal therapy’. A customized patient treatment plan can be designed and calculated by using dedicated computer software known as a treatment planning system (TPS). Beam modifying devices such as wedges or tissue compensators can be inserted to compensate for patient shape with the goal of delivering a uniform, conformal dose to the tumour. The customized treatment plans are developed by trained technologists known as ‘treatment planners’ or ‘dosimetrists’.

Intensity-modulated radiation therapy (IMRT) was conceived of in the 1980s [2,3], developed in the 1990s [4-8] and widely implemented in industrial nations in the 2000s. IMRT uses several beams of complex photon fluence patterns at various gantry angles to achieve an even more conformal dose distribution as compared to 3D-CRT. Multi-leaf collimators (MLCs) are still used to shape the beam to a fine precision and were initially used in 3D-CRT treatments as an automated replacement for labour-intensive, collimating blocks fabricated from lead alloy. Eventually the MLCs were utilized for IMRT delivery, with the leaves forming multiple small fields during irradiation to create a complicated fluence pattern delivered to the patient. Contours of the tumour and OARs on the patient's CT dataset, as delineated by the radiation oncologists and combined with dose objectives and/or constraints for each structure, are used as inputs into the TPS' IMRT optimization algorithm. The optimization algorithm then calculates the optimal fluence distributions required to satisfy the dose objectives and constraints. This typically involves a gradient-descent style optimization algorithm to minimize an objective function created based on the dose objective/constraint inputs. The treatment fields typically contain high dose gradients to deliver a dose pattern in the patient which conforms to the shape of the target, giving rise to the importance of patient positioning for accurate delivery. IMRT fields are non-intuitive compared to those in 3D-CRT, and the complexity of the technique has driven clinics to adopt more detailed treatment verification methods. Recently, rotational IMRT has been introduced into the clinic, adding a further degree of complexity during treatment – IMRT fields are delivered while the gantry is rotating around the patient, combined with modulation of the dose rate and gantry speed.

1.2 DOSIMETRIC ACCURACY

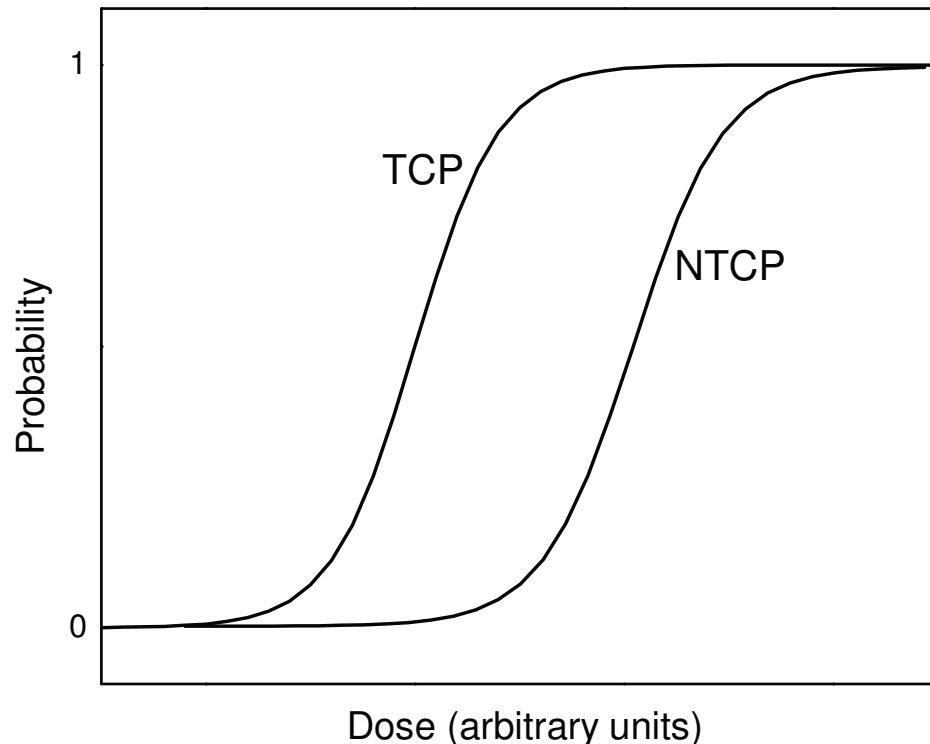
Sources of uncertainty in radiation therapy are classified in two groups – Type A and Type B [9]. Type A uncertainties are estimated from statistical analysis of repeated experiments, with a standard deviation assigned. An example of a Type A uncertainty would be patient setup during a treatment course. Type B uncertainties can be determined by methods other than statistical analysis and the errors are limited to a certain range. An example of a type B uncertainty would be an error in the dose calibration of a linac. All individual uncertainties are added in quadrature to obtain the total uncertainty.

The International Commission on Radiation Units and Measurements (ICRU) states a maximum acceptable dose uncertainty in radiation therapy delivery is $\pm 5\%$ and is based upon what was realistically achievable during treatment (i.e. the minimum uncertainty in linac output and patient setup) and what was most effective (i.e. the reduction of tumour recurrence and normal tissue complications) [10]. Clinically, dose errors of at least 7% have been detected [11]. One clinical example involved the results of a study that was carried out to examine the difference between treating tonsillar carcinoma with photons and electrons [11]. The fractionation schedule and dose delivered was identical in both cases, but there was less tumour regression in the patients treated with the electrons. A new calibration of the photon and electron dosimetry showed that, previously, an erroneous calibration of the electrons resulted in a 7% lower dose in comparison to the photons. In another example, gynecological patients were observed to have severe skin reactions and diarrhea following treatment [11]. The cause was determined to be an underestimation of calibration factors in a photon treatment that resulted in a 7-10 %

overdose. In this case, 50 patients out of a total of 88 were overdosed before the error was detected.

The effect of dose on both the tumour and normal tissues can be approximated as a sigmoid shaped curve obtained from both clinical and radiobiological observations (see Figure 1.1). The tumour control probability (TCP) and normal tissue complication probability (NTCP) can be used to determine prescription dose and dose limits, respectively. The TCP is the probability of tumour control, while NTCP is the probability of tissue complication, each for a given dose. For a treatment to be successful, one needs to treat a patient with a dose that maximizes the probability of tumour control and minimizes the probability of normal tissue complications.

Figure 1.1 [TCP vs. NTCP]: Diagram depicting the relative relationship between the tumour control probability (TCP) and the normal tissue complication probability (NTCP).



Estimates of acceptable uncertainties may be obtained by analyzing the slope of the dose-effect curves. The relative steepness of an individual TCP curve is stated as $\Delta 50/75$, which is an increase in percent dose to improve tumour control probability from 50 to 75%. A steep curve results in a small value of $\Delta 50/75$, i.e. a small increase in dose leads to a large increase in tumour control probability. A similar value is determined to measure the steepness of an NTCP curve and is referred to by $\Delta 25/50$ – the percent increase in dose that results in an increase in normal tissue complication probability from 25 to 50%. A normal tissue that has a small value of $\Delta 25/50$ is more sensitive to an increase in dose than one that has a large value of $\Delta 25/50$. Studies of the $\Delta 25/50$ and $\Delta 50/75$ show that a maximum dose uncertainty of $\pm 3.5\%$ maximizes tumour control probability (through the delivery of a large, uniform dose to the tumour) and minimizes normal tissue complication probability (by limiting the amount of dose delivered to the normal tissues) [9, 12].

Other studies concerning radiobiological modeling have obtained similar maximum uncertainties. For example, Brahme used the results of the linear quadratic model to determine that the uncertainty in the tumour dose must be limited to 5% in low-gradient regions and 3% in high gradient regions to ensure adequate tumour control [13]. Boyer and Schultheiss calculated theoretically that a 1% increase in dosimetric accuracy could increase the cure rate of early stage cancers by 2% [14].

It has been stated that currently the maximum achievable uncertainty (including patient positioning uncertainty, CT data, beam stability and consistency, dose calibration and

dose calculation) is approximately 5%. However, in the future, it is expected that a 3% overall uncertainty will be achievable [11].

1.3 RADIATION THERAPY ACCIDENTS

There have been a number of radiation therapy accidents that could have been prevented or detected sooner if dosimetric verification had taken place during a patient's treatment. Two incidents in the 1960s and 1970s (described in section 1.2) that helped outline the clinical dose uncertainty limit for tumour control and normal tissue tolerance were both due to calibration errors. Other examples include plan errors due to software or data transfer malfunctions. The use of incorrect decay curves of Co-60 to calibrate a teletherapy unit, in which the calculated decay of the source was more rapid than the actual decay, caused overdoses to 426 patients [15]. The Therac-25 linear accelerators that were developed by the Atomic Energy Commission Limited (AECL) for therapy caused at least six accidents between 1985 and 1987. A combination of multiple software malfunctions and a lack of hardware safety interlocks caused the linac to massively overdose patients – resulting in serious injuries and 3 documented deaths [16].

Therapy accidents still happen today in spite of the addition of significant safety monitoring hardware and software (e.g. monitor unit chambers, record and verify software) over the past two decades. In 2001, a linear accelerator in Poland overdosed 5 patients undergoing breast radiation therapy, causing all five to require skin grafts [17]. In 2005 in New York, NY, a computer crash that occurred during planning resulted in the MLC positions not being saved for an IMRT treatment of a tongue patient. Three

fractions of the IMRT treatment were delivered with the MLCs parked – no beam modulation was performed for any gantry angle and the patient died as a result of the significant overdose [18]. In Scotland in 2006, a 15-year old girl received an overdose of 58% because of an erroneous monitor unit value in her treatment plan that was not detected until 19 out of 20 fractions were delivered. She passed away as a result of the overdose [19, 20].

Stereotactic radiation therapy delivers a very high dose of radiation to a tumour, in fact much higher than conventional, external beam radiation therapy, with a high degree of precision. Typically, the number of fractions is also reduced in comparison with conventional radiotherapy. With the increased dose for any individual fraction, it is much more important for every individual fraction to be accurate. In February of 2010, a hospital in Missouri announced that half of its stereotactic patients were overdosed by approximately 50% due to a mistake in commissioning [21].

Accidents like those mentioned above could have been prevented by using dosimetric verification during patient treatment. Even with pretreatment verification of complicated plans, there remains the potential for inadvertent plan changes occurring after the patient plan has been dosimetrically verified. Patient weight loss or organ motion could also result in incorrect doses being delivered to the patient. Dosimetric verification of patient delivery is the only way to ensure that the correct dose was delivered to the correct volume of the patient.

1.4 DOSIMETRIC VERIFICATION FOR RADIATION THERAPY TREATMENTS

Radiation therapy treatments have evolved into complex techniques that are oftentimes non-intuitive. Technology is constantly being improved or changed, so new treatment techniques are often being introduced into the clinic. Dosimetric verification carried out during patient treatments can ensure the accuracy of the entire patient treatment process and would be able to catch significant errors immediately [20, 22]. It is apparent from the above discussion that verification of patient treatment dosimetry is necessary and a very worthy objective.

1.5 HYPOTHESIS

Can the image formation of an amorphous-silicon electronic portal imaging device be modeled within 3%, 3 accuracy for radiation therapy treatments, including IMRT?

REFERENCES

1. Canadian Cancer Society, *Radiation Therapy*, Canadian Cancer Encyclopedia March 11, 2012, <http://info.cancer.ca/cce-ecc/default.aspx?cceid=73&lf=Complementary%2520therapies&Lang=E>.
2. Brahme, A., Roos, J. E., and Lax, I., *Solution of an integral equation encountered in radiation therapy*. Phys Med Biol, 1982. 27: p. 1221-1229.
3. Brahme, A., *Optimization of stationary and moving beam radiation therapy techniques*. Radiother Oncol, 1988. 12: p. 129-140.
4. Webb, S., *Optimization of conformal radiotherapy dose distributions by simulated annealing*. Phys Med Biol, 1989. 34: p. 1349-1370.
5. Bortfeld, T., Burkelbach, J., Boesecke, R., and Schlegel, W., *Methods of image reconstruction from projections applied to conformal radiotherapy*. Phys Med Biol, 1990. 35: p. 1423-1434.
6. Convery, D. J. and Rosenbloom, M. E., *The generation of intensity-modulated fields for conformal radiotherapy by dynamic collimation*. Phys Med Biol, 1992. 37: p. 1359-1374.

7. Bortfeld, T., Kahler, D. L., Waldron, T. J., and Boyer, A. L., *X-ray field compensation with multileaf collimators*. Int J Radiat Oncol Biol Phys, 1994. 28: p. 723-730.
8. Ling, C. C., Burman, C., Chui, C. S., Kutcher, G. J., Leibel, S. A., LoSasso, T., Mohan, R., Bortfeld, T., Reinstein, L., Spirou, S., Wang, X. H., Wu, Q., Zelefsky, M., and Fuks, Z., *Conformal radiation treatment of prostate cancer using inversely-planned intensity-modulated photon beams produced with dynamic multileaf collimation*. Int J Radiat Oncol Biol Phys, 1996. 35(4): p. 721-30.
9. Mijnheer, B. J., Battermann, J. J., and Wambersie, A., *What degree of accuracy is required and can be achieved in photon and neutron therapy?* Radiother Oncol, 1987. 8(3): p. 237-52.
10. International Commission on Radiation Units and Measurements, *Determination of absorbed dose in a patient irradiated by beams of X or gamma rays in radiotherapy procedures*, ICRU Report 24, International Commission on Radiation Units and Measurements: Washington. 1976.
11. *Tissue inhomogeneity corrections for megavoltage photon beams*, AAPM Report No. 85, American Association of Physicists in Medicine: Madison. 2004.
12. Wambersie, A., *What accuracy is required and can be achieved in radiation therapy (review of radiobiological and clinical data)*. Radiochim Acta, 2001. 89: p. 255-264.
13. Brahme, A., *Dosimetric precision requirements in radiation therapy*. Acta Radiol Oncol, 1984. 23(5): p. 379-91.
14. Boyer, A. L. and Schultheiss, T., *Effects of dosimetric and clinical uncertainty on complication-free local tumor control*. Radiother Oncol, 1988. 11(1): p. 65-71.
15. Valentin, J., *Case histories of major accidental exposures in radiotherapy*. Annals of the ICRP, 2000. 30: p. 23-29.
16. Leveson, N. G., Turner, C. S., *An investigation of the Therac-25 accidents*. IEEE Computer, 1993. 26: p. 18-41.
17. *Accidental Overexposure of Radiotherapy Patients in Bialystok*, International Atomic Energy Agency: Vienna. 2004.
18. Bogdanich, W., *Radiation Offers New Cures, and Ways to Do Harm*, The New York Times, January 23, 2010, <http://www.nytimes.com/2010/01/24/health/24radiation.html?ref=radiationboom>.
19. Johnston, A. M., *Report into the unintended overexposure of Lisa Norris at Beatson, Glasgow*, Scottish Ministers for the Ionising Radiation (Medical Exposures) Regulations, Editor. 2006, The Scottish Government: Edinburgh. p. <http://www.scotland.gov.uk/Resource/Doc/153082/0041158.pdf>.
20. Williams, M. V., *Radiotherapy near misses, incident and errors: Radiotherapy incident at Glasgow Clin Oncol (R Coll Radiol)*, 2007. 19: p. 1-3.
21. Bogdanich, W. and Ruiz, R. R., *Radiation Errors Reported in Missouri*, The New York Times, February 24, 2010, http://www.nytimes.com/2010/02/25/us/25radiation.html?_r=1.
22. Ford, E., Terezakis, S., Yang, Y., Harris, K., and Mutic, S., *A quantification of the effectiveness of standard QA measures at preventing errors in radiation therapy and the promise of in vivo EPID-based portal dosimetry (abstract)*. Med Phys, 2011. 38: p. 3808.

CHAPTER TWO: INTRODUCTION

As described in Chapter One, external beam radiation therapy is a complex process where dosimetric accuracy will influence a patient's outcome. The following sections describe how the treatment is modeled or simulated in a treatment planning system and how the treatment is dosimetrically verified and with which devices. Monte Carlo simulation for dose calculation will also be discussed. This chapter also reviews previous work concerning electronic portal imaging devices (EPIDs) as dosimetric verification tools.

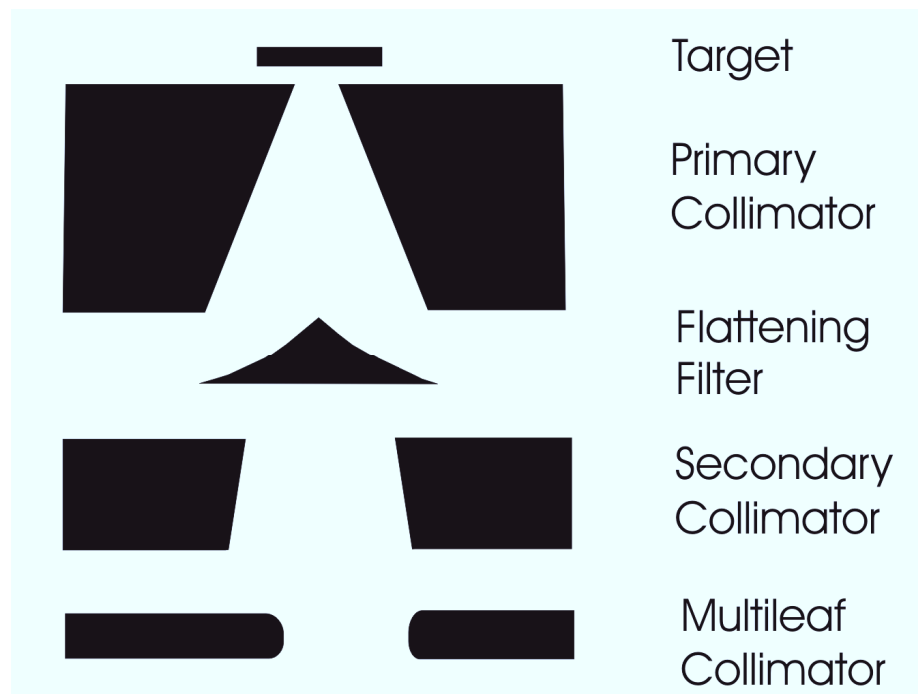
2.1 BEAM MODELING (FOR TREATMENT SIMULATION)

Modern external beam radiation therapy requires extensive and accurate modeling of the radiation that is used to treat patients, in order to plan the customized treatments in the treatment planning system (TPS). An understanding of the linear accelerator head components and its radiation sources, as well as beam characteristics (such as "horns" and off-axis energy spectra softening), is essential in the creation of a portal dose image prediction model, despite whether the effects of the beam are explicitly or empirically modeled. The following sections describe the linear accelerator head components, how the components influence the beam and how these effects are modeled. Monte Carlo simulation as a tool for beam simulation and radiation transport is also described.

2.1.1 The linear accelerator

Clinical linear accelerators possess multiple systems to create the x-ray photon radiation, and to control and conform the radiation to a particular volume, in order to treat patients (see Figure 2.1). A high-energy electron beam is incident upon a target, typically a tungsten alloy, and when an electron decelerates within the target due to collisions with the atomic nuclei, the electron loses kinetic energy. A portion of the energy lost is converted to a spectrum of x-ray photons with a maximum energy equal to the incident energy of the electron beam. The photon beam generated in this manner is described as a bremsstrahlung beam (“braking radiation”); the typical spectrum of photon energies used for treatment ranges from 4 MV to 24 MV. CancerCare Manitoba currently uses a 6 MV spectrum for all IMRT treatments.

Figure 2.1 [Linear Accelerator Head]: Schematic of linear accelerator head with the main components identified. Note the rounded leaf-tips of the multileaf collimator (MLC).

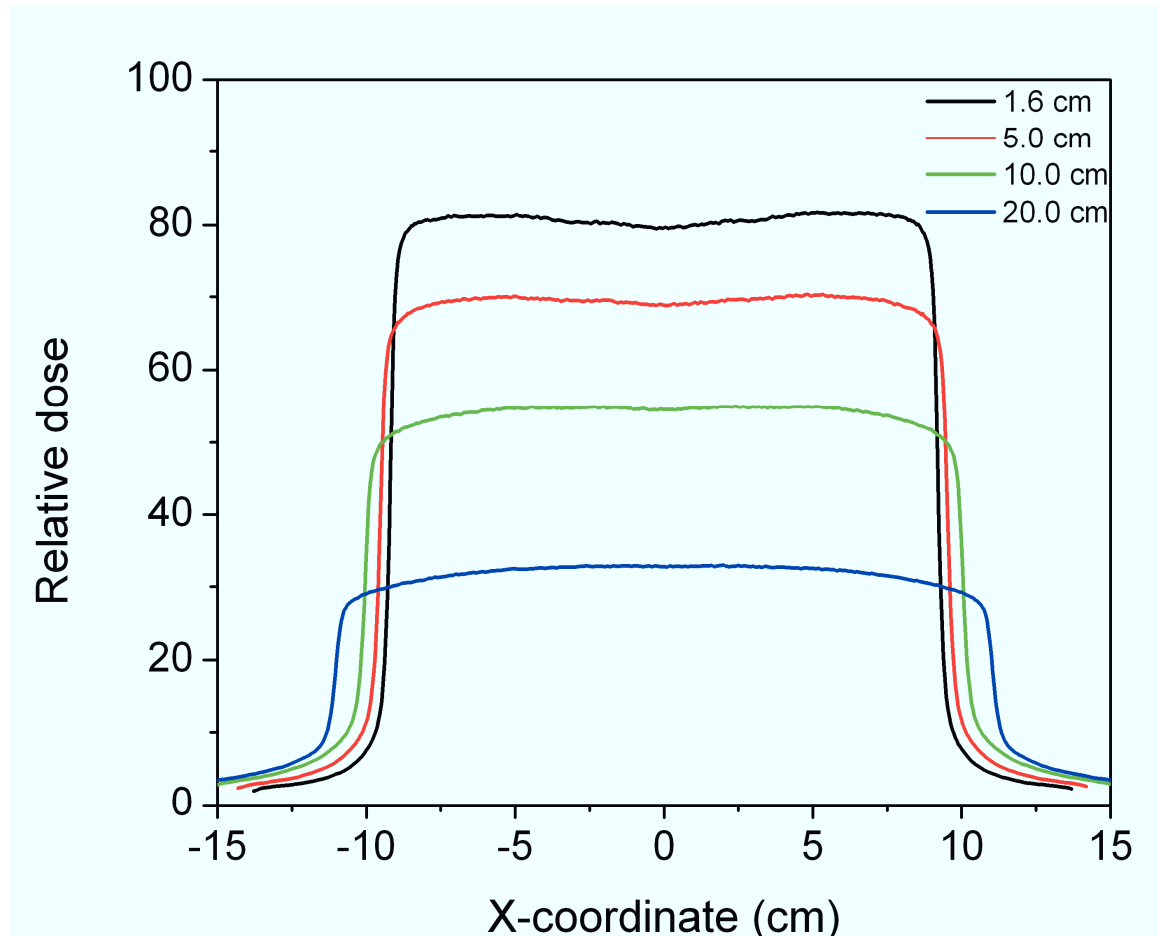


Immediately below the target is the primary collimator, which is typically constructed of thick lead. The primary collimator serves to block scattered photons and electrons emanating from the target in directions away from the patient, thus ensuring the beam is composed of forward-directed photons that will be used for the treatment. The interior cross-section shape of the collimator is a cone opening towards the patient, accounting for the inherently divergent nature of the beam emanating from the nearly point source at the target.

A flattening filter is used to ensure that the photon fluence exiting the linear accelerator treatment head will have a uniform intensity, giving a flat dose profile measured at depth in water. The flattening filter is generally cone-shaped in order to preferentially attenuate the photons on the central axis to obtain the flat profile. Without this, the dose profiles are significantly peaked at the central axis, due to the forward-directed bremsstrahlung photons [1]. Specifically, for a 6 MV beam, the differential attenuation through the flattening filter impacts the x-ray spectrum, creating an increasing proportion of lower energy photons as one moves off-axis (i.e. softening the energy spectrum). Conversely, the central axis photons are of a higher mean energy, with the thickest part of the flattening filter creating a significant hardening of the spectrum. The resulting fluence profile exiting the flattening filter is not perfectly flat but rather increases as one moves off-axis. This results in beam “horns” in the measured profiles at shallow depths (see Figure 2.2). However, due to the softer energy spectrum off-axis resulting in an increased rate of attenuation, these beam horns flatten out at depth in water. Typically, the

flattening filter is designed to provide a flat beam profile at about 10 cm depth in water (see Figure 2.2).

Figure 2.2 [Water Tank Profiles]: Profiles of a 6MV, 20x20 cm² photon field, obtained with measurement in a water tank with depth. Note the beam "horns" towards the edges of the profiles for the 1.6 cm (black) and 5.0 cm (red) depths. The 10 cm (green) profile demonstrates the "flattening" of the profile due to the flattening filter.



The primary collimator and flattening filter do not change for individual patient treatments, although there are specific flattening filters and targets for each of the available beam energies on a linear accelerator. The customization of treatments for individual patients is achieved through secondary collimators (jaws) and a multileaf collimator (MLC). The secondary collimators are able to shape the beam into squares or rectangles of various sizes. The MLC is composed of many narrow “fingers” or “leaves” of tungsten that are moved by a dedicated electric motor under computer control. This is the main component that conforms the beam to the tumour volume and also modulates the fluence allowing for complex fluence delivery. The MLC design is dependent on manufacturer, but individual leaf widths are usually 0.5 cm or 1.0 cm, with a set of 27 to 60 leaf-pairs (up to 120 leaves total) used to shape the beam. The MLC is made from tungsten alloy and are several centimeters thick in the direction of the beam (approximately 6.8 to 7.5 cm).

2.1.2 The dual source model for fluence exiting the treatment head

In order to accurately plan patient treatments and calculate dose distributions, the fluence exiting the linear accelerator head must also be accurately modeled. With the multitude of linac head components, complex geometry and the probabilistic nature of photon interactions, highly accurate calculation of the fluence is possible only with time-intensive Monte Carlo simulation. Physically-based models [2-8] have been created to approximate both the focal source (non-interacting photons directly from the target) and the extrafocal sources (photons from the target that have scattered off other linac head

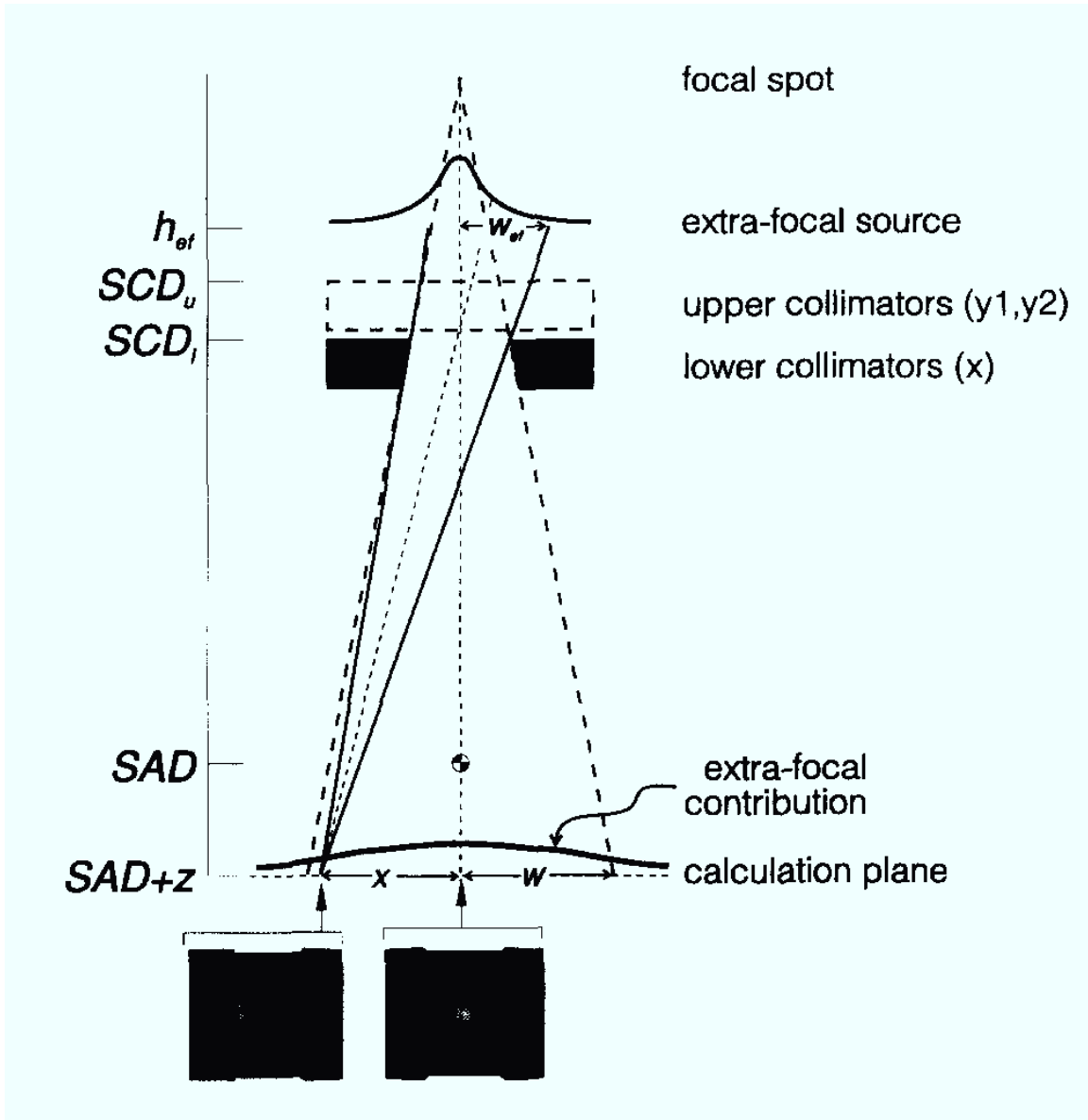
components, which accounts for about 10% of the total radiation incident on the patient [8]).

Work by Jaffray *et al.* [7] investigated the shape and size of the x-ray source for nine clinical linacs, defining the total x-ray source incident on the patient as separate focal radiation and extrafocal radiation sources. The results led to a hypothesis that the total x-ray source should be modeled as a focal source that is the “high-intensity, field size-independent component” and an extrafocal source that has a “low-intensity, field size-dependent component” to improve the calculation accuracy of treatment planning systems [7].

The specifics of the dual-source model were further explored in the work of Sharpe *et al.* [8] (See Figure 2.3). The focal source was assumed to be a distribution with a FWHM (full-width at half-maximum of about 1 to 2 mm, taken from the work by Jaffray *et al.* [7]. The beam profile horns created by attenuation in the flattening filter were modeled as a radially symmetric distribution about the central axis. The extrafocal source was measured with a diode at a large distance (245 cm) using collimators with diameters ranging from 5.3 to 22.9 mm. An increase in extrafocal radiation was detected as the aperture of the collimator became larger. Using the measured data, a flexible extrafocal source model was created that enabled dose calculation in air and water for various field sizes. The amount of extrafocal radiation contributing to each calculation point was determined by backprojecting through the field-defining collimators from the point of interest to the position of the extrafocal source plane (see Figure 2.3). The extrafocal

source was assumed to be at the position of the flattening filter since that component provides the majority of scattered photons in comparison to all other components of the treatment head. The photon spectrum used was that determined by Mohan *et al.* [9]. Dose profiles and dose-per-monitor-unit calibration factors were calculated with the convolution/superposition dose calculation method for various field sizes, with and without the extrafocal source model. The convolution/superposition method involves the convolution of terms with a spatially invariant dose deposition kernel and the superposition with a kernel that is influenced by regional changes in the primary fluence (changes in spectra) or variations in scattering due to patient geometry [10, 11]. The measured values matched closely to the calculation including the extrafocal source model, particularly in the beam penumbra area. Previously, the beam penumbra was empirically fit to measured data [12], but the dual-source model was now able to predict it.

Figure 2.3 [Dual Source Model]: Dual source model with a narrow focal source and broad extrafocal source. When determining the extrafocal contribution at a particular point in the calculation plane, the field aperture is back-projected from the point of interest to the position of the extrafocal source. (Reprinted from Sharpe *et al.* [8] with permission granted by the American Association of Physicists in Medicine (AAPM) on July 19, 2011.)



2.1.3 Pinnacle Treatment Planning System

The Pinnacle Treatment Planning System (TPS) was developed by Philips Medical Systems to plan patient radiation treatments and calculate dose distributions in the patient [13]. The dose calculation mechanism in Pinnacle is mainly based on the work of Mackie *et al.* [10, 14-16], Ahnesjo [16] and Papanikolaou [11]. The fluence modeling is based on work from a variety of sources including Ahnesjo [2], Mohan *et al.*[9] and Graves *et al.* [17] Although the Pinnacle manual [13] does not reference Jaffray *et al.* [7] or Sharpe *et al.* [8], there are many similarities between their methods and the Pinnacle fluence model. The Pinnacle TPS is versatile and can be commissioned for a variety of linear accelerators.

The focal fluence source is modeled as a narrow Gaussian function with an adjustable FWHM, typically on the order of 1 to 2 mm. The extrafocal source is also modeled as a Gaussian function with an adjustable FWHM, but typically using a wider FWHM of several centimeters. The maximum height of the extrafocal Gaussian function is defined as the maximum extrafocal proportion possible (i.e. for the largest field size possible – a 40x40 cm² field) and is also adjustable. For all other field sizes, the proportion of extrafocal fluence is relative to the maximum extrafocal fluence proportion, based on field area. The extrafocal height represents the maximum amount of extrafocal radiation at the central axis (i.e. the amount of extrafocal at isocenter when the jaws are at 40x40 cm²). The extrafocal fluence for every field size is relative to this maximum extrafocal fluence. The extrafocal fluence for each particular point in the dose calculation plane is determined by backprojecting through the collimators to the extrafocal source typically

placed at the flattening filter position. Both the width and height of the extrafocal source function influences the out-of-field characteristics of calculated dose profiles. The model prediction of dose in water is compared to measured dose profiles and depth-dose curves in a water tank; adjustments in the FWHM and extrafocal height can be made so the prediction will better match the shoulder and tail regions of the profiles. The energy spectrum of the incident fluence is adjusted by comparing measured depth dose curves in a tank of water to the calculated depth dose curves. The proportion of photons in each energy bin is adjusted until the calculated depth dose matches the measured. Note that the energy spectrum is due to the combined focal and extrafocal fluences.

Additional parameters are required to more fully model the effects of the flattening filter. First, the decrease in photon attenuation as one moves off-axis is modeled by a user-defined, radially symmetric profile similar in shape to an inverted cone to represent the incident focal fluence. This serves to modify the shape of the dose profiles at depth in a water phantom. The user-defined profile is radially symmetric, reflecting the symmetry of the flattening filter about the beam's central axis. The off-axis softening in the energy spectrum is modeled by an equation that softens the central axis energy spectrum as a function of radius. The parameters used in the equation are dependent on the maximum energy of the central axis spectrum (E_{max}), the energy of the individual bins (E_i) and the weighting of each bin (W_i) on the central axis, the off-axis angle from the radiation source (θ) and an adjustable off-axis softening parameter (OAS). The new weighting of the energy bin (W'_i) at a particular angle is then:

$$(2.1) W_i' = W_i \times \left(\frac{1}{1 + \frac{E_i}{E_{\max}}} \right)^{OAS \times \theta}, \text{ where } \theta = \tan^{-1} \left(\frac{OffAxisDist}{SAD} \right) [13].$$

Both the off-axis softening and the incident fluence profile are adjusted by matching the in-field region of dose profiles for various field sizes and depths.

The transmission through the jaws is handled as a single transmission factor that is compared to the dose profile outside the field [13]. The MLC modeling is more complicated as their design is much more complex than the jaws. The MLC transmission is handled as a single transmission factor directly under the leaf. The MLC's rounded leaf-tip (see Figure 2.1) is approximated by a circle of user-defined radius and is adjusted to match to the penumbra region of dose profiles [13]. The TPS raytraces through the leaf-tip to calculate the transmission relative to the full MLC transmission in order to obtain a more accurate penumbra match. Narrow regions in-between the individual leaves exhibit a higher transmission than in the middle of the leaf, an effect referred to as interleaf leakage and minimized by the tongue and groove design in the profiles of the leaf sides, designed to provide overlapping volumes of leaf collimation (see Figure 2.4). The "tongue-and-groove effect" is an area of underdosage that occurs between adjacent leaf pairs when a tongue and a groove alternately define the field edges of added fields (see Figure 2.5). The tongue-and-groove width parameter in Pinnacle is the section of the MLC that attenuates through half of the leaf thickness. If the width parameter is increased, the penumbra region widens; if it's decreased, the penumbra region narrows.

Figure 2.4 [MLC design]: An image of adjacent leaves of the multileaf collimator edge-on, parallel to the direction of the beam. The adjacent leaves fit together via the tongue and groove, with the region in-between the leaves being where the interleaf leakage originates.

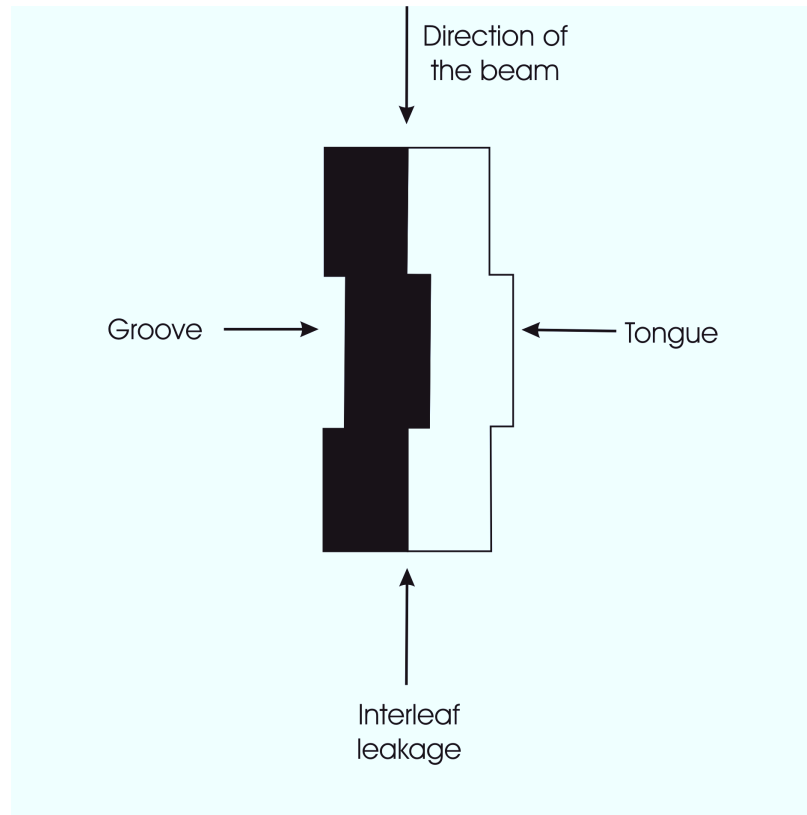
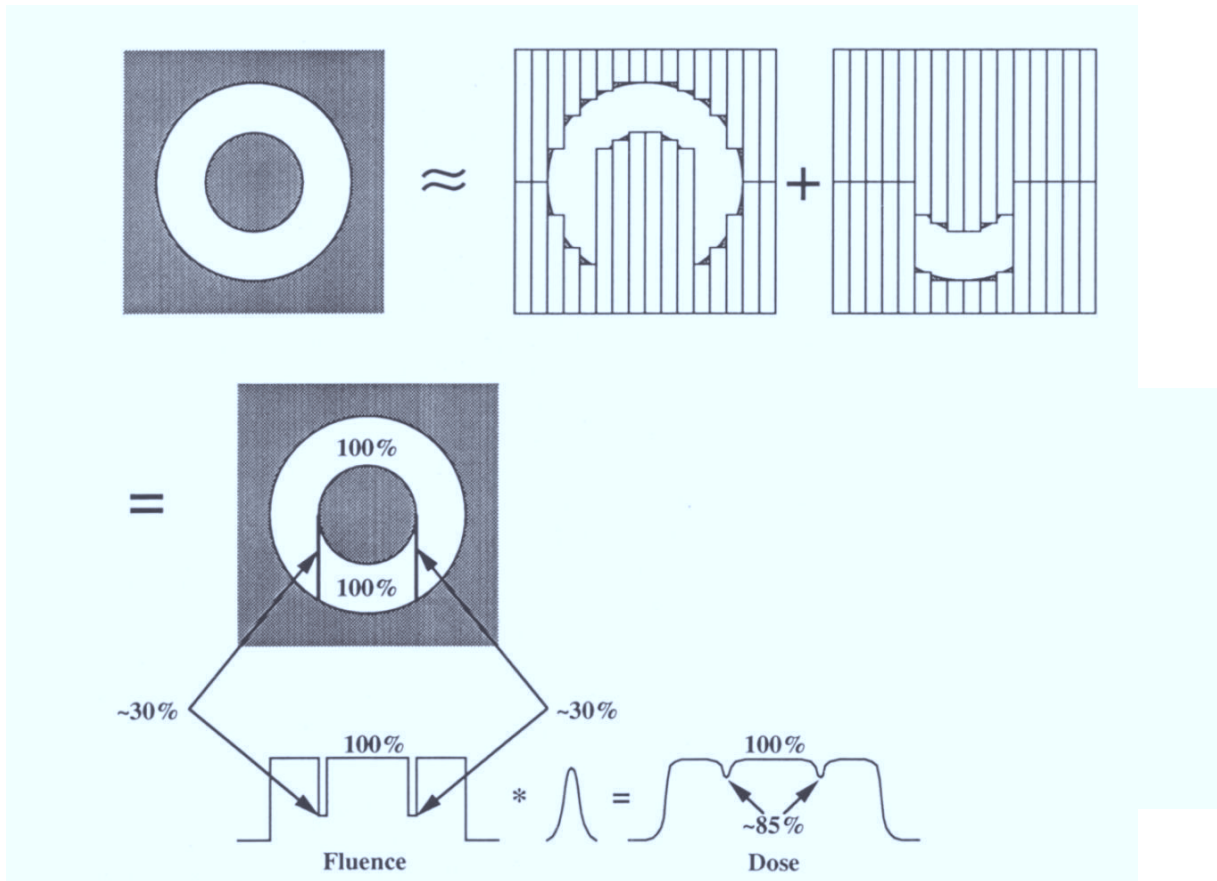


Figure 2.5 [Tongue-and-Groove Effect]: The tongue-and-groove effect is described in this figure. A circular aperture can be achieved by creating two segments with the MLCs. The regions where the tongues and grooves overlie one another are found in the bottom left of the figure. Examining the profile taken across the position of the arrowns, there is approximately a 30% fluence reduction in the areas where the segments overlap. This results in about a 15% dose reduction, taking into account blurring attributed to the lateral scatter of photons. (Adapted figure reprinted from “Seminars in Radiation Oncology, Volume 5, Issue 2, R. Mohan, *Field shaping for three-dimensional conformal radiation therapy and multileaf collimation*, pages 86-99, 1995” with permission from Elsevier granted on June 30, 2011 [18].)



2.1.4 Monte Carlo Simulation and EGSnrc

The gold standard in radiation transport calculations is the Monte Carlo simulation technique [19]. Monte Carlo simulation requires repeated sampling of random numbers in order to describe stochastic processes. This technique is useful in beam modeling and treatment planning applications. Monte Carlo simulation is desirable because it is versatile and able to accurately determine dose distributions in nearly any situation. When Monte Carlo techniques were first used to simulate radiation transport, only simple scenarios were possible (e.g. a point source incident on a homogenous slab phantom). As computing power increased, more complex situations could be simulated; presently, Monte Carlo simulation can be used for patient-specific treatment planning [20, 21]. The drawback of Monte Carlo simulations for most clinically relevant radiation transport is that they take a great deal of time if a high degree of accuracy is required.

There are multiple families of codes that are used to simulate external beam radiation therapy: EGS, MCNP, PENELOPE, GEANT. The most commonly used code in the radiotherapy community is based on EGS4 (Electron Gamma Shower 4) [22]. EGS4 was initially used to simulate the high energy linear accelerator at SLAC (Stanford Linear Accelerator Center), but Kawarakow *et al.* [23], Rogers *et al.* [24] and others [14, 25] at the National Research Council of Canada in the Ionizing Radiation Standards laboratory have customized EGS4 for improved accuracy in the therapeutic and diagnostic energy ranges and renamed the code EGSnrc. The EGSnrc family of codes specifically handles many applications in radiation therapy, including clinical linear accelerators, phantoms, patients (as represented by CT data sets) and ionization chambers.

2.1.4.i *BEAMnrc, DOSXYZnrc, DOSRZnrc and other software related to EGSnrc*

BEAMnrc is a software package that utilizes EGSnrc code to simulate individual components in the linear accelerator head and allows combining the components into a complete description [24]. All head components (complete with dimensions and composition) are created using the manufacturer's design and blueprints. Various component modules are available to describe a wide variety of geometries, such as SLABS (models a series of slabs or a single slab, like the target), CONESTAK (models a series of cones or cylinders), FLATFILT (handles the complex schematics of a flattening filter and is similar to CONESTAK), JAWS (models secondary collimators), DYNVMLC (models the complex Varian MLCs used in IMRT delivery) and others.

The probability of photon interaction is dictated by the linear attenuation coefficient (or interaction cross-section), which is dependent on the properties of the material and energy of the photon. This attenuation information is generated and saved in a look-up file using PEGS4 (Preprocessor for EGS4) [23]. Data about the material (whether it is an element, compound or mixture; atomic composition; etc.) is entered into the program and a series of photon cross-sections for a range of energies is created. The random numbers are sampled against the cross-sections, determining whether the photon will interact in the material, and by what type of interaction. (See Section 8.2 in the Appendix for a more detailed discussion on Monte Carlo simulation.) Compton scattering, pair production, photoelectric effect and Rayleigh scattering are all simulated in BEAMnrc, with all the relevant interaction cross-sections contained in the PEGS4 data file. After the photon interacts, the resulting particles (e.g. scattered photon and electrons) will also be tracked,

with the scattered photon able to interact again according to the cross-sections valid for its energy. Any electrons created will slowly lose kinetic energy while depositing dose in the medium. BEAMnrc is also able to simulate electron interactions including the bremsstrahlung creation process, in order to fully simulate radiation transport in the variety of materials used in radiotherapy including the linear accelerator and patients/phantoms. PEGS4 data files also include bremsstrahlung production cross-sections.

The output of a BEAMnrc simulation is a phase-space file that contains all the information describing the photons and charged particles crossing a user-specified plane. This file can be analyzed to determine fluence exiting the linear accelerator through the phase-space file processing algorithm (BEAMdp) or through in-house software. The phase-space file can also be used as input into other EGS family codes to determine dose delivered to a specific object (detector, phantom, patient CT).

DOSXYZnrc and DOSRZnrc are EGSnrc user-codes and are designed to calculate dose delivered to modeled objects in Cartesian and cylindrical coordinates, respectively. The incident radiation on the modeled object can be an electron beam or photon beam in a variety of source configurations, or a phase-space file generated by BEAMnrc containing a mixture of photons and electrons to take into account electron contamination in the beam.

2.2 IMRT DOSIMETRY DEVICES

As discussed previously, IMRT treatments involve complex processes that deliver highly-modulated fluence patterns. In contrast to three-dimensional conformal radiation therapy (3D-CRT), the fluences of IMRT fields are not easily inferred from the field aperture. IMRT typically creates steeper dose gradients in the patient and more highly conformal dose distributions than those achievable with 3D-CRT. Therefore, dosimetric verification of IMRT fields is even more critical than for 3DCRT fields. The highly modulated fields make the choice of verification detector more challenging compared to simpler fluence delivery scenarios. The detector must have a fine spatial resolution to minimize volume averaging effects, which occurs when the detector's cross-sectional area is larger than the field size or dose gradient being measured. Smaller detector sizes typically exhibit poorer signal-to-noise, though. The detector would ideally exhibit a linear response for ease of modeling, possess the ability to measure absolute dose, and have the potential for an integrated dose reading to obtain a cumulative dose for the entire treatment. A combination of detectors can also be used to satisfy all requirements [26].

IMRT patient-specific dosimetry can be carried out pre-treatment (prior to patient treatment) or during treatment (*in vivo*). Currently at CancerCare Manitoba, every IMRT patient's plan is verified prior to treatment delivery. A point dose measurement in an IMRT quality assurance (QA) phantom and one or more two-dimensional film images are taken for the composite delivery of all beams (usually about 4-9 per patient). The measurements are then compared, using the γ -evaluation [27], to results obtained from the TPS, using the QA phantom in place of the patient's CT dataset for the TPS's

calculations and comparisons. Pre-treatment verification measurement may also be carried out in three dimensions with polymer gel dosimetry devices. Monte Carlo simulation is being investigated by one group as a replacement for film and point dose measurements, as Monte Carlo is considered the gold standard for radiotherapy calculations [28]. This technique would need to be rigorously validated against measurement for a variety of patient plans before being implemented. The authors suggested that Monte Carlo simulation be used as a screening tool to mark TPS plans that do not agree, with measured verification only occurring as a secondary check.

In vivo verification techniques require a measurement obtained during treatment. With IMRT, array detectors are clearly beneficial as the entire field can be examined. Ion chamber arrays, such as IBA Dosimetry's transmission ray detector (Schwarzenbruck, Germany) and PTW's DAVID (Freiburg, Germany), could measure the dose entering the patient and EPIDs [29-35] have been used to measure beams exiting the patient. Comparisons to calculated or TPS results can be carried out in two and three dimensions.

Every verification technique and IMRT dosimetry device has advantages and disadvantages. The following sections describe most devices and what aspect of patient-specific IMRT dosimetry they are useful for.

2.2.1 Point measurement devices

Ionization chambers are usually placed inside a water phantom or a specialized IMRT phantom. Cylindrical ionization chambers are typically used because they possess a

number of useful qualities for dose measurement: 1) linear response with dose and dose rate, 2) high stability, 3) directional independence, 4) independence with respect to beam quality and 5) the ability to calibrate individual chambers to a standard chamber [26]. One drawback of ion chambers is that when using a small chamber, positioning of the chamber becomes extremely important because a small error in the chamber position can potentially result in a large error in the dose measurement due to the presence of steep dose gradients. For this reason, typically one attempts to position ion chambers in homogeneous dose regions away from areas of steep gradients. Large chambers can also be problematic due to the influence of partial volume effects.

Solid state dosimeters, like diodes, MOSFETs and diamond detectors, typically have smaller sensitive volumes than ionization chambers. Their small volume and high sensitivity to radiation in comparison to ion chambers (20 to 100 times greater) [26] make solid state dosimeters suitable for IMRT and small-field dosimetry. Diode detectors are usually used for on-axis field areas but care must be taken when using them for off-axis areas, since they are more sensitive to low-energy photons (as compared to water-equivalent detectors) due to their higher atomic number material (silicon) [26]. Diodes often possess a directional dependence (the value of the dose detected can vary by up to 3% for beams perpendicular to the diode as opposed to parallel beams) [21] and can suffer from irreversible radiation damage, which limits their sensitivity. Metal oxide semiconductor field effect transistors (MOSFETs) are easy-to-use dosimeters that possess a small detector size and a linear response with dose [36]. These detectors possess a directional dependence as well, with a maximum of 2.5% variation at gantry

angle 90°, as compared the value obtained at gantry angle 0° [36]. The atomic composition of diamond detectors is close to tissue-equivalent (carbon), but the physical density is much greater (3.5 times that of water). Diamond detectors also have less of a directional dependence (< 1 % for angles $\pm 135^\circ$ [37]) and a higher resistance to radiation damage in comparison to diode detectors. Unfortunately, diamond detectors possess a dose-rate dependence that makes them unsuitable for IMRT dose distributions [26]. Solid state dosimeters work best as relative dosimeters and as a check to ionization chamber measurements[26].

Thermoluminescent dosimeters (TLDs) are an integrating dosimeter, commonly configured in chip, rod or powder form, with an atomic composition close to tissue. TLDs are very portable and do not need to be connected to a power source during irradiation. TLDs require a sensitivity calibration with each use due to energy response variations and their sensitivity decreases over time with use. The achievable accuracy of TLDs is only about 3-5% with careful use and they should not be used in situations where a precision better than 3% is needed [26]. The use of TLDs is time- and labour-intensive, which limits their use to situations where ionization chamber measurements are unfeasible, such as multiple measurement positions or measurements on the patient skin surface during treatment.

2.2.2 Two-dimensional tools and devices

Radiographic film is useful in relative IMRT dosimetry and modeling beam penumbra due to its high spatial resolution. Disadvantages to using radiographic film include

labour-intensive chemical processing, over-sensitivity to low energy photons (due to silver halide content in the emulsion layer) and a lack of reliable absolute dosimetry capability. Radiochromic film differs from radiographic film in that it is nearly tissue-equivalent and it does not require development with a chemical processor prior to reading the image. However, a long time period is required for the radiochromic film to 'set' after irradiation (typically overnight) before readout. Early versions of radiochromic film were too insensitive to radiation to be used for IMRT measurements. A newer version of radiochromic film has an improved sensitivity, but pixel-to-pixel noise may limit its precision, especially in low dose areas [26]. Radiographic and radiochromic film can be used for absolute dose measurements but their use is challenging and typically results in large dose uncertainties. Film does work very well for two-dimensional IMRT field relative dosimetry, can be used for field-by-field verification and when used in combination with an ion chamber, is effective for absolute dosimetry [26].

Array detectors are attractive for IMRT dosimetry because unlike film, they operate in real-time, obtaining a two-dimensional image after each field delivery. Diode array detectors typically have low spatial resolution compared to film – the first commercially available diode detector array had a resolution of 0.707 cm in a 10x10 cm² central region, with a 1.414 cm resolution in the outer areas of the array. Ionization chamber arrays also typically have a larger pixel size of about 1 cm, but are quite stable (1% within 4 months) and very linear with dose. Neither type of array detector (diode or ionization chamber) is suitable for commissioning a linear accelerator that will deliver IMRT treatments due to

the low spatial resolution, but they are useful for routine quality assurance (QA) checks [26].

EPIDs, in particular a-Si EPIDs, have been investigated for a variety of IMRT QA processes including leaf-positioning verification [38, 39], clinical IMRT verification [29-35, 40, 41] and radiation vs. light field checks [42]. EPIDs are already available with most clinical linear accelerators, they operate in real-time (as opposed to film) and they possess a much finer spatial resolution in comparison to array detectors. A drawback to using EPIDs are that the only way to obtain a cumulative dose value for an entire treatment is to carry out a full patient dose reconstruction, for which there currently is no commercial software available [26]. Other drawbacks are that the EPID cannot be placed within a phantom (unlike film and ion chambers) and the EPID measures dose to phosphor instead of dose to water. EPIDs, however, can be used for pretreatment IMRT field QA and transit dosimetry through a patient or phantom if one compares the measurement to a predicted EPID image (see Section 2.4 on Portal Dosimetry). At this time, EPIDs are recommended by AAPM Task Group 120 [26] to be used for individual field QA once patient IMRT verification is established with an ion chamber and film.

2.2.3 Three-dimensional detectors

Three-dimensional dosimetry comprises techniques that allow a full 3D dose distribution to be measured. The technique is particularly attractive for the investigation of new treatment delivery procedures [26]. Original 3D dosimeters were gel-based, leading to the term “gel-dosimetry”, but there has been development of 3D dosimeters that are plastic

instead [43, 44]. Currently, 3D dosimetry techniques are typically explored in a research capacity.

Polymerizing polyacrylamide gels (PAGs) contain molecules which polymerize when exposed to radiation, proportional to the dose accumulated. The gel polymerization changes other properties, notably the water protons' magnetic resonance (MR) characteristics and optical scattering capabilities. A disadvantage to some types of PAGs is that the gels are susceptible to atmospheric oxygen and need to be manufactured in a hypoxic environment [45]. Another gel dosimeter was created [46] using a gelled version of the liquid Fricke dosimeter [47] (a ferrosulphate solution). One drawback to the Fricke gel dosimeter is that the dose distribution fades with time and must be scanned within 2 hours of irradiation [48]. The dose distributions of both PAGs and Fricke gels may be determined using MR and optical-CT (with a laser replacing the x-ray source) scanning; IMRT verification with the PAG technique in particular appears promising [49-51]. Currently, the only commercial product capable of 3D dosimetry is one made of polyacrylamide gel (named "BANG" after its component compounds [52]) from MGS Research Inc. (Madison, CT) [26].

A new polymerizing material has been created for 3D dosimetry: PRESAGE [43, 44]. PRESAGE is composed of a radiochromic plastic and has shown potential as a 3D dosimeter because the dose response is insensitive to atmospheric oxygen, unlike gel dosimeters. Also, the polymers absorb light rather than scatter it during optical-CT scanning, leading to a more accurate dose read-out [53].

2.3 PORTAL IMAGING

A portal image is a digital or film image created from a field (or “port”) of radiation exiting the patient. Portal imaging devices were originally used in the clinic to verify patient set-up, with the images compared to planning images or digitally reconstructed radiographs from the planning CT data. The patient’s bony anatomy is compared between the two images to ensure the patient is in the correct position – the planned position. In addition, portal images of the treatment field may be used to verify the aperture shape.

A variety of portal imaging techniques have been used over the years, with the first widely-adopted approach being film cassettes in the mid-1970s [54]. Although film creates a portal image with high spatial resolution, it has a few drawbacks. The film needs to be developed in a chemical film processor unit after every exposure, creating a time delay between obtaining the set-up image, verifying position and delivering treatment, adding to the overall patient treatment time. This is undesirable since setup errors increase the longer the patient remains on the couch [55]. Image contrast is highly dependent on delivering an appropriate dose to the film, which then depends on the human operator selecting the appropriate setting on the treatment unit for an estimated patient thickness. Furthermore, the physical bulk of film poses challenges for long term storage, recall and reference.

Due to these issues, film for portal imaging has largely been replaced by electronic portal imaging devices (EPIDs) [54-56]. These devices provide a much faster read-out (real-time or nearly real-time) and allow for the patient to be repositioned more quickly. The

first generation of commercial EPIDs was either camera-based (Siemens, Elekta/Philips) or a matrix of liquid ionization chambers (Varian). The second generation of EPIDs became available in the early 2000s and employ an active matrix flat-panel imager (AMFPI). This technology is the current standard in the clinic and is available from most radiation therapy linear accelerator vendor.

2.3.1 Camera-based EPIDs

A prototype for the camera-based EPID dates back to the 1950s [57, 58], but was not commercially implemented until the 1990's [59-70], likely due to lack of cost-effective technology. A metal plate (usually copper), backed with a scintillating screen (usually a phosphor such as gadolinium oxysulphide) converts incident x-rays to optical photons. The incident x-rays interact in both the metal plate and the phosphor, creating high-energy electrons that deposit energy in the phosphor. This energy is converted to optical photons in the phosphor layer, some of which leave the phosphor and are observed by the camera. Due to the camera being very susceptible to radiation damage, the camera is positioned outside of the primary beam, usually mounted in a shielded area recessed within the gantry. Therefore, camera-based systems need one or two mirrors to redirect the optical photons from the phosphor to the camera. These systems then also require a light-tight enclosure surrounding the phosphor-mirror-camera components, resulting in a somewhat cumbersome device. If the camera is analog instead of digital, then the signal is digitized before recording.

A weakness of this system is its low detective quantum efficiency (DQE), an image quality measure based on the efficiency of the imager to create an output signal from an input signal. The maximum DQE achieved using a camera-based system is approximately 1% [71, 72], even after much research into optimizing the performance (i.e. using CCD cameras) [70]. The main reason the DQE is low is due to the bulky design of these systems incorporating a long, inefficient optical path (consisting of mirrors and lenses) between the phosphor and the camera, resulting in large optical photon losses. Also, optical photons from the phosphor may scatter but still be detected by the camera. The scattered optical photons appear to be created at one position in the screen when they actually originate elsewhere. This is called the optical glare effect and is present when scattered optical photons reach the camera. The glare effect in the final image can account for more than 25% of the total signal, and serves to degrade image contrast [72]. The camera optical components usually add barrel-distortion into the image, degrading geometric accuracy. The camera-based EPIDs do have a high spatial resolution (0.8 to 1.0 mm) [73], but the resulting image quality is still fairly poor due to the low DQE and presence of significant optical glare.

2.3.2 Scanning liquid ionization chamber (SLIC) EPID

The scanning liquid ionization chamber (SLIC) EPID was developed by a group at the Netherlands Cancer Institute in the 1980s [74-78]. The EPID consists of two planes of electrodes, separated by a 0.8 mm gap filled with fluid (iso-octane) and a plastoferrite plate. X-rays interacting with the plastoferrite plate create high energy electrons, which then ionize the fluid. A matrix of 256x256 electrodes (at a resolution of 1.27 mm for each

pixel) collect the ions. Each row of electrodes is read sequentially and then recorded, which results in an image in about five seconds.

Advantages to the SLIC EPID are its compact design and its lack of geometric distortion in the resulting image. A disadvantage is the low DQE of ~0.5%. The sequential read-out (i.e. high voltage applied to one electrode at a time) of the system also causes much of the generated signal in the liquid to be lost. Although the image is available in near real-time and digitally, the image quality is fairly poor.

2.3.3 Active matrix flat-panel imagers (AMFPIs)

Active matrix flat-panel imagers are currently the standard type of portal imager used in cancer treatment centers [54-56]. Like the camera-based EPIDs, the AMFPIs are also comprised of a metal plate backed by a phosphor screen. However, the optical photons are captured by a two-dimensional grid of photodiodes instead of a camera. The photodiodes and accompanying thin-film transistor switches of current commercial flat-panel imagers are made of hydrogenated amorphous silicon (a-Si). When the photons interact in the copper layer of the EPID (through Compton scatter, the photoelectric effect and pair production), the scattered electrons create optical photons in the phosphor layer. The generated optical photons create electron-hole pairs in the photodiodes, where the accumulated charge is converted to a digital signal. The a-Si EPIDs are read out line-by-line, but at a much faster rate than the SLIC EPID, with achievable read-out times less than ~ 0.125s [79]. Due to the use of a scintillator to convert incident x-ray energy to optical photons, this design is described as an “indirect detection” a-Si EPID. Although

not clinically used, several research groups have also investigated “direct detection” a-Si EPIDs which do not incorporate a phosphor layer to generate optical photons [80, 81]. In direct detection EPIDs the x-rays generate electron-hole pairs directly in the photodiodes. These distinctions in a-Si EPID design are mentioned here as a reference to the reader, but it should be noted that all current commercially available a-Si EPIDs are indirect detectors.

Investigations into the image quality of indirect a-Si EPIDs, showing that they have lower system noise (about 1%) than either camera or scanning liquid ionization chamber EPIDs, possess a detective quantum efficiency (DQE) 70-80% greater than camera-based EPIDs [82] and a modulation transfer function (MTF – a measure of spatial resolution) comparable to that of a camera-based EPID [55, 73, 82]. Amorphous-silicon EPIDs have a higher resolution than previous systems (1024x768 or 1024x1024, over a detector area of about 40x30 cm² or 40x40cm²), at about 0.39 mm per pixel side. The proximity of the phosphor to the light collectors (the photodiodes) improves optical photon collection efficiency and also reduces the optical photon glare observed in comparison to camera-based systems, resulting in a larger DQE compared to other EPID technologies.

The a-Si portal imagers are resistant to radiation damage, as long as the electronics surrounding the detector area are not irradiated. The imagers have been shown to be stable and reproducible over long periods of time [79, 83]. One potential drawback of a-Si EPIDs is the evidence of ghosting, or image lag, that occurs when charge in the photodiodes from a previous image remains and is read-out in the subsequent image to

create a latent image [83, 84]. The severity of this effect is dependent on the number of monitor units (MU – a measure of how long the beam is on) delivered to the EPID and the frame rate of the EPID. This effect is largest when imaging with a large number of MUs then a small number of MUs (>2% difference for a first to second dose ratio of greater than five times) [83]. During image collection of IMRT fields, the ghosting effect remains uncorrected due to the small effect on clinical fields (low MU and low delivery energies – 6 to 10 MV) [85].

A-Si EPIDs are known to possess desirable dose-measuring characteristics as well. Apart from the high efficiency and high spatial resolution of the system, the a-Si EPID is linear with dose and dose rate [79, 86]. The energy response of the flat-panel imager is not uniform; that is, the imager over-responds to low-energy photons (less than 1 MeV) in comparison to a water-equivalent detector [86, 87]. The over-response of the imager at low-energies needs to be accounted for when using the EPID for dosimetric purposes. Also, the flood-field processing of the image carried out automatically by the clinical acquisition software removes beam-specific information from the image (i.e. the beam “horns” or characteristic off-axis profile shape). However, this dosimetric information can be reintroduced into the image using a technique proposed by Greer [88] to remove the flood-field correction and account for the pixel sensitivity information. The acquired image (I) is automatically corrected from its raw form (I_{raw}) by subtracting the dark-field image (DF) and multiplying by the ratio of the mean value of the flood-field image (FF_{mean}) and the two-dimensional flood-field image (FF):

$$(2.2) \quad I(i, j) = \left(\frac{I_{raw}(x, y) - DF(x, y)}{FF(x, y)} \right) \cdot FF_{mean}.$$

To reintroduce the flood-field and obtain the raw image (retaining the dark-field correction), the acquired image is multiplied by the flood-field ratio:

$$(2.3) I_{raw}(x, y) = I(x, y) \cdot \frac{FF(x, y)}{FF_{mean}}.$$

The flood-field inherently corrects for any pixel-to-pixel sensitivities, therefore a measure of pixel sensitivity matrix (PSM) is required to account for this effect. In the work by Greer [88], the EPID was irradiated with a 10x25 cm² field and the EPID was displaced by 2.5 cm in the cross-plane direction after each irradiation. This created a cross-plane CAX profile of the pixel sensitivity. The PSM can be extended into two dimensions by assuming that the ratio of the flood-field profile to PSM profile is radially symmetric, and can be applied to the raw image to obtain the flood-field corrected image (I'):

$$(2.4) I'(x, y) = \frac{I_{raw}(x, y)}{PSM(x, y)}.$$

2.4 PORTAL DOSIMETRY

Verification of patient treatments with portal imaging may be carried out in a variety of methods generally classified as either “forward” or “inverse” approaches. A forward approach predicts the dose in the EPID via calculation and compares the results to measurement. An inverse approach uses a measured EPID image to derive the primary fluence at the EPID, which is then backprojected to calculate dose in the patient. The calculated patient dose is typically compared to the dose distribution determined by the treatment planning system. The inverse and forward approaches may be further divided into categories related to when the measurement is taken, i.e., ahead of treatment

delivery, often termed ‘pre-treatment’, or during treatment with the patient present, often termed ‘*in vivo*’.

Forward approaches can be performed with or without attenuating material in the beam. Groups have delivered the treatment fields to the EPID directly (no phantom) as a method of pre-treatment verification and compared the measured data to corresponding predicted images involving simulation of the EPID response [40, 89-94]. Transmission-dependent forward methods, that would be appropriate for use with a patient in the beam, have been developed and tested with simple water-equivalent slabs and anthropomorphic phantoms [86, 95-99]. Again, the measured EPID image is then compared to a calculation of the predicted portal dose image.

There has been some application of the forward method for patient dosimetry verification in the clinical setting. Kroonwijk *et al.* [34] compared EPID images acquired during patients’ prostate treatments with predicted images created using the patients’ planning CT data. Rectal gas pockets during the time of treatment caused differences between measurement and prediction of up to 15%. Van Elmpt *et al.* [99] collected data during a breast treatment, with the measurement compared to an image prediction technique that converts the patient’s CT to an equivalent homogeneous phantom (EHP). The prediction generally agreed with measurement within a 3% dose difference, but there were discrepancies seen at the border of the lung. In Pasma *et al.* [35], disagreements between measured and predicted portal images of more than 5% were found in prostate treatment images when the patient had large rectal gas pockets. van Zijtveld *et al.* [32] determined

that discrepancies between measured *in vivo* images and their portal dose image prediction were due to the differences in patient geometry compared to the planning CT and the effect of the treatment couch.

Inverse approaches can also be performed as pre-treatment or *in vivo*. For pre-treatment cases, the dose reconstruction is carried out in a virtual phantom or in the patient's planning CT dataset. McNutt *et al.* [100, 101] iteratively adjusted the incident primary energy fluence of the linac in the treatment planning system until the portal dose image prediction matched with the measured data. The prediction was carried out using an "extended phantom", which is an amalgamation of the phantom's CT dataset and the EPID [97]. This energy fluence was then used to determine the three-dimensional dose distribution in the planning CT to within 3%. van Zijtveld *et al.* [102] converted measured open images to delivered fluence in a fashion similar to McNutt *et al.* [100, 101]. The measured and predicted portal dose images (calculated using fluence exported from the TPS) were compared, and the fluence was iteratively adjusted until the measured and predicted images converged. This fluence was then imported into the TPS to calculate dose distributions in the patient's planning CT and was accurate within 2% and 2 mm. Van Elmpt *et al.* [103-105] calculated the three-dimensional dose distribution with Monte Carlo simulations in inhomogeneous phantoms and patients' planning CTs by extracting the energy fluence from measured non-transit portal images to an accuracy of 3% at isocentre. To obtain the energy fluence, van Elmpt *et al.*, deconvolved the lateral scatter dose from the open-field image to obtain the dose delivered to the EPID. The energy fluence is assumed to be proportional to the EPID dose, accounting for attenuation

in the EPID [105]. In another open image approach, Ansbacher reconstructed the three-dimensional dose distribution in a cylindrical virtual phantom using a non-transit image of an IMRT field [106]. This work used a calibration of the acquired EPID image to a calculation made with in-house software, as if the EPID was replaced by a cylindrical phantom, and compared to ionization chamber measurements acquired at the phantom. The author stresses that using a physical measurement is not required as a calculation in a TPS could also be employed [106]. The reconstruction results were within 2% of ionization chamber and film measurements. Spies *et al.* [107] determined primary energy fluence of fields delivered to a slab phantom by iteratively correcting for the phantom scatter. This is carried out using precalculated Monte Carlo scatter kernels that are dependent on the phantom's radiological pathlength. The energy fluence, determined from the removal of the scatter from the measured image, was then backprojected to the phantom. Partridge *et al.* [108] extended this method to involve more complex phantoms and a megavoltage cone-beam CT of the phantom to determine the phantom's exact position. IMRT fields were then delivered to the phantom, with the EPID collecting images during the "treatment". The energy fluence was backprojected to the megavoltage CT dataset to determine the dose distributions, which were within 3% and 3 mm of the planned distributions.

The inverse approach can also be performed *in vivo*, with the measured images acquired during patient treatment. McDermott *et al.*[29] collected EPID images during prostate patient treatments, with the *in vivo* verifications eventually replacing the pre-treatment verifications of IMRT treatments. van Zijtveld *et al.*[33] used daily cone-beam CT data to

determine prostate patients' daily delivered dose to within 3% and 3 mm. However, currently the vast majority of EPID dosimetry applications are carried out with radiation delivery directly to the EPID without phantoms or patients in the beam path.

2.4.1 Portal dosimetry research at the Antoni von Leeuwenhoek Hospital

At this time there is only one research group in the world that has significant experience with *in vivo* patient dose reconstruction using EPID dosimetry, and therefore warrants a focused discussion here. The Antoni van Leeuwenhoek Hospital in Amsterdam, The Netherlands, has used EPIDs for pre-treatment verification and delivery verification with two- and three-dimensional dose reconstruction in phantoms and patients since the mid-1990s. Their method was originally developed for liquid ionization chamber EPIDs [109] and has since been applied with a-Si EPIDs [29-31, 41, 103-105, 110-114]. The procedure includes a large set of empirical correction factors to account for i) the dose response of the EPID, ii) scatter dose within the EPID, iii) scatter from the patient or phantom incident on the EPID, as well as iv) scatter within the phantom or patient and v) attenuation within the phantom or patient that contributes to the total dose distribution [29, 31, 41, 103, 104, 112]. Factors i, ii and iv are corrected using profiles measured with an ion chamber and the functions used in each step were empirically fitted to the measured profiles.

The measured image first converts the EPID greyscale to dose values with the correction factor function that accounts for the dose response of the EPID (factor i). A pair of empirically derived EPID scatter kernels are applied to the portal dose image that is

corrected for lateral scatter (factor ii). The parameters of one of the scatter kernels (K_1), which itself is deconvolved from the dose image, are determined by matching CAX values between EPID measured images and ion chamber measurements. The parameters of the second scatter kernel (K_2) are derived from fits of EPID dose profiles to film measurements; K_2 is convolved with the result of the deconvolution. The scatter on the EPID due to the patient (factor iii) was determined by calculating the transmission of the patient – by taking the ratio of two measured portal dose images, one with and one without the patient in the beam. The signal remaining after removing the primary transmission is the scatter. With this method, for every image acquired with a patient or phantom, an image without the patient is required to estimate the transmission and therefore determine the primary dose delivered to the EPID. The primary dose and the patient transmission are required to calculate the primary dose at the radiological or geometrical midplane of the patient or phantom (factors iii and v). The scattered mid-plane dose (factor iv) is then determined by the convolution of an empirical kernel with the primary mid-dose and the scatter-to-primary ratio, which is a function of the primary transmission. In Wendling *et al.* [111], the dose from an IMRT field was reconstructed in simple, homogenous phantoms within a 2% dose difference and a 2 mm distance-to-agreement (DTA) as determined by the γ -evaluation.

Patient-specific IMRT QA with a homogeneous slab phantom in the beam eventually replaced film for pre-treatment verification at the Antoni van Leeuwenhoek center [41]. The resulting measured EPID image was then backprojected to the mid-plane of the slab using the method described in the previous paragraph. The two-dimensional dose

distributions generally agreed within 3% and 3 mm, with seven plans revealing small underdosage regions ranging from 5% to 16%. The underdosed areas exposed an error in the treatment planning system's model of the tongue-and-groove width; the error was not identified with the standard TPS commissioning fields. Further investigations of this verification technique into other treatment sites led to completely replacing the pre-treatment technique with *in vivo* dose verifications with success [29]. McDermott *et al.* determined that calculating the dose distributions for the first three to five fractions of a treatment was sufficient to verify the treatment fully [29].

The group then extended their procedure to enable calculations in three-dimensions. Initially, Monte Carlo simulations were used to calculate the three-dimensional dose. The EPID energy fluence was extracted from the measured image taken without a phantom in the beam, with Monte Carlo simulation providing the dose distribution calculation in a homogeneous phantom [105]. This pre-treatment method was extended to include dose calculation in an inhomogeneous phantom [104] and then patient CT data [103]. The group also extended the full backprojection technique (as presented in Wendling *et al.*[111]) to three dimensions [112]. The original two-dimensional method was employed and calculated in many planes parallel to the EPID plane. The patients' CT datasets were used in place of the phantoms, but the inhomogeneity of the patient was not accounted for. These three-dimensional dose calculations then required depth-dependent corrections to be added to the model. The beam hardening with depth was explicitly modeled as an attenuation correction and depth dependence was added to the function used to determine

the scatter within the patient. The dose build-up effect was empirically modeled to improve accuracy.

The Dutch group has had much success with their empirical modeling of portal dose image formation, as well as backprojection-based patient dose reconstruction. A recent (2011) investigation included an explicit calculation for patient transmission, removing the requirement for acquiring an open-field image and an image with the patient for each field delivered [114]. However, many aspects of the calculation are still based upon empirical fits instead of physics basis – which would be highly desirable. A physical model based on a greater understanding of the physics of portal dose imaging would facilitate a deeper understanding of the processes occurring and allow for greater flexibility in the types of treatments that could be modeled.

The approach investigated in this thesis includes a physics-motivated portal dose image prediction model, that uses results from Monte Carlo simulation to model the primary and patient scatter fluence incident on the EPID and the dose delivered to the EPID. The measured data required to create a fluence model is limited to that required for “commissioning” of the portal dose image prediction model (i.e. open-field, square and rectangular images). The source parameters of the fluence model are adjusted to match the predicted results to the measured results to account for the individuality of the linac being modeled. This is an empirical determination of the parameters but the functions are based on analytical representations of the photon sources confirmed by the literature (focal source) and Monte Carlo simulation (extrafocal source).

The leaves of the MLC are accurately modeled by taking into account the interleaf leakage and rounded leaf-tips. The fluence of any linac could be modeled with this method, as long as the manufacturer schematics are available for the Monte Carlo simulation and MLC model. As the MLC modulate the fluence in IMRT treatments, the patient treatment plan which includes the weighted MLC positions for every field (i.e. how many monitor units (MU) are delivered for a particular MLC position). The algorithm created here can implement treatment plans from two most common TPSs for calculation of the incident fluence: Eclipse (Varian Medical Systems, Palo Alto, CA) and Pinnacle (Philips Medical Systems, Milpitas, CA).

The attenuation of the beam by the patient is calculated directly through an equivalent homogeneous phantom (EHP) created from the patient's CT dataset. The patient scatter fluence incident on the EPID is calculated with the use of pre-calculated patient scatter fluence kernels. The scatter fluence kernels are created from the results of Monte Carlo simulation of a polyenergetic beam incident on a range of water slab thicknesses and reconstructed over a clinically relevant range of air gaps.

The dose calculated at the EPID plane used pre-calculated dose kernels, specific to the EPID used to collect the measured images. The Monte Carlo-simulated dose kernels used the manufacturer schematics of each layer in the EPID and represent dose delivered to the phosphor layer of the EPID – the image formation layer – due to an ideal incident pencil beam of photons. This method inherently models the over-response of the EPID with

respect to water for low-energy photons. The optical photon glare is modeled using a result of a Monte Carlo simulation (taken from the literature). Furthermore, an empirical model to estimate the asymmetric backscatter of the EPID support arm was included to further improve accuracy. Finally, to ensure greater accuracy in the model, an empirical correction related to the phantom thickness, field size and air gap was implemented in a manner similar to that seen in TPSs.

The portal dose image prediction method presented in this thesis is general enough to be implemented in any clinic and requires little *a priori* knowledge to predict an accurate, patient-specific portal dose image.

2.5 THESIS SUMMARY

IMRT for patient radiotherapy TPS consists of complex processes, both in treatment planning and delivery. Due to this inherently intricate nature of the plans, verification of patient treatments *in vivo* would be highly advantageous. The portal dose image prediction model described in this thesis is applicable to a wide variety of treatment plans and treatment sites.

In Chapter Three, the parallel dose kernel assumption for EPID dose calculation is examined. For treatment planning and patient dose calculations, a dose kernel derived in a parallel geometry is typically used, even though the beam is divergent, to increase the speed of dose calculation. This assumption had never been tested for EPID dose calculation. In this chapter, the effect of using parallel vs. tilted dose kernels (ranging

from incident pencil beam angles of 2° to 14°) to calculate EPID dose is tested through convolution (parallel) and superposition (tilted) with a simple fluence. It was shown that the parallel dose kernel assumption is valid for clinically relevant situations.

Chapter Four discusses the development of a versatile, physics-based fluence model. This model is based on the Pinnacle TPS (Philips Medical Systems, Milpitas, CA). The comprehensive fluence model consists of a focal source (represented by a Gaussian function) and an extrafocal source (a Gaussian-like function). Aspects of the MLC are accounted for in a similar fashion to Pinnacle (i.e. a half-circle to represent the rounded leaf-tip and transmission factors to account for interleaf leakage and transmission through the MLCs). The effect of the jaws and the tongue-and-groove effect were also modeled. The energy spectra for each source was calculated using Monte Carlo and the focal spectrum was softened off-axis. The portal dose image was determined through the convolution of the energy fluence with a series of monoenergetic dose kernels specific to the aS1000 EPID, also calculated using Monte Carlo. The comprehensive fluence model was commissioned with square and rectangular open-field images obtained with the EPID. The model parameters were adjusted until the predicted and measured images matched within 2% and 2 mm. The fluence model was then tested on 10 prostate and 10 head-and-neck IMRT treatments, with the EPID images obtained with no attenuating material in the beam. The results showed that the comprehensive fluence model was able to predict IMRT treatments within 2% and 3 mm.

Chapter Five includes a discussion of the improvements to the comprehensive fluence model and the incorporation of a patient scatter prediction. In the comprehensive fluence model, blueprints obtained from the vendor improved the modeling of the MLC leaves. Transmission through the MLC was then explicitly calculated using Monte Carlo-simulated energy fluence, as was the incident energy fluence across the entire field. The patient/phantom scatter was determined with a precalculated library of Monte Carlo-generated scatter fluence kernels, for various water thicknesses and air gaps. The appropriate scatter kernel would be applied at the EPID plane to account for the scatter fluence due to the phantom. The algorithm was tested against measured images for a number of thicknesses of slab phantoms (2 to 25 cm) and air gaps (15 to 50 cm) for square fields. A prostate and a head-and-neck IMRT plan were also delivered to slab phantoms, yielding in a prediction accuracy of 3% and 3 mm.

Chapter Six is an examination of portal dose images obtained during patient treatment, or also commonly described as *in vivo*. Transit images for 11 IMRT patients (5 prostate and 6 head-and-neck plans) were acquired throughout the entire treatment. The portal dose image prediction algorithm was able to predict portal dose images generally within 3% and 3 mm. Details of the patient treatment bed were not accounted for in the prediction and led to some areas of disagreement, particularly for the prostate patients. Prostate patient image prediction also was influenced by gas pockets found in the rectum, leading to areas of underprediction. Head and neck patients were seen to have lost weight during treatment, illustrated by an increase in measured dose.

Chapter Seven summarizes the thesis and discusses future investigations that will be performed building on the portal dose image prediction model developed and tested here, and its application to the dosimetric verification of patient treatments.

The appendix to this thesis contains a glossary of commonly used technical terms, details concerning Monte Carlo simulation, the analysis of images and how to acquire EPID images. The specific parameters used in Chapters 4 and 5 are also further described. The appendix also includes permissions acquired to reprint the previously copyrighted material presented in this thesis.

REFERENCES

1. Vassiliev, O. N., Titt, U., Ponisch, F., Kry, S. F., Mohan, R., and Gillin, M. T., *Dosimetric properties of photon beams from a flattening filter free clinical accelerator*. Phys Med Biol, 2006. **51**: p. 1907-1917.
2. Ahnesjo, A., *Analytic modeling of photon scatter from flattening filters in photon therapy beams*. Med Phys, 1994. **21**(8): p. 1227-35.
3. Ahnesjo, A., *Collimator scatter in photon therapy beams*. Med Phys, 1995. **22**(3): p. 267-78.
4. Ahnesjo, A., Saxner, M., and Trepp, A., *A pencil beam model for photon dose calculation*. Med Phys, 1992. **19**(2): p. 263-73.
5. Ahnesjo, A., Weber, L., Murman, A., Saxner, M., Thorslund, I., and Traneus, E., *Beam modeling and verification of a photon beam multisource model*. Med Phys, 2005. **32**(6): p. 1722-37.
6. Ahnesjo, A., Weber, L., and Nilsson, P., *Modeling transmission and scatter for photon beam attenuators*. Med Phys, 1995. **22**(11 Pt 1): p. 1711-20.
7. Jaffray, D. A., Battista, J. J., Fenster, A., and Munro, P., *X-ray sources of medical linear accelerators: focal and extra-focal radiation*. Med Phys, 1993. **20**(5): p. 1417-27.
8. Sharpe, M. B., Jaffray, D. A., Battista, J. J., and Munro, P., *Extrafocal radiation: a unified approach to the prediction of beam penumbra and output factors for megavoltage x-ray beams*. Med Phys, 1995. **22**(12): p. 2065-74.
9. Mohan, R., Chui, C., and Lidofsky, L., *Energy and angular distributions of photons from medical linear accelerators*. Med Phys, 1985. **12**(5): p. 592-7.
10. Mackie, T. R., Scrimger, J. W., and Battista, J. J., *A convolution method of calculating dose for 15-MV x rays*. Med Phys, 1985. **12**(2): p. 188-96.

11. Papanikolaou, N., Mackie, T. R., Meger-Wells, C., Gehring, M., and Reckwerdt, P., *Investigation of the convolution method for polyenergetic spectra*. Medical Physics, 1993. **20**(5): p. 1327-1336.
12. Johns, H. E. and Cunningham, J. R., *The Physics of Radiology*. 4th ed. 1983, Springfield, IL: C. C. Thomas,
13. Philips Medical Systems, *Pinnacle³ Physics Reference Guide, Release 7.6*, 2005.
14. Mackie, T. R., Bielajew, A. F., Rogers, D. W. O., and Battista, J. J., *Generation of photon energy deposition kernels using the EGS Monte Carlo code*. Physics in Medicine and Biology, 1988. **33**(1): p. 1-20.
15. Ma, C. M. and Jiang, S. B., *Monte Carlo modelling of electron beams from medical accelerators*. Phys Med Biol, 1999. **44**(12): p. R157-89.
16. Ahnesjo, A., *Collapsed cone convolution of radiant energy for photon dose calculation in heterogeneous media*. Med Phys, 1989. **16**(4): p. 577-92.
17. Deng, J., Lee, M. C., and Ma, C. M., *A Monte Carlo investigation of fluence profiles collimated by an electron specific MLC during beam delivery for modulated electron radiation therapy*. Med Phys, 2002. **29**(11): p. 2472-83.
18. Mohan, R., *Field shaping for three-dimensional conformal radiation therapy and multileaf collimation*. Semin Radiat Oncol, 1995. **5**(2): p. 86-99.
19. Verhaegen, F. and Seuntjens, J., *Monte Carlo modelling of external radiotherapy photon beams*. Physics in Medicine and Biology, 2003. **48**: p. R107-R164.
20. Ma, C. M., Mok, E., Kapur, A., Pawlicki, T., Findley, D., Brain, S., Forster, K., and Boyer, A. L., *Clinical implementation of a Monte Carlo treatment planning system*. Med Phys, 1999. **26**(10): p. 2133-43.
21. Ma, C. M., Li, J. S., Pawlicki, T., Jiang, S. B., Deng, J., Lee, M. C., Koumrian, T., Luxton, M., and Brain, S., *A Monte Carlo dose calculation tool for radiotherapy treatment planning*. Phys Med Biol, 2002. **47**(10): p. 1671-89.
22. *The EGS4 Code System*, Stanford Linear Accelerator Center: Stanford, California. 1985.
23. Kawarakow, I., Mainegra-Hing, E., Rogers, D. W. O., Tessier, F., and Walters, B. R. B., *The EGSnrc code system: Monte Carlo simulation of electron and photon transport*. 2010, Ionizing Radiation Standards, National Research Council of Canada.
24. Rogers, D. W. O., Faddegon, B. A., Ding, G. X., Ma, C. M., We, J., and Mackie, T. R., *BEAM: a Monte Carlo code to simulate radiotherapy treatment units*. Med Phys, 1995. **22**(5): p. 503-24.
25. Sheikh-Bagheri, D. and Rogers, D. W. O., *Monte Carlo calculation of nine megavoltage photon beam spectra using the BEAM code*. Med Phys, 2002. **29**(3): p. 391-402.
26. Low, D. A., Moran, J. M., Dempsey, J. F., Dong, L., and Oldham, M., *Dosimetry tools and techniques for IMRT*. Medical Physics, 2011. **38**(3): p. 1313-38.
27. Low, D. A., Harms, W. B., Mutic, S., and Purdy, J. A., *A technique for the quantitative evaluation of dose distributions*. Med Phys, 1998. **25**: p. 656-61.
28. Goetzfried, T., Rickhey, M., Treutwein, M., Koelbl, O., and Bogner, L., *Monte Carlo simulations to replace film dosimetry in IMRT verification*. Zeitschrift für Medizinische Physik, 2011. **21**(1): p. 19-25.

29. McDermott, L., Wendling, M., Sonke, J., Vanherk, M., and Mijnheer, B., *Replacing Pretreatment Verification With In Vivo EPID Dosimetry for Prostate IMRT*. Int J Radiat Oncol Biol Phys, 2007. **67**(5): p. 1568-77.
30. Mans, A., Wendling, M., McDermott, L. N., Sonke, J. J., Tielenburg, R., Vijlbrief, R., Mijnheer, B., van Herk, M., and Stroom, J. C., *Catching errors with in vivo EPID dosimetry*. Med Phys, 2010. **37**(6): p. 2638-44.
31. McDermott, L., Wendling, M., Nijkamp, J., Mans, A., Sonke, J., Mijnheer, B., and Vanherk, M., *3D in vivo dose verification of entire hypo-fractionated IMRT treatments using an EPID and cone-beam CT*. Radiother Oncol, 2008. **86**(1): p. 35-42.
32. van Zijtveld, M., Dirkx, M., Breuers, M., de Boer, H., and Heijmen, B., *Portal dose image prediction for in vivo treatment verification completely based on EPID measurements*. Med Phys, 2009. **36**: p. 946-952.
33. van Zijtveld, M., Dirkx, M., Breuers, M., Kuipers, R., and Heijmen, B., *Evaluation of the 'dose of the day' for IMRT prostate cancer patients derived from portal dose measurements and cone-beam CT*. Radiother Oncol, 2010. **96**: p. 172-177.
34. Kroonwijk, M., Pasma, K. L., Quint, S., Koper, P. C., Visser, A. G., and Heijmen, B. J., *In vivo dosimetry for prostate cancer patients using an electronic portal imaging device (EPID); demonstration of internal organ motion*. Radiother Oncol, 1998. **49**(2): p. 125-32.
35. Pasma, K. L., Kroonwijk, M., Quint, S., Visser, A. G., and Heijmen, B. J., *Transit dosimetry with an electronic portal imaging device (EPID) for 115 prostate cancer patients*. Int J Radiat Oncol Biol Phys, 1999. **45**(5): p. 1297-303.
36. Chuang, C. F., Verhey, L. J., and Xia, P., *Investigation of the use of MOSFET for clinical IMRT dosimetric verification*. Med Phys, 2002. **29**: p. 1109-1115.
37. Rustgi, S. N., *Evaluation of the dosimetric characteristics of a diamond detector for photon beam measurements*. Med Phys, 1995. **22**: p. 567-570.
38. Chang, J., Obcemea, C. H., Sillanpaa, J., Mechalakos, J., and Burman, C., *Use of EPID for leaf position accuracy QA of dynamic multi-leaf collimator (DMLC) treatment*. Med Phys, 2004. **31**(7): p. 2091-6.
39. Warkentin, B., Steciw, S., Rathee, S., and Fallone, B. G., *Dosimetric IMRT verification with a flat-panel EPID*. Med Phys, 2003. **30**(12): p. 3143-55.
40. Van Esch, A., Depuydt, T., and Huyskens, D. P., *The use of an aSi-based EPID for routine absolute dosimetric pre-treatment verification of dynamic IMRT fields*. Radiotherapy and Oncology, 2004. **71**(2): p. 223-34.
41. McDermott, L. N., Wendling, M., van Asselen, B., Stroom, J., Sonke, J. J., van Herk, M., and Mijnheer, B. J., *Clinical experience with EPID dosimetry for prostate IMRT pre-treatment dose verification*. Medical Physics, 2006. **33**(10): p. 3921-30.
42. Prisciandaro, J. I., Herman, M. G., and Kruse, J. J., *Utilizing an electronic portal imaging device to monitor light and radiation field congruence*. J Appl Clin Med Phys, 2003. **4**(4): p. 315-20.
43. Adamovics, J. and Maryanski, M. J., *Characterisation of PRESAGE: A new 3-D radiochromic solid polymer dosemeter for ionising radiation*. Radiat Prot Dosimetry, 2006. **120**(1-4): p. 107-12.

44. Sakhalkar, H. S., Adamovics, J., Ibbott, G., and Oldham, M., *A comprehensive evaluation of the PRESAGE/optical-CT 3D dosimetry system*. Med Phys, 2009. **36**(1): p. 71-82.
45. Baldock, C., De Deene, Y., Doran, S., Ibbott, G., Jirasek, A., Lepage, M., McAuley, K. B., Oldham, M., and Schreiner, L. J., *Polymer gel dosimetry*. Physics in Medicine and Biology, 2010. **55**(5): p. R1-R63.
46. Staffurth, J., *A Review of the Clinical Evidence for Intensity-modulated Radiotherapy*. Clinical Oncology, 2010. **22**(8): p. 643-657.
47. Fricke, H. and Hart, E. L., *The chemical action of roentgen rays on dilute ferrosulphate solutions as a measure of dose*. Am. J. Roentgenol., Radium Ther. Nucl. Med, 1927. **18**: p. 430-432.
48. Baldock, C., Harris, P. J., Piercy, A. R., and Healy, B., *Experimental determination of the diffusion coefficient in two-dimensions in ferrous sulphate gels using the finite element method*. Australas Phys Eng Sci Med, 2001. **24**(1): p. 19-30.
49. Low, D. A., Dempsey, J. F., Venkatesan, R., Mutic, S., Markman, J., Mark Haacke, E., and Purdy, J. A., *Evaluation of polymer gels and MRI as a 3-D dosimeter for intensity-modulated radiation therapy*. Med Phys, 1999. **26**(8): p. 1542-51.
50. Scheib, S. G. and Gianolini, S., *Three-dimensional dose verification using BANG gel: a clinical example*. J Neurosurg, 2002. **97**(5 Suppl): p. 582-7.
51. Vergote, K., De Deene, Y., Claus, F., De Gerssem, W., Van Duyse, B., Paelinck, L., Achten, E., De Neve, W., and De Wagter, C., *Application of monomer/polymer gel dosimetry to study the effects of tissue inhomogeneities on intensity-modulated radiation therapy (IMRT) dose distributions*. Radiother Oncol, 2003. **67**(1): p. 119-28.
52. Maryanski, M. J., Schulz, R. J., Ibbott, G. S., Gatenby, J. C., Xie, J., Horton, D., and Gore, J. C., *Magnetic resonance imaging of radiation dose distributions using a polymer gel dosimeter*. Phys Med Biol, 1994. **39**: p. 1437-1455.
53. Oldham, M., *Optical-CT scanning of polymer gels*. J Phys, 2004. **3**: p. 122-135.
54. Langmack, K. A., *Portal imaging*. Br J Radiol, 2001. **74**(885): p. 789-804.
55. Antonuk, L. E., *Electronic portal imaging devices: a review and historical perspective of contemporary technologies and research*. Phys Med Biol, 2002. **47**(6): p. R31-65.
56. Kirby, M. C. and Glendinning, A. G., *Developments in electronic portal imaging systems*. Br J Radiol, 2006. **79 Spec No 1**: p. S50-65.
57. Strandqvist, M. and Rosengren, B., *Television-controlled pendulum therapy*. Br J Radiol, 1958. **31**(369): p. 513-4.
58. Andrews, J. R., Swain, R. W., and Rubin, P., *Continuous visual monitoring of 2 mev. roentgen therapy*. Am J Roentgenol Radium Ther Nucl Med, 1958. **79**(1): p. 74-8.
59. Munro, P., Rawlinson, J. A., and Fenster, A., *Therapy imaging: a signal-to-noise analysis of metal plate/film detectors*. Med Phys, 1987. **14**(6): p. 975-84.
60. Munro, P., Rawlinson, J. A., and Fenster, A., *Therapy imaging: source sizes of radiotherapy beams*. Med Phys, 1988. **15**(4): p. 517-24.

61. Munro, P., Rawlinson, J. A., and Fenster, A., *Therapy imaging: a signal-to-noise analysis of a fluoroscopic imaging system for radiotherapy localization*. Med Phys, 1990. **17**(5): p. 763-72.
62. Munro, P., Rawlinson, J. A., and Fenster, A., *A digital fluoroscopic imaging device for radiotherapy localization*. Int J Radiat Oncol Biol Phys, 1990. **18**(3): p. 641-9.
63. Bissonnette, J. P., Cunningham, I. A., Jaffray, D. A., Fenster, A., and Munro, P., *A quantum accounting and detective quantum efficiency analysis for video-based portal imaging*. Med Phys, 1997. **24**(6): p. 815-26.
64. Bissonnette, J. P., Cunningham, I. A., and Munro, P., *Optimal phosphor thickness for portal imaging*. Med Phys, 1997. **24**(6): p. 803-14.
65. Bissonnette, J. P., Jaffray, D. A., Fenster, A., and Munro, P., *Optimal radiographic magnification for portal imaging*. Med Phys, 1994. **21**(9): p. 1435-45.
66. Jaffray, D. A., Battista, J. J., Fenster, A., and Munro, P., *Monte Carlo studies of x-ray energy absorption and quantum noise in megavoltage transmission radiography*. Med Phys, 1995. **22**(7): p. 1077-88.
67. Leong, J., *Use of digital fluoroscopy as an on-line verification device in radiation therapy*. Phys Med Biol, 1986. **31**(9): p. 985-92.
68. Swindell, W., Morton, E. J., Evans, P. M., and Lewis, D. G., *The design of megavoltage projection imaging systems: some theoretical aspects*. Med Phys, 1991. **18**(5): p. 855-66.
69. Swindell, W., *The lens coupling efficiency in megavoltage imaging*. Med Phys, 1991. **18**(6): p. 1152-3.
70. Drake, D. G., Jaffray, D. A., and Wong, J. W., *Characterization of a fluoroscopic imaging system for kV and MV radiography*. Med Phys, 2000. **27**(5): p. 898-905.
71. Pang, G. and Rowlands, J. A., *Electronic portal imaging with an avalanche-multiplication-based video camera*. Med Phys, 2000. **27**(4): p. 676-84.
72. Heijmen, B. J., Pasma, K. L., Kroonwijk, M., Althof, V. G., de Boer, J. C., Visser, A. G., and Huizenga, H., *Portal dose measurement in radiotherapy using an electronic portal imaging device (EPID)*. Phys Med Biol, 1995. **40**(11): p. 1943-55.
73. Herman, M. G., Balter, J. M., Jaffray, D. A., McGee, K. P., Munro, P., Shalev, S., Van Herk, M., and Wong, J. W., *Clinical use of electronic portal imaging: Report of AAPM Radiation Therapy Committee Task Group 58*. Medical Physics, 2001. **28**(5): p. 712.
74. Meertens, H., van Herk, M., and Weeda, J., *A liquid ionisation detector for digital radiography of therapeutic megavoltage photon beams*. Phys Med Biol, 1985. **30**(4): p. 313-21.
75. Meertens, H., van Herk, M., Bijhold, J., and Bartelink, H., *First clinical experience with a newly developed electronic portal imaging device*. Int J Radiat Oncol Biol Phys, 1990. **18**(5): p. 1173-81.
76. van Herk, M. and Meertens, H., *A matrix ionisation chamber imaging device for on-line patient setup verification during radiotherapy*. Radiother Oncol, 1988. **11**(4): p. 369-78.

77. van Herk, M., *Physical aspects of a liquid-filled ionization chamber with pulsed polarizing voltage*. Med Phys, 1991. **18**(4): p. 692-702.
78. van Herk, M., Bijhold, J., Hoogervorst, B., and Meertens, H., *Sampling methods for a matrix ionization chamber system*. Med Phys, 1992. **19**(2): p. 409-18.
79. Greer, P. B. and Popescu, C. C., *Dosimetric properties of an amorphous silicon electronic portal imaging device for verification of dynamic intensity modulated radiation therapy*. Medical Physics, 2003. **30**(7): p. 1618-27.
80. Zhao, W. and Rowlands, J. A., *X-ray imaging using amorphous selenium: feasibility of a flat panel self-scanned detector for digital radiology*. Med Phys, 1995. **22**(10): p. 1595-604.
81. Sabet, M., Menk, F. W., and Greer, P. B., *Evaluation of an a-Si EPID in direct detection configuration as a water-equivalent dosimeter for transit dosimetry*. Med Phys, 2010. **37**(4): p. 1459-67.
82. Munro, P. and Bouius, D. C., *X-ray quantum limited portal imaging using amorphous silicon flat-panel arrays*. Med Phys, 1998. **25**(5): p. 689-702.
83. Winkler, P., Hefner, A., and Georg, D., *Dose-response characteristics of an amorphous silicon EPID*. Medical Physics, 2005. **32**(10): p. 3095-105.
84. McDermott, L. N., Louwe, R. J. W., Sonke, J. J., van Herk, M. B., and Mijnheer, B. J., *Dose-response and ghosting effects of an amorphous silicon electronic portal imaging device*. Medical Physics, 2004. **31**(2): p. 285-95.
85. Winkler, P., Hefner, A., and Georg, D., *Implementation and validation of portal dosimetry with an amorphous silicon EPID in the energy range from 6 to 25 MV*. Physics in Medicine and Biology, 2007. **52**(15): p. N355-N365.
86. McCurdy, B. M. C., Luchka, K., and Pistorius, S., *Dosimetric investigation and portal dose image prediction using an amorphous silicon electronic portal imaging device*. Med Phys, 2001. **28**(6): p. 911-24.
87. Jaffray, D. A., Battista, J. J., Fenster, A., and Munro, P., *X-ray scatter in megavoltage transmission radiography: physical characteristics and influence on image quality*. Med Phys, 1994. **21**(1): p. 45-60.
88. Greer, P. B., *Correction of pixel sensitivity variation and off-axis response for amorphous silicon EPID dosimetry*. Medical Physics, 2005. **32**(12): p. 3558-68.
89. Chytyk, K. and McCurdy, B. M. C., *Comprehensive fluence model for absolute portal dose image prediction*. Med Phys, 2009. **36**(4): p. 1389-98.
90. Siebers, J. V., Kim, J. O., Ko, L., Keall, P. J., and Mohan, R., *Monte Carlo computation of dosimetric amorphous silicon electronic portal images*. Medical Physics, 2004. **31**(7): p. 2135-46.
91. Li, W., Siebers, J. V., and Moore, J. A., *Using fluence separation to account for energy spectra dependence in computing dosimetric a-Si EPID images for IMRT fields*. Medical Physics, 2006. **33**(12): p. 4468-80.
92. Greer, P. B., Cadman, P., Lee, C., and Bzdusek, K., *An energy fluence-convolution model for amorphous silicon EPID dose prediction*. Medical Physics, 2009. **36**(2): p. 547-55.
93. Parent, L., Seco, J., Evans, P. M., Fielding, A., and Dance, D. R., *Monte Carlo modelling of a-Si EPID response: the effect of spectral variations with field size and position*. Med Phys, 2006. **33**(12): p. 4527-40.

94. van Zijtveld, M., Dirkx, M. L. P., de Boer, H. C. J., and Heijmen, B. J. M., *Dosimetric pre-treatment verification of IMRT using an EPID; clinical experience*. Radiother Oncol, 2006. **81**: p. 168-175.
95. McCurdy, B. M. and Pistorius, S., *A two-step algorithm for predicting portal dose images in arbitrary detectors*. Med Phys, 2000. **27**(9): p. 2109-16.
96. Pasma, K. L., Heijmen, B. J., Kroonwijk, M., and Visser, A. G., *Portal dose image (PDI) prediction for dosimetric treatment verification in radiotherapy. I. An algorithm for open beams*. Med Phys, 1998. **25**(6): p. 830-40.
97. McNutt, T. R., Mackie, T. R., Reckwerdt, P., Papanikolaou, N., and Paliwal, B. R., *Calculation of portal dose using the convolution/superposition method*. Med Phys, 1996. **23**(4): p. 527-35.
98. Dahlgren, C. V., Ahnesjo, A., Montelius, A., and Rikner, G., *Portal dose image verification: formalism and application of the collapsed cone superposition method*. Phys Med Biol, 2002. **47**(24): p. 4371-87.
99. van Elmpt, W. J. C., Nijsten, S. M. J. J. G., Mijnheer, B. J., and Minken, A. W. H., *Experimental verification of a portal dose prediction model*. Medical Physics, 2005. **32**(9): p. 2805-18.
100. McNutt, T. R., Mackie, T. R., and Paliwal, B. R., *Analysis and convergence of the iterative convolution/superposition dose reconstruction technique for multiple treatment beams and tomotherapy*. Med Phys, 1997. **24**: p. 1465-1476.
101. McNutt, T. R., Mackie, T. R., Reckwerdt, P., and Paliwal, B. R., *Modeling dose distributions from portal dose images using the convolution/superposition method*. Med Phys, 1996. **23**(8): p. 1381-92.
102. van Zijtveld, M., Dirkx, M. L. P., de Boer, H. C. J., and Heijmen, B. J. M., *3D dose reconstruction for clinical evaluation of IMRT pretreatment verification with an EPID*. Radiother Oncol, 2007. **82**: p. 201-207.
103. van Elmpt, W., Nijsten, S., Mijnheer, B., Dekker, A., and Lambin, P., *The next step in patient-specific QA: 3D dose verification of conformal and intensity-modulated RT based on EPID dosimetry and Monte Carlo dose calculations*. Radiotherapy and Oncology, 2008. **86**(1): p. 86-92.
104. van Elmpt, W. J. C., Nijsten, S. M. J. J. G., Dekker, A. L. A. J., Mijnheer, B. J., and Lambin, P., *Treatment verification in the presence of inhomogeneities using EPID-based three-dimensional dose reconstruction*. Medical Physics, 2007. **34**(7): p. 2816-26.
105. van Elmpt, W. J. C., Nijsten, S. M. J. J. G., Schiffeleers, R. F. H., Dekker, A. L. A. J., Mijnheer, B. J., Lambin, P., and Minken, A. W. H., *A Monte Carlo based three-dimensional dose reconstruction method derived from portal dose images*. Medical Physics, 2006. **33**(7): p. 2426-34.
106. Ansbacher, W., *Three-dimensional portal image-based dose reconstruction in a virtual phantom for rapid evaluation of IMRT plans*. Med Phys, 2006. **33**(9): p. 3369-82.
107. Spies, L., Partridge, M., Groh, B. A., and Bortfeld, T., *An iterative algorithm for reconstructing incident beam distributions from transmission measurements using electronic portal imaging*. Phys Med Biol, 2001. **46**: p. N203-N211.

108. Partridge, M., Ebert, M., and Hesse, B. M., *IMRT verification by three-dimensional dose reconstruction from portal beam measurements*. Medical Physics, 2002. **29**(8): p. 1847.
109. Boellaard, R., Essers, M., van Herk, M., and Mijnheer, B. J., *New method to obtain the midplane dose using portal in vivo dosimetry*. Int J Radiat Oncol Biol Phys, 1998. **41**(2): p. 465-74.
110. van Elmpt, W., Petit, S., De Ruyscher, D., Lambin, P., and Dekker, A., *3D dose delivery verification using repeated cone-beam imaging and EPID dosimetry for stereotactic body radiotherapy of non-small cell lung cancer*. Radiotherapy and Oncology, 2010. **94**(2): p. 188-194.
111. Wendling, M., Louwe, R. J. W., McDermott, L. N., Sonke, J.-J., van Herk, M., and Mijnheer, B. J., *Accurate two-dimensional IMRT verification using a back-projection EPID dosimetry method*. Medical Physics, 2006. **33**(2): p. 259-73.
112. Wendling, M., McDermott, L. N., Mans, A., Sonke, J.-J., van Herk, M., and Mijnheer, B. J., *A simple backprojection algorithm for 3D in vivo EPID dosimetry of IMRT treatments*. Med Phys, 2009. **36**(7): p. 3310-21.
113. Mans, A., Remeijer, P., Olaciregui-Ruiz, I. g., Wendling, M., Sonke, J.-J., Mijnheer, B., van Herk, M., and Stroom, J. C., *3D Dosimetric verification of volumetric-modulated arc therapy by portal dosimetry*. Radiother Oncol, 2010. **94**: p. 181-187.
114. Pecharromán-Gallego, R., Mans, A., Sonke, J.-J., Stroom, J. C., Olaciregui-Ruiz, I. g., van Herk, M., and Mijnheer, B. J., *Simplifying EPID dosimetry for IMRT treatment verification*. Medical Physics, 2011. **38**(2): p. 983-92.

CHAPTER THREE: INVESTIGATION OF TILTED DOSE KERNELS FOR PORTAL DOSE PREDICTION IN ELECTRONIC PORTAL IMAGERS

In Chapter Two, beam modeling, dose verification devices and portal dosimetry were discussed. This chapter will examine the parallel dose kernel assumption for portal dose prediction and the effect of using kernels generated with a divergent (or tilted) beam versus kernels generated with a parallel beam. This chapter was previously published in the peer-reviewed journal *Medical Physics*.*

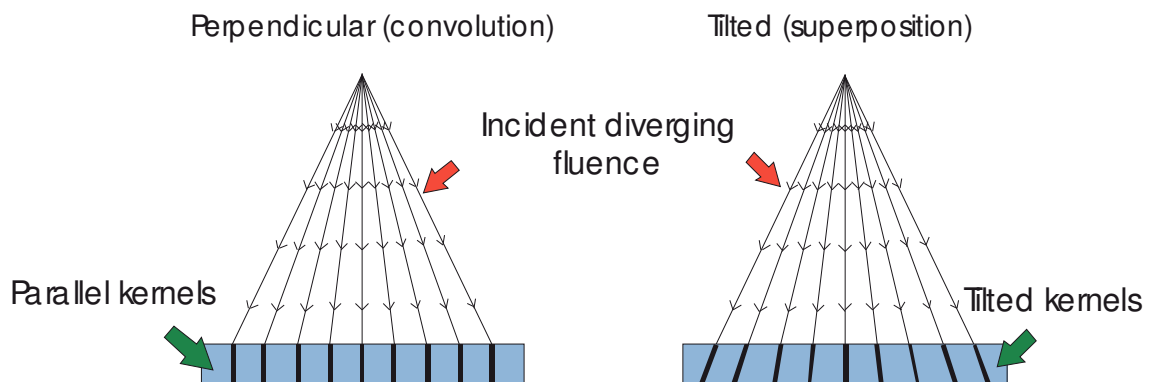
3.1 INTRODUCTION

Dose delivery accuracy has been shown to have a considerable effect on patient outcome [1, 2]. Various authors have recommended that dose delivery uncertainty be limited to 5% [3], 3.5% [4] and 3% [2]. Currently, a 2% to 3% dose calculation uncertainty is satisfactory, contributing to a total delivery uncertainty of approximately 5% [5]. In the future, with improvements in linear accelerator operation, patient set-up, dose calibration, patient data and dose calculation accuracy, an overall uncertainty of 3% will be achievable [5]. That corresponds to a dose calculation uncertainty of about 1%. This accuracy increase emphasizes the need to strive for accurate dose calculation algorithms not only in patients, but also radiation detectors used in quantitative dose measurements.

* Reprinted with permission from the AAPM, granted on April 8, 2011.
K. Chytyk and B. M. C. McCurdy, "Investigation of tilted dose kernels for portal dose image prediction in electronic portal images," *Med Phys*, 2006. **33** (9): p. 3333-3339.

There has been great interest in the use of flat-panel amorphous-silicon electronic portal imaging devices (a-Si EPIDs) as dosimetric verification tools [6-19]. Implementing a portal dose image prediction technique in a clinical setting requires that the calculation method be fast as well as accurate. To achieve these goals, several authors have produced calculated portal dose images through the application of precalculated Monte Carlo dose kernels representing the dose spread in the detector system [7, 10, 12, 15, 18, 19]. A two-step approach which convolves these precalculated dose kernels with incident EPID photon fluence has been utilized by McCurdy *et al.* [7, 18] and Siebers *et al.* [19]. These EPID dose kernels are typically generated in the plane of the dosimetric detection material using an incident photon pencil beam parallel to the central axis of the beam. The calculation approach does not account for the true divergent nature of a clinical beam (this is known as the ‘parallel kernel approximation’, as illustrated in Figure 3.1) in order to minimize image prediction time.

Figure 3.1 [Parallel vs. Tilted Kernels]: Illustration of the parallel kernel assumption and tilted kernels applied to a divergent fluence.



A number of groups [20-26] have investigated the various effects of beam divergence (inverse-square primary dose reduction and linear increase in field dimensions with depth, and tilting of the dose kernels) [5] on patient dose calculations. Examining the effect of kernel tilting on tissue maximum ratios (TMRs) for 15 MV x-rays, Mackie *et al.* [20] discovered a difference of less than 1% on the central axis up to a depth of 20 cm for a 20 x 20 cm² field at a 100 cm source-to-surface-distance (SSD). To reduce computation time, one study did not physically tilt the kernels, but accounted for the divergent beam by applying an inverse-square correction to the dose deposition site [24]. Liu *et al.* [25] investigated the difference between this dose deposition approach, an inverse-square correction of the terma (total energy released per unit mass) at the photon interaction site and actually tilting the kernels. Compared to full Monte Carlo simulations, the tilted kernels resulted in the greatest calculation accuracy of the three methods.

Sharpe *et al.* [26] conducted a study that considered the parallel kernel approximation with respect to patient dose calculations for radiotherapy treatment planning in a comprehensive investigation. Various situations were examined for a range of monoenergetic photon energies (2, 6 and 10 MeV) and a number of source-to-surface-distances (SSDs) and field sizes (50 to 100 cm and 5 x 5 to 30 x 30 cm²). A polyenergetic 6 MV beam was also simulated and both parallel and tilted kernels were compared to experimental data. Discrepancies of up to 4.4% of the maximum dose on the central axis were observed for a monoenergetic 10 MeV beam with a 30 x 30 cm² field size and a 50 cm SSD, due to the large field size, short SSD and high energy of the scenario.

These studies indicate that a parallel kernel approach may be acceptable for portal dose image prediction. However, to date there has been no investigation of the accuracy of portal dose calculations when applying parallel dose kernels in a divergent clinical geometry where incident fluence is not parallel across the field. This study examined the validity of this parallel dose kernel assumption for an a-Si EPID (aS500 or aS1000, Varian Medical Systems Inc., Palo Alto, CA) although results should be similar for similarly constructed EPIDs. Other topics concerning this type of EPID, such as optical glare, detector lag or backscatter from objects near the detector, were not explicitly considered in the detector model or dose calculations since the focus of this exercise was to consider the specific effect of the parallel kernel approximation. It should be noted that optical glare in the phosphor layer has been studied extensively via Monte Carlo simulation [15, 27, 28]. It has been determined that the linear relationship between radiation energy deposition and optical photon creation ensures that a convolution calculation is appropriate to model that phenomenon. Detector lag is an electronic effect that may be reduced or removed through acquisition techniques. Backscatter from objects near the detector (such as the detector support arm) has been approximated by introducing equivalent backscatter material into the simulation (see Section 3.2.1), as determined by Siebers *et al.* [12].

‘Tilted’ dose kernels for this detector were obtained at a number of incident angles (0° to 14° , every 2°) for a range of monoenergetic photon energies (0.1, 2, 6 and 18 MeV). These kernels were obtained in Cartesian coordinates (instead of cylindrical coordinates) to allow detection of asymmetries. The parallel kernels were then convolved with a

simple incident fluence map; a superposition employing the tilted kernels (simulating a divergent beam) and the same incident fluence map was also carried out. The incident fluence map was defined as a flat field in order to more easily isolate the difference between the predicted dose images. For the field sizes and source-to-detector distances (SDDs) examined here, the two predicted images were compared using the χ -comparison test [29] (a revision of Low *et al.*'s [30] γ -evaluation) with a dose gradient threshold $\Delta D = 1.0\%$ and a distance-to-agreement, $\Delta d = 0.0784$ cm (the detector pixel width) in order to quantify the difference between the two methods and assess the significance of the parallel kernel assumption. The gain in time when applying the parallel kernels rather than the tilted kernels was a factor of approximately 6000 (10.5 seconds vs. 18 hours, respectively).

3.2 MATERIALS AND METHODS

3.2.1 Monte Carlo simulations

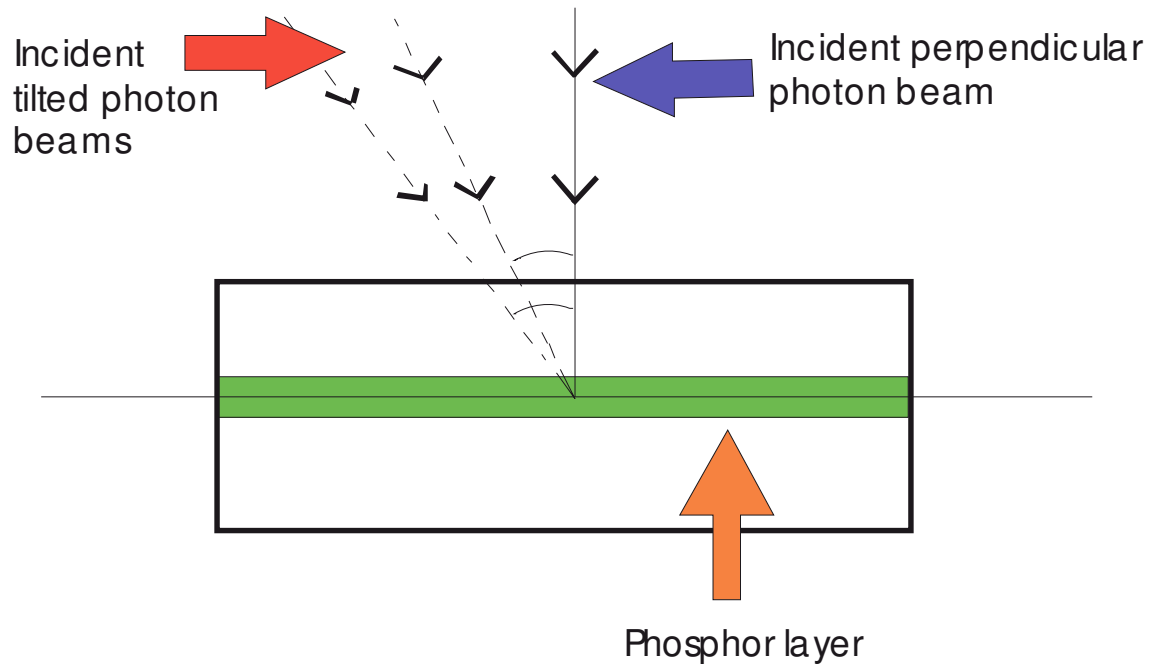
EGSnrc [31], with electron transport algorithm PRESTA-II and user codes DOSXYZnrc and DOSRZnrc, was utilized to simulate an a-Si flat-panel EPID dose response in Cartesian and cylindrical coordinates, respectively. The simulated detector design (specifications provided by Varian Medical Systems Inc., Palo Alto, CA) consisted of an uniform epoxy front cover followed by a 2.2 cm air gap and the imaging cassette. The imaging cassette includes a 0.1 cm thick copper buildup plate and a Lanex Fast-B phosphor (gadolinium oxysulphide, density of 3.5 g/cm^3) screen surrounded by hard foam shielding. The phosphor was modeled as three individual layers of equal thickness since dose deposition varies with depth in the phosphor [15, 28]. The dose delivered to

the phosphor is the dose of interest for the dose kernels since this dose is proportional to the number of optical photons created in the phosphor, and therefore proportional to the signal collected in the photodiodes. The screen is sandwiched between two 0.8 cm thick layers of polymethacrylimide hard foam, which protects the interior of the imaging cassette. A 2.1 cm air gap and 1.0 cm uniform water slab placed downstream from the imaging cassette was determined by Siebers *et al.* [12] to behave as equivalent backscatter material to the rear housing. An additional 3.0 cm slab of uniform water buildup was added directly upstream of the detector front cover, since several authors have used additional buildup to ensure electronic equilibrium in the phosphor layer [7, 10, 15]. The simulated area of the detector for dose kernel generation was approximately 40 x 40 cm² (slightly larger than the clinical detector area of 40 x 30 cm²) for the ease of calculating with a square geometry rather than a rectangular one.

Dose kernels in the phosphor layer of the detector were generated with an incident pencil beam of monoenergetic photons of energies 0.1, 2, 6 and 18 MeV. The cut-off energies of the electrons and photons in the simulation (below which all lower energies are no longer tracked) used for all the dose kernel simulations were ECUT = 0.521 MeV and PCUT = 0.01 MeV, respectively. DOSRZnrc was utilized to create a kernel (using 1x10⁸ photon histories and a circular incident pencil beam radius of 0.00044 cm) of non-uniform radial resolution (smoothly varying from 0.005 cm to 5.0 cm), for each energy. Only perpendicularly incident photon pencil beams were simulated in cylindrical coordinates.

DOSXYZnrc was used to simulate dose kernels at high and low spatial resolutions in Cartesian coordinates. The high spatial resolution dose kernels used $0.0784 \times 0.0784 \text{ cm}^2$ voxels (equivalent to the pixel size of the aS500 detector), while the low spatial resolution dose kernels used $\sim 1 \times 1 \text{ cm}^2$ to $\sim 3 \times 3 \text{ cm}^2$ voxels, depending on the incident photon energy. Two spatial resolutions were used to provide data with low statistical uncertainties in low gradient, low dose, outlying regions while retaining spatial resolution in high gradient, high dose regions. A square incident pencil beam of dimensions $0.00078 \times 0.00078 \text{ cm}^2$ was employed to achieve an equivalent beam area to the incident circular beam used in the DOSRZnrc simulations. The number of histories run for the high and low resolution kernels were 1×10^9 and 5×10^8 , respectively. Dose was scored in the phosphor (where the portal dose image is formed) with incident pencil beam angles ranging from 0° to 14° in 2° increments relative to the perpendicular (see Figure 3.2). The pencil beams were tilted along the negative x-axis of the detector geometry. The x- and y-axes of the detector lie in the plane of the phosphor.

Figure 3.2 [Set-up for Dose Kernel Generation]: Pencil beam orientations for Cartesian geometry Monte Carlo simulations. The pencil beams are incident on the center of the a-Si detector's phosphor layer. The y-axis of the detector is in the plane of the phosphor and orthogonal to the x-axis.



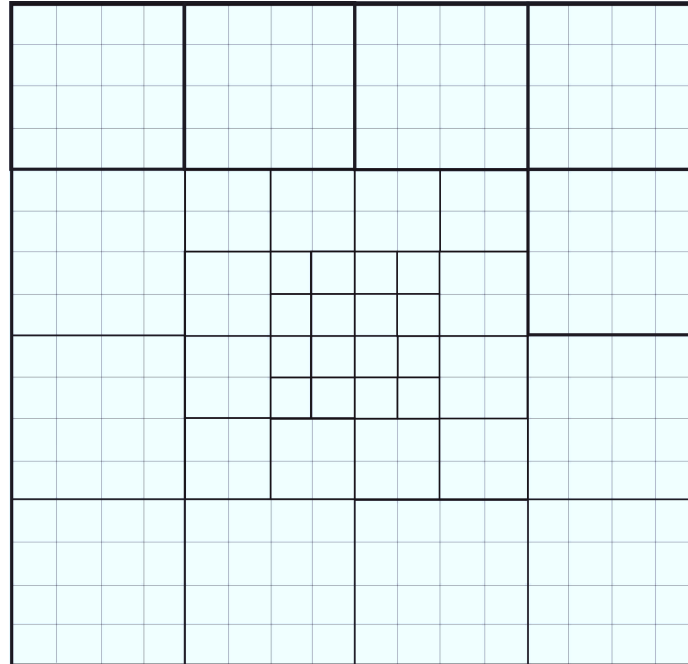
For a 105 cm source to detector distance (SDD) and a $35.7 \times 26.8 \text{ cm}^2$ field defined at isocentre, the maximum angle incident upon the detector was less than 14° along the diagonal of the field. This choice of SDD and field size represented the ‘worst-case-scenario’ where the incident angle of the ray-lines of the photon beam was maximized (largest angle was 14°). For more clinically applicable smaller fields and increased SDDs, the maximum angle of primary radiation incident upon the detector would be less than 14° as well.

3.2.2 Dose kernel analysis

To ensure consistency between the DOSRZnrc and DOSXYZnrc user codes, the Cartesian dose kernels were compared to the radial dose kernels. Dose in the three phosphor layers of the kernels was combined through weightings described by Kirkby *et al.* [15]. The change in total energy per incident fluence of the kernels with respect to tilt angle was examined.

Since the kernels were bilaterally symmetric about the pencil beam, the voxels were averaged about the x-axis to reduce statistical fluctuations in the Cartesian kernels [32]. The bilaterally symmetric kernel data was then combined into concentric, square rings of voxels (Figure 3.3), to further reduce statistical uncertainty in any single voxel to less than 2% (less than 0.08% of the maximum dose). The doses were averaged over the combined squares, with the dose defined at the average coordinate of the combined voxels.

Figure 3.3 [Rebinning of Cartesian Dose Kernels]: The creation of concentric rings of squares through voxel combination. This figure is representative of the geometry of the high resolution kernels. The dose is defined at the effective center of the combined voxels.



The interior region of the high resolution dose kernels was then combined with the outlying region of the low resolution dose kernels by a single replacement of interior region data. The extent of this replacement depended on the size of the low resolution voxels. These irregularly gridded data sets (due to the voxel-combining step) were then interpolated to regular grids of $0.0784 \times 0.0784 \text{ cm}^2$, matching the detector pixel resolution. This was accomplished by linearly interpolating from triangles generated through Delaunay triangulation [33]. The resulting interpolated data (resulting from the voxel combination and linear interpolation) were compared to the radial dose kernels to establish reliability.

3.2.3 Tilted vs. parallel kernels

The clinical impact of employing parallel dose kernels instead of tilted dose kernels (Figure 3.1) was estimated by applying the parallel and tilted kernels to a flat field of photon fluence incident on the EPID, represented by a top-hat function with a value of 1 within the field size and 0 elsewhere. The convolution (parallel kernels) and superposition (tilted kernels) methods of dose calculation were employed for two field sizes (35.7×26.8 and $27.2 \times 20.4 \text{ cm}^2$ at isocentre) and two SDDs (105 and 140 cm). The 2 field sizes just covered the $40 \times 30 \text{ cm}^2$ phosphor area of the detector in the 105 and 140 cm SDD trials, respectively. The parallel dose kernels were convolved with the incident fluence (using the two-dimensional Fast Fourier Transform (2-D FFT) method) to calculate dose. To utilize the superposition method, the appropriate tilted kernel for an exact angle of incidence for a given calculation voxel was interpolated from the available regularly gridded kernels. The resulting kernel was rotated azimuthally by the angle between the x-axis and the vector joining the central axis and the voxel of interest, and then translated to the voxel of interest. The repositioned kernel was then interpolated to the detector pixel coordinates.

Some fluctuations in the superposition results were observed due to a violation of energy conservation. The spurious errors were due to the rotation and interpolation of the dose kernels during the superposition process. To remove this effect, these interpolated kernels were normalized in order to maintain the total energy of the non-translated, non-rotated kernel, thus ensuring energy conservation. A similar rationale was used during the normalization of tilted kernels in a previous study by Liu *et al.* [25].

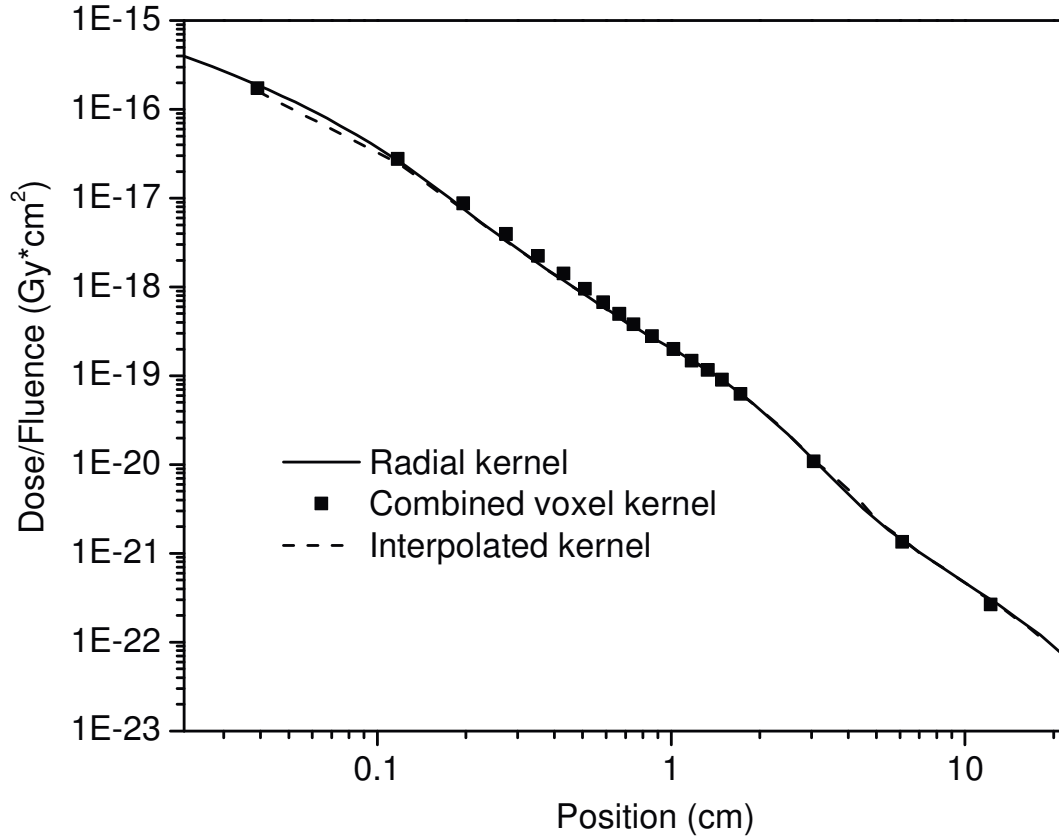
The results of the convolution versus full superposition approach were evaluated by the χ -comparison test [29] with $\Delta d = 0.0784$ cm (the detector resolution) and $\Delta D = 1.0\%$. The χ -comparison test is a quantitative dose distribution evaluation (based on the local dose error) that is founded on and analogous to the γ -evaluation [30]. If the resulting χ -comparison scores are between (or equal to) -1 and +1, the acceptance criteria ΔD and Δd have been satisfied.

3.3 RESULTS AND DISCUSSION

3.3.1 Dose kernel comparison

The consistency of the parallel Cartesian kernels in relation to the parallel radial kernels was demonstrated by comparing x-axis profiles through the 0° kernels, as shown in Figure 3.4. This comparison established the compatibility of the simulations in the cylindrical and Cartesian geometries, which was important since they employ two separate EGSnrc user codes. The dose variations between the respective points in the two geometries differed by 15% for the innermost Cartesian voxel, where one expects the maximum difference between the geometries to occur. All remaining points showed less than a 1.4% difference with respect to the maximum dose, and a mean difference of 0.07% for all points. As well, the total energy of the kernels scored in the two coordinate systems disagrees by a maximum of 0.47%. Discrepancies between the two kernel geometries, particularly at small radii, could be attributed to differences in pixel size since at small radial distances the radial kernel has a higher resolution than the Cartesian kernel [34].

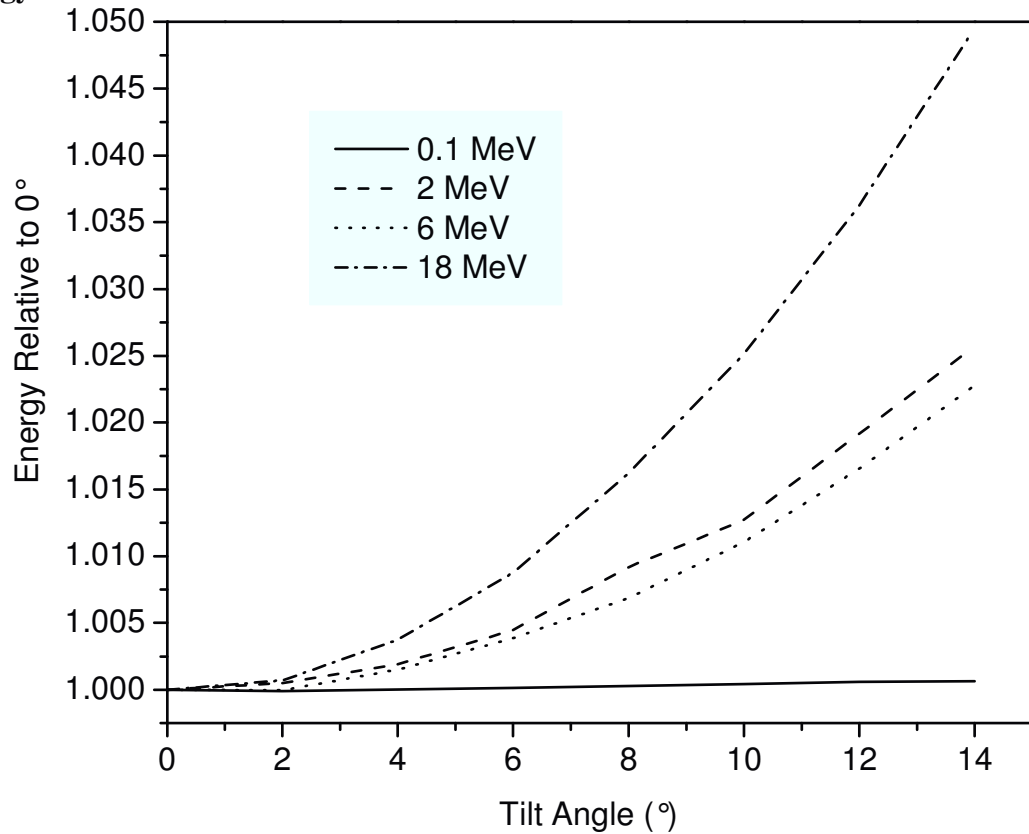
Figure 3.4 [Dose Kernel Radial Profiles]: Profiles of 6 MeV parallel, Cartesian kernels (interpolated from the combined voxel kernel) and parallel radial kernels to demonstrate consistency between the two geometries. All errors are less than 2% (0.08% of maximum dose).



The total energy per incident fluence of the kernels varied up to 4.6% with tilt angle, particularly for the 18 MeV kernel (see Figure 3.5). This energy discrepancy may have been caused by the fact that the thickness of water buildup (3.0 cm) used on the detector was actually not sufficient to achieve d_{\max} for a monoenergetic 18 MeV photon beam. The buildup thickness chosen was consistent with the buildup implemented in our clinic for dosimetric EPID applications. The total energy per incident fluence of the dose kernels with increasing photon energy (not presented here) was in agreement with the previous work of Jaffray *et al.* [35] and McCurdy *et al.* [7]. Regarding total energy deposited in the phosphor layer of the detector, a less than 0.9% difference was observed

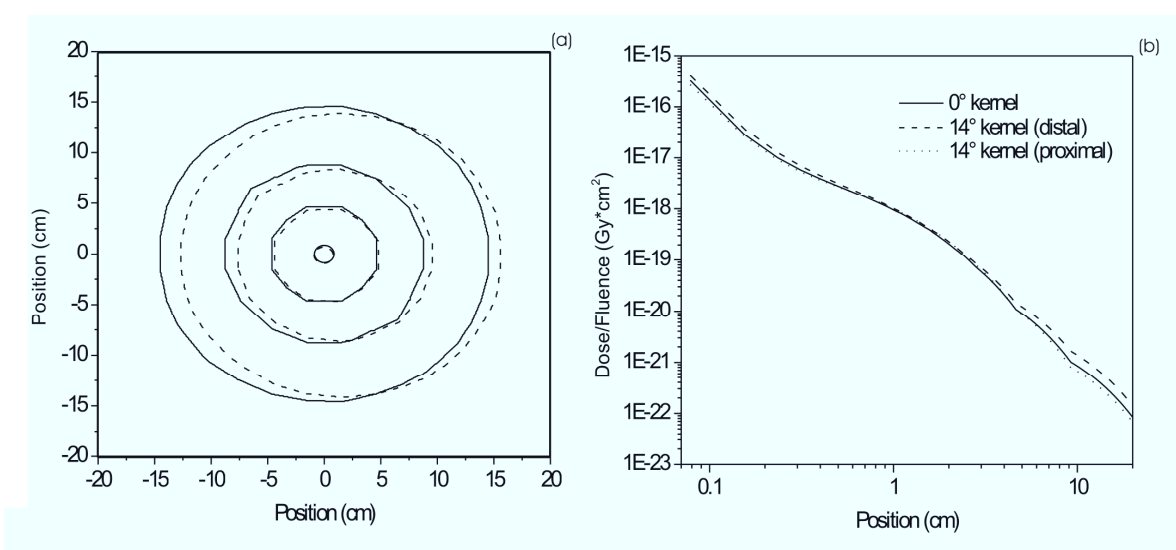
between the ‘raw’ and interpolated Cartesian kernels. This systematic discrepancy in total energy can be attributed to the processing of the kernels through the Delaunay triangulation and linear interpolation to a higher resolution [34]. The convolution and superposition calculations both used only the interpolated kernels so this difference did not affect the comparison or the final conclusion.

Figure 3.5 [Total Energy with Tilt Angle]: Differences in total energy of the tilted pencil beam kernels relative to the total energy of the 0° kernel for each photon energy.



X-axis profiles of the tilted and perpendicular Cartesian kernels were also compared. The higher energy kernel profiles (6 and 18 MeV) demonstrated noticeable asymmetry at the maximum tilt angle (14°) while only minimal discrepancies at the lower energies (2 and 0.1 MeV) were observed. Figure 3.6 illustrates the asymmetry of the 18 MeV dose kernel at 14° incidence.

Figure 3.6 [Comparison of 0° and 14° Kernels]: (a) Isodose contours of the 0° (solid line) and 14° (dashed line) kernels. The contours range from 1×10^{-18} Gy cm^2 to 5×10^{-22} Gy cm^2 (b) Radial profiles illustrating the discrepancies between the perpendicularly incident and maximum tilt (14°) angle, 18 MeV, Cartesian kernels for the proximal (-x) and distal (+x) halves (see Fig 3.2).

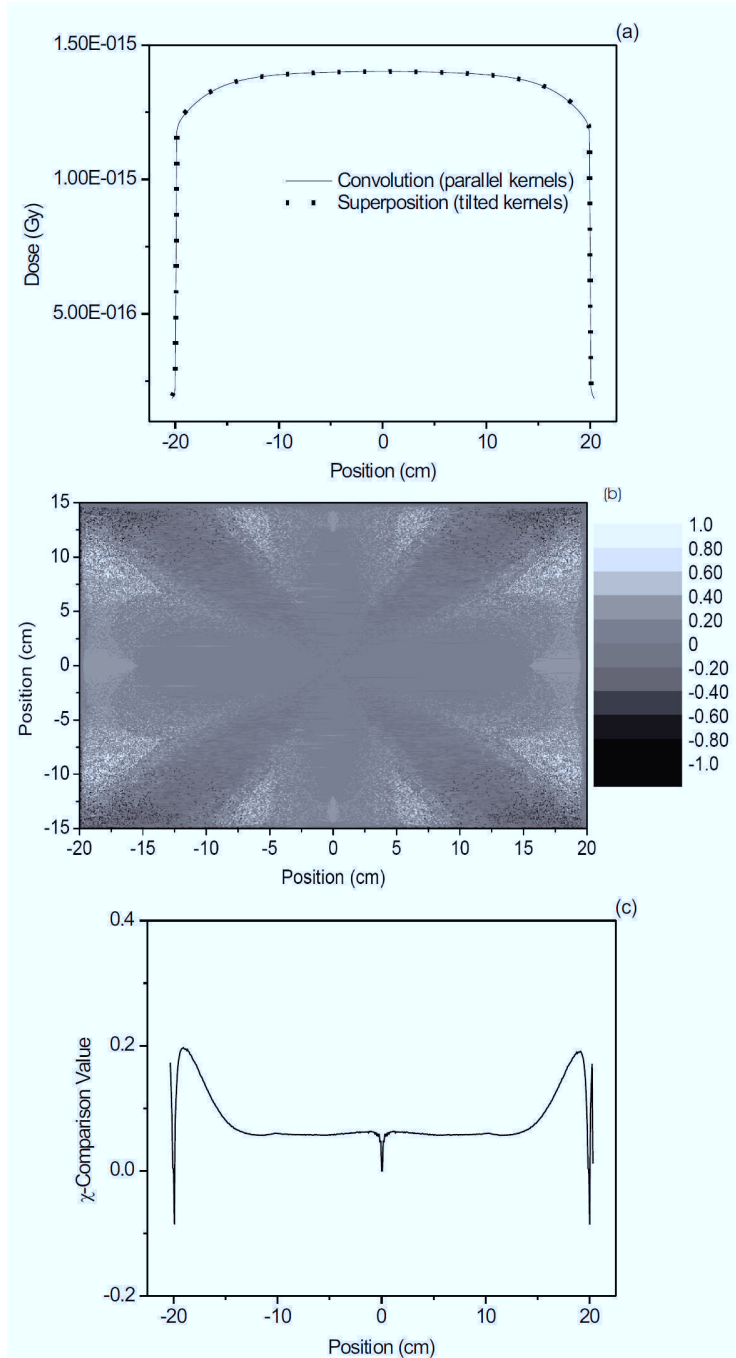


3.3.2 Superposition vs. convolution of dose kernels

The assessment of the parallel dose kernel assumption was achieved through dose calculations using both the tilted and parallel kernels applied to an ideal uniform field of fluence incident on the EPID. Figure 3.7 (a) presents an x-axis profile of the superposition and convolution dose calculations for the more clinically relevant scenario ($27.2 \times 20.4 \text{ cm}^2$ field size, 140 cm SDD). The χ -comparison in this situation yielded

similar results for all energies, demonstrating a distance-to-agreement within the detector pixel resolution and a dose difference maximum of 1.0% (Figure 3.8). Positive values of the χ -comparison indicated that the parallel kernel assumption underestimated the tilted kernel superposition results (Figures 3.7 (c), 3.8, and 3.9). Approaching the field edges, it was demonstrated that the parallel kernel assumption created an increasing underestimation of the superposition (Figure 3.7 (c)). Beyond the field edges, the underestimation continued. This behaviour trend was expected due to the gradual change in kernel energy content with tilt angle. At the field edge, a small overestimation occurred likely due to a change from 'dose difference' to 'distance-to-agreement' and back again in the underlying χ -comparison calculation.

Figure 3.7 [Profiles and χ -comparisons of Convolution vs. Superposition]: (a) Convolution (parallel kernels) vs. superposition (tilted kernels) with an incident top-hat function fluence, displayed as dose profiles. (b) Greyscale intensity image of the χ -comparison scores between the convolution and superposition methods. Note the radial symmetry. (c) Profile (along the x-axis of the detector's phosphor layer) of χ -comparison scores between the convolution and superposition results. If $|\chi| \leq 1$, then the acceptance criteria are satisfied. All data is for the 0.1 MeV, 140 cm SDD, 27.2 x 20.4 cm² field size scenario with $\Delta d = 0.0784$ cm and $\Delta D = 1.0\%$.



The fraction of pixels which satisfied the acceptance criteria of the χ -comparison test ($\Delta d = 0.0784$ cm, $\Delta D = 1.0\%$) are represented by histograms (Figures 3.8 and 3.9). Figure 3.8 demonstrates the increasing asymmetry in the χ -comparison with increasing incident photon beam energy, indicating a slightly greater tendency for the parallel kernel assumption to underestimate the superposition with higher incident photon energies. This was most likely due to the lack of buildup in the 18 MeV monoenergetic case. The other energies did show a variation between tilted and parallel dose kernels, as shown in Figures 3.8 and 3.9, particularly for the “extreme” case of a short SDD.

Figure 3.8 [χ -comparison Histograms of Clinical Scenario]: (a) Low and (b) high energy histograms of χ -comparison displaying the fraction of voxels satisfying the threshold criteria. The 140 cm SDD, 27.2×20.4 cm² field size is shown, with thresholds of $\Delta d = 0.0784$ cm and $\Delta D = 1.0\%$. If $|\chi| \leq 1$, then the acceptance criteria are satisfied.

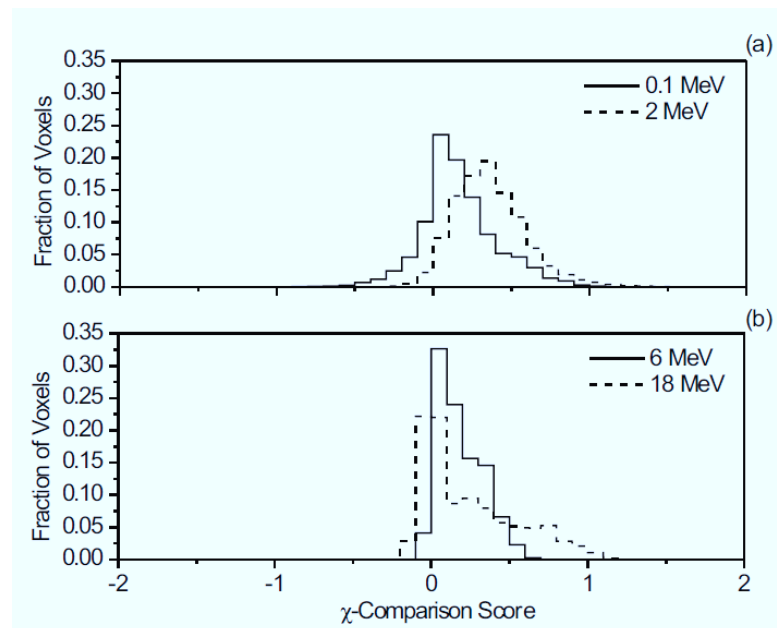
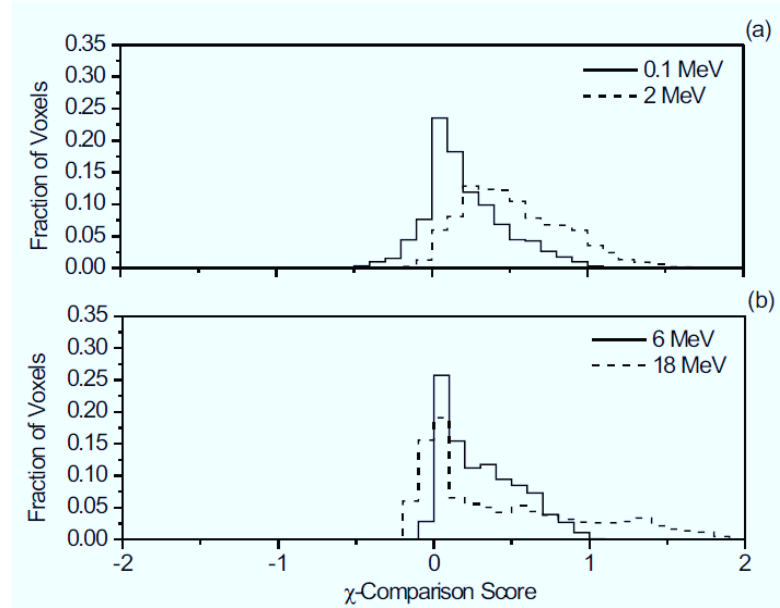


Figure 3.9 [χ -comparison Histograms of Extreme Scenario]: (a) Low and (b) high energy histograms of χ -comparison displaying the fraction of voxels satisfying the threshold criteria. The 105 cm SDD, 35.7 x 26.8 cm² field size trial is shown, with thresholds of $\Delta d = 0.0784$ cm and $\Delta D = 1.0\%$.



The worst-case scenario (35.7 x 26.8 cm² field size, 105 cm SDD) resulted in higher dose differences for the χ -comparison for each energy within 1.8 % (Figure 3.9). Higher dose differences were expected as the SDD was decreased and field size was increased, resulting in larger incident angles of primary radiation fluence into the detector, ie. the kernels were further from being parallel than at longer SDDs. Qualitatively similar to the clinically relevant case, a general underestimation by the parallel kernel assumption was demonstrated (Figure 3.9).

Comparisons of the parallel vs. tilted dose calculation for all energies exhibited the greatest disagreement along diagonal profiles, coinciding with the largest rotation of the tilted kernels and the largest error in the full superposition calculation, most likely due to the repositioning and interpolating operations. There were some fluctuations in the χ -

comparison results (Figure 3.7 (c)) near the origin since the azimuthal angle of many of the low radius voxels immediately surrounding it was approximately 45° , corresponding to the largest rotation imposed on the kernels. Evidence of radial symmetry in the χ -comparison (Figure 3.7 (b), a greyscaled intensity map of the 2-D χ -comparison scores) was consistent with the introduction of the tilted kernels into the superposition dose calculation. The radial symmetry demonstrated increasing differences from the parallel kernel as a function of tilt angle, as would be expected.

3.4 CONCLUSIONS

This study validates the practice of applying parallel dose kernels in a divergent clinical geometry to determine the dose deposited in an a-Si EPID, allowing fast calculation of portal dose images using the two-step algorithm. Monte Carlo dose kernels for an aS500 detector were generated with DOSXYZnrc at incident angles ranging from 0° to 14° and monoenergetic photon energies of 0.1, 2, 6 and 18 MeV. To improve statistics, the voxels were averaged bilaterally and then combined into concentric square rings to reduce statistical uncertainty to less than 0.08% of the maximum voxel dose. The parallel dose kernels were convolved with a top-hat function fluence incident on the EPID while the tilted kernels were used to perform a full superposition with the same incident fluence, in order to calculate the dose deposited using both calculation methods. Two field sizes and two SDDs were examined for each photon energy. A χ -comparison test compared the convolution and superposition results and produced an agreement between the methods for $\Delta D = 1.8\%$ and $\Delta d = 0.0784$ cm for the worst-case-scenario of 35.7×26.8 cm² field size and 105 cm SDD at all energies. The more clinically relevant cases (27.2×20.4 cm²

field size, 140 cm SDD) showed a $\Delta D = 1.0\%$ and $\Delta d = 0.0784$ cm agreement over all energies. In a clinical spectrum, the effects of the parallel kernel assumption would be expected to be smaller due to the larger proportion of low energy photons. It was observed that generally the parallel kernel assumption slightly underestimated the deposited dose, showing increasing differences with increasing radii from the central axis.

The time for the algorithm to compute the full superposition (18 h) was approximately 6000 times greater than the convolution time (10.5 s). The calculations were carried out using Interactive Data Language (IDL; RSI, Boulder, CO). Implementation on different software and hardware combinations may affect this ratio.

This work demonstrates that Monte Carlo generated EPID dose kernels applied with a parallel geometry assumption are sufficient in predicting portal dose images, and that a full superposition is not required for dosimetric accuracy of better than 1.8% for extreme cases and less than 1.0% for clinically relevant scenarios.

REFERENCES

1. Boyer, A. L. and Schultheiss, T., *Effects of dosimetric and clinical uncertainty on complication-free local tumor control*. *Radiother Oncol*, 1988. **11**(1): p. 65-71.
2. Brahme, A., *Dosimetric precision requirements in radiation therapy*. *Acta Radiol Oncol*, 1984. **23**(5): p. 379-91.
3. ICRU, *Determination of absorbed dose in a patient irradiated by beams of X or gamma rays in radiotherapy procedures*. 1976, International Commission on Radiation Units and Measurements: Washington.
4. Mijneer, B. J., Battermann, J. J., and Wambersie, A., *What degree of accuracy is required and can be achieved in photon and neutron therapy?* *Radiother Oncol*, 1987. **8**(3): p. 237-52.

5. Ahnesjo, A. and Aspradakis, M. M., *Dose calculations for external photon beams in radiotherapy*. Phys Med Biol, 1999. **44**(11): p. R99-155.
6. El-Mohri, Y., Antonuk, L. E., Yorkston, J., Jee, K. W., Maolinbay, M., Lam, K. L., and Siewerdsen, J. H., *Relative dosimetry using active matrix flat-panel imager (AMFPI) technology*. Med Phys, 1999. **26**: p. 1530-1541.
7. McCurdy, B. M. C., Luchka, K., and Pistorius, S., *Dosimetric investigation and portal dose image prediction using an amorphous silicon electronic portal imaging device*. Med Phys, 2001. **28**(6): p. 911-24.
8. Grein, E. E., Lee, R., and Luchka, K., *An investigation of a new amorphous silicon electronic portal imaging device for transit dosimetry*. Med Phys, 2002. **29**: p. 2262-2268.
9. Greer, P. B. and Popescu, C. C., *Dosimetric properties of an amorphous silicon electronic portal imaging device for verification of dynamic intensity modulated radiation therapy*. Medical Physics, 2003. **30**(7): p. 1618-27.
10. Warkentin, B., Steciw, S., Rathee, S., and Fallone, B. G., *Dosimetric IMRT verification with a flat-panel EPID*. Med Phys, 2003. **30**(12): p. 3143-55.
11. McDermott, L. N., Louwe, R. J. W., Sonke, J. J., van Herk, M. B., and Mijnheer, B. J., *Dose-response and ghosting effects of an amorphous silicon electronic portal imaging device*. Medical Physics, 2004. **31**(2): p. 285-95.
12. Siebers, J. V., Kim, J. O., Ko, L., Keall, P. J., and Mohan, R., *Monte Carlo computation of dosimetric amorphous silicon electronic portal images*. Medical Physics, 2004. **31**(7): p. 2135-46.
13. Menon, G. and Sloboda, R., *Quality Assurance measurements of a-Si EPID performance*. Med Dosim, 2004. **29**(1): p. 11-17.
14. Van Esch, A., Depuydt, T., and Huyskens, D. P., *The use of an aSi-based EPID for routine absolute dosimetric pre-treatment verification of dynamic IMRT fields*. Radiotherapy and Oncology, 2004. **71**(2): p. 223-34.
15. Kirkby, C. and Sloboda, R., *Comprehensive Monte Carlo calculation of the point spread function for a commercial a-Si EPID*. Medical Physics, 2005. **32**(4): p. 1115-27.
16. Winkler, P., Hefner, A., and Georg, D., *Dose-response characteristics of an amorphous silicon EPID*. Medical Physics, 2005. **32**(10): p. 3095-105.
17. Greer, P. B., *Correction of pixel sensitivity variation and off-axis response for amorphous silicon EPID dosimetry*. Medical Physics, 2005. **32**(12): p. 3558-68.
18. McCurdy, B. M. and Pistorius, S., *A two-step algorithm for predicting portal dose images in arbitrary detectors*. Med Phys, 2000. **27**(9): p. 2109-16.
19. Siebers, J. V. and Li, W., *Fast Monte Carlo-based computation of a-Si EPID dose images for IMRT treatment fields*. in *9th International Workshop on Electronic Portal Imaging*. 2006. Melbourne, Australia.
20. Mackie, T. R., Scrimger, J. W., and Battista, J. J., *A convolution method of calculating dose for 15-MV x rays*. Med Phys, 1985. **12**(2): p. 188-96.
21. Ahnesjö, A., *Invariance of convolution kernels applied to dose calculations for photon beams*. in *9th International Conference on Computer in Radiotherapy*. 1987. Haag, Amsterdam: Elsevier.

22. Mackie, T. R., Ahnesjö, A., Dickoff, P., and Snider, A. *Development of a convolution/superposition method for photon beams.* in *9th International Conference on Computers in Radiotherapy.* 1987. Haag, Amsterdam: Elsevier.
23. Bourland, J. D. and Chaney, E. L., *A finite-size pencil beam model for photon dose calculations in three dimensions.* *Med Phys*, 1992. **19**(6): p. 1401-12.
24. Papanikolaou, N., Mackie, T. R., Meger-Wells, C., Gehring, M., and Reckwerdt, P., *Investigation of the convolution method for polyenergetic spectra.* *Medical Physics*, 1993. **20**(5): p. 1327-1336.
25. Liu, H. H., Mackie, T. R., and McCullough, E. C., *Correcting of kernel tilting and hardening in convolution/superposition dose calculations for clinical divergent and polychromatic photon beams.* *Med Phys*, 1997. **24**: p. 1729-1741.
26. Sharpe, M. B. and Battista, J. J., *Dose calculations using convolution and superposition principles: The orientation of dose spread kernels in divergent x-ray beams.* *Med Phys*, 1993. **20**: p. 1685-1694.
27. Radcliffe, T., Barnea, G., Wowk, B., Rajapakshe, R., and Shaley, S., *Monte Carlo optimization of metal/phosphor screens at megavoltage energies.* *Med Phys*, 1993. **20**: p. 1161-1169.
28. Kausch, C., Schreiber, B., Kreuder, F., Schmidt, R., and Dossel, O., *Monte Carlo simulations of the imaging performance of metal plate/phosphor screens used in radiotherapy.* *Med Phys*, 1999. **26**: p. 2113-2124.
29. Bakai, A., Alber, M., and Nusslin, F., *A revision of the gamma-evaluation concept for the comparison of dose distributions.* *Phys Med Biol*, 2003. **48**(21): p. 3543-53.
30. Low, D. A., Harms, W. B., Mutic, S., and Purdy, J. A., *A technique for the quantitative evaluation of dose distributions.* *Med Phys*, 1998. **25**: p. 656-61.
31. Kawarakow, I. and Rogers, D. W. O., *The EGSnrc code system: Monte Carlo simulation of electron and photon transport.* 2003, Ionizing Radiation Standards, National Research Council of Canada.
32. Bevington, P. R., *Data Reduction and Error Analysis for the Physical Sciences.* 1969, New York: McGraw-Hill,
33. Edelsbrunner, H., *Triangulation and meshes in computational geometry.* *Acta Numerica*, 2000: p. 133-213.
34. Rathee, S., McClean, B. A., and Field, C., *An improved method for rebinning kernels from cylindrical to Cartesian coordinates.* *Med Phys*, 1993. **20**: p. 1343-1351.
35. Jaffray, D. A., Battista, J. J., Fenster, A., and Munro, P., *X-ray scatter in megavoltage transmission radiography: physical characteristics and influence on image quality.* *Med Phys*, 1994. **21**(1): p. 45-60.

CHAPTER FOUR: COMPREHENSIVE FLUENCE MODEL FOR ABSOLUTE PORTAL DOSE IMAGE PREDICTION

Chapter Three discussed the validation of the parallel dose kernel assumption for portal dose image prediction. The current chapter will outline the development of a versatile, physics-motivated fluence model to use for pre-treatment verification of open IMRT fields. This chapter was previously published in the peer-reviewed journal *Medical Physics*.*

4.1 INTRODUCTION

As radiation therapy techniques grow increasingly complex, a need for thorough dosimetric verification of these treatments is evident. These techniques typically deliver higher doses to the tumour with a more conformal dose distribution. High dose gradients are present and are inherent to the techniques. These factors increase the demand for verifying that the planned dose distribution was actually delivered to the patient. One verification tool under investigation is the amorphous silicon electronic portal imaging device (a-Si EPID) [1-16]. This EPID is commonly used for geometric verification in the clinic [1], but it has also shown promise as a means for dosimetric validation [2-14]. The response of the a-Si EPID is linear with dose [1, 7, 16], but it also possesses other favourable imaging characteristics such as high quantum efficiency, spatial resolution,

* Reprinted with permission from the AAPM, granted on April 8, 2011.
K. Chytky and B. M. C. McCurdy, "Comprehensive fluence model for absolute portal dose image prediction," *Med Phys*, 2009. **36** (4): p. 1389-98.

signal-to-noise ratio and noise power spectra [16]. There is a particular interest in utilizing the a-Si EPID for the verification of IMRT treatments [3-13].

One approach for a-Si EPID dosimetric verification is transit dosimetry, where the measured image is used to determine energy fluence exiting the patient or phantom. The energy fluence may then be backprojected through the patient CT dataset and used to calculate patient dose, which is compared to the planned dose distribution [10, 13, 14] or to film [11, 12]. Another method is to generate a 2-dimensional predicted portal dose image, which is created by simulating the portal image formation process as determined by the imager characteristics. By comparing information from predicted images to measured treatment images captured by EPIDs [2-4, 6] and assuming patient setup has been verified, one can determine whether the expected fluence pattern exited the patient, and therefore if the correct dose was delivered within a desired tolerance.

There are many proposed methods for portal dose image prediction. One approach is a full Monte Carlo technique, where radiation transport through the treatment head and dose deposition in the detector are simulated [3]. Some groups have used precalculated Monte Carlo dose kernels [2, 4, 17] or analytical dose kernels [6, 8] to represent the dose delivered to the detector system. Usually, these dose kernels are convolved with a photon fluence map incident on the EPID. A two-step approach which convolves Monte Carlo dose kernels with an incident EPID photon fluence for static fields has been utilized in our earlier work [2, 17]. However, the fluence exiting the treatment head in that work was estimated with a cumbersome ionization chamber measurement of fluence profiles for

every portal dose image predicted. Therefore, the field was measured twice – once with an ionization chamber and once with an EPID.

Li *et al.* extracted the energy fluence of the treatment field from the TPS, convolving the extracted fluence with dose kernels [4]. Their model consisted of separate dose kernels for MLC-transmitted and open regions of the field to obtain a more accurate portal dose image prediction. Greer *et al.* [8] also found a difference in EPID response between open and MLC-blocked fields and determined that a correction for this difference should improve IMRT dosimetry. A recent investigation carried out by the same group [9] has provided further insight into a method conceived by van Esch *et al.* [6] and employed by the Eclipse Treatment Planning System (TPS) (Varian Medical Systems, Palo Alto, CA). In that work, Vial *et al.* studied the effect of MLC transmitted radiation on the portal dose image prediction method that was originally proposed by van Esch *et al.* [6]. To obtain a predicted dose image, the detector response function was convolved with the fluence extracted from the TPS. The detector response function (or dose kernel) was a sum of triple Gaussians that were iteratively adjusted to fit a predicted image to an acquired test image specified by the vendor. A collimator scatter factor was employed in the prediction algorithm to account for linear accelerator output with respect to field size, while a correction was added to better predict MLC-blocked fields. A reference dosimetry dose calibration was also incorporated into the algorithm. Although this method had previously been found to be adequate for IMRT fields (an agreement within a dose difference of 3%, and a distance-to-agreement or DTA of 3 mm) [6], the work of Vial *et al.* [9] found the algorithm to be insufficient for accurate portal dose prediction. The

EPID response to MLC-transmitted radiation was reduced to 0.79 times that of an open field, and was further reduced with respect to off-axis distance. To improve prediction accuracy, the authors suggested that the EPID response function and the incident fluence need to be modeled in more detail.

This work addresses the issues of a detailed EPID response function and an improved source model specifically for portal dose image prediction. To efficiently implement treatment verification using our previous work [2, 17], a general fluence determination for portal dose image prediction is required, especially to model the complex modulation of IMRT. A physically-based fluence model, analogous to that used by the Pinnacle TPS (Philips Medical Systems, Milpitas, CA) [18], was developed. Model parameters were adjusted in order to match MLC-defined predicted images to a series of measured ‘commissioning’ images taken with an aS1000 EPID (Varian Medical Systems, Inc., Palo Alto, CA). The model presented here accounts for the initial fluence profile, MLC transmission, interleaf leakage, tongue and groove effect, rounded leaf tips, extrafocal scatter, primary fluence, off-axis spectra softening and jaw transmission. Monte Carlo studies resulted in the proposed modifications to the extrafocal source shape and energy spectrum of the fluence model. Improvements over the approach taken by the TPS include using a non-Gaussian extrafocal source distribution and separating the energy spectrum and off-axis softening of the focal and extrafocal sources. The conversion of predicted energy fluence to a portal dose image is accomplished by convolving the energy fluence with a series of monoenergetic dose kernels, calculated via Monte Carlo. The fluence model parameters were manually adjusted in order to match predicted

images to measured images of MLC-defined fields, in a process analogous to the commissioning of a TPS utilizing a physical head fluence model. Once the model was commissioned, it was tested on ten clinical prostate and ten clinical oropharyngeal IMRT fields. It is demonstrated that the proposed fluence model, combined with a dose deposition calculation accounting for the detector energy response, is capable of accurate portal dose image prediction as shown by agreement with static and IMRT field measurements.

4.2 METHODS AND MATERIALS

4.2.1 Measured images of MLC-defined fields for commissioning

Measured EPID images were taken with an aS1000 EPID mounted on a Clinac iX (Varian Medical Systems, Palo Alto, CA). The active detection area of the amorphous silicon EPID is 40x30 cm² with a resolution of 1024x768 pixels. The imaging cassette of the detector consists of a 1 mm thick copper buildup plate and a Lanex Fast-B phosphor (gadolinium oxysulphide) screen. The Clinac iX is a dual-energy (6 MV and 23 MV) linear accelerator equipped with 120-leaf Millenium MLCs. Our institute's IMRT treatments are delivered with 6 MV only, therefore all measurements here were taken with a 6 MV photon beam. However, the methods presented are probably applicable to any beam energy as the process is analogous to the Pinnacle TPS [18]. Using the IAS3 (Image Acquisition System v.3) Service Monitor of PortalVision (Varian Medical Systems, Palo Alto, CA), a total integrated image for each delivered field is obtained, where the integrated image is averaged over the total number of frames taken throughout

the field delivery. Details on acquiring images are included in the Appendix (Section 8.1).

The MLC-defined fields for the commissioning of our model were similar to the fields used for TPS commissioning (1x1, 2x2, 5x5, 5x20, 10x10, 20x5 and 20x20 cm², with the jaws positioned at 25x25cm²), with 100 MUs delivered to the imager. These images were re-acquired over a range of SDDs including 100, 115, 130, 140 and 160 cm. The 160 cm SDD image set did not include the 20x20 and 5x20 cm² fields because these fields extended beyond the EPID detector area at that distance. Commissioning was performed at an SDD of 140 cm since this distance is commonly used for our clinical imaging. The model parameters (outlined in Section 4.2.4) were manually adjusted to match the predicted images to the measure images. Images acquired at SDDs other than 140 cm were used to check the robustness of the model at various SDDs.

During image processing of the aS1000 images, a dark-field and a flood-field correction are applied. Unfortunately, the flood-field correction eliminates profile fluence information inherent to the beam and creates difficulty in using the a-Si EPID for accurate dosimetry. By following a procedure described by Greer [15], the beam profile of the measured image was reintroduced.

4.2.2 Dose calibration

A calibration of the imager to absolute dose units through reference dosimetry was desired for IMRT validation. Since the majority of our current and future work is or will

be carried out at a SDD of 140 cm or greater, the chosen image for the calibration was a 10x10 cm² field at 140 cm SDD (100 MU delivered), although any SDD and field size could be used. For the calibration, 1 MU delivers 1 calibrated unit (CU) to the center of the imager. For an integrated image taken during the entire beam-on time, PortalVision (Varian Medical Systems, Palo Alto, CA) obtains data for a number of frames which is dependent on beam-on time, with the resulting image being an average over the total number of frames. The total integrated signal of the image (i.e. resulting image multiplied by the number of frames) is denoted as S_{total}^{ref} on the central axis for the 10x10 cm² measured image. In practice, an averaged signal over a 24x24 pixel region of interest on the central axis is used (~1x1 cm²). Then 1 CU is defined as:

$$(4.1) 1CU = \frac{S_{total}^{ref}}{100} .$$

The central axis dose of the predicted image for the same field size (D_{pred}^{ref}) and SDD is proportional to the CUs of the corresponding measured image with the constant α , defined as:

$$(4.2) \alpha = 100 \cdot \frac{D_{pred}^{ref}}{S_{total}^{ref}} .$$

Therefore, to obtain a predicted image in CU (S_{total}^{pred}),

$$(4.3) S_{total}^{pred} = \frac{D_{pred}}{\alpha} \cdot N_{MUs}$$

and to obtain a measured image in CU (S_{total}^{meas}),

$$(4.4) S_{total}^{meas} = S_{mean}^{meas} \cdot N_{frames} ,$$

where N_{MUs} is the number of monitor units delivered (valid for both IMRT and static fields), N_{frames} is the number of frames taken, D_{pred} is the dose of the predicted image in

dose units and S_{mean}^{meas} is the dose of the raw measured image in greyscale (averaged over N_{frames}) and α is given as in Equation 4.2. This provides a simple method to give predicted and measured dose images in arbitrary ‘calibrated units’.

4.2.3 Monte Carlo simulation of linear accelerator

To examine the characteristics of both the focal and extrafocal fluence independently, the linear accelerator was simulated using BEAMnrc [19], with the DYNVMLC component module for simulation of the Millenium MLC [20]. The phase-space files (generated at the isocenter plane) were applied to a simulated water tank in DOSXYZnrc [21] to validate the BEAMnrc model predictions against measured water tank data. A large (20x20 cm²) and small (5x5 cm²) field size were defined by MLC, with jaws set to 25x25 cm². The fluence generated by each component of the linear accelerator model was tracked using the latch mechanism in BEAM. The default electron and photon cut-off (ECUT and PCUT) values were used – 0.521 MeV and 0.01 MeV, respectively. After validation, the phase-space files were analyzed with BEAMDP [22]. The extrafocal fluence was investigated, examining energy spectrum, profile and contributions of the various linear accelerator head components. In addition, the focal fluence was analyzed for its profile shape.

4.2.4 Fluence model for predicted images

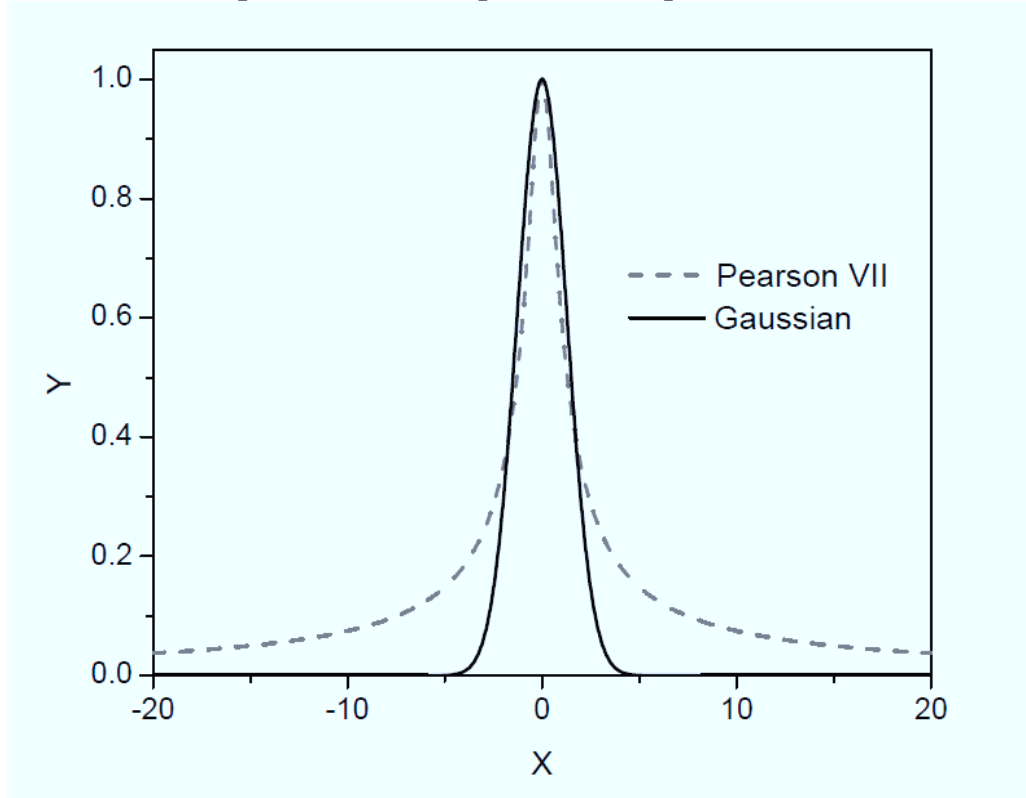
The proposed fluence model consists of a focal fluence source and an extrafocal fluence source [18, 23, 24]. Based on the results of the Monte Carlo simulations described in Section 4.2.3, the Pearson VII function (see Figure 4.1 and Equation 4.5) was used to

model the extrafocal source. The Pearson VII is similar in shape to the Gaussian (a common function used to approximate an extrafocal source [18, 23]), but the Pearson VII tails fall off more slowly. The Pearson VII is defined as:

$$(4.5) \quad y = \frac{a}{\left(1 + \frac{4(x-b)^2 \left(2^{1/d} - 1\right)}{c^2}\right)^d},$$

where a as the amplitude, b is the center, c is the FWHM and d is the parameter which controls the approach to zero of the function. As the d parameter approaches a value of ten, the Pearson VII approaches a Gaussian. Other functions may be proposed with similar properties to the Pearson VII. However, we chose this function since it maintains simplicity by only adding one additional fit parameter compared to that of the Gaussian. The focal fluence source was modeled as a Gaussian and both sources had a user-defined FWHM and adjustable contribution. The relative contributions of both the focal and extrafocal sources can be adjusted to match the tails and shoulders of the predicted profiles to the measured profiles. These contributions are governed by the extrafocal height parameter, which is the proportion of extrafocal fluence scatter at the central axis for the largest field possible (in this case, a 40x40 cm² jaw-defined field). The amount of extrafocal fluence at the central axis for each field calculated is then relative to this parameter, with the focal fluence contribution being defined as ($1 - \text{extrafocal height}$). This approach is analogous to the TPS method of weighting the focal versus extrafocal fluence.

Figure 4.1 [Gaussian and Pearson VII Functions]: Profiles of sample Gaussian and Pearson VII. Both functions have the same FWHM of 3.0 and amplitude of 1.0, with the Pearson VII's 'd' parameter (see Equation 4.5) equal to 0.5.



The attenuation through the flattening filter in the linear accelerator head creates the characteristic beam profile of the focal fluence. In this work, the Monte Carlo simulation of the linear accelerator provided our 'initial focal fluence profile' estimate. The initial focal fluence profile is a radially symmetric function that is used by the fluence model to account for field shape and focal source effects. The fluence profile also characterizes the attenuation effects of the flattening filter on the focal fluence component. The off-axis softening of the focal fluence, also due to the presence of the flattening filter in the beam, is taken into account with Equation 4.6, as in the TPS [18]:

$$(4.6) \quad W_i' = W_i \times \left(\frac{1}{1 + \left(\frac{E_i}{E_{\max}} \right)} \right)^{OASoft \times \theta},$$

where the adjustable parameter $OASoft$ is the ‘off-axis softening parameter’. E_i is the energy of the photon with corresponding weight W_i , E_{max} is the maximum photon energy in the spectrum, θ is the angle from source to calculation point and W_i' is the proportion of photons with energy E_i off-axis. The focal fluence energy spectrum was defined by the Monte Carlo simulation analysis outlined in Section 4.2.3 since, in contrast to measurements with a water phantom, it is not possible to obtain percentage depth dose data for energy spectra adjustment with an EPID. Whereas the TPS uses a single energy spectrum for focal and extrafocal fluences, we employed an extrafocal spectrum that was separate from the focal spectrum and also defined by the BEAMnrc simulation analysis. This extrafocal energy spectrum was radially constant, i.e. the extrafocal spectrum was not softened off-axis.

The magnitude of extrafocal fluence for a particular point on the EPID was calculated in the standard manner, by determining the amount of extrafocal fluence ‘seen’ at that point through the MLC-defined field [25]. The MLC-defined field is projected onto the plane of the extrafocal fluence source (in this model, the base of the flattening filter) and then convolved with the extrafocal source function. Convolution may be used here since the MLC defines the field aperture at a single plane perpendicular to the beam central axis.

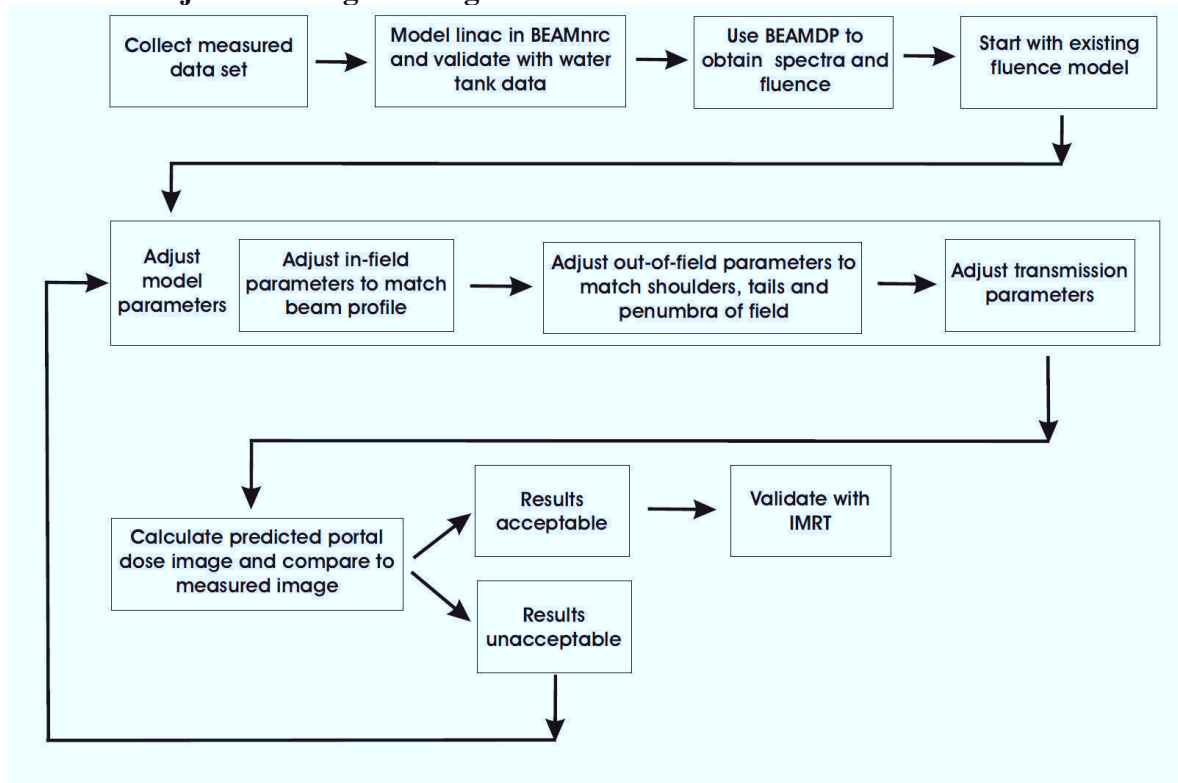
A number of details concerning the multi-leaf collimators were modeled. The MLCs were assigned a transmission factor to account for the transmitted fluence through the full thickness of the leaves. The MLC transmitted photon spectrum was assumed to be equal to that of the incident photon spectrum, as is assumed in Pinnacle [18]. The rounded-leaf

tips of the MLCs were approximated as a circle of user-defined radius, with raytracing occurring through the tips. Clinical leaf offsets were used to correct the difference between the light field and the radiation field. The phenomenon that occurs when MLCs are non-adjacent, known as the tongue and groove effect, was represented as the transmission through one-half the MLC thickness. The interleaf leakage of adjacent leaves was assigned a transmission factor for the tongue and groove width.

The secondary collimators were assigned their own transmission factor to account for the transmitted fluence through the jaws.

This fluence model consists of a number of parameters that are to be adjusted during the commissioning process (see Figure 4.2). All parameters are manually adjusted until all open-field profiles agree within 2% and 2 mm, to obtain one set of parameters for all square and rectangular fields. To adjust the fluence in-field, the incident focal fluence profile and the off-axis softening parameter (see Equation 4.6) are varied. The shoulders, tails and penumbra of the field are controlled with the full-width half-maximums (FWHMs) of the focal and extrafocal source functions and the radius of curvature of the MLC leaves. Transmission coefficients for the jaws, MLCs and interleaf leakage also account for out-of-field characteristics, as does the tongue-and-groove width. The focal and extrafocal spectra are not adjusted after being determined by BEAMnrc. The leaf-offsets are determined by the vendor and are not adjusted either. A list of the parameters and their values is found in the Appendix (Chapter 8.4).

Figure 4.2 [Comprehensive Fluence Model Commissioning]: Procedure to determine fluence model. In-field parameters to adjust are the focal fluence incident profile and off-axis softening parameter (see Equation 4.6). Out-of-field parameters refer to the full-width half-maximums (FWHMs) of the focal and extrafocal sources, the extrafocal height (percentage of Gaussian contribution) and the radius of curvature of the MLC leaves (match to penumbra of field). The transmission variables include a jaw, a MLC and an interleaf leakage transmission coefficient, as well as an adjustable tongue-and-groove width.



4.2.5 Converting the fluence to dose

A library of monoenergetic dose kernels (0.1 – 6.0 MeV) was generated by DOSRZnrc [21]. These dose kernels were specific to the aS1000 imager and the simulation geometry included detailed specifications provided by the manufacturer. To approximate the backscatter from the rear housing of the detector, a 21 mm air gap and 10 mm uniform water slab placed downstream from the imaging cassette, as determined by Siebers *et al.* [3] and employed by Li *et al.* [4], was included. This additional backscatter also provides

an increased detector dose response which emulates an optical glare effect, so the optical glare effect is not explicitly modeled here [4]. A pencil beam of photons was simulated perpendicularly incident to the detector, with dose bins in the phosphor layer consisting of concentric rings of varying width (high resolution at lower radius and low resolution at higher radius). The dose kernels for all energies were converted to Cartesian coordinates and then convolved with the resulting predicted energy fluence from the model and the results summed over energy to find total dose in the detector. This method for converting fluence to dose for EPIDs has been used previously [2, 17], since energy response of the EPID is modeled and the assumption of perpendicularly incident fluence has been shown to be accurate in most clinical situations [26].

4.2.6 Clinical IMRT validation

The developed portal dose image prediction model was tested with clinical IMRT fields incident on the EPID. Ten prostate and ten oropharyngeal clinical plans were chosen for validation. These plans each contained seven fields and were designed by the Pinnacle TPS using direct machine parameter optimization, with step-and-shoot delivery. The predicted and measured images were evaluated in-field, by applying a threshold of 10% of the maximum dose, and using the χ -comparison [27] (a computationally efficient implementation of the γ -evaluation [28]) for an absolute local dose difference of 2% and a DTA of 3 mm. Whereas our institution uses values of 3%, 3 mm as part of routine, clinical, non-EPID IMRT quality assurance, we decided to impose a more stringent acceptance criteria. The prostate cases were part of the PROFIT trial (*prostate fractionated irradiated trial* – Ontario Clinical Oncology Group). The oropharyngeal cases

were planned using the RTOG 0022 trial guidelines (Radiation Therapy Oncology Group), although these patients did not formally participate in the trial.

One oropharyngeal field (plan 5, field 5) was calculated using the Gaussian model (with combined focal and extrafocal spectra) and compared to the Pearson VII model (with independent focal and extrafocal spectra) for accuracy against the measured IMRT field.

4.3 RESULTS AND DISCUSSION

4.3.1 Monte Carlo simulation of linear accelerator

The BEAMnrc simulation of the linear accelerator was validated with measured water tank data taken with a silicon diode (PFD, IBA Dosimetry, Schwarzenbruck, Germany). The in-plane and cross-plane profiles through central axis at depths of 1.5 cm, 5.0 cm, 10.0 cm and 20.0 cm agreed within a 1% dose difference for a 20x20 cm² and 5x5 cm² field (90 cm SSD setup). The percentage depth doses also agreed within a dose difference of less than 1% from 1.5 cm to 30 cm depth. Therefore, we assume our BEAMnrc model of the linear accelerator is accurate.

Analysis of the BEAMnrc simulation of the linear accelerator with the BEAMDP tool revealed the extrafocal fluence outside the defined field, the magnitude of which is dependent on field size and slowly decreasing with radius (see Figure 4.4). However, if one calculates extrafocal fluence based on the best fit Gaussian function matching the predicted and measured dose images at 140 cm SDD, the fall off is much sharper than that observed with the best fit Pearson VII function. For example, see the extrafocal

fluence distributions for a 20x20 and a 5x5 cm² field in Figure 4.3. The Gaussian function may provide a slightly better match to the Monte Carlo in-field, but any variations in this region can be compensated for with other model features, such as initial focal fluence profile, as is common in TPS commissioning. In Figure 4.3 (b), the 5x5 cm² Monte Carlo determined extrafocal fluence is not as accurately predicted by the Pearson VII extrafocal fluence well away from the field edge in the MLC-blocked regions of the image in comparison to the 20x20cm² field, but improved compared to the best fit Gaussian result.

Figure 4.3 [Profiles of Extrafocal Source Fluences]: Profiles of Monte Carlo, Gaussian and Pearson VII calculated extrafocal source fluences for a (a) 20x20 cm² and a (b) 5x5 cm² field. Note the sharp drop-off to zero of the Gaussian extrafocal fluence as compared to the Monte Carlo and Pearson VII extrafocal fluence

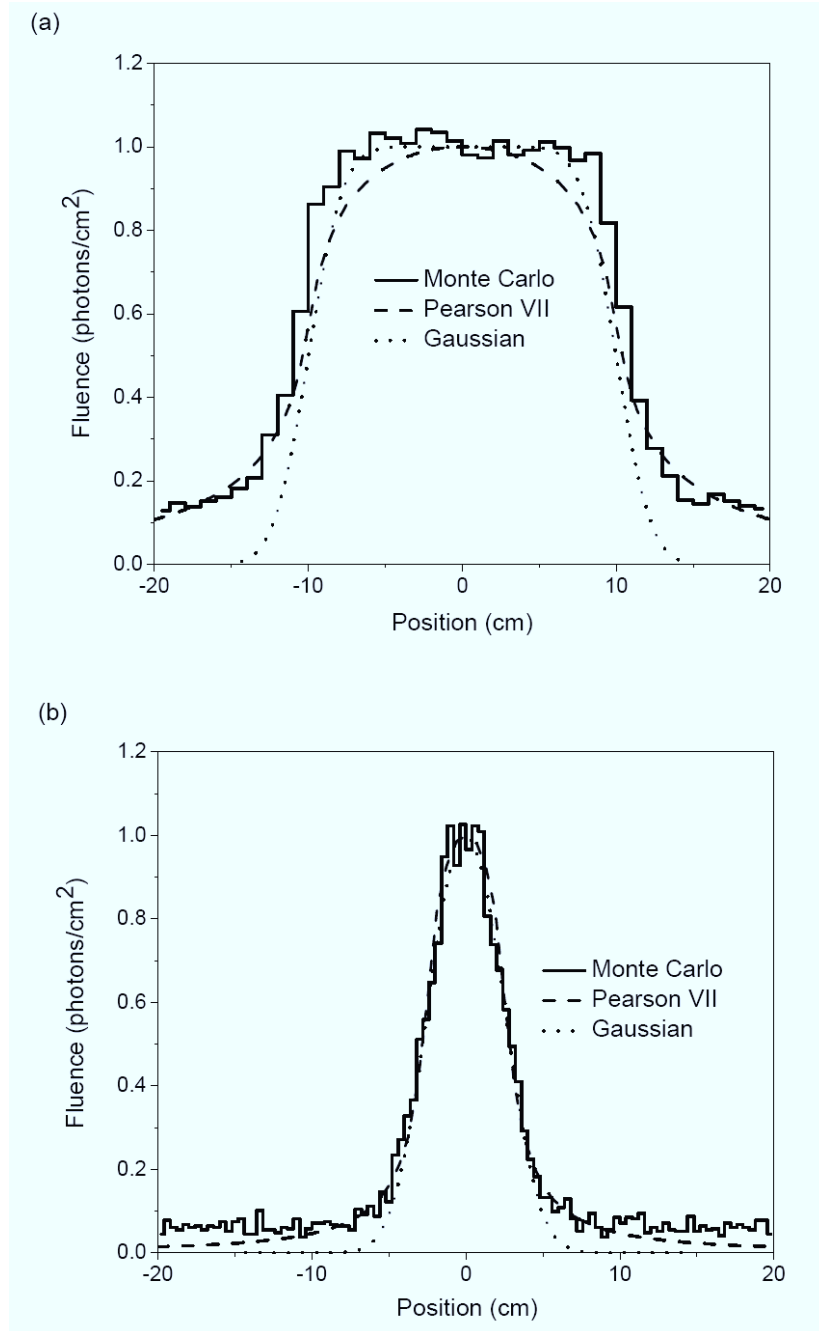
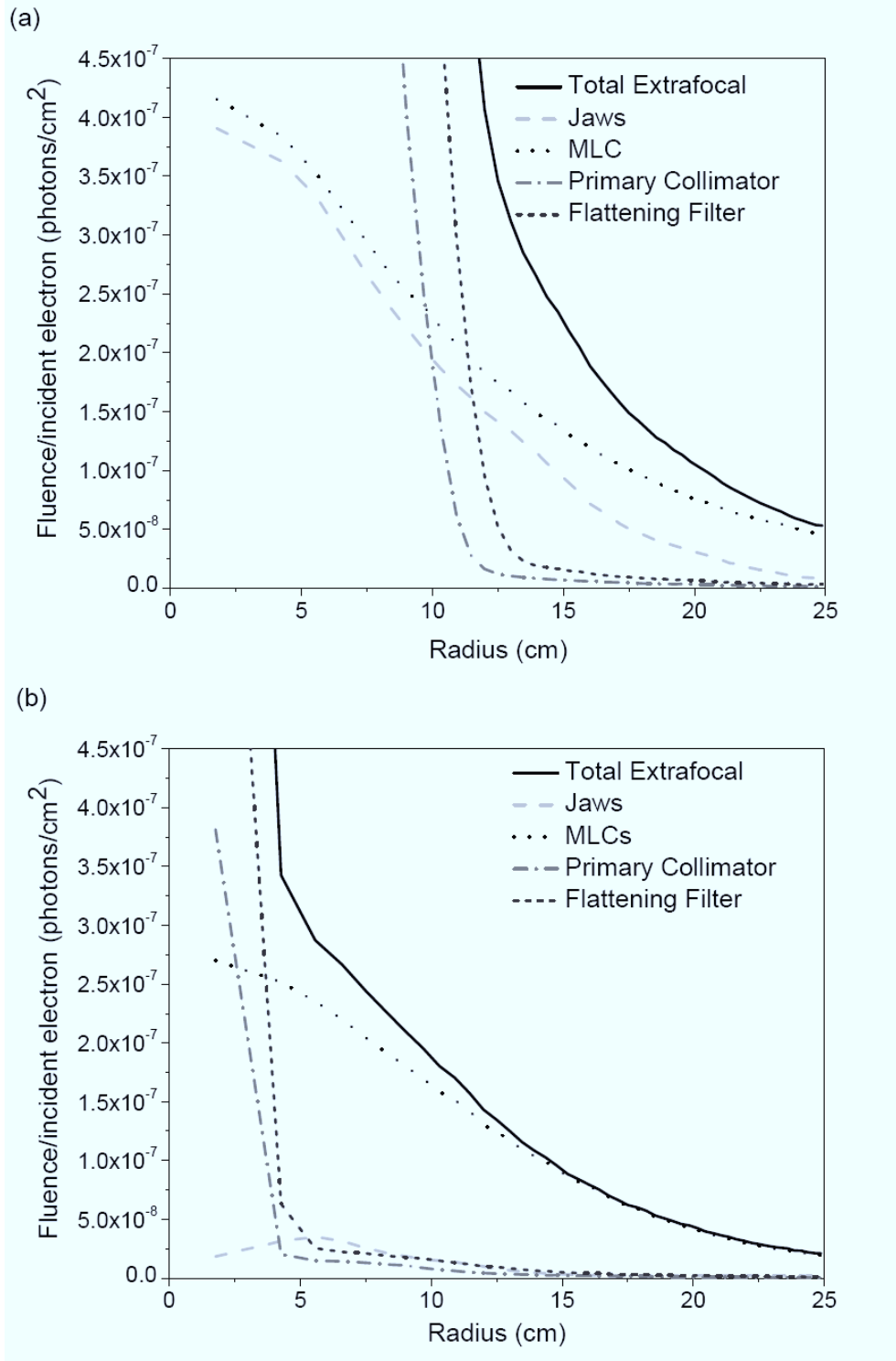


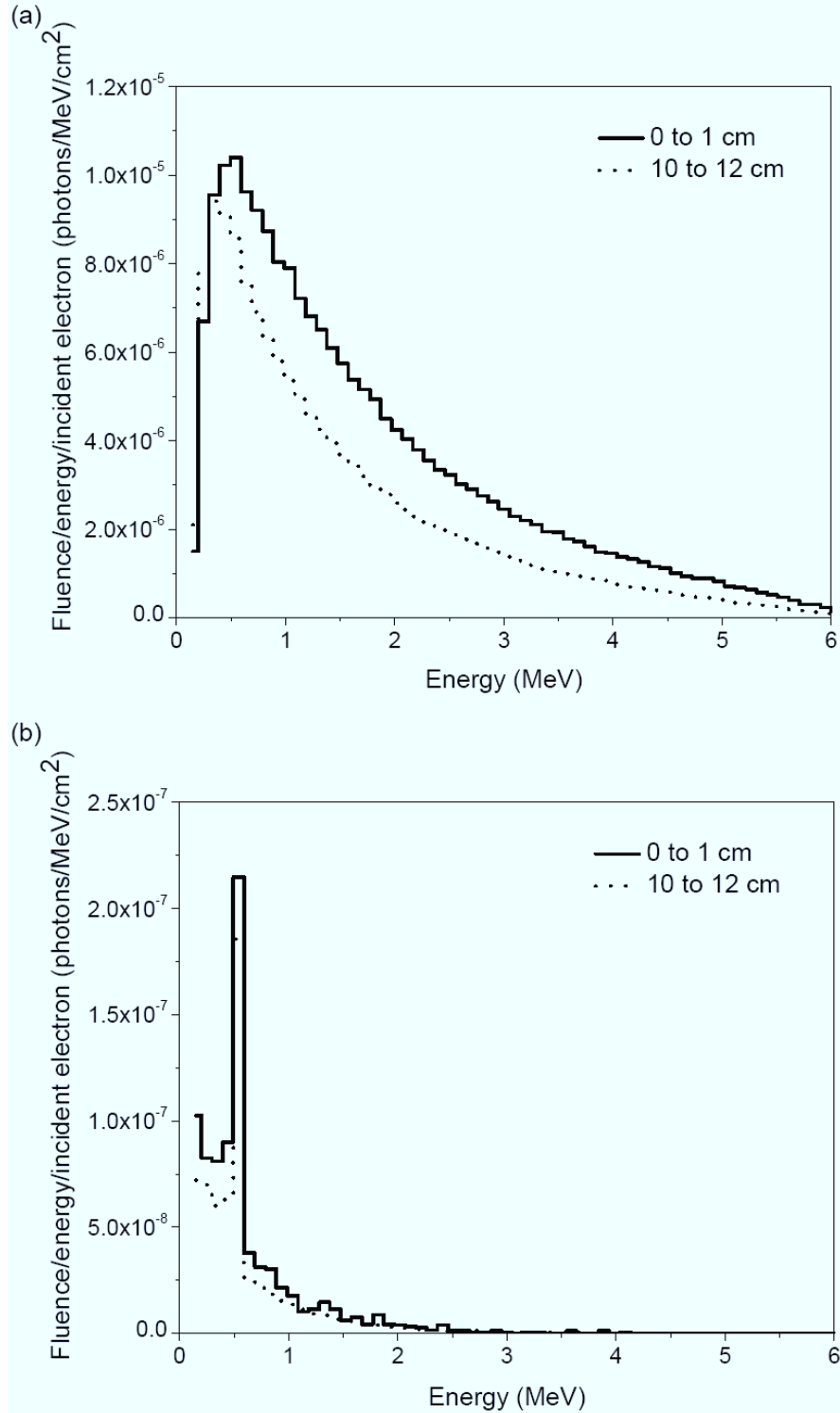
Figure 4.4 [Extrafocal Fluence from Linac Components]: Contributions of each linear accelerator component to the total extrafocal fluence as determined by Monte Carlo simulation. The graph ranges are chosen to emphasize the low fluence range outside of the field for (a) a 20x20 cm² and (b) a 5x5 cm² field at an SAD = 100 cm. The high fluence range in the central area of the field was dominated by the flattening filter scatter.



BEAMDP analysis further revealed that the non-zero, out-of-field extrafocal fluence was due mostly to scatter from the MLC, with a small contribution from the secondary collimators (see Figure 4.4). Kim *et al.* [29] found that the MLC scatter was also dependent on field size and could be estimated as a constant background, their results focusing on the examination of in-field properties. MLC scatter increases with field size due to increased surface area of the MLCs exposed to the beam [30]. The Pearson VII function allows the spatially broad MLC scattered extrafocal fluence to be modeled more accurately than can be achieved with a single Gaussian function. Inside the field, the majority of extrafocal scatter comes from the flattening filter, as expected.

The extrafocal fluence spectrum was also studied with BEAMDP. In the TPS fluence model, the extrafocal and focal spectra have been combined and handled as a single spectrum that varies with off-axis distance. The focal spectrum clearly softens off-axis, but Monte Carlo simulation reveals that the extrafocal spectrum varies little with radius (see Figure 4.5) and is the justification for a radially independent extrafocal spectrum that is separate from the focal spectrum.

Figure 4.5 [Focal and Extrafocal Spectra]: (a) Focal spectra as determined by Monte Carlo modeling for scoring rings from 0 to 1 cm and 10 to 12 cm. Note the change in spectra off-axis, particularly in comparison to (b). (b) Extrafocal spectra as determined for scoring rings from 0 to 1 cm and 10 to 12 cm. Note that the spectrum does not change noticeably off-axis, with respect to the central axis.



As a starting point for the beam modeling, the focal fluence profile determined by the Monte Carlo simulation was used as the initial fluence profile. The initial fluence profile only required minor adjustments ($< 2\%$) to accurately model the measured images.

In the literature, a variety of functions have been investigated as extrafocal source functions, including, but not limited to: a polynomial [31], an exponential [32], a triangular function [33] and a Gaussian [34-37]. The use of the Pearson VII as the extrafocal source in this model is better able to account for the field-size dependency of the MLC scatter, particularly outside the field. The extrafocal source function used in this work improves prediction of MLC scatter especially outside defined apertures, but an alternative approach could be to add a third source to the model specifically to predict MLC scatter. Yang *et al.* [32] proposed a three-source model, with one focal point source and two extrafocal sources to account for flattening filter scatter (modeled as an exponential) and primary collimator scatter, respectively, but the model did not explicitly include a source for MLC scatter. Ahnesjö [38] explicitly modeled jaw scatter via analytical methods, but did not extend the model to the MLC. Furthermore, other work by Ahnesjö found that a triangular function more accurately matched a flattening filter scatter source, in comparison with a Gaussian [33]. Zhu and Bjärngård stated their use of a Gaussian function to represent extrafocal scatter should not be taken to be the definition of the ‘distributed’ extrafocal source [35]. They emphasized that the Gaussian function is modeling many linear accelerator components and may ‘capture the essential features’ of the extrafocal source. Thus, there appears to be no physical significance in using a specific analytical function form (i.e. Gaussian) as the extrafocal source function. The

Pearson VII is a simple analytical function that provides slightly more functionality than a Gaussian to the application of empirical modeling of an extrafocal source function.

4.3.2 MLC-defined fields for commissioning

The predicted and measured EPID profiles agreed in-field (10% of the maximum dose) within a relative dose difference of 2% and a DTA of 2 mm for all field sizes at 140 cm SDD – the only fields that did not achieve a percentage of pixels greater than 98% (pixels with $\chi < 1$) were the 10x10 cm² field (96.4%) and the 20x20 cm² field (90.6%). The disagreement for these fields was localized to the edges of the field. The average number of pixels agreeing within the 2%, 2 mm criteria for all field sizes at 140 cm SDD was 97.9%, while prediction at the other SDDs agreed similarly, with an average number of pixels with $\chi < 1$ ranging from 98.1% to 99.0%. The slightly better agreement for SDDs other than the 140 cm SDD could be due to the smaller size of the fields incident on the EPID (despite the same size of the fields at isocentre) for the shorter SDDs. In this case, field edge effects as described further at the end of this section would be less pronounced. For the 160 cm SDD case, the fields largest in the gantry-couch direction (i.e. 20x20 cm² and 5x20 cm²) were not measured as the fields would extend past the edge of the detector.

The model utilizing the Gaussian extrafocal source predicted the 1x1, 2x2, 5x5 and 10x10 cm² fields to within 2%, 2 mm for at least 99% of the pixels in-field. The 20x20, 20x5 and 5x20 cm² fields only agreed for 83.6%, 92.4% and 80.4% of the pixels, respectively.

Large differences between the models occur out-of-field (defined as less than 10% of the maximum dose). The Pearson VII model agrees out-of-field (within 2%, 2 mm with respect to the local dose) for at least 99% of the pixels for all MLC-defined fields, while the Gaussian model agrees out-of-field for at least 98% of the pixels for only the three smallest fields. The 10x10, 20x20, 20x5 and 5x20 cm² agree out-of-field for 77.7%, 13.2%, 77.6% and 76.7% of pixels, respectively. Overall, the Pearson VII model agrees more accurately than the Gaussian model over the variety of field sizes used in commissioning – both in-field and out-of-field.

As shown in Figures 4.6 (a) and 4.7 (a), a model utilizing the Gaussian extrafocal source and a combined focal and extrafocal spectrum underpredicts the tails of the profiles for fields larger than or equal to 5x5 cm². In our clinic, underprediction of tails is also observed in the TPS commissioning data, but not to this extent. Examining a 20x20 cm² field for example, there is about a 2% dose difference in the TPS using water tank data, as opposed to 6.5% dose difference for the Gaussian fluence prediction using EPID data. This difference occurs in the MLC-blocked region of the field and not the jaw-blocked region. The cause of the difference in underprediction could be that the measured images were acquired with an EPID and not a water tank as in the TPS. Another point to consider is that this model is only mimicking the TPS and is not the commercial TPS itself. Aspects of the TPS that are not explicitly outlined in the user manual are not incorporated in the proposed model, thus behaviour of the TPS model may not be exactly reproduced.

Figure 4.6 [Measured and Predicted Profiles of Open 20x20 Field]: (a) X-profiles (cross-plane) of a 20x20 cm² field demonstrating agreement between the model and the measured data. ‘Pearson’ denotes the model with the Pearson VII extrafocal source, while ‘Gaussian’ is the model with the Gaussian extrafocal source. Note that the ‘Gaussian’ model underestimates the measured profiles outside the field. (b) Y-profiles (gantry-couch plane) of 20x20 cm² field for both the measured and predicted model (i.e. with Pearson VII extrafocal source). Noticeable differences in the Y-profiles at the field edges are likely due to the differences between the estimated flood-field correction and the flood-field actually used, including a slight asymmetry and field edge effects.

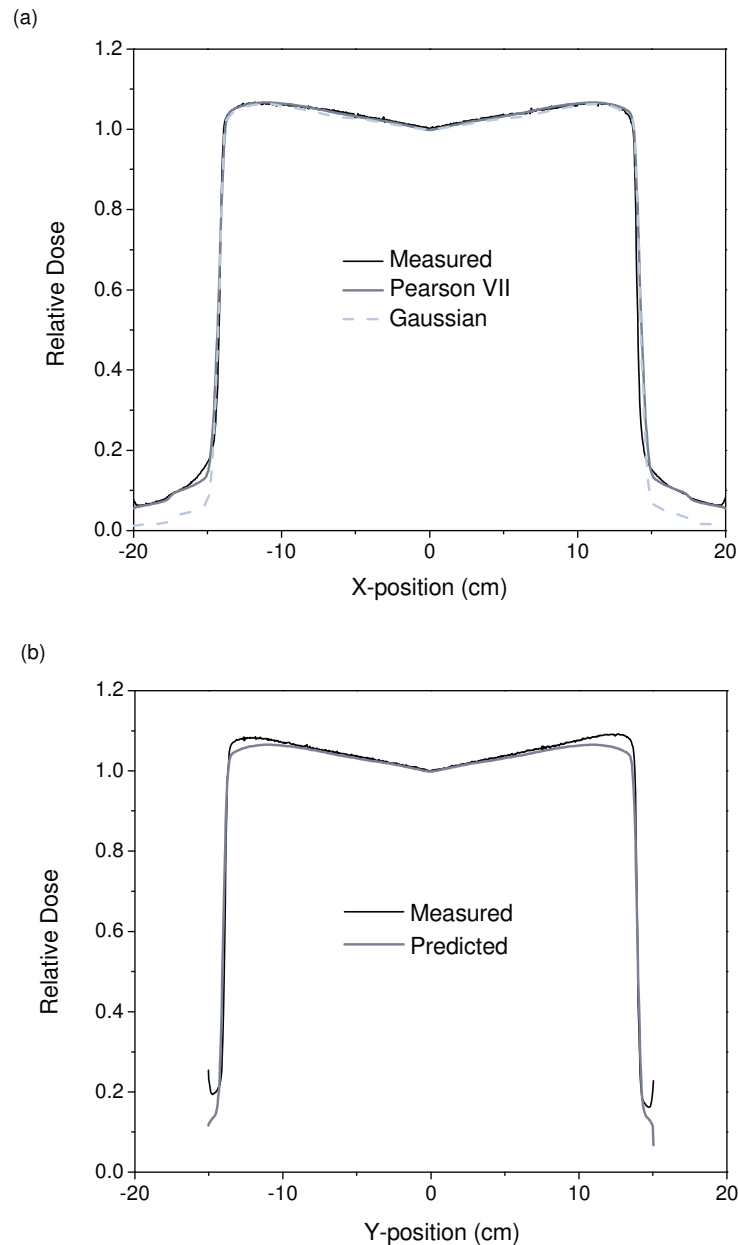
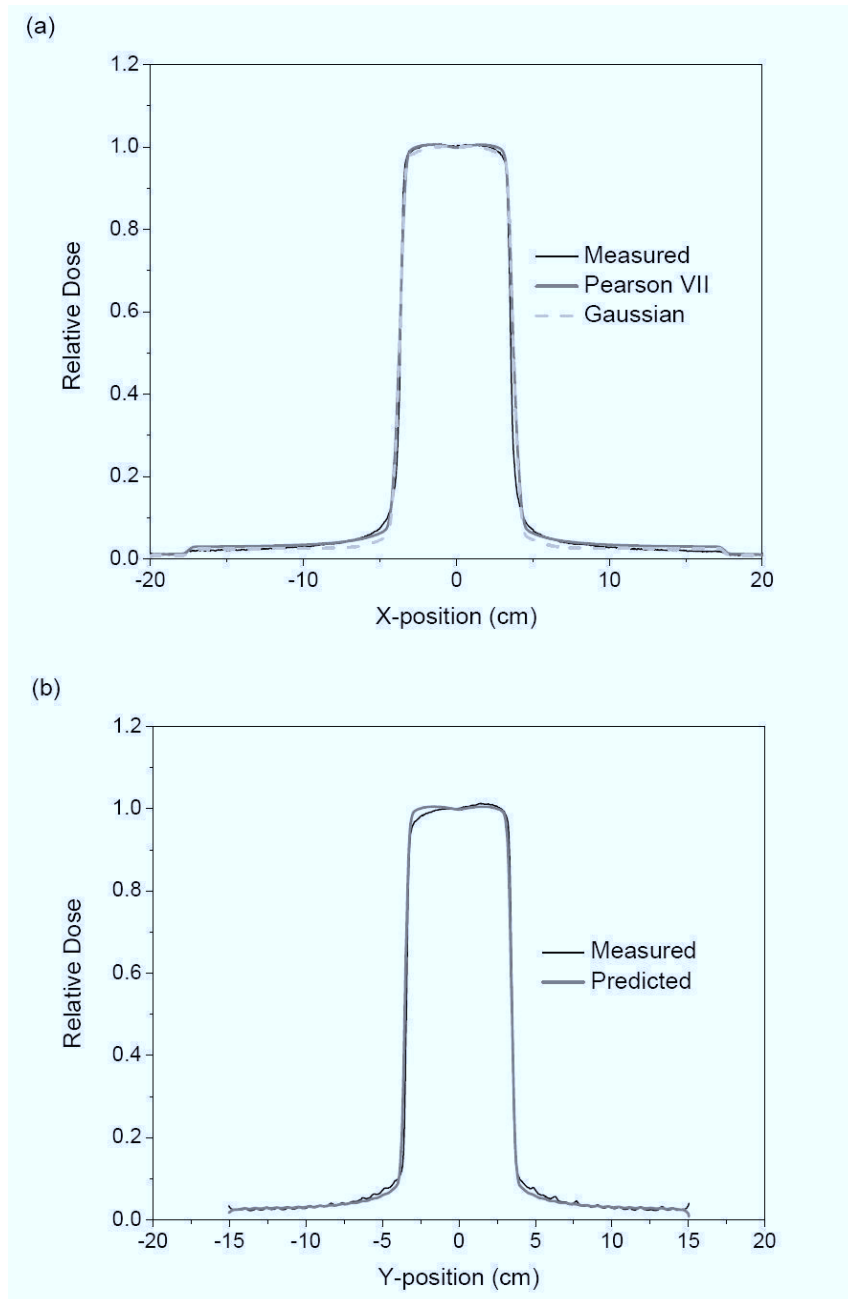


Figure 4.7 [Measured and Predicted Profiles of Open 5x5 Field]: (a) X-profiles of a 5x5 cm² field demonstrating agreement between the model and the measured data. ‘Pearson’ denotes the model with the Pearson VII extrafocal source, while ‘Gaussian’ is the model with the Gaussian extrafocal source. Note that the ‘Gaussian’ model underestimates the measured profile outside the field. The blocking of the jaws at 17.5 cm and -17.5 cm is evident. (b) Y-profiles of a 5x5 cm² field for both the measured and predicted model (i.e. with Pearson VII extrafocal source). Asymmetry in measured Y-profiles is likely due to differences between the estimated flood-field correction and the flood-field actually used, with asymmetry being introduced by the EPID mount arm.



The remaining disagreement within the open-field images was mainly caused by an observed asymmetry in the gantry-couch direction of the EPID images (see Figures 4.6 (b) and 4.7 (b)). This effect has been noted in other work [3] and is likely related to asymmetric backscatter from robotic arm components and has not been accounted for in the current proposed model. The amount of asymmetry (defined as the maximum ratio between points symmetric within the central 80% of profile) for the 20x20 cm² and 5x5 cm² fields is estimated as 1.003 and 1.010, respectively. Additionally, the model slightly underpredicts the measured images at the field edges in the gantry-couch direction, irrespective of the asymmetry in that same direction. This effect is evident at greater SDDs where the edges of the larger fields approach the edges of the detector. The observed underprediction, illustrated in Figure 4.6 (b), is possibly the result of reintroducing the beam profile into the measured image. The correction for the profile was obtained in the cross-plane (or X) direction of the EPID and a radially symmetric profile correction was assumed that does not account for edge effects of the 40x30 cm² flood-field. A method to correct for asymmetric scatter due to the EPID's robotic mount arm, as well as the flood-field edge effects, needs to be developed to further increase the accuracy of the fluence model presented here. Furthermore, the detector is nearly encompassed by the 20x20cm² field in the gantry-couch direction and could cause discrepancies in the measured data due to a lack of lateral scattering material in this direction.

4.3.3 Validation of IMRT fields

The IMRT fields agreed within an absolute dose difference of 2% and a DTA of 3 mm in-field for a minimum of 90% of the pixels (see Tables 4.1 and 4.2 and Figures 4.8 and 4.9). Only 3 out of 70 prostate fields scored below this (at 87.6%, 87.3% and 89.5%) and no oropharyngeal fields scored below 90%. The majority of the fields (112 out of 140 fields) agreed within 2%, 3 mm for at least 95% of the pixels. In general, the prostate field agreement was similar to that of the oropharyngeal fields as each site possessed 14 fields with less than 95% of the pixels in agreement with the 2%, 3 mm criteria. Over all IMRT fields, a mean of 96.6% of pixels were in agreement with the 2%, 3 mm criteria. Overall agreement was within clinical acceptability for in-house IMRT quality assurance.

Table 4.1 [χ -comparison Results of Prostate Open Fields]: Number of pixels with χ -comparison values less than 1.0 for each field within each clinical prostate plan for a dose difference of 2% and 3 mm DTA criteria. The last row shows the average accepted pixel percentages over all fields.

Field	Plan 1	Plan 2	Plan 3	Plan 4	Plan 5	Plan 6	Plan 7	Plan 8	Plan 9	Plan 10
1	98.3%	97.6%	98.1%	99.5%	98.5%	97.6%	98.8%	99.0%	99.3%	97.5%
2	98.3%	98.9%	99.6%	92.8%	97.6%	99.3%	97.7%	98.5%	98.3%	90.1%
3	98.8%	99.1%	94.3%	95.6%	87.3%	98.7%	98.7%	97.5%	96.5%	98.1%
4	87.6%	99.4%	94.8%	93.8%	92.2%	98.7%	97.6%	97.2%	92.2%	97.6%
5	97.5%	98.7%	93.2%	92.9%	93.0%	98.7%	95.9%	97.5%	89.5%	96.4%
6	98.6%	96.0%	98.9%	97.5%	97.9%	99.1%	98.6%	99.3%	96.6%	98.3%
7	99.3%	92.0%	95.2%	98.7%	98.2%	96.0%	98.8%	96.7%	97.2%	99.1%
Average	96.9%	97.4%	96.3%	95.8%	95.0%	98.3%	98.0%	97.9%	95.7%	96.7%

Table 4.2 [χ -comparison Results of Head and Neck Open Fields]: Number of pixels with χ -comparison values less than 1.0 for each field within each clinical oropharyngeal plan for a dose difference of 2% and 3 mm DTA.

Field	Plan 1	Plan 2	Plan 3	Plan 4	Plan 5	Plan 6	Plan 7	Plan 8	Plan 9	Plan 10
1	97.8%	93.3%	96.6%	98.0%	96.3%	93.8%	98.1%	94.5%	97.7%	97.1%
2	98.9%	97.4%	95.9%	97.5%	97.1%	95.7%	97.0%	96.0%	98.3%	96.3%
3	97.2%	96.4%	99.0%	97.8%	96.1%	98.4%	96.3%	94.1%	98.8%	97.8%
4	98.6%	92.5%	97.8%	96.8%	95.7%	97.3%	96.8%	96.4%	97.3%	98.2%
5	98.4%	97.3%	95.1%	96.0%	94.4%	96.5%	95.8%	94.4%	97.6%	95.7%
6	99.2%	95.8%	96.4%	92.6%	94.3%	97.9%	90.0%	93.9%	93.5%	93.5%
7	98.3%	96.6%	97.6%	96.9%	96.0%	94.2%	95.3%	98.0%	97.9%	95.3%
Average	98.4%	95.6%	96.9%	96.5%	95.7%	96.3%	95.6%	95.3%	97.3%	96.3%

Figure 4.8 [Profiles of Prostate Field]: X-profiles of a prostate IMRT field (Plan 2, Field 4) comparing measured to predicted images. The top-left inset is the predicted image (the white line indicates the position of the profile), with the corresponding χ -comparison below. The greyscale legend refers to values of the χ -comparison image.

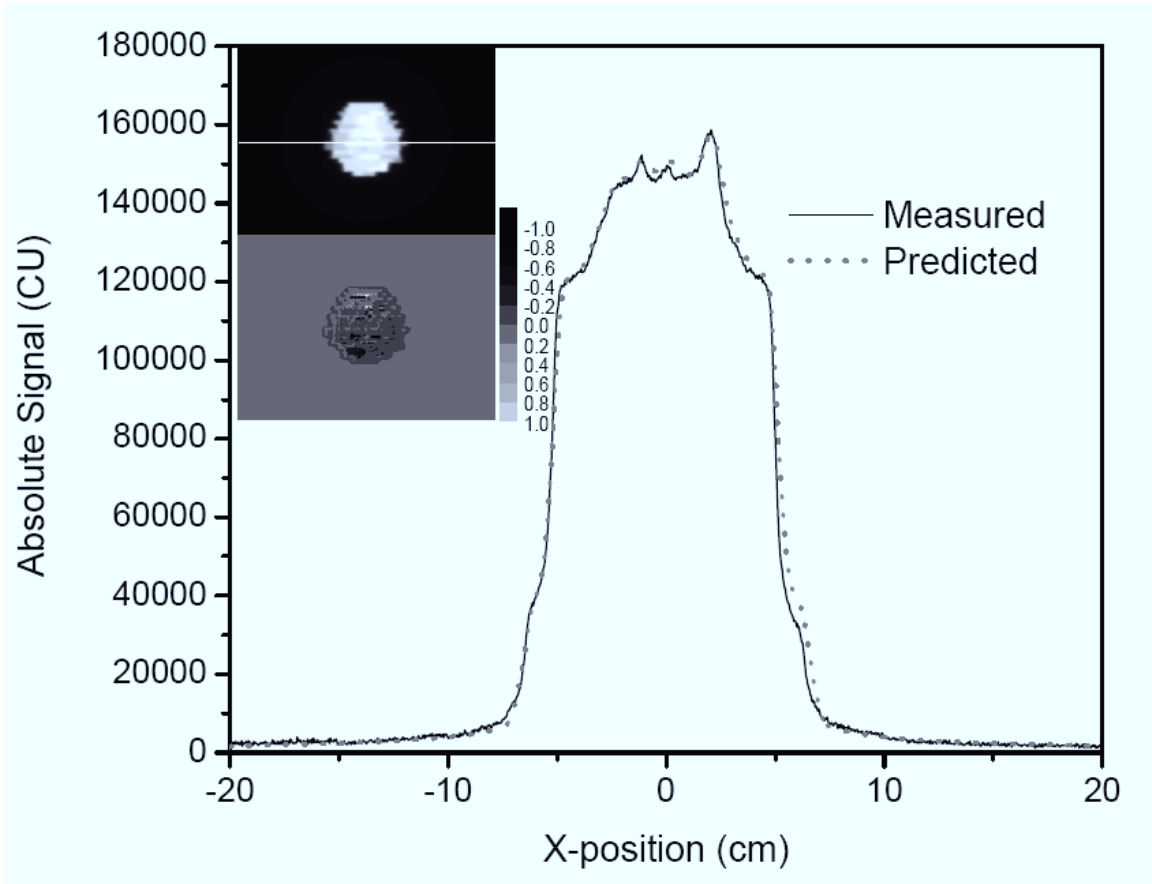
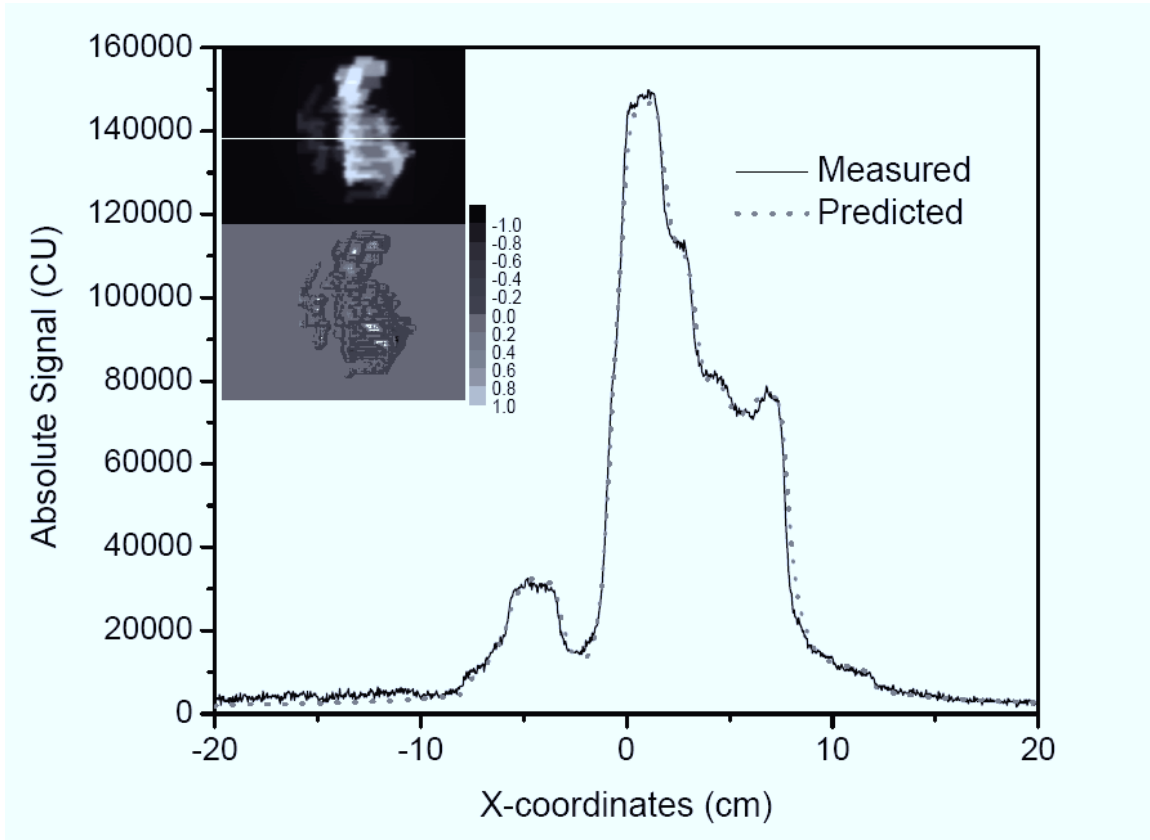


Figure 4.9 [Profiles of Head and Neck Field]: X-profiles of an oropharyngeal IMRT field (Plan 1, Field 6) comparing measured to predicted images. The top-left inset is the predicted image (the white line indicates the position of the profile), with the corresponding χ -comparison below. The greyscale legend refers to values of the χ -comparison image.



Additionally, one oropharyngeal IMRT field (Plan 5, field 5) calculated with the Gaussian model (with combined focal and extrafocal spectrum) was tested against the Pearson VII model (with the separated focal and extrafocal spectra). The Gaussian model agreed within 2%, 3 mm for 87.7% of pixels as opposed to the Pearson model's 94.4% for the same acceptance criteria (see Table 4.2). The Gaussian model prediction underpredicted the measured portal image more than the Pearson VII.

4.4. CONCLUSIONS

A comprehensive fluence model used to predict portal dose images for both static and IMRT fields has been designed and validated. The approach incorporates a detailed two-source model for fluence prediction and accounts for the EPID energy response when converting fluence entering the EPID to dose deposited in the EPID. This model demonstrates the accuracy ($< 2\%$, 3 mm) typical of IMRT pre-treatment verification with portal dose image prediction in complex clinical examples. The fluence model was based on that of a commercial TPS, but incorporated several improvements due to the analysis of Monte Carlo simulations of the linear accelerator. The fluence model improvements described here in the context of an EPID application could potentially be incorporated into patient specific dose calculation algorithms. Future work aims at implementing this model with a previously developed algorithm [2, 17] which predicts patient scatter energy fluence in the EPID.

REFERENCES

1. Kirby, M. C. and Glendinning, A. G., *Developments in electronic portal imaging systems*. Br J Radiol, 2006. **79 Spec No 1**: p. S50-65.
2. McCurdy, B. M. C., Luchka, K., and Pistorius, S., *Dosimetric investigation and portal dose image prediction using an amorphous silicon electronic portal imaging device*. Med Phys, 2001. **28**(6): p. 911-24.
3. Siebers, J. V., Kim, J. O., Ko, L., Keall, P. J., and Mohan, R., *Monte Carlo computation of dosimetric amorphous silicon electronic portal images*. Medical Physics, 2004. **31**(7): p. 2135-46.
4. Li, W., Siebers, J. V., and Moore, J. A., *Using fluence separation to account for energy spectra dependence in computing dosimetric a-Si EPID images for IMRT fields*. Medical Physics, 2006. **33**(12): p. 4468-80.
5. Warkentin, B., Steciw, S., Rathee, S., and Fallone, B. G., *Dosimetric IMRT verification with a flat-panel EPID*. Med Phys, 2003. **30**(12): p. 3143-55.
6. Van Esch, A., Depuydt, T., and Huyskens, D. P., *The use of an aSi-based EPID for routine absolute dosimetric pre-treatment verification of dynamic IMRT fields*. Radiotherapy and Oncology, 2004. **71**(2): p. 223-34.

7. Greer, P. B. and Popescu, C. C., *Dosimetric properties of an amorphous silicon electronic portal imaging device for verification of dynamic intensity modulated radiation therapy*. Medical Physics, 2003. **30**(7): p. 1618-27.
8. Greer, P. B., Vial, P., Oliver, L., and Baldock, C., *Experimental investigation of the response of an amorphous silicon EPID to intensity modulated radiotherapy beams*. Med Phys, 2007. **34**: p. 4389-4398.
9. Vial, P., Greer, P. B., Hunt, P., Oliver, L., and Baldock, C., *The impact of MLC transmitted radiation on EPID dosimetry for dynamic MLC beams*. Med Phys, 2008. **35**: p. 1267-1277.
10. Ansbacher, W., *Three-dimensional portal image-based dose reconstruction in a virtual phantom for rapid evaluation of IMRT plans*. Med Phys, 2006. **33**(9): p. 3369-82.
11. Wendling, M., Louwe, R. J. W., McDermott, L. N., Sonke, J.-J., van Herk, M., and Mijnheer, B. J., *Accurate two-dimensional IMRT verification using a back-projection EPID dosimetry method*. Medical Physics, 2006. **33**(2): p. 259-73.
12. van Elmpt, W. J. C., Nijsten, S. M. J. J. G., Schiffeleers, R. F. H., Dekker, A. L. A. J., Mijnheer, B. J., Lambin, P., and Mincken, A. W. H., *A Monte Carlo based three-dimensional dose reconstruction method derived from portal dose images*. Medical Physics, 2006. **33**(7): p. 2426-34.
13. Partridge, M., Ebert, M., and Hesse, B. M., *IMRT verification by three-dimensional dose reconstruction from portal beam measurements*. Medical Physics, 2002. **29**(8): p. 1847.
14. McNutt, T. R., Mackie, T. R., Reckwerdt, P., and Paliwal, B. R., *Modeling dose distributions from portal dose images using the convolution/superposition method*. Med Phys, 1996. **23**(8): p. 1381-92.
15. Greer, P. B., *Correction of pixel sensitivity variation and off-axis response for amorphous silicon EPID dosimetry*. Medical Physics, 2005. **32**(12): p. 3558-68.
16. Munro, P. and Bouius, D. C., *X-ray quantum limited portal imaging using amorphous silicon flat-panel arrays*. Med Phys, 1998. **25**(5): p. 689-702.
17. McCurdy, B. M. and Pistorius, S., *A two-step algorithm for predicting portal dose images in arbitrary detectors*. Med Phys, 2000. **27**(9): p. 2109-16.
18. Philips Medical Systems, *Pinnacle³ Physics Reference Guide, Release 7.6*, 2005.
19. Rogers, D. W. O., Faddegon, B. A., Ding, G. X., Ma, C. M., We, J., and Mackie, T. R., *BEAM: a Monte Carlo code to simulate radiotherapy treatment units*. Med Phys, 1995. **22**(5): p. 503-24.
20. Heath, E. and Seuntjens, J., *Development and validation of a BEAMnrc component module for accurate Monte Carlo modelling of the Varian dynamic Millennium multileaf collimator*. Phys Med Biol, 2003. **48**(24): p. 4045-63.
21. Kawarackow, I., Mainegra-Hing, E., Rogers, D. W. O., Tessier, F., and Walters, B. R. B., *The EGSnrc code system: Monte Carlo simulation of electron and photon transport*. 2010, Ionizing Radiation Standards, National Research Council of Canada.
22. Ionizing Radiation Standards, *BEAMDP as a general purpose utility*, National Research Council of Canada: 1995.

23. Sharpe, M. B., Jaffray, D. A., Battista, J. J., and Munro, P., *Extrafocal radiation: a unified approach to the prediction of beam penumbra and output factors for megavoltage x-ray beams*. Med Phys, 1995. **22**(12): p. 2065-74.
24. Liu, H. H., Mackie, T. R., and McCullough, E. C., *A dual source photon beam model used in convolution/superposition dose calculations for clinical megavoltage x-ray beams*. Med Phys, 1997(22): p. 1960-1974.
25. Van Dyk, J., *The Modern Technology of Radiation Oncology*. Vol. 2. 2005, Madison: Medical Physics,
26. Chytyk, K. and McCurdy, B. M. C., *Investigation of tilted dose kernels for portal dose prediction in a-Si electronic portal imagers*. Medical Physics, 2006. **33**(9): p. 3333.
27. Bakai, A., Alber, M., and Nusslin, F., *A revision of the gamma-evaluation concept for the comparison of dose distributions*. Phys Med Biol, 2003. **48**(21): p. 3543-53.
28. Low, D. A., Harms, W. B., Mutic, S., and Purdy, J. A., *A technique for the quantitative evaluation of dose distributions*. Med Phys, 1998. **25**: p. 656-61.
29. Kim, J. O., Siebers, J. V., Keall, P. J., Arnfield, M. R., and Mohan, R., *A Monte Carlo study of radiation transport through multileaf collimators*. Med Phys, 2001. **28**: p. 2497-2506.
30. Arnfield, M. R., Siebers, J. V., Kim, J. O., Wu, Q., Keall, P. J., and Mohan, R., *A method for determining multileaf collimator transmission and scatter for dynamic intensity modulated radiotherapy*. Med Phys, 2000. **27**: p. 2231-2241.
31. Jursinic, P. A., *Clinical implementation of a two-component x-ray source model for calculation of head-scatter factors*. Med Phys, 1997. **24**(12): p. 2001-7.
32. Yang, Y., Xing, L., Boyer, A. L., Song, Y., and Hu, Y., *A three-source model for the calculation of head scatter factors*. Med Phys, 2002. **29**: p. 2024-2033.
33. Ahnesjo, A., *Analytic modeling of photon scatter from flattening filters in photon therapy beams*. Med Phys, 1994. **21**(8): p. 1227-35.
34. Fippel, M., Haryanto, F., Dohm, O., Nusslin, F., and Kriesen, S., *A virtual photon energy fluence model for Monte Carlo dose calculation*. Med Phys, 2003. **30**(3): p. 301-11.
35. Zhu, T. C. and Bjarngard, B. E., *The fraction of photons undergoing head scatter in x-ray beams*. Phys Med Biol, 1995. **40**(6): p. 1127-34.
36. Zhu, T. C., Bjarngard, B. E., Xiao, Y., and Yang, C. J., *Modeling the output ratio in air for megavoltage photon beams*. Med Phys, 2001. **28**(6): p. 925-37.
37. Dunscombe, P. B. and Nieminen, J. M., *On the field-size dependence of relative output from a linear accelerator*. Med Phys, 1992. **19**(6): p. 1441-4.
38. Ahnesjo, A., *Collimator scatter in photon therapy beams*. Med Phys, 1995. **22**(3): p. 267-78.

CHAPTER FIVE: MODEL-BASED PREDICTION OF PORTAL DOSE IMAGES DURING PATIENT TREATMENT

The previous chapter outlined the creation of a comprehensive, physics-based fluence model that was accurate for the portal dose image prediction of open, square and IMRT fields (i.e. without scattering material in the beam path). The next step in the portal image prediction process is to implement a method to account for the effect of a patient or phantom in the beam, which is discussed in Chapter Five.*

5.1 INTRODUCTION

The advent of computed tomography (CT) primarily contributed to the development of customized treatments for radiation therapy patients planned in three-dimensions. From three-dimensional conformal radiation therapy achieved with large beam modifying devices, to innovations such as multileaf collimator-delivered intensity modulated radiation therapy (IMRT), treatments are continuously increasing in complexity. Through the use of computer optimization and the creation of steep dose gradients, IMRT treatments are able to deliver tumoricidal doses with distributions that accurately conform to the tumour, while sparing normal tissues.

However, there have been a number of serious radiotherapy accidents over the last decade that could have been prevented with patient treatment verification [1]. In one

* Manuscript in preparation. Aspects of this work were presented as a poster in “K. Chytk, E. Van Uytven, T. Van Beek, P. B. Greer and B. M. C. McCurdy, ‘Physical model for *in vivo* dose image prediction’, Canadian Organization of Medical Physicists Annual Scientific Meeting, 2011, Vancouver, BC.

incident, three fractions of a patient's IMRT treatment for a tongue tumour were delivered with the MLC parked (i.e. retracted outside the beam path), and therefore providing no beam modulation. The error occurred because of a computer crash during planning which resulted in the MLC positions not being saved. The patient died because of the error [1]. Unfortunately, the fluence maps of IMRT are non-intuitive because they rely on treatment planning optimization algorithms to determine the best possible fluence patterns for a patient's treatment. The combination of high doses, steep gradients and the complex methods by which IMRT treatments are calculated and delivered indicate a requirement for thorough dosimetric verification of treatment delivery. In general, IMRT quality assurance (QA) programs contain elements of machine-specific QA tests and patient-specific tests. Typically, a patient's clinical IMRT plan is verified prior to the start of a patient's treatment, described as pre-treatment verification. This usually involves a point dose measurement obtained in a phantom, often in conjunction with a few two-dimensional film images. However, to obtain the most valuable assessment of a patient's treatment, dosimetric validation would ideally also occur during treatment delivery to the patient, for every beam and every fraction delivered for the course of radiotherapy. This process is rarely carried out clinically, with centers relying solely on pre-treatment verification. Even with pre-treatment verification, plans could be inadvertently changed between pretreatment verification and the first delivered patient fraction.

In the clinic, amorphous silicon electronic portal imaging devices (a-Si EPIDs) are primarily used for patient set-up verification. Throughout the last few years, a-Si EPIDs

have gained acceptance as tools for dosimetry [2-5], particularly for IMRT [6-28]. Non-transmission images are taken without a patient or phantom in the beam [6-8, 11-13, 20, 22, 23, 25-27], while transmission imaging may take place during a patient treatment (typically termed *in vivo*) [5, 15-21] or outside of treatment time with a phantom [2, 14, 24]. A measured image obtained by either method could then be compared to the prediction at the plane of the EPID or backprojected to compare to the TPS dose distribution. A comprehensive literature review of EPID dosimetry investigations was presented by van Elmpt *et al.* [29].

Transmission dosimetry with portal imaging currently focuses on using the inverse approach, by comparing the predicted dose distribution to that of the TPS [14-24, 30]. McDermott *et al.* [15] showed that it was possible to replace pretreatment verification with *in vivo* verification, and achieved dose distributions in the patient's CT dataset within a 3% dose difference and a 3 mm distance-to-agreement (DTA). However, much of the work with this approach requires a correction-based approach to account for various parameters in the portal dose calculation (e.g. dose response of the EPID and patient scatter incident on the EPID) [14-24].

Past forward transmission approaches have relied on measured ionization chamber data to determine the fluence incident on the phantom [2] or scatter fluence incident on the EPID due to the patient or phantom [5, 31, 32]. Van Zijtveld *et al.* [33] used measured EPID images with and without the patient to determine primary fluence and a series of EPID images to fit scatter fluence kernels. Other methods have included an extraction of

the primary energy fluence from measured EPID images to use in the prediction model [30, 34, 35] and incorporating the EPID into the TPS calculation [36]. Although the dose in the patient is not directly calculated with forward methods, these techniques could potentially be used to calculate dose in the patient by comparing the predicted image to the measured image and iteratively adjusting it [37, 38]. Another prospective use for forward transmission techniques is in real-time dosimetry, where a series of measured images are collected in *cine* (or ‘movie’) mode to be compared to corresponding predicted images – potentially detecting dosimetric errors in real-time or near real-time [39].

The current work presents a semi-analytical model to accurately predict portal dose images with the patient in the beam, in absolute dose units. The EPID-optimized comprehensive fluence model originally described by Chytyk and McCurdy [8] has been modified and expanded here for improved accuracy, including manufacturer-specific details of the MLC leaves and explicit calculation of Monte-Carlo calculated fluence attenuation through the MLC. This fluence model is interfaced to an algorithm for predicting portal dose images with attenuating material in the beam, accounting for primary transmission, patient or phantom scatter, EPID optical glare, EPID support-arm backscatter and EPID energy response [2, 40-42]. This portion of the portal dose image prediction model is based on previous work, but has been significantly updated here. To date, a detailed incident fluence model has not been used for portal dose image prediction with a-Si EPIDs– the previous work of McCurdy *et al.* [2] required measured incident fluences for every field. Also, the entire algorithm generally exploits the understanding of

the underlying physics and is not simply a series of empirical corrections. We feel this approach is attractive for robustness and the ability to maintain accuracy over a wide variety of clinical situations. The advantages are similar to those offered by model-based treatment planning systems (TPSs) over correction-based methods [43]. In the current work, the model-based portal dose image prediction algorithm is validated on a variety of homogenous slab phantoms, using square fields and several clinical IMRT fields.

5.2 METHODS AND MATERIALS

5.2.1 Improved fluence model

A detailed fluence model used to determine the fluence incident on an EPID and specifically optimized for portal dose image prediction was previously presented by Chytyk and McCurdy [8] and described in Chapter 4. The model is significantly modified and improved in this work. The fluence model was based on the two-source fluence model in the Pinnacle treatment planning system (Philips Radiation Oncology Systems, Andover, MD), and will be briefly reviewed here. The original fluence model included a focal Gaussian source and an extrafocal Gaussian-like source, which was concluded to more accurately match Monte Carlo simulations of the extrafocal fluence [8]. The individual spectrum for each source was determined via Monte Carlo simulation of the specific linear accelerator (Clinac 2100iX, Varian Medical Systems, Palo Alto, CA). An initial fluence profile was used to match the in-field beam shape, and a radially-dependent factor was used to determine the amount of off-axis beam softening occurring due to the flattening filter for the focal source alone. Transmission factors were employed to model the transmission of the beam through the jaws and MLC. Transmission through

the rounded leaf-tips of the MLC was calculated by approximating the leaf-tips as a circle of user-defined radius and raytracing through the tip. Raylengths that were less than the full leaf thickness were assigned a transmission directly proportional to the full MLC transmission, relative to the raylength through the MLC.

This early model calculates the fluence of the treatment beam incident on the EPID, as a function of energy. Energy fluence incident on the EPID is binned into discrete energy bins and then converted to a predicted dose image by a superposition with a series of monoenergetic dose kernels determined from Monte Carlo simulation. The values of the parameters of the fluence model were determined by manually adjusting them to match predicted images to measured images for a series of simple, MLC-defined fields (1x1, 2x2, 5x5, 10x10, 20x20, 20x5, 5x20 cm²). Once an accurate model was obtained for the square and rectangular fields, the fluence model was used to predict IMRT open-field images to within a 2% dose difference and a 3 mm distance-to-agreement (DTA) [8].

The current work employs an improved fluence model algorithm, created in-house with MATLAB® (Mathworks Inc., Natwick, MA); the modified features are described here. Several parameters, which were previously adjustable, have been fixed using the vendors' engineering schematics as well as Monte Carlo simulation results (see Table 5.1 for a compilation of the portal dose image prediction model improvements). The MLC is now more accurately modeled with the exact dimensions of the tongue-and-groove width and the exact MLC leaf-tip profile. Also, Monte Carlo simulation was used to generate pre-MLC fluence profiles to calculate the MLC attenuation and beam-hardened energy

fluence exiting the MLC analytically at the isocentric plane (Φ_{iso}), as shown in Equation 5.1:

$$(5.1) \Phi_{iso} \left(x \cdot \frac{z_{iso}}{z_{pre-MLC}}, y \cdot \frac{z_{iso}}{z_{pre-MLC}}, E_i \right) = \Phi_{pre-MLC} (x, y, E_i) \cdot e^{-\left(\frac{\mu}{\rho}\right)_{W,E_i} \cdot (\rho_{MLC} \cdot \ell_{MLC}(x,y))} \cdot \frac{z_{pre-MLC}^2}{z_{iso}^2}.$$

The pre-MLC fluence ($\Phi_{pre-MLC}$) for each photon energy bin (E_i) was extracted from a phase-space file generated using BEAMnrc [44-46] simulations of the linear accelerator head; the energy fluence was extracted using phase-space analysis software developed in-house. The energy fluence was then attenuated using the energy-dependent mass-attenuation coefficient specific to tungsten ($(\mu/\rho)_{W,E_i}$) since the MLC are manufactured from a tungsten alloy. From comparison to measured EPID profiles, the density of the alloy (ρ_{MLC}) was determined to be 18.0 g/cm³. By raytracing through the MLC using the manufacturer plans, the thickness of MLC leaf each rayline passes through is calculated to obtain ℓ_{MLC} . This is an improvement over the original fluence model in which the effects of both attenuation and beam-hardening were accounted for with the application of a single transmission factor. The energy fluence for both the focal and extrafocal sources exiting the treatment head are now determined with this analytical calculation, with the algorithm sampling the energy fluence in any two-dimensional plane perpendicular to the beam axis below the MLC. The modification in the energy fluence determination removes the need for an arbitrary fluence profile and an off-axis-softening factor that both needed to be manually adjusted in the original fluence model.

The full-width half maximums (FWHMs) of the two sources, the extrafocal source height (the maximum amount of extrafocal fluence possible, i.e. for a 40x40 cm² field), the extrafocal tail parameter (to lift or lower tails of the source) and the MLC physical density are determined via computerized nonlinear least squares optimization based on the interior point method called ‘fmincon’ (a function in the Optimization Toolbox of MATLAB and described in the Appendix, Section 8.4). The objective function is based on the sum of the squared differences between the central axis values of the predicted and measured images for a series of open square fields (2x2, 5x5, 10x10, 20x20 cm²). Each parameter is assigned an upper and lower bound based on literature values, to ensure physical relevance (e.g. extrafocal height range is constrained between 8% and 12%). We can predict fluence of the treatment beam at any arbitrary plane using our fluence model, which can then be positioned at the entrance to a patient, phantom, or the EPID. All parameters and their values are included in the Appendix, Section 8.4.

Table 5.1 [Fluence Model Updates]: Summary of changes between the original and current portal dose image prediction models.

Modeled Feature	Original method (Chapter 4)	Current work (Chapter 5)
MLC transmission	Single transmission factor	Attenuated pre-MLC spectrum through tungsten leaves
MLC leaf-tip	Circle of variable radius matched to penumbra of measured data	Used MLC schematics to obtain exact shape and dimensions
Tongue-and-groove width	Variable width based on measured data	Tongue-and-groove design for each type of leaf acquired through schematics
Field shape and horns	Arbitrary incident fluence profile and factor to soften spectrum off-axis	Energy fluence profiles from BEAMnrc
Backscatter from EPID arm	Backscattering material downstream of EPID model added during simulation of dose kernels	Backscatter prediction technique from Rowshanfarzad <i>et al.</i> [53]
Optical photon glare	Accounted for implicitly in dose kernels (ie. through added backscatter layers in Monte Carlo simulation [25,26])	Modeled using exponential function from Kirkby <i>et al.</i> [54]
EPID-specific dose kernels	Monoenergetic photons incident on EPID model for mid-point of each energy bin	Uniform distribution of photons incident on EPID model for each energy bin

Since the IMRT beams are modulated by the MLC, the MLC leaf-positions and control point weights for each field segment are required to determine the incident fluence of an IMRT treatment. This is accomplished through the use of ‘The Computational Environment for Radiotherapy Research’ (CERR) software [47], written in the MATLAB programming language. This software package provided utilities to import DICOM and RTOG files exported by the TPS (defining the CT dataset, contours, dose distributions and machine parameters required to deliver the desired fluence). Both Eclipse and Pinnacle plans have been processed in CERR by our group.

5.2.2 Fluence modification due to the patient

5.2.2.i Scatter fluence kernels

To account for patient scatter, the model uses a superposition of patient scatter fluence kernels. Each kernel is generated using Monte Carlo techniques and describes the spatial and energy distribution of scatter fluence at the EPID due to a pencil beam of fluence incident on a homogeneous solid water phantom, with center of mass positioned at isocentre. The kernels are specific to a phantom thickness and air gap as determined along the raylines through the patient from the focal source to the EPID. A patient scatter prediction model developed previously at our centre used a pencil beam of 6 MV photons (generated with a polyenergetic spectrum from Mohan *et al.* [48]) that was incident on various uniform thicknesses of water at the central axis [2, 40-42]. For each water thickness, the radially-symmetric scattered energy fluence was recorded for a range of air gaps using a customized version of the DOSRZ user code from EGS4 [49] and saved as a library for easy implementation.

The patient scatter fluence kernels were recalculated in the current work, utilizing BEAMnrc 2009 [44] and more accurate energy spectrum data. The 6 MV energy spectrum used for the patient scatter kernels is now generated using a validated BEAMnrc simulation of the local linac. BEAMnrc is also used to simulate the effect of the uniform water slabs on the incident pencil beam of photons (radius of 0.0005 cm), with the scattered photon energy fluence extracted from a phase-space file located at the slab exit surface, using an in-house MATLAB algorithm. A library of the radially-symmetric patient scatter fluence kernels for a range of water slab thicknesses (0-10 cm,

incremented by 1 cm; 10-20, incremented by 2 cm; >20 and up to 50 cm, incremented by 5 cm) and a range of air gaps (0-100 cm, incremented by 5 cm) was created for application during the superposition process. The slabs' length and width were each 30 cm, and were placed at isocentre for the simulations. These were created by forward projecting every photon particle in the exit-surface phase-space file over the appropriate air gap distance. This approach allowed use of the BEAMnrc code (which is limited to a maximum of three phase-space planes), but ignored the contribution of photon scatter generated in the air volume between the patient and the EPID since it was negligible.

5.2.2.ii Equivalent homogeneous phantom (EHP) conversion

To employ the patient scatter fluence kernels, the algorithm first needs to convert the phantom or patient to an equivalent homogeneous phantom, or EHP [31], based on the radiological thickness of the object, which is determined by raytracing through it. For complex objects, a three-dimensional CT dataset is required. The standard conversion from CT number to electron density is executed using a calibration performed with an electron density phantom (Gammex 467, Gammex Inc., Madison, WI). A raytracer [50] is used to calculate a radiological pathlength through the patient density array between the source and a point of interest on the EPID. This is done for every calculation point on the EPID plane at a resolution of $0.2 \times 0.2 \text{ cm}^2$, and provides the 'homogenous phantom thickness' in two dimensions, represented mathematically by $EHP(x, y)$. The air gap, denoted by $g(x, y)$ is also calculated over the EPID plane by re-positioning each rayline to preserve the location of its center-of-mass (i.e. for each rayline, the centre-of-mass of the homogenous phantom thickness is the same location as the centre-of-mass from the

original CT-based density map). Both $EHP(x, y)$ and $g(x, y)$ are used to determine the choice of scatter energy fluence kernel to apply to the EPID at location (x, y) .

5.2.3 Predicted fluence incident on EPID

In this work, the incident energy fluence is initially calculated over a regular grid on a plane perpendicular to the beam central axis and intersecting the isocentre, with $0.05 \times 0.05 \text{ cm}^2$ resolution. If there is a patient or phantom in the beam, the incident energy fluence is then scaled to a plane above the EHP, as shown below:

$$(5.2) \Phi_{EHP} \left(x \cdot \frac{z_{EHP}}{z_{iso}}, y \cdot \frac{z_{EHP}}{z_{iso}}, E_i \right) = \Phi_{iso} (x, y, E_i) \cdot \frac{z_{iso}^2}{z_{EHP}^2},$$

where Φ_{iso} is the 2-D energy fluence below the MLC and scaled to isocentre (z_{iso}), and Φ_{EHP} is the 2-D energy fluence scaled to the plane above the EHP (the incident fluence on the EHP) at distance from source z_{EHP} . The term z_{iso}/z_{EHP} accounts for geometric scaling between the different distances, while z_{iso}^2/z_{EHP}^2 corrects for the inverse square effect. The patient density array or EHP, as determined from the CT dataset, is assumed to have the atomic composition of water, but the method could be modified to account for atomically heterogeneous tissues such as bone, muscle and fat. The primary fluence (i.e. photons from the focal and extrafocal sources, $\Phi_{P,EPID}$) at the plane of the EPID (z_{EPID}) is then determined by attenuating the incident energy fluence (Φ_{EHP}) calculated by the fluence model using the radiological pathlength information contained in the EHP:

$$(5.3) \Phi_{P,EPID} \left(x \cdot \frac{z_{EPID}}{z_{EHP}}, y \cdot \frac{z_{EPID}}{z_{EHP}}, E_i \right) = \Phi_{EHP} (x, y, E_i) \cdot e^{-\left(\frac{\mu}{\rho}\right)_{water, E_i} \cdot (\rho_{water} \cdot EHP(x, y))} \cdot \frac{z_{EHP}^2}{z_{EPID}^2},$$

where $(\mu/\rho)_{water,E_i}$ is the energy-dependent attenuation coefficient for water, $EHP(x, y)$ is the pathlength for each particular (x, y) position and the other terms are as previously described in Equation 5.2.

The patient scatter fluence delivered to the EPID is calculated through the sum of convolutions of incident fluence on the phantom with the scatter energy fluence kernels described in Section 5.2.2.i. The radiological pathlength and air gap from the EHP are used to choose the appropriate scatter fluence kernel from the pre-calculated library for each sampled rayline to apply to the EPID. The kernel needs to be scaled by the incident fluence associated with the rayline to yield the scatter that is associated with that single rayline at the EPID. Discretely summing this product over all raylines yields the distribution of patient-generated scatter fluence entering the EPID:

$$(5.4) \Phi_{S,EPID} \left(x \cdot \frac{z_{EPID}}{z_{EHP}}, y \cdot \frac{z_{EPID}}{z_{EHP}}, E_i \right) = \sum \left(\Phi_{EHP}(x, y, E_i) \cdot K_s(EHP(x, y), g(x, y), E_i) \right) \Delta x \Delta y$$

where $\Phi_{S,EPID}$ is the scattered energy fluence incident on the EPID and $K_s(EHP(x, y), g(x, y), E_i)$ is a scatter energy fluence kernel dependent on the pathlength ($EHP(x, y)$) and air gap ($g(x, y)$) along the rayline at point (x, y) through the EHP to the EPID plane. Values Δx and Δy account for the discretized step size of the integration, representing the user-defined resolution of this calculation (0.5 cm for this work). The resolution of the scatter fluence calculation is lower than that of the primary fluence calculation resolution since the patient scatter is a broad, slowly varying function. This reduces the time it takes to perform this computationally intensive step.

Energy spectra information is retained by performing the primary fluence and scatter fluence calculations for each of the energy bins, E_i , that the polyenergetic spectrum is divided into. For this work, the upper energy bounds of the bins were 0.10, 0.20, 0.30, 0.40, 0.50, 0.60, 0.80, 1.00, 1.25, 1.50, 2.00, 3.00, 4.00, 5.00 and 6.00 MeV. This allows a detailed accounting of fluence as a function of energy spectra, and is required to accurately account for the energy response of the EPID as detailed below. The predicted fluence from the algorithm was compared to the Monte Carlo-calculated fluence for a 10x10 cm² field, with two phantoms in the beam (10 and 25 cm thick), as well as without a phantom. Results were obtained at a distance of 140 cm from the source.

5.2.4 Converting incident fluence on the EPID to dose delivered to the EPID

5.2.4.i Generating dose kernels

The energy fluence incident on the EPID (Φ_{EPID}) is composed of primary (i.e. originating from the linac head) and patient scatter components, and is defined as:

$$(5.5) \Phi_{EPID}(x, y, E_i) = \Phi_{P,EPID}(x, y, E_i) + \Phi_{S,EPID}(x, y, E_i),$$

from Equations 5.3 and 5.4. The predicted energy fluence on the EPID is converted to dose in the phosphor layer through a superposition with the EPID dose kernels. Practically, this is accomplished with a convolution of integrated fluence for each energy bin, $\Phi_{EPID}(E_i)$, with the EPID dose kernel, $k(E_i)$, valid for energy bin i , and summed over all energy bin contributions for a point (x,y) :

$$(5.6) D_{EPID}(x, y) = \sum_i \Phi_{EPID}(x, y, E_i) \otimes k(x, y, E_i).$$

This approach models the energy response of the EPID, known to be more sensitive to low energy photons as compared to a water-equivalent detector [2].

The EPID dose kernels used in McCurdy *et al.* [2], originally calculated in cylindrical coordinates using DOSRZ [49], have been calculated here directly in Cartesian coordinates using DOSXYZnrc [51], with a simulated detector resolution identical to that of the imager. This approach removes the effects of rebinning and interpolating the dose kernel from cylindrical to Cartesian coordinates, a potential source of error. The new EPID dose kernels are no longer generated with monoenergetic incident photons, but are now generated with photons whose energy is uniformly sampled over the range of the individual energy bins (for example, photons of energy 0 to 0.1 MeV are used in the 0.1 MeV bin). Furthermore, the EPID dose kernel simulations no longer include additional backscatter material (in the form of a slab of water) to mimic the effect of photon backscatter from the EPID arm [25, 26, 52].

5.2.4.ii Accounting for backscatter from the EPID support arm

Until recently, the backscatter effect due to the EPID support arm, when accounted for at all, has been typically modeled as a symmetric effect [8, 11, 12, 25, 26], although it is well-known to be asymmetric [7, 8, 26]. The work of Rowanshanfarzad *et al.* [53], demonstrated the asymmetry of the support arm backscatter, which has been shown to have up to a 6% dosimetric effect in the portal dose image. This measurement-based approach to modeling the asymmetric support arm backscatter [53] was incorporated into our current EPID image prediction algorithm.

5.2.4.iii Accounting for optical glare

While our previous method [8], and works such as Siebers *et al.* [25, 26], implicitly accounted for the optical glare phenomenon through their simulation methods, we now explicitly model this effect using a linear systems approach. This method involves convolving the dose deposited in the EPID's phosphor layer with a spatially invariant point spread function representing the optical photon spread in the scintillator due to an impulse energy input. Kirkby *et al.* [54] determined the optical glare point spread function for this EPID as:

$$(5.7) g = e^{-49.3r},$$

where r is the radial distance (in cm) and -49.3 is the decay parameter (in cm^{-1}) for a 6 MV beam. The equation and the decay parameter were determined by Monte Carlo modeling of optical photon transport, and were verified with measurement. This was implemented in our EPID image prediction algorithm via a convolution with the backscatter-corrected dose image [53]. The result is the final predicted EPID image that is to be compared with the corresponding measured EPID image.

5.2.5 Measured data and analysis

All measured data were obtained with a 6 MV beam from a Clinac 2100iX linear accelerator and an aS1000 EPID (Varian Medical Systems, Palo Alto, CA). Homogeneous plastic water phantom slabs (ranging from 2 to 37 cm thick) were placed in the beam centered at isocentre and irradiated with a variety of fields (from 2×2 to $20 \times 20 \text{ cm}^2$), with the EPID positioned at a variety of distances from the bottom of the phantom in order to create air gaps of 15, 25, 40 and 50 cm. The predicted and measured

images were converted to absolute dose (in calibrated units, CU) for direct comparison. For the simple square field measurements, the images were initially calibrated to a single image of a 10x10 cm² field with no phantom in the beam. However, a more robust calibration method (termed ‘robust calibration’ for this work) was achieved by incorporating a lookup table of calibration values based on a range of phantom thicknesses, field sizes and air gaps. This approach is analogous to field-based output correction factors used in some commercial treatment planning systems. Practically, the calibration factor for a treatment scenario is selected based on the average phantom thickness, average air-gap, and field size (as defined by pixels $\geq 10\%$ of the maximum value). It is noted that this approach represents a relatively small adjustment of the absolute dose output, as the range of values for calibration factors over the range of phantoms, airgaps and field sizes examined here is [-2%, +3%] as described in the Section 5.3.2.

Images were also acquired during the delivery of two clinical seven-field IMRT treatment plans (one prostate patient plan and one head and neck patient plan) to homogenous slab phantoms with thicknesses representative of their treatment sites (25 cm and 12 cm, respectively). The predicted and measured images were then compared using the χ -comparison [55], which is a computationally efficient variation of the γ -evaluation [56], for a 3% dose difference and 3 mm distance-to-agreement (DTA). The percentage of in-field pixels (in-field defined as $\geq 10\%$ of maximum dose) passing this criterion was calculated to evaluate the quality of the comparison.

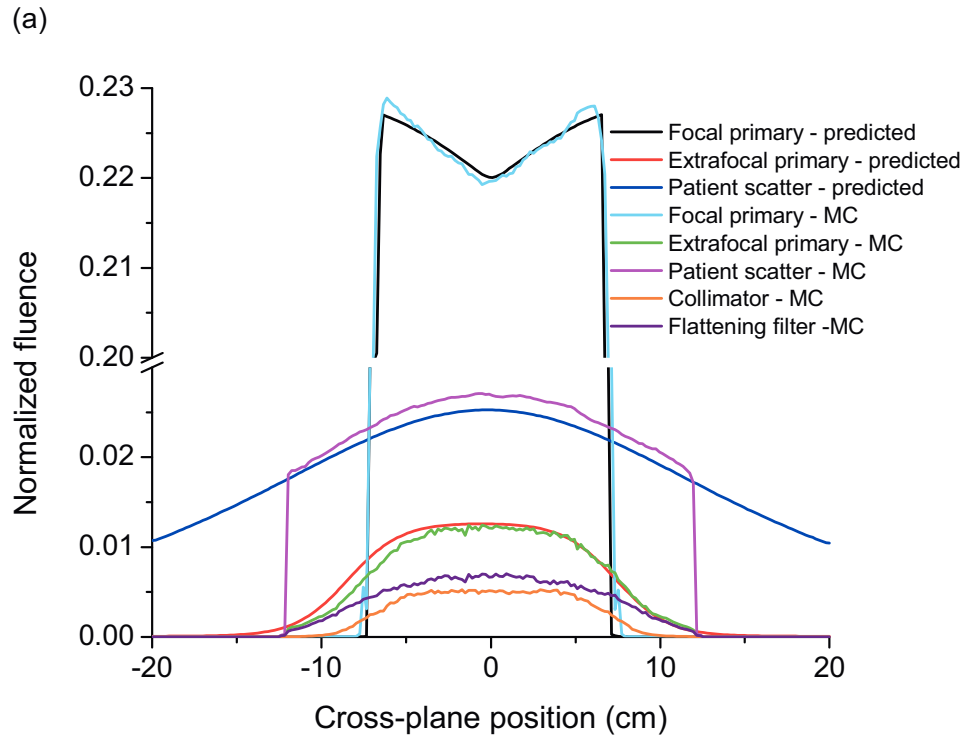
5.3 RESULTS AND DISCUSSION

5.3 Monte Carlo simulations

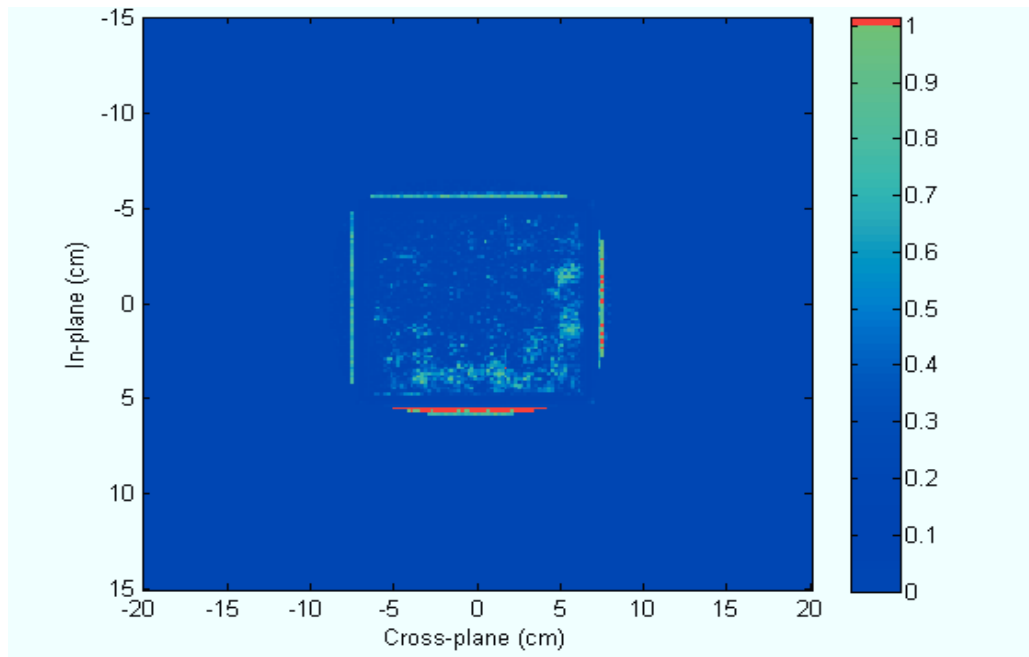
5.3.1.a Comparison of predicted fluence with Monte Carlo-calculated fluence

The predicted fluence calculated by the algorithm was compared to the Monte Carlo-calculated fluence of a $10 \times 10 \text{ cm}^2$ field with no phantom, a 10 cm thick phantom and a 25 cm thick phantom in the beam. All Monte Carlo fluence distributions were normalized to the Monte Carlo $10 \times 10 \text{ cm}^2$, no phantom, central axis fluence, while the predicted fluences were normalized to the predicted $10 \times 10 \text{ cm}^2$, no phantom, central axis fluence. For this purpose, the central axis was defined as the average fluence value in a $1 \times 1 \text{ cm}^2$ region around the true (geometric) central axis. The Monte Carlo data was resampled to a lower resolution to reduce noise ($0.2 \times 0.2 \text{ cm}^2$ voxels). Examining Figure 5.1 (a), the focal, extrafocal and patient scatter fluence profiles calculated by the prediction algorithm correspond closely to the Monte Carlo-calculated profiles ($<1\%$ difference with respect to the total fluence at the central axis). The χ -comparisons of the no phantom, 10 cm phantom and 25 cm phantom scenarios agreed within 2%, 2 mm for 100.0%, 100.0% and 98.6% of pixels, respectively. Note that the Monte Carlo-calculated patient scatter in Figure 5.1 (a) drops to zero at $\pm 12.0 \text{ cm}$. This occurs since the photons outside $\pm 12.0 \text{ cm}$ were not tracked in order to reduce simulation time.

Figure 5.1 [Monte Carlo Fluence vs. Algorithm Fluence]: (a) Fluence profiles from the prediction algorithm and the Monte Carlo simulation of a 10x10 cm² field incident on a 25 cm thick phantom, obtained at a plane 140 cm from the source. Note the discontinuous fluence axis. (b) The accompanying χ -comparison of the fluence. The pixels in red do not agree within 3%, 3 mm.



(b)



5.3.1.b Patient scatter kernels

The recent patient scatter fluence kernels generated using BEAMnrc possess similar properties as those generated in McCurdy and Pistorius [42]. The scatter fraction decreases with increasing air gap and the mean energy increases as the lower energy photons (which scatter at larger angles on average) scatter away from the scoring plane. Also, the mean energy of the kernels decreases with distance from the central axis as the higher energy photons are typically single-scattered photons and are more forward-directed. Also, as the phantom thickness increased, the scatter fraction increased until the 25 cm thickness when the scatter fraction began to decrease. Determining the exact peak phantom thickness for scatter production is not possible because the thickness resolution of the patient scatter kernels is 5 cm for thicknesses greater than 20 cm – however the peak would lie between 20 cm and 25 cm. This effect was also observed previously, with a thickness peak for multiple scattering at 25 cm for 6 MV [42]. The mechanism of scatter for the new fluence kernels was not distinguished, therefore the proportion of singly-scattered, multiply-scattered and bremsstrahlung photons is not compared to the scatter fluence kernels of the previous work..

5.3.2 Square field analysis

The central axis values of the predicted and measured dose images (using a single, open 10x10 cm² field image for calibration) were compared and found to be within a range of -2% to +3% (a 5% spread in the data points) for all phantom thicknesses, field sizes and air gaps (see Figure 5.2). For individual field sizes, the largest spread across all thicknesses and air gaps was 4%. Discrepancies between measured and predicted dose

images were uniform across the entire field (see Figure 5.3 for sample profiles). The interleaf leakage magnitude and location is observed qualitatively to compare well for the in-plane profile in Figure 5.3 (b). Note that data for larger fields delivered to thicker phantoms (i.e. 20x20 cm² field, 37 cm thick phantom, 50 cm air gap scenario) were not obtainable due to the limited size of the imager.

Figure 5.2 [Plot of Normalization Values]: The ratio of predicted to measured central-axis absolute doses for a range of slab thicknesses, field sizes and air gaps. The 140 cm air gap data with 0 cm thickness are open-field images. The images are calibrated to a 10x10 cm² open-field image.

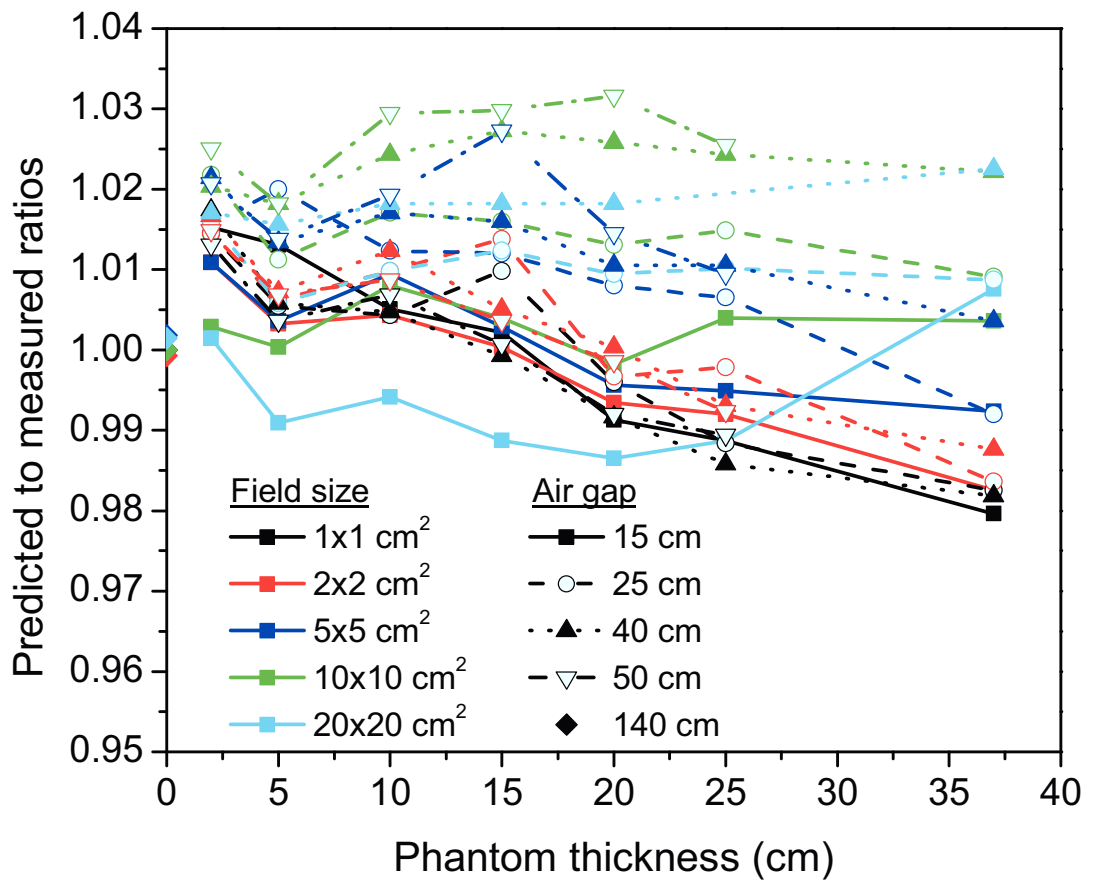
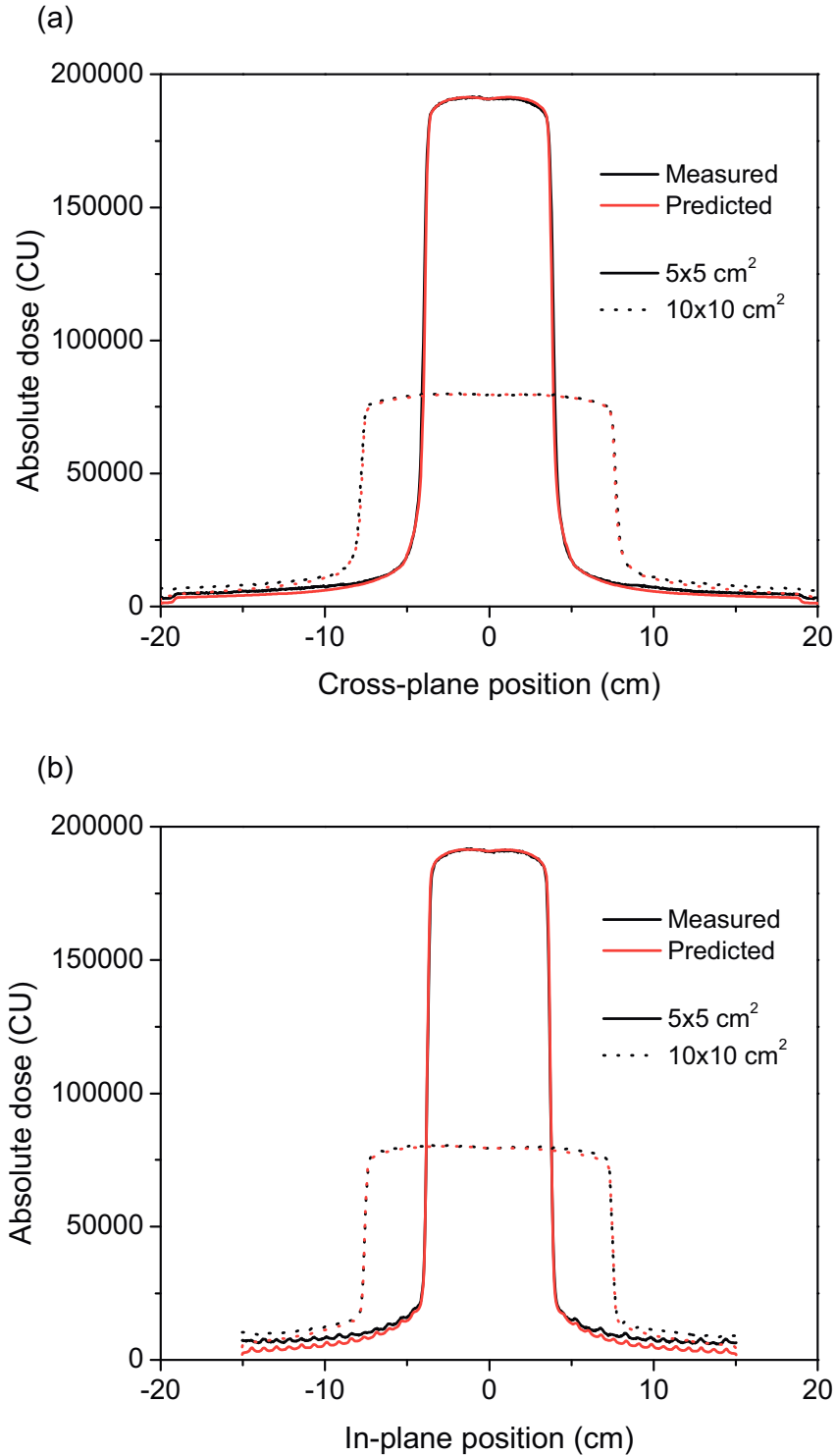


Figure 5.3 [Square Fields Delivered to Phantom Slabs]: Measured and predicted profiles of images acquired using phantom slabs in the beam, in the (a) cross-plane and (b) in-plane directions. The solid line is the 5x5 cm² field with a 5 cm thick phantom and 50 cm air gap. The dashed line is the 10x10 cm² field with a 25 cm thick phantom and a 40 cm air gap.

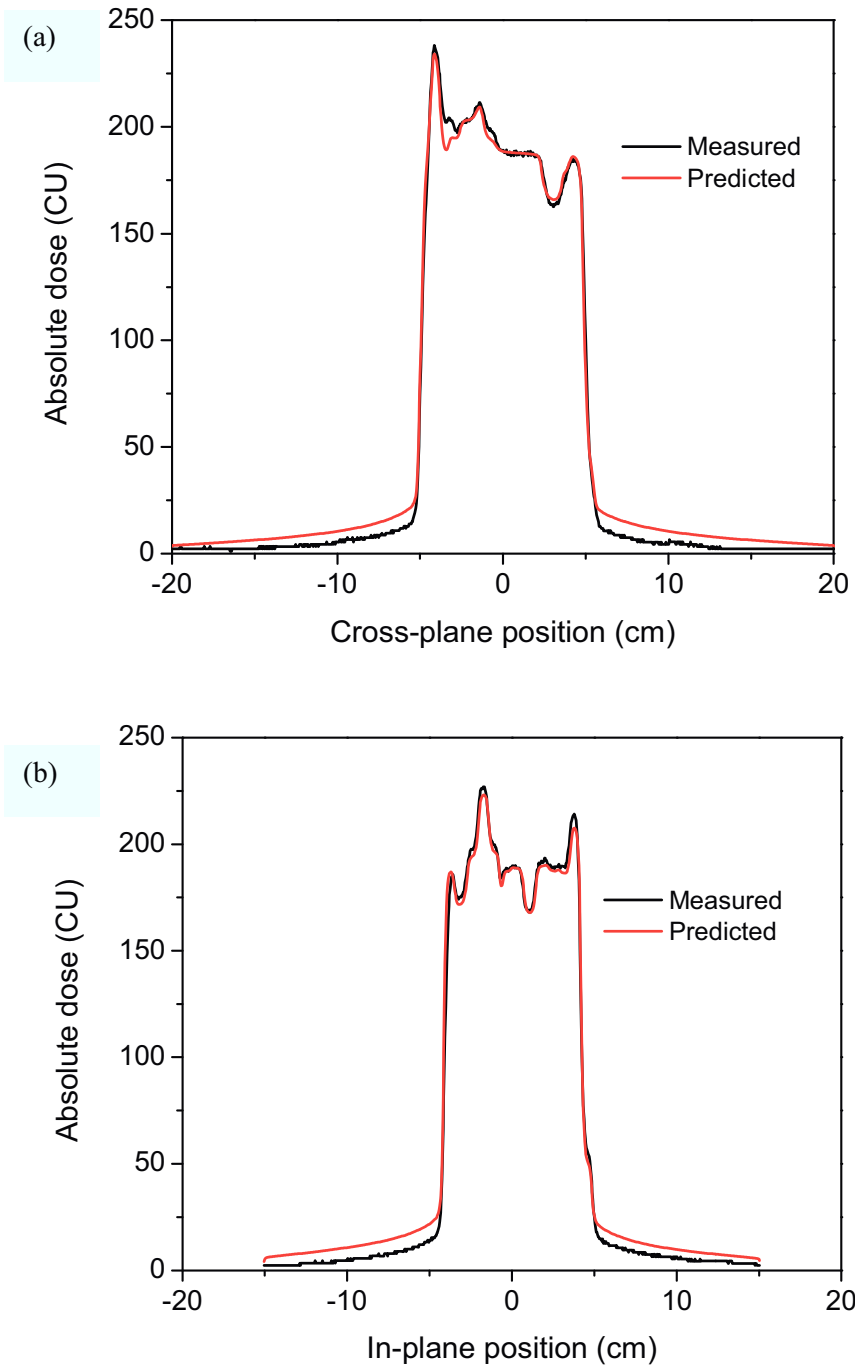


Comparing the results of the slab phantom image prediction to previous work [41], the results are not entirely consistent. An overprediction by the model should be observed for large field sizes, but is not seen for a combination of a short air gaps (15 cm) and phantoms ≤ 25 cm. As a function of air gap, the accuracy of the patient scatter fluence algorithm should increase with increasing air gap. Instead, the greatest overprediction is found with the largest air gap. Previous work by McCurdy and Pistorius [41], used semi-infinite slabs to generate the patient scatter kernels, resulting in a systematic overestimate of the multiple scatter fluence.

5.3.3 IMRT fields

Using the robust calibration method described in Section 5.2.5, the EPID dose image predictions of the IMRT fields through slab phantoms had a minimum agreement of 96.2% of in-field pixels lying within 3% and 3 mm (see Figures 5.4 and 5.5 and Table 5.2). Sharp dose gradients delivered to the EPID were accurately reproduced by the portal dose image prediction algorithm. The mean χ -value for the seven prostate fields ranged from 0.07 to 0.15, with a maximum χ -value of 2.92 and maximum percent difference of 3.3%. The seven head-and-neck fields also agreed well, with mean χ -values ranging from 0.03 to 0.06 and a maximum χ -value of 1.34 over all fields. This close agreement using clinical fields from two disease sites demonstrates the accuracy of the model to calculate the total fluence entering the EPID due to complex IMRT fields and the subsequent conversion to imager signal.

Figure 5.4 [Prostate IMRT Field (Slab Phantom)]: Profiles of a prostate IMRT field (Field 5 of Table 5.2) in the (a) cross-plane and (b) in-plane directions. The corresponding χ -comparison resulting from the evaluation of the predicted and measured images is shown in (c) with the colour table indicating the calculated χ value. Pixels that do not agree within the required criteria are in red. The inset image is the predicted dose image with red indicating higher fluence and blue indicating lower fluences.



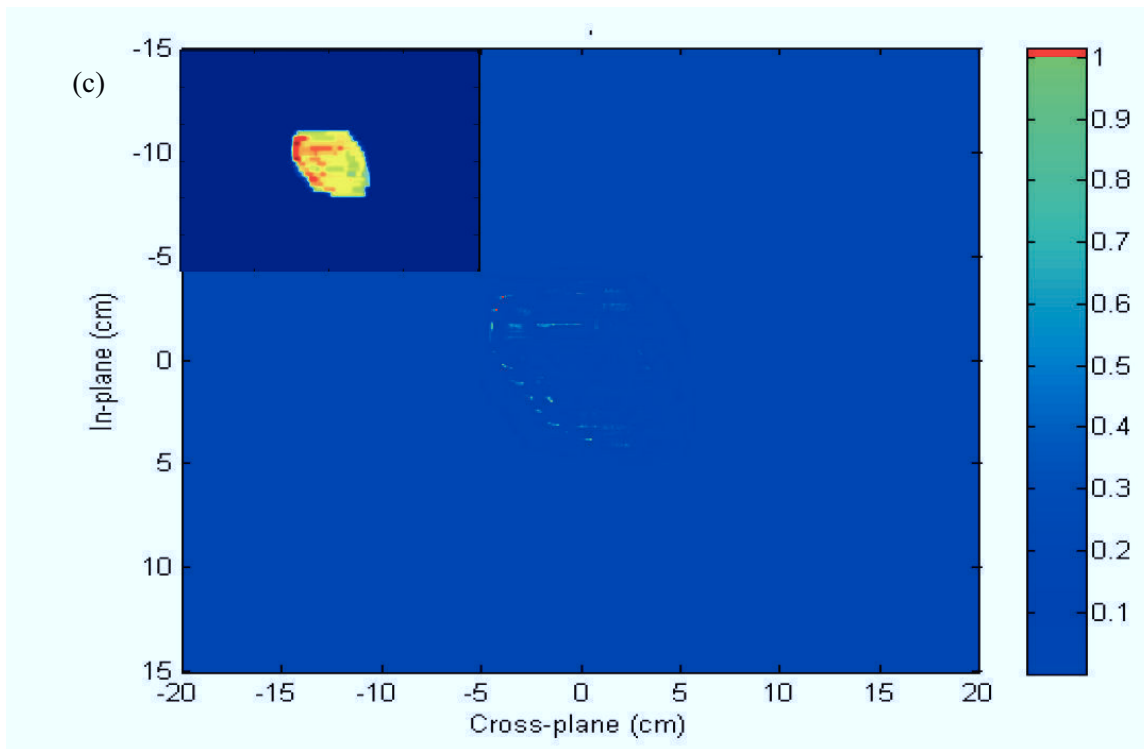
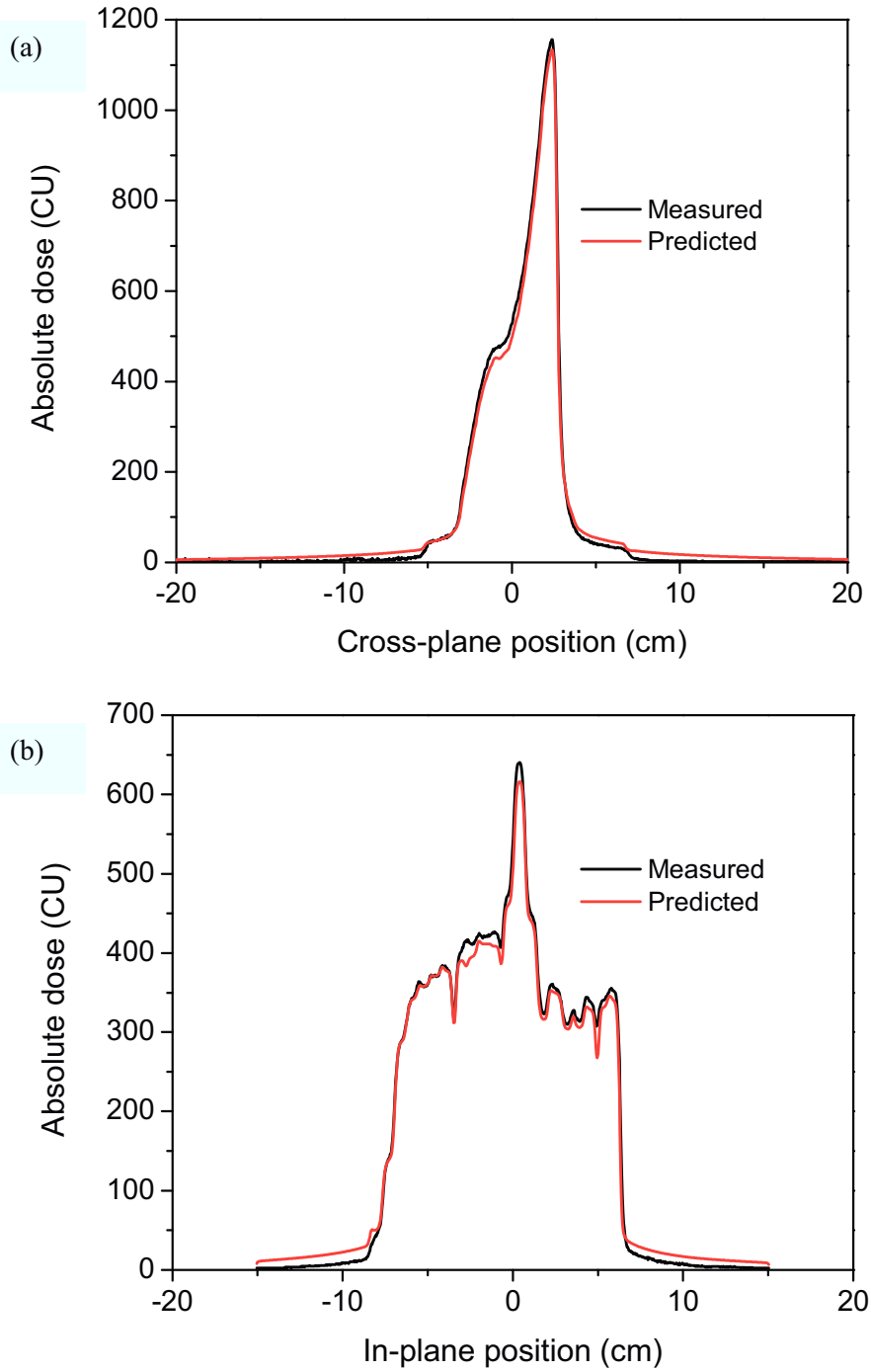


Table 5.2 [χ -comparison Results of Prostate IMRT Fields (Slab Phantom)]: Results of χ -comparison for the prostate fields incident on a 25 cm slab, including the percentage of pixels agreeing, mean χ , maximum χ and the mean percentage difference.

Field	% pixels agreeing	Mean χ	Max χ	Mean % difference
1	99.96	0.17	2.39	2.59
2	99.90	0.15	1.36	2.31
3	96.22	0.28	2.37	3.34
4	99.85	0.14	1.89	2.51
5	99.98	0.07	1.33	1.90
6	99.90	0.18	1.45	2.66
7	99.81	0.22	2.92	2.66
Average	99.38	0.17	1.96	2.57

Figure 5.5 [Head and Neck IMRT Field (Slab Phantom)]: Profiles of a head and neck IMRT field (Field 1 in Table 5.3) in the (a) cross-plane and (b) in-plane directions. The corresponding χ -comparison resulting from the evaluation of the predicted and measured images is shown in (c) with the colour table indicating the calculated χ value. Pixels that do not agree within the required criteria are in red. The inset image is the predicted dose image with red indicating higher fluence and blue indicating lower fluences.



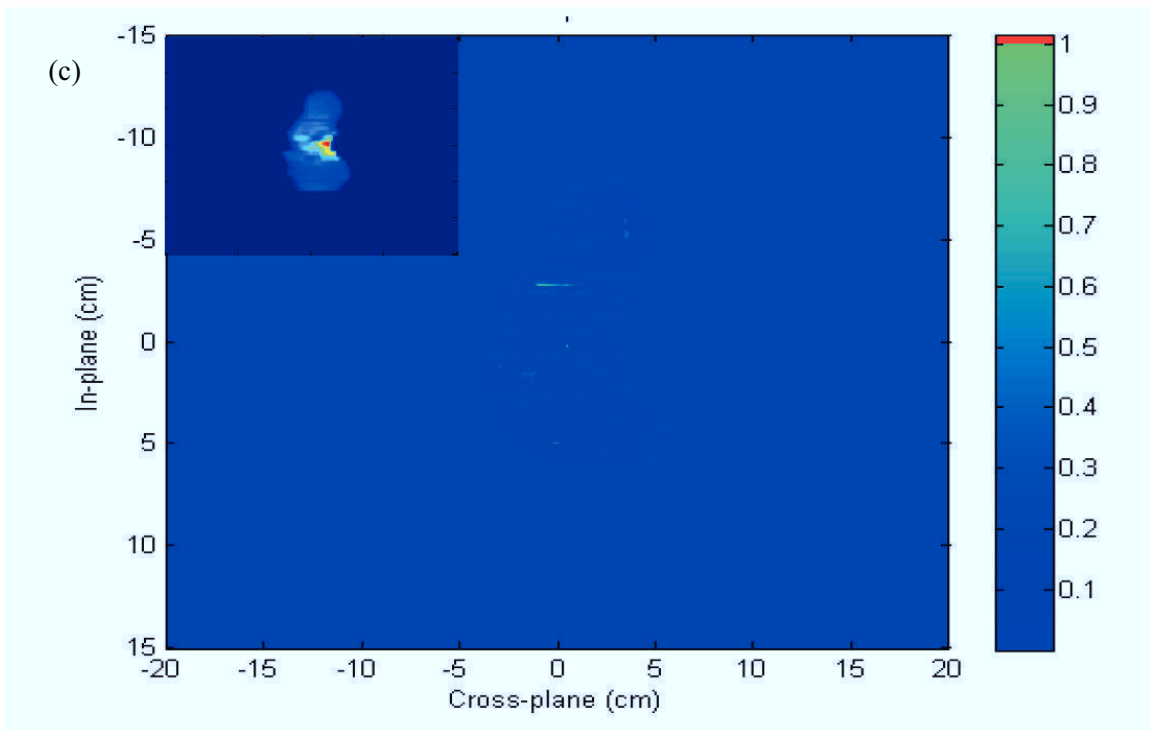


Table 5.3 [χ -comparison Results of Head and Neck IMRT Fields (Slab Phantom)]: Results of χ -comparison of head and neck fields on a 12 cm phantom slab, including the percentage of pixels agreeing, mean χ , maximum χ and the mean percentage difference.

Field	% pixels agreeing	Mean χ	Max χ	Mean % difference
1	100.00	0.05	1.59	1.27
2	100.00	0.03	0.86	0.64
3	100.00	0.05	2.55	1.70
4	100.00	0.05	0.88	1.54
5	100.00	0.05	0.81	0.97
6	99.98	0.06	1.13	1.66
7	99.97	0.06	1.36	1.75
Average	99.99	0.05	1.31	1.36

5.4 CONCLUSIONS

A previously developed fluence model has been refined and extended to include fewer user-adjustable parameters and more detailed physical models to improve accuracy. A patient scatter model has been updated with scatter fluence kernels calculated with newer, more accurate simulation software. EPID specific dose kernels have also been updated using the newer simulation software, and scored directly in the required Cartesian coordinate system. These models have been integrated together to form a complete model-based method to predict portal dose images with a patient in the beam path, with only a small reliance on empirical modeling. An accuracy of 3% and 3 mm has been shown to be achievable with this portal dose image prediction method using clinical IMRT fields. Future work will evaluate the robustness of this portal dose image prediction model on images obtained during patient treatment delivery.

REFERENCES

1. Bogdanich, W., *Radiation Offers New Cures, and Ways to Do Harm*, The New York Times, January 23, 2010, <http://www.nytimes.com/2010/01/24/health/24radiation.html?ref=radiationboom>.
2. McCurdy, B. M. C., Luchka, K., and Pistorius, S., *Dosimetric investigation and portal dose image prediction using an amorphous silicon electronic portal imaging device*. Med Phys, 2001. **28**(6): p. 911-24.
3. Winkler, P., Hefner, A., and Georg, D., *Dose-response characteristics of an amorphous silicon EPID*. Medical Physics, 2005. **32**(10): p. 3095-105.
4. McDermott, L. N., Louwe, R. J. W., Sonke, J. J., van Herk, M. B., and Mijnheer, B. J., *Dose-response and ghosting effects of an amorphous silicon electronic portal imaging device*. Medical Physics, 2004. **31**(2): p. 285-95.
5. van Elmpt, W. J. C., Nijsten, S. M. J. J. G., Mijnheer, B. J., and Mincken, A. W. H., *Experimental verification of a portal dose prediction model*. Medical Physics, 2005. **32**(9): p. 2805-18.
6. Van Esch, A., Depuydt, T., and Huyskens, D. P., *The use of an aSi-based EPID for routine absolute dosimetric pre-treatment verification of dynamic IMRT fields*. Radiotherapy and Oncology, 2004. **71**(2): p. 223-34.

7. Greer, P. B., Cadman, P., Lee, C., and Bzdusek, K., *An energy fluence-convolution model for amorphous silicon EPID dose prediction*. Medical Physics, 2009. **36**(2): p. 547-55.
8. Chytyk, K. and McCurdy, B. M. C., *Comprehensive fluence model for absolute portal dose image prediction*. Med Phys, 2009. **36**(4): p. 1389-98.
9. McCurdy, B. M. C. and Greer, P. B., *Dosimetric properties of an amorphous-silicon EPID used in continuous acquisition mode for application to dynamic and arc IMRT*. Medical Physics, 2009. **36**(7): p. 3028-39.
10. Greer, P. B. and Popescu, C. C., *Dosimetric properties of an amorphous silicon electronic portal imaging device for verification of dynamic intensity modulated radiation therapy*. Medical Physics, 2003. **30**(7): p. 1618-27.
11. Warkentin, B., Steciw, S., Rathee, S., and Fallone, B. G., *Dosimetric IMRT verification with a flat-panel EPID*. Med Phys, 2003. **30**(12): p. 3143-55.
12. Steciw, S., Warkentin, B., Rathee, S., and Fallone, B. G., *Three-dimensional IMRT verification with a flat-panel EPID*. Medical Physics, 2005. **32**(2): p. 600-12.
13. Ansbacher, W., *Three-dimensional portal image-based dose reconstruction in a virtual phantom for rapid evaluation of IMRT plans*. Med Phys, 2006. **33**(9): p. 3369-82.
14. McDermott, L. N., Wendling, M., van Asselen, B., Stroom, J., Sonke, J. J., van Herk, M., and Mijnheer, B. J., *Clinical experience with EPID dosimetry for prostate IMRT pre-treatment dose verification*. Medical Physics, 2006. **33**(10): p. 3921-30.
15. McDermott, L., Wendling, M., Sonke, J., Vanherk, M., and Mijnheer, B., *Replacing Pretreatment Verification With In Vivo EPID Dosimetry for Prostate IMRT*. Int J Radiat Oncol Biol Phys, 2007. **67**(5): p. 1568-77.
16. McDermott, L., Wendling, M., Nijkamp, J., Mans, A., Sonke, J., Mijnheer, B., and Vanherk, M., *3D in vivo dose verification of entire hypo-fractionated IMRT treatments using an EPID and cone-beam CT*. Radiother Oncol, 2008. **86**(1): p. 35-42.
17. Wendling, M., McDermott, L. N., Mans, A., Sonke, J.-J., van Herk, M., and Mijnheer, B. J., *A simple backprojection algorithm for 3D in vivo EPID dosimetry of IMRT treatments*. Med Phys, 2009. **36**(7): p. 3310-21.
18. Mans, A., Remeijer, P., Olaciregui-Ruiz, I. g., Wendling, M., Sonke, J.-J., Mijnheer, B., van Herk, M., and Stroom, J. C., *3D Dosimetric verification of volumetric-modulated arc therapy by portal dosimetry*. Radiother Oncol, 2010. **94**: p. 181-187.
19. Mans, A., Wendling, M., McDermott, L. N., Sonke, J. J., Tielenburg, R., Vijlbrief, R., Mijnheer, B., van Herk, M., and Stroom, J. C., *Catching errors with in vivo EPID dosimetry*. Med Phys, 2010. **37**(6): p. 2638-44.
20. van Elmpt, W., Nijsten, S., Mijnheer, B., Dekker, A., and Lambin, P., *The next step in patient-specific QA: 3D dose verification of conformal and intensity-modulated RT based on EPID dosimetry and Monte Carlo dose calculations*. Radiotherapy and Oncology, 2008. **86**(1): p. 86-92.

21. Pecharromán-Gallego, R., Mans, A., Sonke, J.-J., Stroom, J. C., Olaciregui-Ruiz, I. g., van Herk, M., and Mijnheer, B. J., *Simplifying EPID dosimetry for IMRT treatment verification*. Medical Physics, 2011. **38**(2): p. 983-92.
22. van Elmpt, W. J. C., Nijsten, S. M. J. J. G., Schiffeleers, R. F. H., Dekker, A. L. A. J., Mijnheer, B. J., Lambin, P., and Mincken, A. W. H., *A Monte Carlo based three-dimensional dose reconstruction method derived from portal dose images*. Medical Physics, 2006. **33**(7): p. 2426-34.
23. van Elmpt, W. J. C., Nijsten, S. M. J. J. G., Dekker, A. L. A. J., Mijnheer, B. J., and Lambin, P., *Treatment verification in the presence of inhomogeneities using EPID-based three-dimensional dose reconstruction*. Medical Physics, 2007. **34**(7): p. 2816-26.
24. Wendling, M., Louwe, R. J. W., McDermott, L. N., Sonke, J.-J., van Herk, M., and Mijnheer, B. J., *Accurate two-dimensional IMRT verification using a back-projection EPID dosimetry method*. Medical Physics, 2006. **33**(2): p. 259-73.
25. Li, W., Siebers, J. V., and Moore, J. A., *Using fluence separation to account for energy spectra dependence in computing dosimetric a-Si EPID images for IMRT fields*. Medical Physics, 2006. **33**(12): p. 4468-80.
26. Siebers, J. V., Kim, J. O., Ko, L., Keall, P. J., and Mohan, R., *Monte Carlo computation of dosimetric amorphous silicon electronic portal images*. Medical Physics, 2004. **31**(7): p. 2135-46.
27. Parent, L., Seco, J., Evans, P. M., Fielding, A., and Dance, D. R., *Monte Carlo modelling of a-Si EPID response: the effect of spectral variations with field size and position*. Med Phys, 2006. **33**(12): p. 4527-40.
28. Winkler, P., Hefner, A., and Georg, D., *Implementation and validation of portal dosimetry with an amorphous silicon EPID in the energy range from 6 to 25 MV*. Physics in Medicine and Biology, 2007. **52**(15): p. N355-N365.
29. van Elmpt, W., McDermott, L., Nijsten, S., Wendling, M., Lambin, P., and Mijnheer, B., *A literature review of electronic portal imaging for radiotherapy dosimetry*. Radiother Oncol, 2008. **88**(3): p. 289-309.
30. Spies, L., Partridge, M., Groh, B. A., and Bortfeld, T., *An iterative algorithm for reconstructing incident beam distributions from transmission measurements using electronic portal imaging*. Phys Med Biol, 2001. **46**: p. N203-N211.
31. Pasma, K. L., Heijmen, B. J., Kroonwijk, M., and Visser, A. G., *Portal dose image (PDI) prediction for dosimetric treatment verification in radiotherapy. I. An algorithm for open beams*. Med Phys, 1998. **25**(6): p. 830-40.
32. Kroonwijk, M., Pasma, K. L., Quint, S., Koper, P. C. M., Visser, A. G., and Heijmen, B. J. M., *In vivo dosimetry for prostate cancer patients using an electronic portal imaging device (EPID); demonstration of internal organ motion*. Radiotherapy and Oncology, 1998. **49**: p. 125-132.
33. van Zijtveld, M., Dirkx, M., Breuers, M., de Boer, H., and Heijmen, B., *Portal dose image prediction for in vivo treatment verification completely based on EPID measurements*. Med Phys, 2009. **36**: p. 946-952.
34. Hansen, V. N., Swindell, W., and Evans, P. M., *Extraction of primary signal from EPIDs using only forward convolution*. Medical Physics, 1997. **24**(9): p. 1477-1484.

35. Fielding, A., Evans, P., and Clark, C., *Verification of patient position and delivery of IMRT by electronic portal imaging*. *Radiotherapy and Oncology*, 2004. **73**(3): p. 339-347.
36. McNutt, T. R., Mackie, T. R., Reckwerdt, P., Papanikolaou, N., and Paliwal, B. R., *Calculation of portal dose using the convolution/superposition method*. *Med Phys*, 1996. **23**(4): p. 527-35.
37. McNutt, T. R., Mackie, T. R., and Paliwal, B. R., *Analysis and convergence of the iterative convolution/superposition dose reconstruction technique for multiple treatment beams and tomotherapy*. *Med Phys*, 1997. **24**: p. 1465-1476.
38. McNutt, T. R., Mackie, T. R., Reckwerdt, P., and Paliwal, B. R., *Modeling dose distributions from portal dose images using the convolution/superposition method*. *Med Phys*, 1996. **23**(8): p. 1381-92.
39. Fuangrod, T., O'Connor, D. J., McCurdy, B. M. C., and Greer, P. B., *Development of EPID-based real-time dose verification for dynamic IMRT*. *Proceedings of World Academy of Science, Engineering and Technology*, 2011. **80**: p. 609-612.
40. McCurdy, B. M. and Pistorius, S., *A two-step algorithm for predicting portal dose images in arbitrary detectors*. *Med Phys*, 2000. **27**(9): p. 2109-16.
41. McCurdy, B. M. and Pistorius, S., *Photon scatter in portal images: Accuracy of a fluence based pencil beam superposition algorithm*. *Med Phys*, 2000. **27**(5): p. 913-22.
42. McCurdy, B. M. and Pistorius, S., *Photon scatter in portal images: Physical characteristics of pencil beam kernels generated using the EGS Monte Carlo code*. *Med Phys*, 2000. **27**(2): p. 312-20.
43. Mackie, T. R., Reckwerdt, P., and Papanikolaou, N., *3-D photon beam dose algorithm*. in *Proceedings from the 1996 AAPM Summer School*, 1996. Published by Medical Physics Publishing, Madison, WI, p.201-222.
44. *BEAMnrc users manual*, Report No. PIRS-0509a, Ionizing Radiation Standards, National Research Council Canada: 2009.
45. Rogers, D. W. O., Faddegon, B. A., Ding, G. X., Ma, C. M., We, J., and Mackie, T. R., *BEAM: a Monte Carlo code to simulate radiotherapy treatment units*. *Med Phys*, 1995. **22**(5): p. 503-24.
46. Kawarakow, I., Mainegra-Hing, E., Rogers, D. W. O., Tessier, F., and Walters, B. R. B., *The EGSnrc code system: Monte Carlo simulation of electron and photon transport*. 2010, Ionizing Radiation Standards, National Research Council of Canada.
47. Deasy, J. O., Apte, A., Khullar, D., and Alaly, J., *The Computational Environment for Radiotherapy Research (CERR)*. 2010.
48. Mohan, R., Chui, C., and Lidofsky, L., *Energy and angular distributions of photons from medical linear accelerators*. *Med Phys*, 1985. **12**(5): p. 592-7.
49. *The EGS4 Code System*, Stanford Linear Accelerator Center: Stanford, California. 1985.
50. Siddon, R. L., *Fast calculation of the exact radiological path for a three-dimensional CT array*. *Medical Physics*, 1985. **12**(2): p. 252-255.
51. *DOSXYZnrc users manual*, Report no. PIRS-0794, National Research Council Canada: 2009.

52. Ko, L., Kim, J. O., and Siebers, J. V., *Investigation of the optimal backscatter for an aSi electronic portal imaging device*. *Physics in Medicine and Biology*, 2004. **49**(9): p. 1723-1738.
53. Rowshanfarzad, P., McCurdy, B. M. C., Sabet, M., Lee, C., O'Connor, D. J., and Greer, P. B., *Measurement and modeling of the effect of support arm backscatter on dosimetry with a Varian EPID*. *Medical Physics*, 2010. **37**(5): p. 2269-78.
54. Kirkby, C. and Sloboda, R., *Comprehensive Monte Carlo calculation of the point spread function for a commercial a-Si EPID*. *Medical Physics*, 2005. **32**(4): p. 1115-27.
55. Bakai, A., Alber, M., and Nusslin, F., *A revision of the gamma-evaluation concept for the comparison of dose distributions*. *Phys Med Biol*, 2003. **48**(21): p. 3543-53.
56. Low, D. A., Harms, W. B., Mutic, S., and Purdy, J. A., *A technique for the quantitative evaluation of dose distributions*. *Med Phys*, 1998. **25**: p. 656-61.

CHAPTER SIX: *IN VIVO* DOSIMETRIC VERIFICATION OF INTENSITY-MODULATED RADIATION THERAPY

Chapter Five discussed the addition of a patient scatter algorithm to the portal dose image prediction model to account for the effect of phantom or patient scatter incident on the EPID during image acquisition. Chapter Six* applies the complete portal dose image prediction model to predict images acquired during patient treatment, or *in vivo*.

6.1 INTRODUCTION

Dosimetric verification of radiation therapy is becoming increasingly important with the widespread use of complex treatment techniques like IMRT and VMAT. In general, patient-specific dosimetric verification of intensity-modulated treatment beams is performed prior to the start of the patient's treatment course, using film and/or point dose measurements. Pre-treatment verification can detect data transfer, machine, MLC positioning and quantitative dose errors [1]. However, pre-treatment verification clearly will not detect patient-related errors, such as patient positioning errors, patient weight loss, changes in tumour size, internal organ motion or errors in linac output during treatment. *In vivo* dosimetric verification occurring at treatment with the patient present, is the only way to know, with certainty, how accurately the treatment was actually delivered.

* Manuscript in preparation. Aspects of this work were presented as a poster in "K. Chytky, E. Van Uytven, T. Van Beek, P. B. Greer and B. M. C. McCurdy, 'Physical model for *in vivo* dose image prediction', Canadian Organization of Medical Physicists Annual Scientific Meeting, 2011, Vancouver, BC.

In vivo dosimetric verification of radiation therapy is not customarily performed at most cancer clinics, but its potential through the use of electronic portal imaging devices (EPIDs) has been examined over the last two decades. Kroonwijk *et al.* compared predicted transit portal dose images to measured portal images acquired during prostate patient treatments with a camera-based EPID [2]. Their work demonstrated that variations in predicted and measured doses were due to discrepancies between the patient anatomy represented in the planning CT and the patient anatomy during treatment, and were caused by rectal gas. Pasma *et al.* [3] built on the group's *in vivo* method to be able to distinguish the differences in measured and predicted images caused by internal organ motion from those caused by an error in monitor units delivered. This was achieved by comparing the backprojected dose at a 5 cm depth in the patient to that of the TPS (treatment planning system) at the same depth [3]. Further work at the same centre introduced a portal dose image prediction algorithm that was able to predict *in vivo* portal images acquired during prostate patient treatments [4]. The prediction, carried out for the first fraction, was accurate to a 3% local dose difference and 3 mm for at least 87% of pixels, with larger disagreements due to patient anatomy and interferences with the patient table. A dose reconstruction method, which registered daily cone-beam CT datasets to the planning CT to account for patient anatomy changes, was capable of calculating the 50% isodose surface to within 3% and 3 mm (in comparison to the TPS calculation) [5].

In vivo verification has also been investigated using amorphous-silicon (a-Si) EPIDs with work by McDermott *et al.* [6, 7], Wendling *et al.* [8] and Mans *et al.* [9, 10]. McDermott

et al. [6] determined that it was possible to replace all prostate patients' pre-treatment verification with *in vivo* verification of the treatments, created by two-dimensional dose reconstruction from back-projected EPID images. A combination of γ -comparison statistics (mean γ , maximum γ and the percentage of points with γ less than one, for various acceptance criteria) from the first three fractions was deemed accurate enough to distinguish systematic errors that would impact a patient's treatment from random linac output and daily patient anatomy discrepancies (e.g. caused by rectal gas). With an extension of the dose reconstruction algorithm to three-dimensions, Wendling *et al.* reproduced the treatment planning dose for the first 3 fractions and verified *in vivo* to within 3%, 3 mm for prostate, rectum and head-and-neck patients [8], while McDermott *et al.* demonstrated the same accuracy for the dose reconstruction of all five fractions of nine hypo-fractionated rectal cancer patients [7]. Daily cone-beam CTs of the hypo-fractionated patients were acquired and registered to the planning CT to ensure proper patient positioning. This technique has also been successfully adapted to the verification prior to and during the treatment of volumetric-modulated arc therapy patients [9]. Mans *et al.* outlined the types of errors discovered during the Netherlands Cancer Institute's *in vivo* verification of prostate, rectum, head-and-neck, breast, lung and other treatment sites between January 2005 and July 2009 [10]. Out of the 17 errors detected from the 4337 patients, seven were due to a change in patient anatomy from the time the planning CT was acquired, two of which were due to patient weight loss, and six errors were due to data transfer problems or accidental plan modification [11, 12].

To date, there is a lack of *in vivo* EPID dosimetry imaging data obtained throughout a patient's entire course of treatment (for non-hypo-fractionated treatments). In the current work, images were acquired during the treatments of prostate and head-and-neck IMRT patients. The measured images were compared, via the χ -comparison method, to predicted portal dose images of the patient treatment to dosimetrically verify patient IMRT treatments.

6.2 METHODS AND MATERIALS

6.2.1 Patient plans and image acquisition

Portal mages were acquired during treatment of five prostate and six head-and-neck patients, for most fractions. Approximately 386 images out of 2300 possible images were missed, spread over all patients. These were mainly due to conflicting scheduling (~ 350) and occasionally failed acquisitions (~36). Recent clinical software changes at our treatment centre will help reduce scheduling-related misses in the future.

The prostate IMRT plans were planned according to the PROFIT trial [13]. Beam arrangement consisted of seven fields at angles of 0°, 40°, 85°, 110°, 250°, 275° and 310°, with small adjustments in angle allowed if needed for improvements in individual patient plans. Three of the prostate plans were delivered as static treatments (i.e. 'step and shoot') and two as dynamic delivery treatments (i.e. 'sliding window'). Patients in the hypofractionated arm received 60 Gy in 20 fractions total (two patients) while in the standard arm patients received 78 Gy in 39 fractions (three patients). To verify patient positioning prior to delivery, two orthogonal megavoltage (MV) images were taken daily

for four patients, with one patient using kilovoltage (KV) imaging. Daily image guidance was performed by tracking three radio-opaque gold seeds that were implanted in each patient's prostate ahead of CT simulation, using a match tolerance of 5 mm.

The head-and-neck plans were static IMRT, seven-field plans at equally spaced gantry angles (0°, 51°, 102°, 153°, 204°, 255° and 306°), planned in accordance with RTOG 0522, although delivering 70 Gy in 30 fractions. The patients were imaged daily with orthogonal portal images, prior to treatment delivery. The patients' bony anatomy, evident in the set-up image, was matched to that in a digitally reconstructed radiograph (DRR) created from the patient's CT dataset. The patient position was adjusted to match the DRR, and therefore the planning CT within a tolerance of 5 mm.

Upon image review, images acquired over approximately a three month time frame (May 2009 to July 2009) were observed to have used incorrect calibration images (i.e. dark and flood-field images) when the images were processed. Specifically, this manifested in the images as vertical streaking and increased noise localized to the central $\sim 25 \times 30 \text{ cm}^2$ region of the EPID (Figure 6.1 (a) – the affected region is between the white lines). The values out-of-field for each row along each column were constant. The dark and flood-field images used for processing these integrated images were found to have been inadvertently erased from the system so reintroduction of the calibrations and then application of correct dark and flood-field images was impossible. This problem affected images across three patients. A method was developed to correct for this problem. The images were corrected by obtaining a profile at the extreme in-plane edge (black outline

in Figure 6.1 (b), called $P_{in-plane}$) where the artifact was not present, and corresponding to an unirradiated area. This profile was subtracted from the profile at the extreme cross-plane edge (black outline in Figure 6.1 (c), called $P_{cross-plane}$), which was affected by the artifact:

$$(6.1) P_{Correction} = P_{cross-plane} - P_{in-plane} .$$

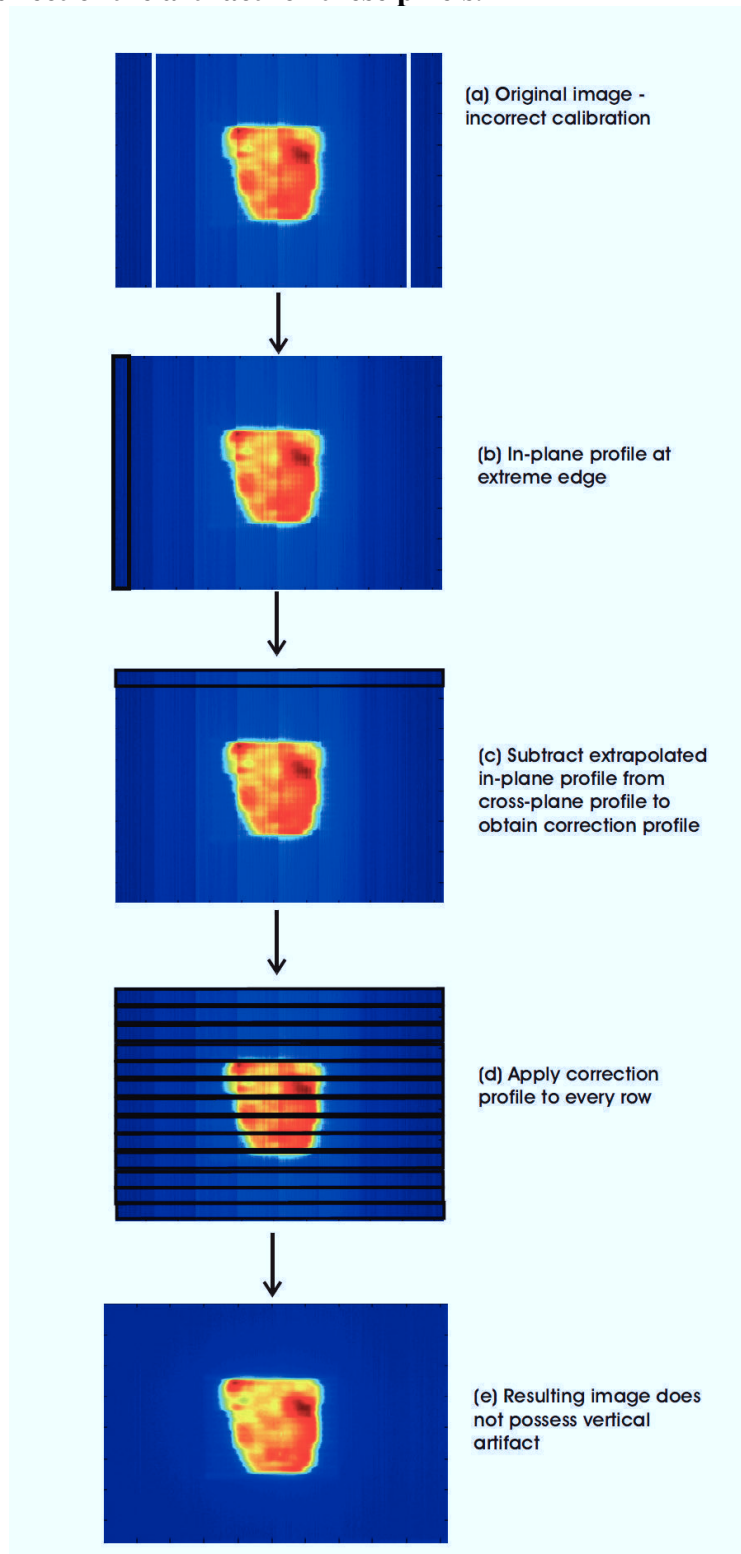
Assuming that the out-of-field signal would be symmetric, the subtraction of the two profiles provides a correction off-set ($P_{correction}$) that can be applied to each affected cross-plane row (Figure 6.1 (d)) to obtain the corrected image, $I_{corrected}$ (Figure 6.1 (e), from the incorrectly calibrated image, $I_{incorrect}$:

$$(6.2) I_{corrected}(j) = I_{incorrect}(j) - P_{correction} .$$

Each j represents a cross-plane row of the image – the subtraction is applied row-by-row. The assumption of a symmetric out-of-field signal is accurate to about 1% of the maximum dose, based on symmetry observed in dose profile tails comparing in-plane to cross-plane orientations in the measured data.*

* RTU-K Commissioning Profile Scans, 6 MV, September 2006, Medical Physics Department, CancerCare Manitoba.

Figure 6.1 [Image Correction Method]: Diagram of image correction method. The artifact is characterized by streaks in the in-plane direction, with a constant off-set for each column. The off-set is applied in the cross-plane direction, along each row, removing the effect of the artifact for these pixels.



6.2.2 Portal dose image prediction model

The transit portal images were predicted using an amalgamation of the comprehensive fluence model [14] and the patient scatter prediction model [15], as described in Chapter Five, and created in-house with the MATLAB® (Mathworks Inc., Natwick, MA) programming language. Only a brief review will be presented here. The incident fluence model is a two-source, physics-based model which models the MLC leaves using the specifications provided by the vendor (Varian Medical Systems, Palo Alto, CA). The energy fluence transmitted through the MLCs is determined via an attenuation calculation using Monte Carlo calculated energy fluence upstream of the MLC. The patient scatter prediction model involves a library of pre-calculated scatter fluence kernels, generated for a range of water thicknesses and air gaps. An equivalent homogeneous phantom (EHP) is created, based on the radiological pathlength of the raylines cast through the patient's CT dataset. The scatter incident on the EPID due to patient scatter is determined by the superposition of the appropriate scatter fluence kernel for each rayline, based on the radiological pathlength and the distance from the patient to the EPID (air gap). The primary fluence is determined by an attenuation calculation using the incident fluence model, the radiological pathlength of the CT dataset and the attenuation of water. The total fluence (scatter plus primary fluence) incident on the EPID is converted to a predicted dose image through the superposition of the fluence with monoenergetic, EPID-specific dose kernels, also derived using Monte Carlo simulation. The portal dose image prediction algorithm was able to predict images of simple square fields and IMRT fields delivered to slab phantoms within 3% and 3 mm.

The patient treatment plan was integrated into the portal dose image prediction model through the use of code from The Computational Environment for Radiotherapy Research (CERR) software platform [16], written in the MATLAB programming language. The plans were exported from both the Pinnacle TPS (Philips Medical Systems, Milpitas, CA) and Eclipse (Varian Medical Systems, Palo Alto, CA) planning systems and imported into CERR. The MLC leaf-positions, segment weights and CT dataset were used by the algorithm described in Chapters Four and Five of this thesis to predict the corresponding portal dose images.

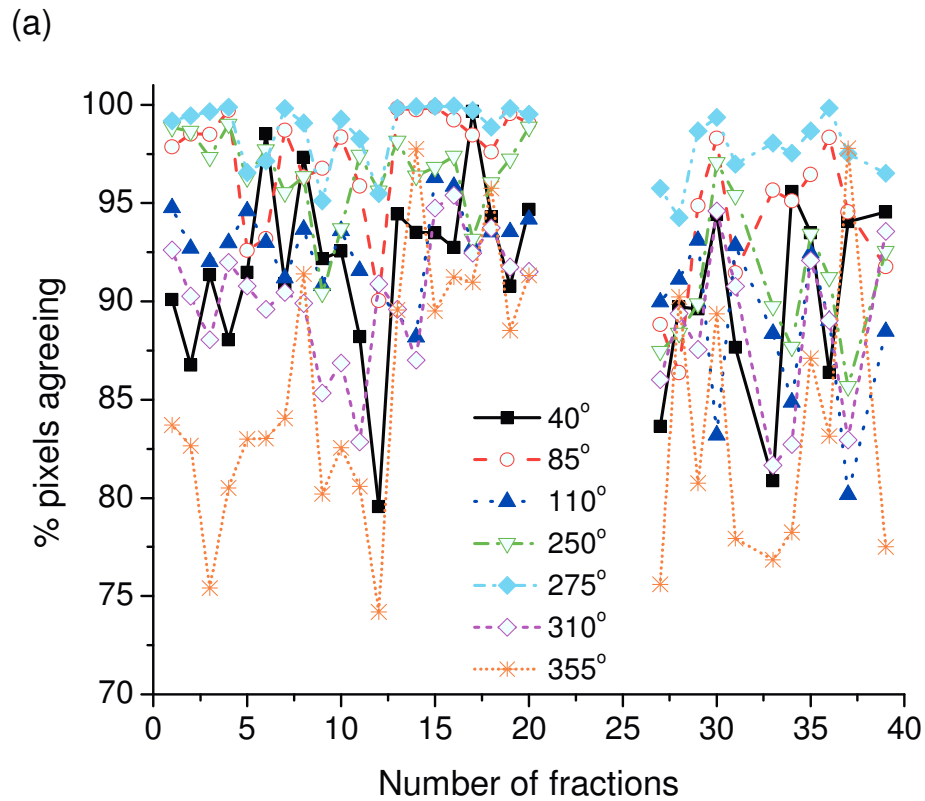
6.3 RESULTS AND DISCUSSION

6.3.1 Prostate patients

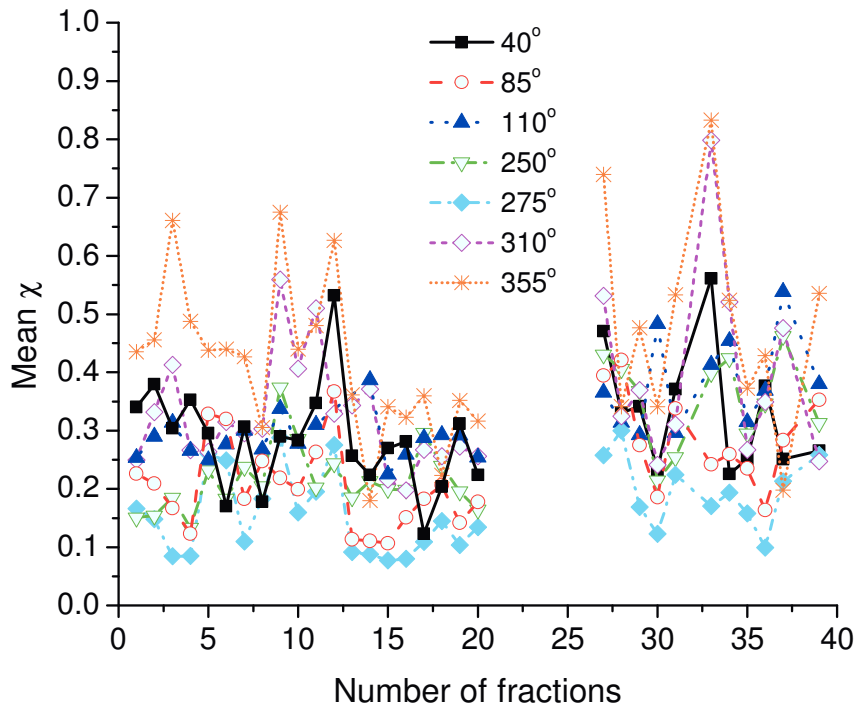
One prostate patient treatment will be examined here in detail; in particular, the results of the χ -comparison metrics (see Figures 6.2) and percentage difference of the predicted field from the measured field. The gantry angles providing measured images that were the most consistent with predictions were those that did not have the treatment couch in either the entrance or exit beam (i.e. the lateral beams at gantry 85° and 275°). As seen in Figure 6.2, there is much inter-fraction variability for each gantry angle, and there is no evidence of a trend with time in percentage of pixels that agree within 3% and 3 mm, mean χ , maximum χ or percentage difference, with time. The percentage of pixels that agree within 3% and 3 mm, mean χ , maximum χ and mean percentage difference were determined to be 92.3%, 0.30, 3.81, 3.99, respectively. The effect of the adjustable couch rails was seen as an overpredicted vertical “bar” in the in-plane direction of the percentage difference image (see Figure 6.3 (a), the blue bar). Also obvious in the

percentage difference image are rectal gas pockets, variable in size, intensity and location from fraction to fraction, seen as an underprediction in Figure 6.3 (l) as the red area.

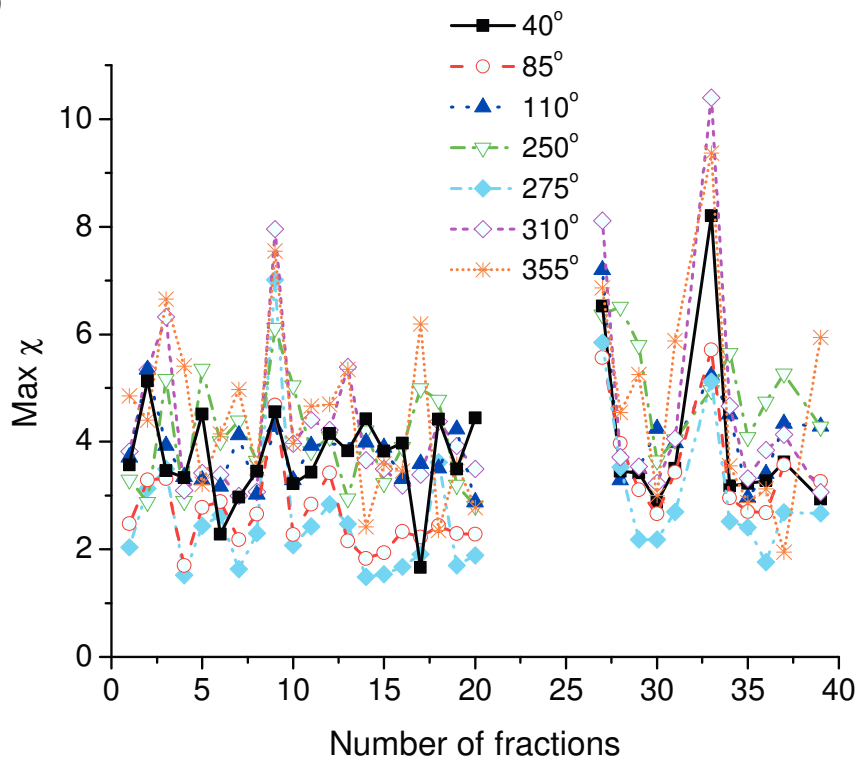
Figure 6.2 [Prostate Patient Case Study]: Comparison results of prostate patient case study, for each field, denoted by gantry angle, and for each fraction. (a) is the percent of pixels that agree within 3% and 3 mm using the χ -comparison, (b) is the mean value of χ in-field (defined as $\geq 10\%$ of the maximum dose) and (c) is the maximum value of χ in-field. (d) is the mean percentage dose difference in-field. There is a high fraction-to-fraction variability due to the effect of the treatment couch and rectal gas pockets. Note that image data for fraction 21-26 were not obtained for this patient.



(b)



(c)



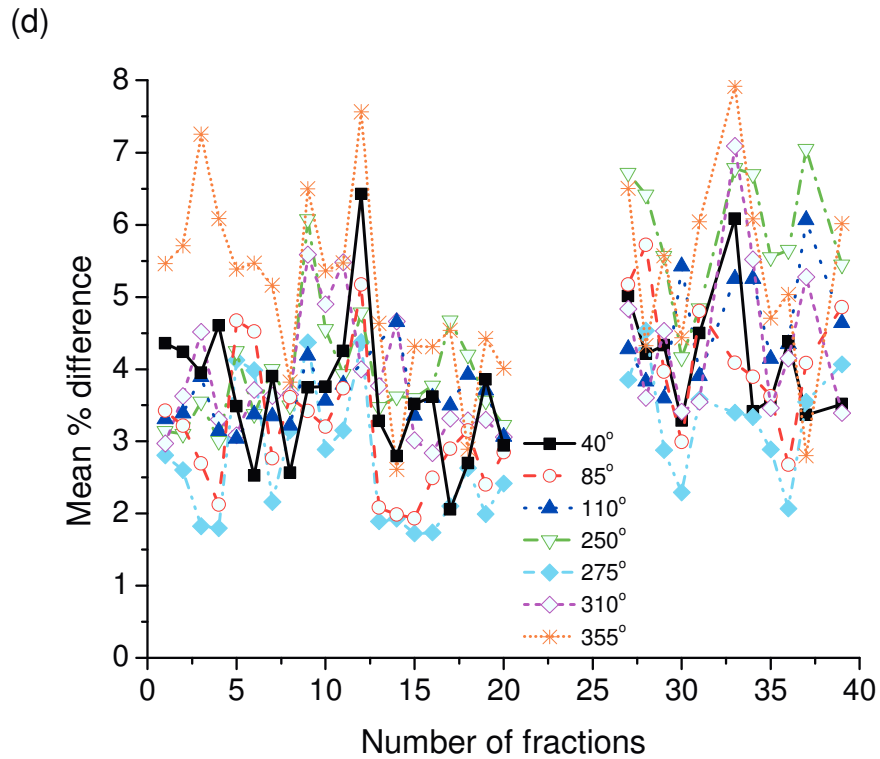
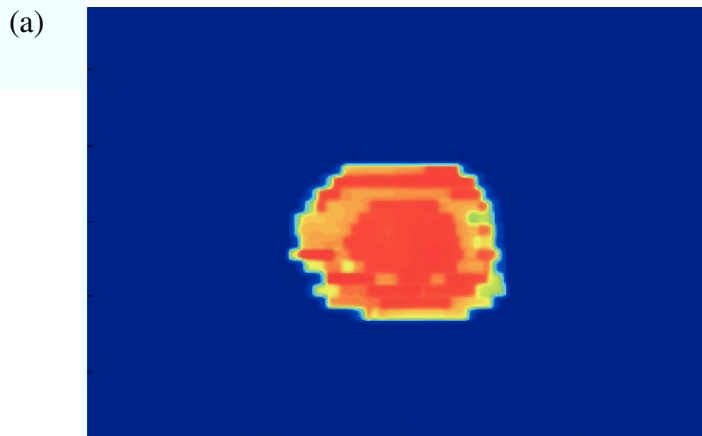
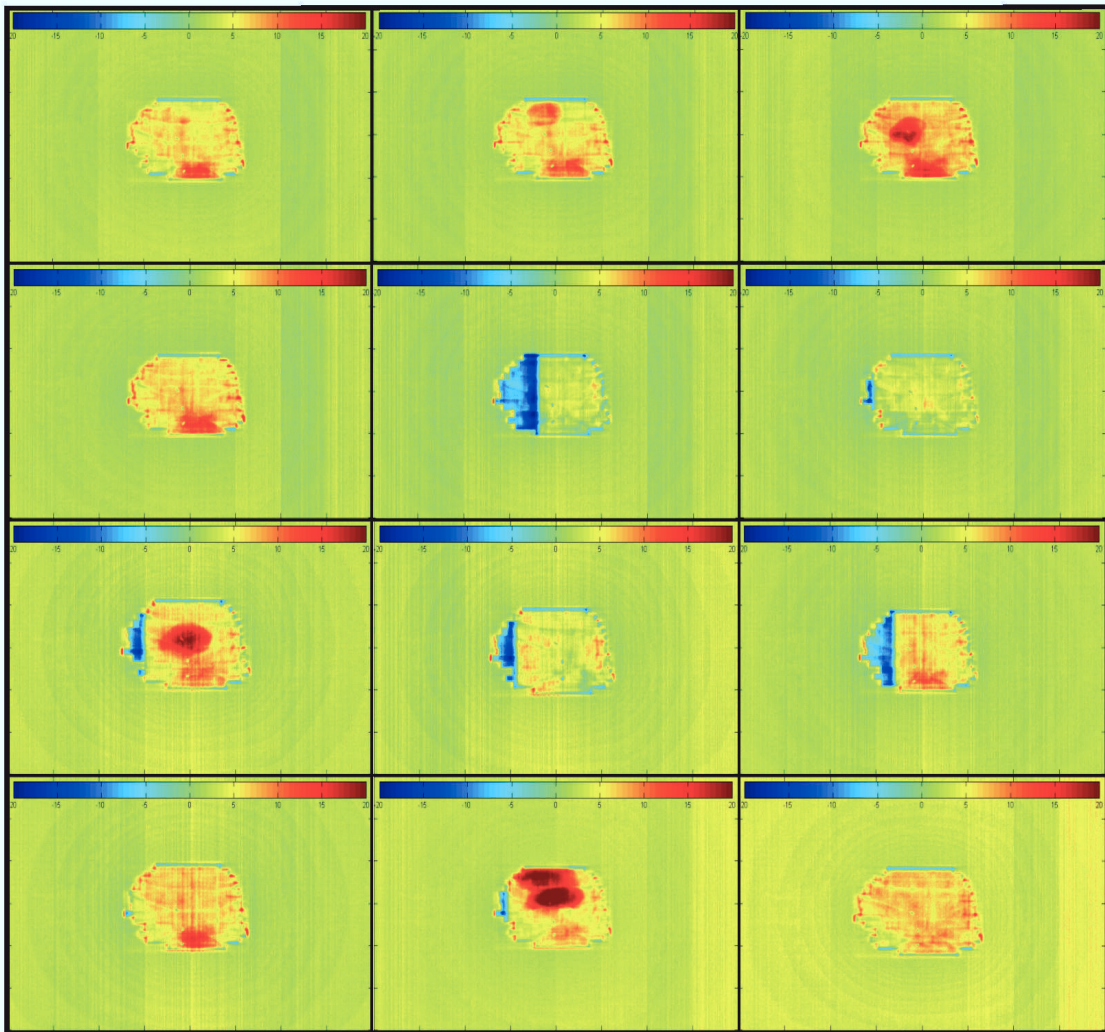


Figure 6.3 [Prostate Patient Percent Difference with Fraction]: (a) A predicted dose image for prostate field (gantry angle 355°) and (b) the percentage difference maps for twelve fractions (fractions 1, 2, 3, 4, 17, 18, 27, 28, 29, 31, 33, 34). The dark blue on the legend corresponds to a 20% overprediction, while the dark red corresponds to a 20% underprediction. Note the blue bar, oriented in the in-plane direction and at the left side of the field in several images (fractions 17, 18, 27, 28, 29, 31), is due to the moveable rail on the treatment couch. The red area near the centre of the field in several fractions corresponds to gas pockets in the rectum.



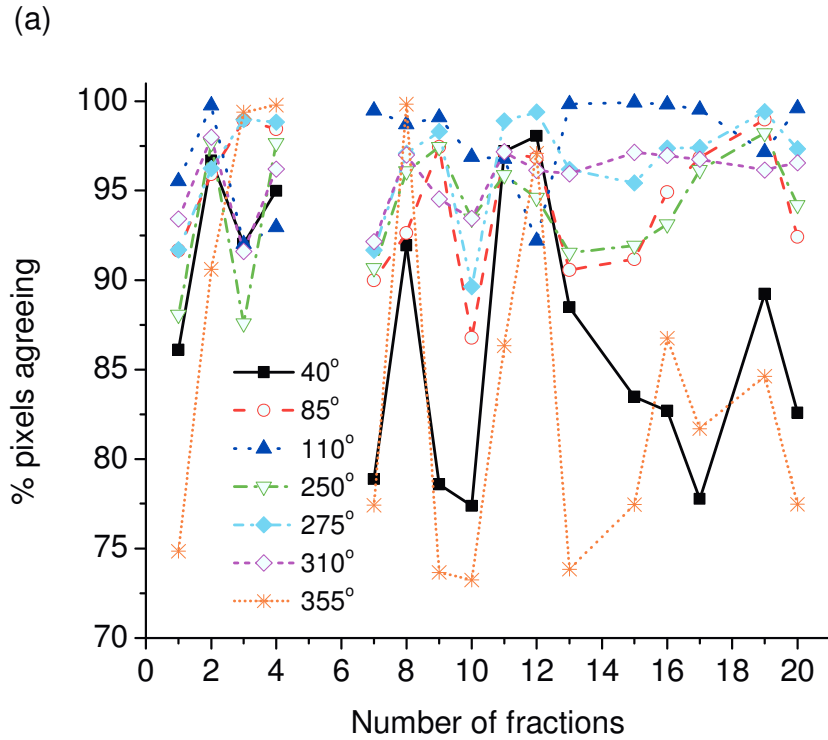
(b)



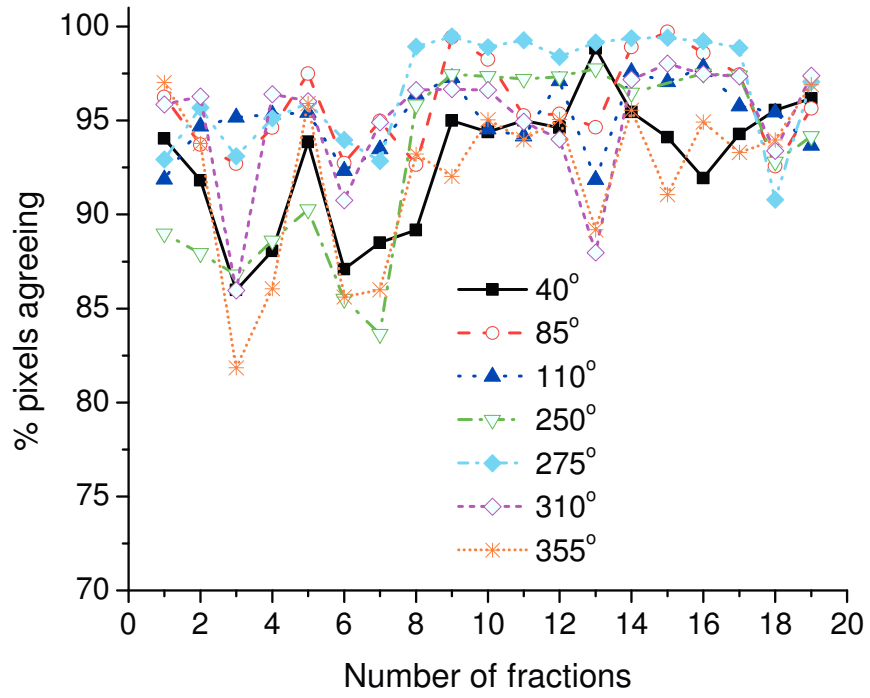
The rest of the prostate patients show similar characteristics as demonstrated in the case study (see Figure 6.4). Gas pockets and the moveable treatment couch create intra-fraction variation in all fields. The lateral beam angles without the couch in the path of the beam tend to provide more accurate χ -comparison results, as demonstrated by the percentage of pixels that agree in-field and shown in Figure 6.4. The average number of pixels that agree within 3% and 3 mm, over all fields and for each patient are 92.3% (the case study), 92.8%, 94.3%, 98.5% and 97.6%.

The results of the χ -comparison for the patient in Figure 6.4 (c) demonstrated poor agreement for three fields: gantry angle 153, fraction 8 (55.1% pixels agree); gantry angle 51, fraction 19 (49.8% pixels agree); and gantry angle 0, fraction 26 (49.0% pixels agree). These discrepancies were due to separate interrupted beam deliveries, where only part of a field was delivered to the patient before the beam was halted because of an interlock in the system. The interlock was then cleared and the rest of the beam was delivered to the patient. When the beam turns off, the EPID also turns off and collects no more data. Unless the EPID is manually turned on again, the remainder of the field delivery is not recorded by the EPID. Therefore, the resulting measured image contains only a portion of the true field delivered to the patient. If the image was manually acquired, the EPID could be turned on again to collect the remainder of the beam and the two images could be added together. This loss of data occurs infrequently (thrice out of 273 delivered fields for the patient in Figure 6.4 (c)).

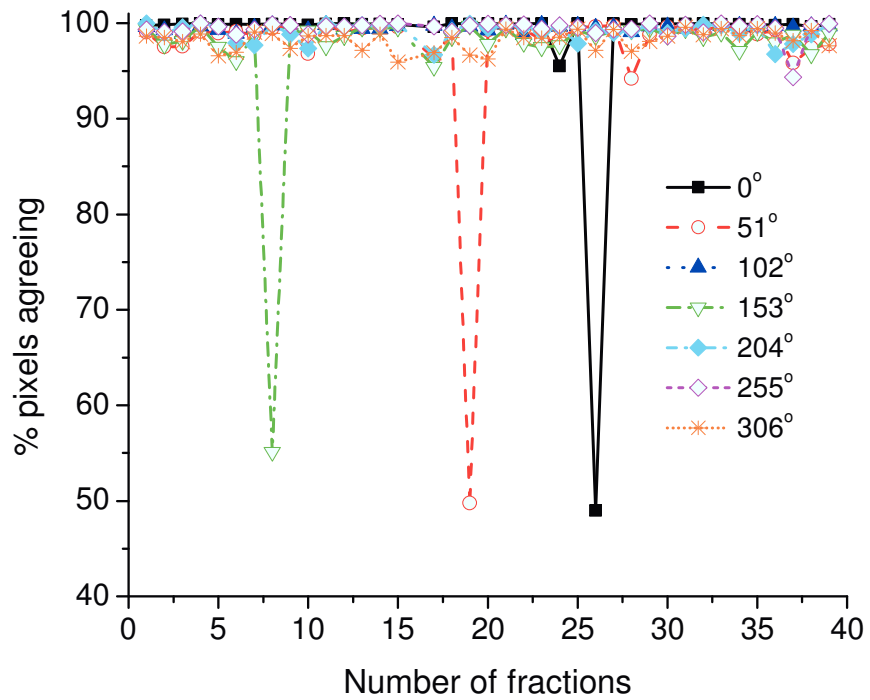
Figure 6.4 [Summary of Prostate Patients' Agreement]: Percentage of pixels that agree with the χ -comparison criteria (3%, 3 mm) for the prostate patients over all fractions, for each field, (denoted by gantry angle). Note the inter-fraction variability due to the effect of the treatment couch rails and rectal gas pockets.



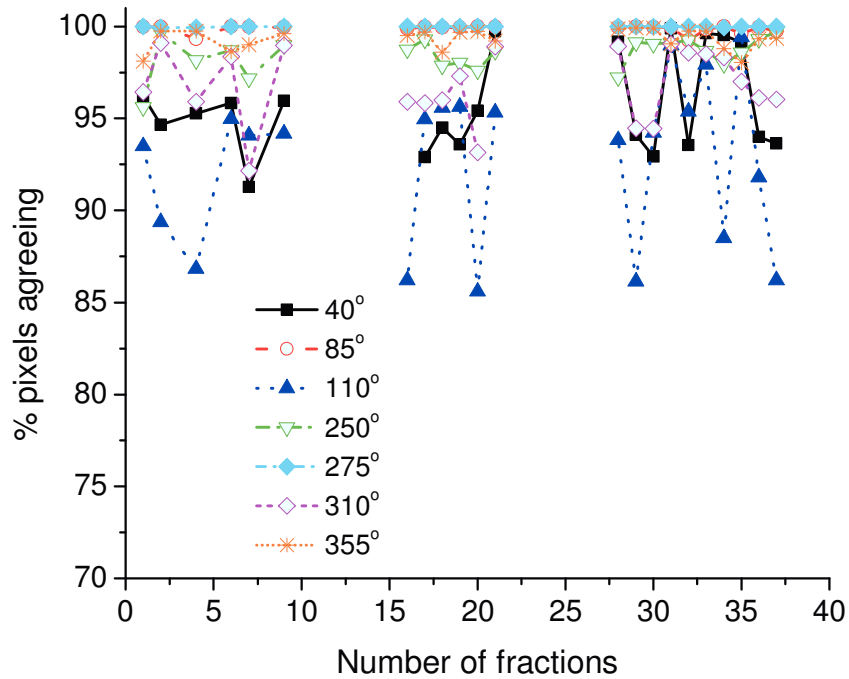
(b)



(c)



(d)



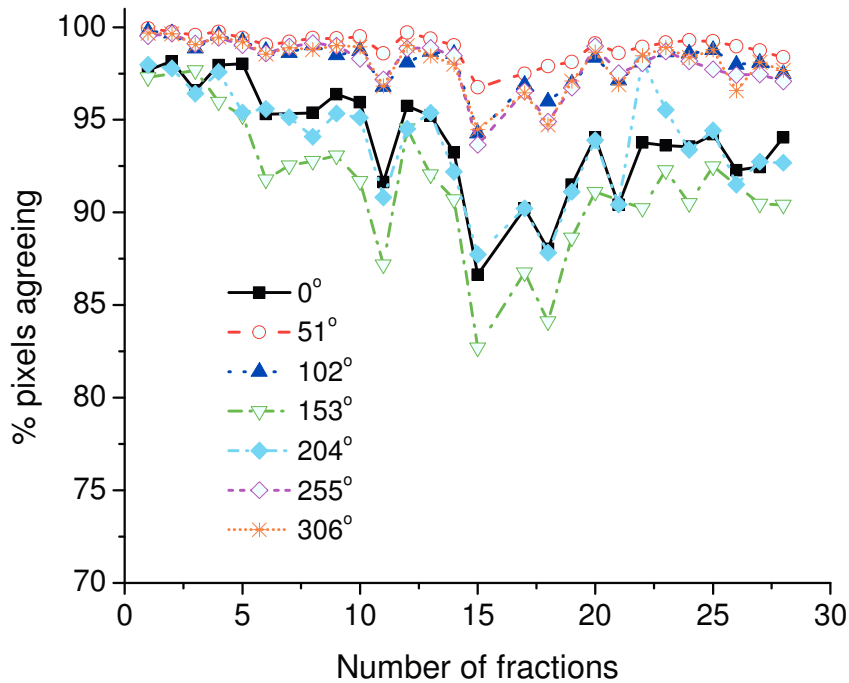
The measured data for the patient of Figure 6.4 (c) had the best agreement with prediction over all the patients. Excluding the three fields where the EPID turned off after a beam interlock, the fields agreed within at least 95%. This data was acquired more recently (December 2011 versus January 2008 to August 2009), in comparison to the other patient data, and after the error in the calibration was detected. This emphasizes the importance of routine, detailed EPID QA. Another explanation for the improved accuracy of the most recent patient dataset was that the patient was set-up using kilovoltage orthogonal images, as opposed to the megavoltage orthogonal imaging. The contrast of the KV imaging is superior to that of the MV imaging, thus it is possible that the set-up of the patient was more accurate.

6.3.2 Head and Neck Patients

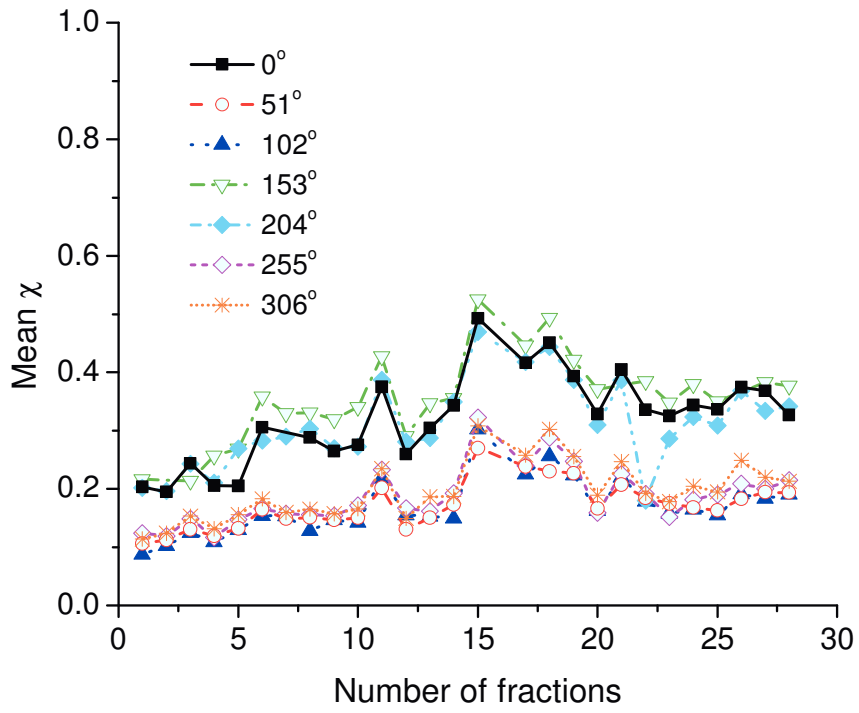
One head and neck patient is also examined in detail (see Figure 6.5). This patient does not show the same magnitude of variability between fractions as observed in the prostate patients. Figures 6.5 (b) and 6.5 (c) show that there is a general increase in measured dose over all angles with increasing fraction number (or time), corresponding to a decrease in the number of pixels agreeing within 3% and 3 mm as illustrated in Figure 6.5 (a). The percentage of pixels that agree within 3% and 3 mm, mean χ , maximum χ and mean percentage difference were determined to be 96.1%, 0.24, 7.34 and 3.61, respectively. Typically, as the treatment progresses, the measured image dose increases. This is especially pronounced at the edge of each field (see Figure 6.6) and is likely due to a reduction in the patient's weight. Weight loss during the course of treatment is common with head and neck patients since they typically develop feeding problems.

Figure 6.5 [Head and Neck Patient Case Study]: Comparison results of the head and neck patient case study for each field (denoted by gantry angle) and for each fraction. (a) is the percent of pixels that agree within 3% and 3 mm using the χ -comparison, (b) is the mean value of χ in-field (defined as $\geq 10\%$ of the maximum dose) and (c) is the maximum value of χ in-field. (d) is the mean percentage dose difference in-field. Note that the mean χ values (b) and mean percentage dose difference (d) tend to increase with fraction number, while the percentage of pixels that agree within 3% and 3 mm decreases with time. The maximum χ shows variability between fractions, likely due to the high modulation of the fields. The average number of pixels that agrees within 3% and 3 mm, over all fields, is 96.1%.

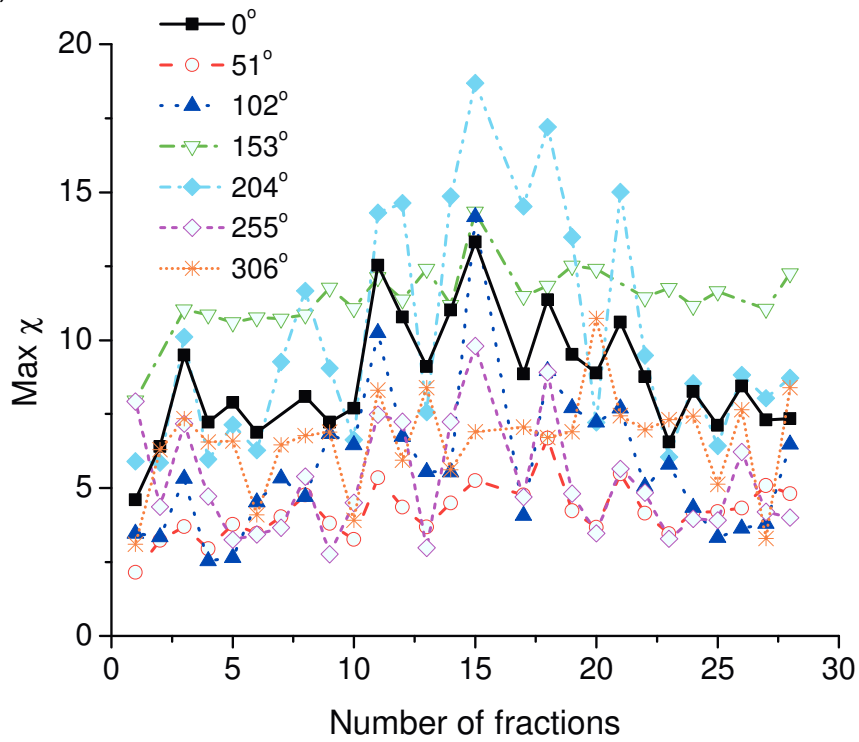
(a)



(b)



(c)



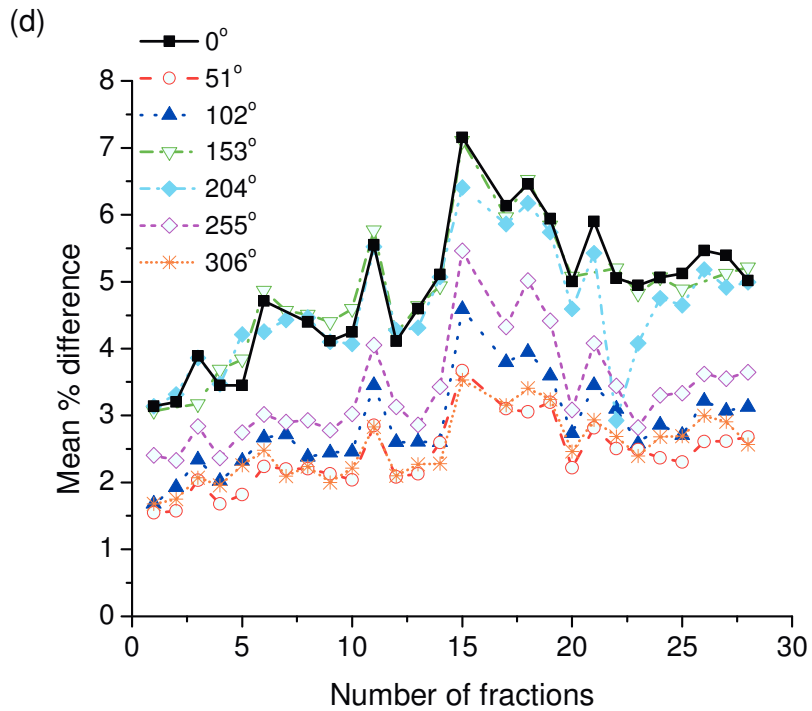
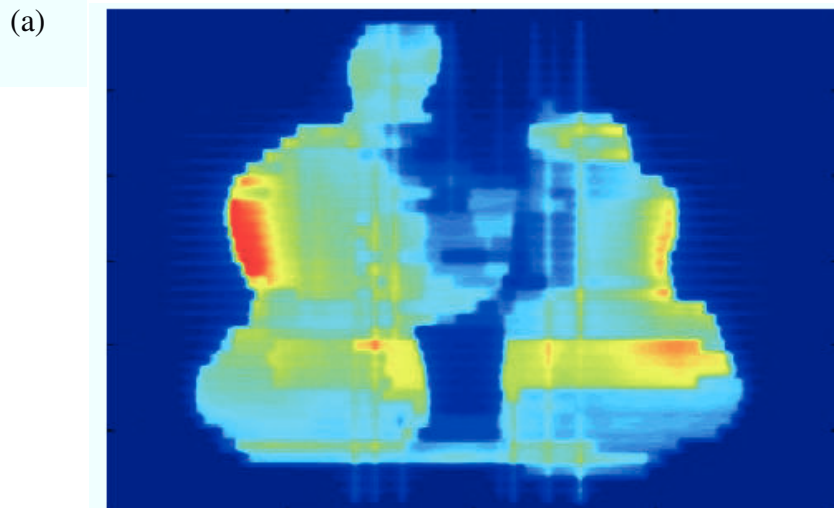
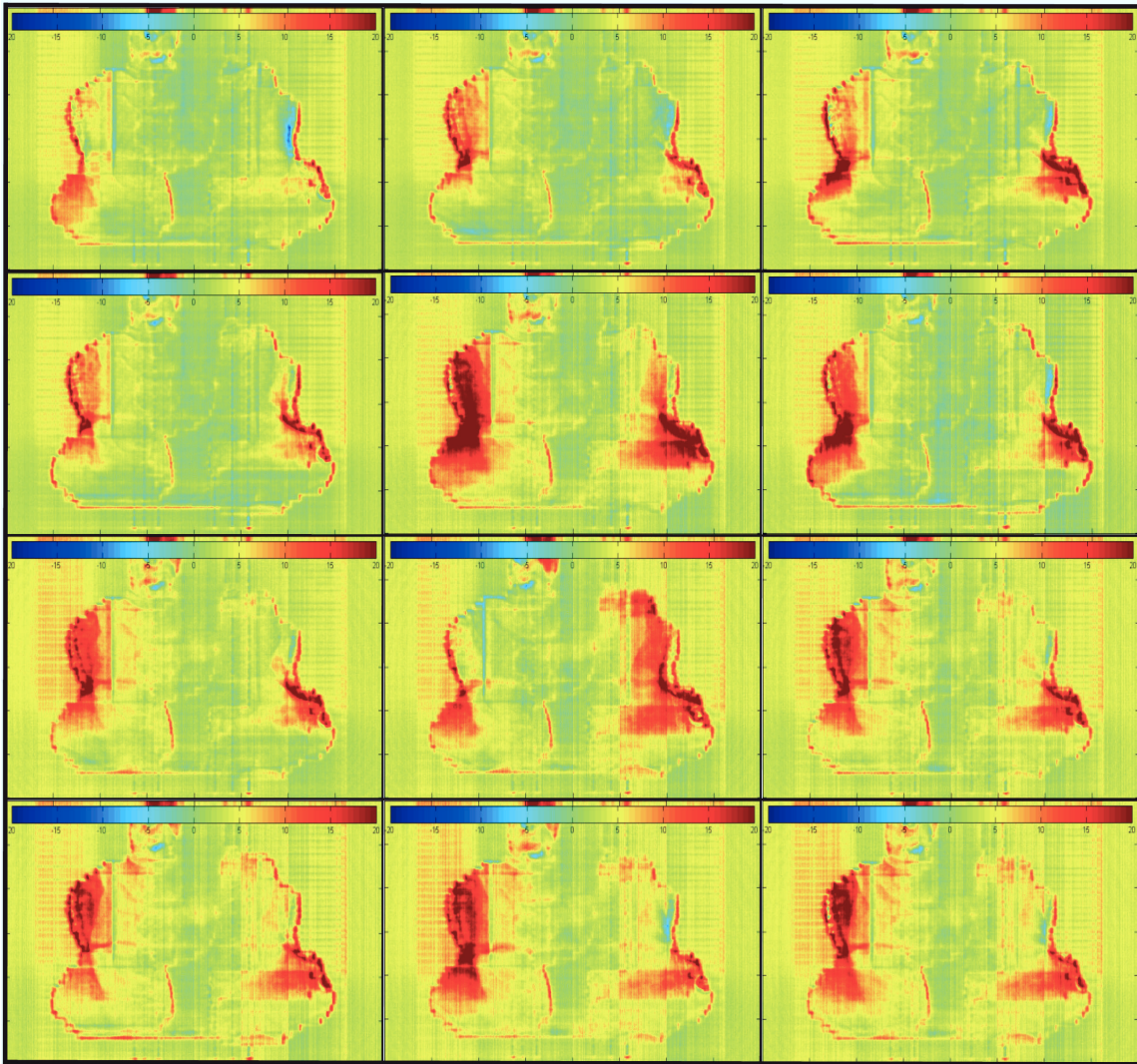


Figure 6.6 [Head and Neck Patient Percent Difference with Fraction]: (a) A predicted dose image for a head and neck field (gantry angle 0°) and (b) the percentage difference maps for twelve fractions (fraction 1, 2, 3, 4, 12, 13, 14, 24, 25, 26, 27, 28). Note the dark red area at the edges of the field, corresponding to a more than 20% underprediction of the model. The underprediction is likely due to increased transmission through the patient due to weight loss with time.

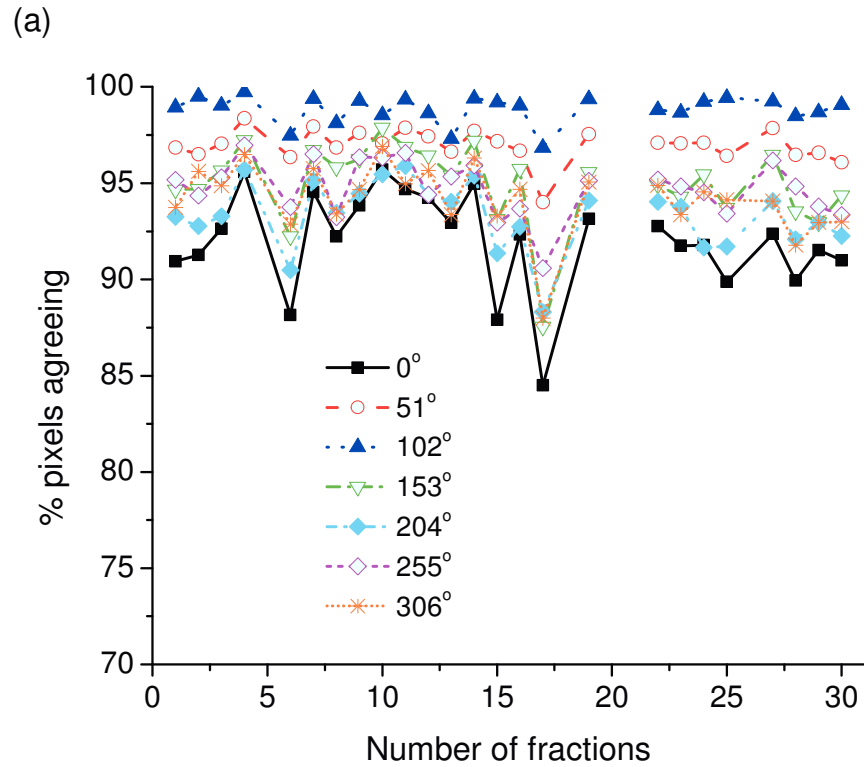


(b)

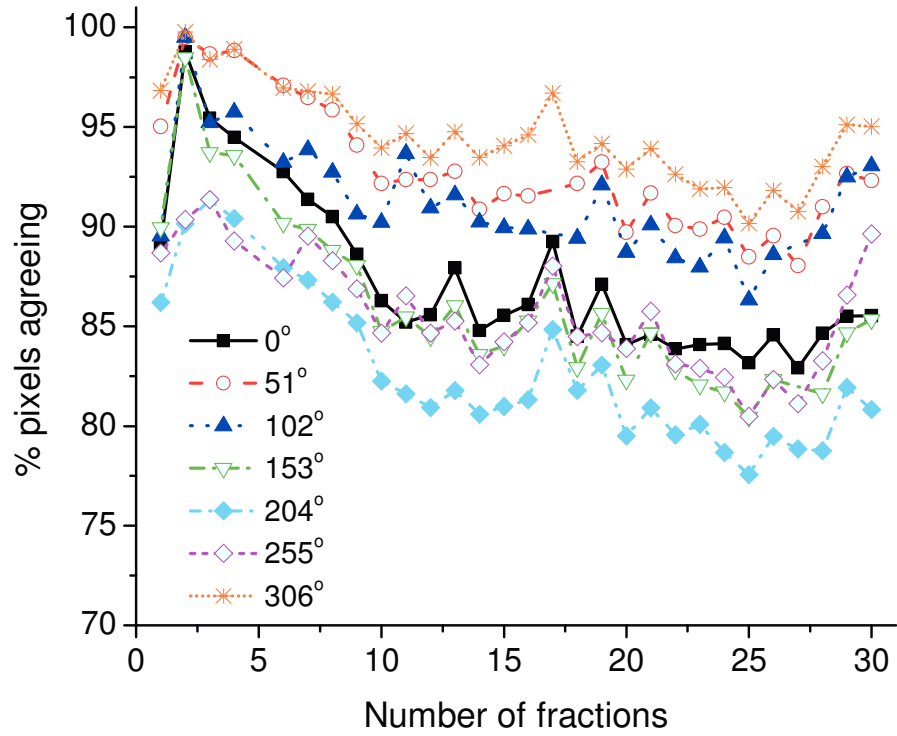


Most of the head and neck patient data illustrated in Figure 6.7 also show a decrease in percentage of pixels agreeing within 3% and 3 mm over time. Only the patient in Figure 6.7 (c) does not show the general trend of decreasing percentage of pixels agreeing with time. All percentage pixel values of the head and neck fields have an average of nearly 90% for each patient – demonstrating good agreement. The average number of pixels that agree within 3% and 3 mm, for each patient over all fields is 96.1% (case study patient), 95.0%, 88.6%, 91.0%, 90.7% and 91.1%.

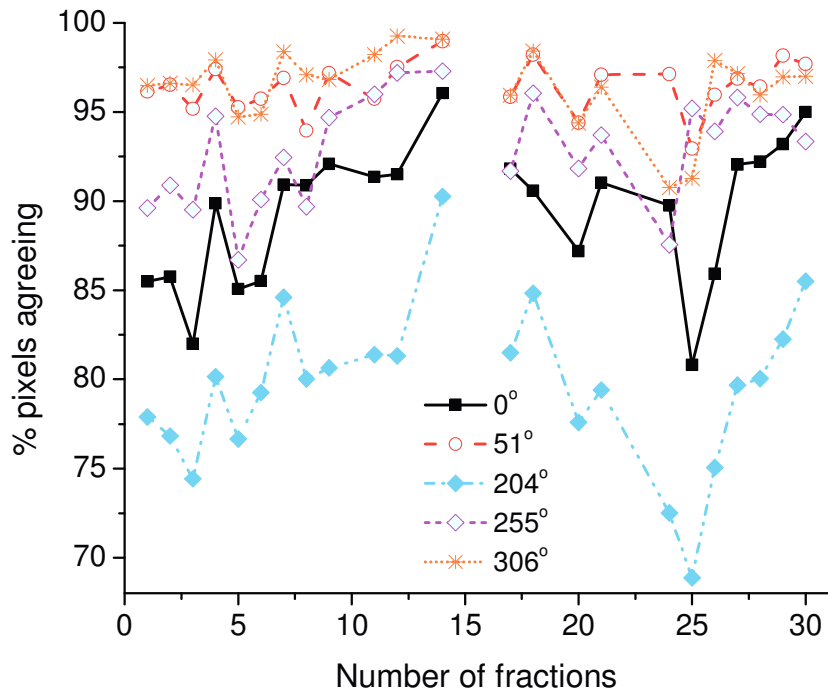
Figure 6.7 [Summary of Head and Neck Patients' Agreement]: Percentage of pixels that agree with the χ -comparison criteria (3%, 3 mm) for the head and neck patients over all fractions, for each field, (denoted by gantry angle). Note the trend to decreasing percentage of pixels agreeing for most patients, except for the patient data represented in (c).



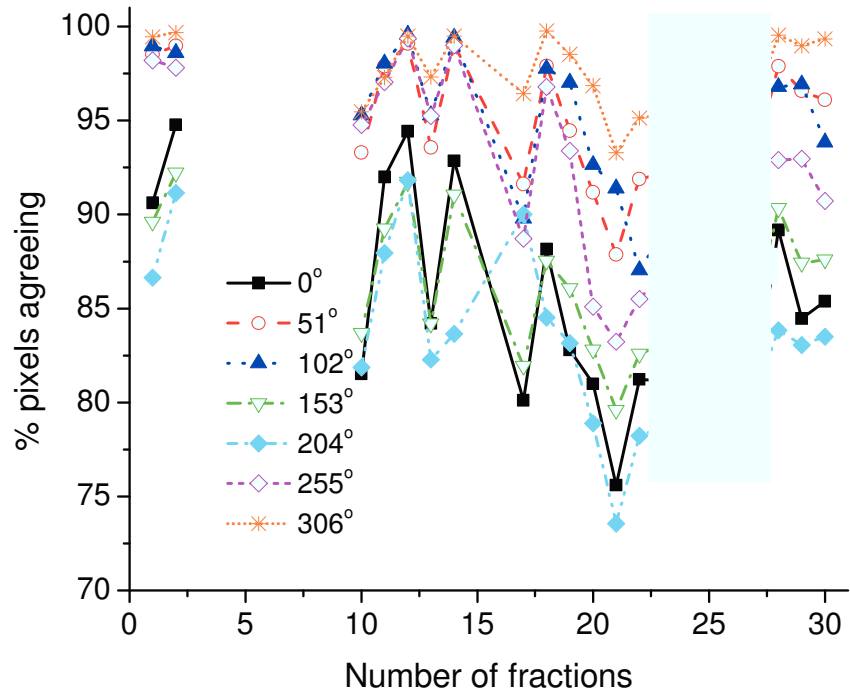
(b)



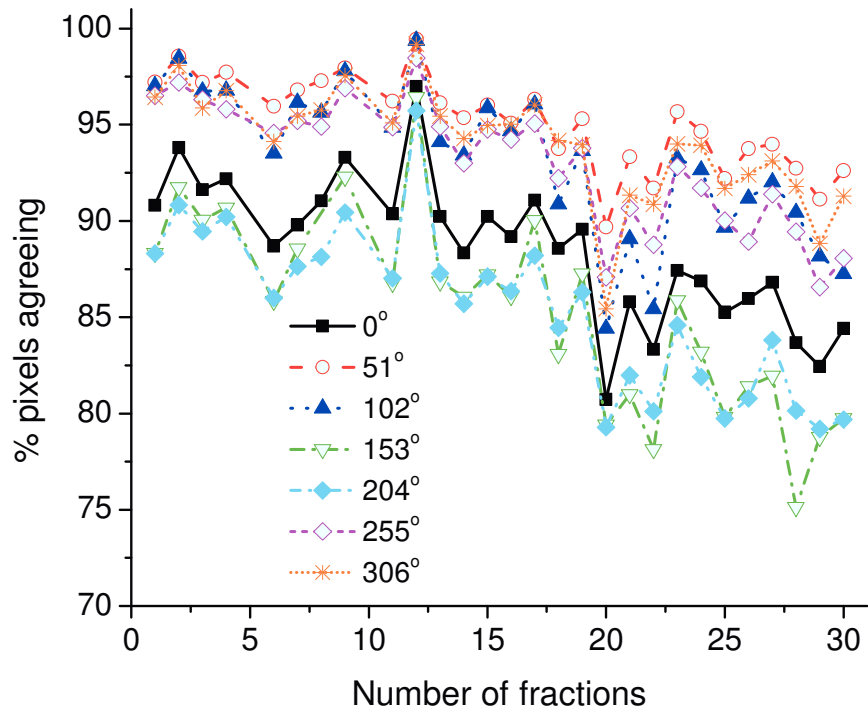
(c)



(d)



(e)



Most fields agree within 3% and 3 mm for more than 90% of the pixels in-field, while the mean χ value is typically less than 0.5.

Unlike the prostate patients, the couch did not have an effect on the results because the patient's immobilization device was cantilevered off the superior end of the couch, so that the treatment volume was not overlying the couch. Despite a general trend to an increased disagreement with increasing fraction number in the area at the periphery of the patient, there are exceptions to this. In Figure 6.5 (a), all fields in fractions 15 and 18 agree less than the fractions surrounding them. A possible explanation for this observation is a change in patient anatomy, such as patient motion after geometric verification or internal organ motion. This disagreement could be due to a change in patient anatomy, such as patient motion after geometric verification or possibly internal organ motion. Also, if a patient loses weight during a treatment, it's possible that their immobilization cast does not fit as well as it did during CT simulation, causing the patient to be more difficult to reproducibly set up. Additional on-treatment imaging, such as cone-beam CT, could help resolve these discrepancies.

6.5 CONCLUSIONS

The EPID dose image prediction algorithm developed previously in Chapter 5 has been applied to a large amount of clinical data with promising results. Most fields agree within 3% and 3 mm for more than 90% of the pixels in-field, while the mean χ value of the comparison between predicted and measured images is less than 0.5. Prostate images demonstrate a large amount of dosimetric variability between fractions due to the

presence of variable rectal gas pockets and the use of manually adjusted moveable rails on the treatment couch. Head and neck images show that the patients lost weight during the treatment period, illustrated by the trend of increasing measured dose signal with time.

Complex treatments would ideally be verified *in vivo* to ensure that a patient's treatment was accurate. This work demonstrates the types of patient anatomy changes that are detectable using the portal dose image prediction method, and could be used in the clinic to determine whether a treatment was delivered correctly. This work has provided us with valuable experience as we seek to implement this algorithm in our clinic in the near future. Important lessons learned in this work, that need to be considered for large-scale clinical implementation, include (1) the method needs to account for the treatment couch in order to remove this unnecessary source of inter-fraction variability, (2) the portal image acquisition during the treatment needs to be scheduled electronically and also additional training of the treatment floor therapists is helpful, in order to minimize the number of missed images and (3) a regular, rigorous quality assurance program for the EPIDs must be maintained to help ensure the highest quality imaging data.

With this useful initial clinical experience, we are confident that a large scale clinical implementation of the comprehensive portal dose image prediction algorithm developed in this thesis will proceed more efficiently and effectively.

REFERENCES

1. van Elmpt, W., McDermott, L., Nijsten, S., Wendling, M., Lambin, P., and Mijnheer, B., *A literature review of electronic portal imaging for radiotherapy dosimetry*. *Radiother Oncol*, 2008. **88**(3): p. 289-309.
2. Kroonwijk, M., Pasma, K. L., Quint, S., Koper, P. C., Visser, A. G., and Heijmen, B. J., *In vivo dosimetry for prostate cancer patients using an electronic portal imaging device (EPID); demonstration of internal organ motion*. *Radiother Oncol*, 1998. **49**(2): p. 125-32.
3. Pasma, K. L., Kroonwijk, M., Quint, S., Visser, A. G., and Heijmen, B. J., *Transit dosimetry with an electronic portal imaging device (EPID) for 115 prostate cancer patients*. *Int J Radiat Oncol Biol Phys*, 1999. **45**(5): p. 1297-303.
4. van Zijtveld, M., Dirkx, M., Breuers, M., de Boer, H., and Heijmen, B., *Portal dose image prediction for in vivo treatment verification completely based on EPID measurements*. *Med Phys*, 2009. **36**: p. 946-952.
5. van Zijtveld, M., Dirkx, M., Breuers, M., Kuipers, R., and Heijmen, B., *Evaluation of the 'dose of the day' for IMRT prostate cancer patients derived from portal dose measurements and cone-beam CT*. *Radiother Oncol*, 2010. **96**: p. 172-177.
6. McDermott, L., Wendling, M., Sonke, J., Vanherk, M., and Mijnheer, B., *Replacing Pretreatment Verification With In Vivo EPID Dosimetry for Prostate IMRT*. *Int J Radiat Oncol Biol Phys*, 2007. **67**(5): p. 1568-77.
7. McDermott, L., Wendling, M., Nijkamp, J., Mans, A., Sonke, J., Mijnheer, B., and Vanherk, M., *3D in vivo dose verification of entire hypo-fractionated IMRT treatments using an EPID and cone-beam CT*. *Radiother Oncol*, 2008. **86**(1): p. 35-42.
8. Wendling, M., McDermott, L. N., Mans, A., Sonke, J.-J., van Herk, M., and Mijnheer, B. J., *A simple backprojection algorithm for 3D in vivo EPID dosimetry of IMRT treatments*. *Med Phys*, 2009. **36**(7): p. 3310-21.
9. Mans, A., Remeijer, P., Olaciregui-Ruiz, I. g., Wendling, M., Sonke, J.-J., Mijnheer, B., van Herk, M., and Stroom, J. C., *3D Dosimetric verification of volumetric-modulated arc therapy by portal dosimetry*. *Radiother Oncol*, 2010. **94**: p. 181-187.
10. Mans, A., Wendling, M., McDermott, L. N., Sonke, J. J., Tielenburg, R., Vijlbrief, R., Mijnheer, B., van Herk, M., and Stroom, J. C., *Catching errors with in vivo EPID dosimetry*. *Med Phys*, 2010. **37**(6): p. 2638-44.
11. Ford, E., Terezakis, S., Yang, Y., Harris, K., and Mutic, S., *A quantification of the effectiveness of standard QA measures at preventing errors in radiation therapy and the promise of in vivo EPID-based portal dosimetry (abstract)*. *Med Phys*, 2011. **38**: p. 3808.
12. Williams, M. V., *Radiotherapy near misses, incident and errors: Radiotherapy incident at Glasgow Clin Oncol (R Coll Radiol)*, 2007. **19**: p. 1-3.
13. U. S. National Institutes of Health, *PROFIT - Prostate Fractionated Irradiation Trial*, 2006 www.clinicaltrials.gov/ct/show/NCT00304759.
14. Chytky, K. and McCurdy, B. M. C., *Comprehensive fluence model for absolute portal dose image prediction*. *Med Phys*, 2009. **36**(4): p. 1389-98.

15. McCurdy, B. M. C., Luchka, K., and Pistorius, S., *Dosimetric investigation and portal dose image prediction using an amorphous silicon electronic portal imaging device*. *Med Phys*, 2001. **28**(6): p. 911-24.
16. Deasy, J. O., Apte, A., Khullar, D., and Alaly, J., *The Computational Environment for Radiotherapy Research (CERR)*. 2010.

CHAPTER SEVEN: SUMMARY AND CONCLUSIONS

7.1 SUMMARY

Dosimetric verification of patient treatments is increasingly important because of the trend in radiation oncology towards more complex radiation therapy treatments, like intensity-modulated radiation therapy (IMRT) and volumetric-modulated arc therapy (VMAT). IMRT plans create dose distributions conformal to the tumour, necessitating the need for geometric and dosimetric accuracy during treatment. The treatments use elaborate computer software, which operate with very little technician interaction. There have been several radiotherapy accidents over the last decade using the new, computer-controlled treatment software, some due to technician error and some due to computer crashes or server transfer errors. Most cancer clinics verify IMRT treatments prior to a patient's treatment, but usually not during treatment.

Amorphous silicon portal imaging devices have been shown to be useful for dosimetric verification, particularly for IMRT. Several groups have investigated both pretreatment and *in vivo* methods of verification using a-Si imaging devices, and one research group in the Netherlands possesses extensive clinical experience in portal dosimetry. Their method depends on a series of empirical corrections to calculate the dose delivered to the patient during treatment via backprojection, using the measured EPID images. In this thesis, a physics-motivated, model-based method was developed to verify patient treatments both before treatment and during treatment within an accuracy of 3% dose difference and 3

mm distance-to-agreement. The advantage of physics-motivated modeling over correction-based empirical methods is in its robustness. This is the same advantage offered by physics-based patient dose models, such as the convolution/superposition method, in comparison to the previous generation of correction-based methods, such as the Batho method [1].

The accuracy of employing parallel dose kernels to calculate the dose delivered by an incident diverging fluence was examined in this thesis, with a focus on the accuracy of the EPID dose image calculation. Amorphous-silicon EPID-specific monoenergetic dose kernels of photon energies 0.1, 2, 6 and 18 MeV were generated using EGSnrc for incident angles ranging from 0° to 14° (the maximum angle to the edge of the detector). The theoretical dose calculation was carried out assuming an incident step function fluence, using convolution to calculate the dose due to the parallel (0°) dose kernels. To determine the dose using the tilted dose kernels, a superposition between the incident fluence and the kernels of the appropriate angles was carried out. A difference in dose of less than 1.0% between the results of the parallel and tilted dose kernels was detected for clinically relevant scenarios (i.e. detector distances over 140 cm from the source, with the largest field size possible of over 20x20 cm²) for all energies investigated. The time savings for using the convolution of the parallel dose kernels over the superposition with the tilted dose kernels was large – a factor of ~6000 (10.5s vs. 18h). This investigation, therefore, validated the use of parallel dose kernels for the EPID dose calculation due to the significant time savings for little loss in accuracy.

A comprehensive fluence model was created to determine the fluence incident on the EPID, which was used to calculate the dose delivered to the EPID for open-field beams (i.e. no patient or phantom in the beam). The fluence model was based on the Pinnacle Treatment Planning System fluence model, with several modifications determining parameters of the model through the use of Monte Carlo simulation. The fluence model developed here consisted of two sources – a focal Gaussian and an extrafocal Gaussian-like function, with respective full-width half-maxima. The fluence model also accounted for several aspects of the multileaf collimator, such as the transmission through the leaves, the rounded leaf-tips, the tongue-and-groove effect and interleaf leakage. The photon energy spectra for the independent focal and extrafocal fluences were determined using Monte Carlo simulation, with only the focal spectrum being softened off-axis. The EPID dose image was calculated using a series of monoenergetic, parallel dose kernels that were convolved with the fluence. Adjustable parameters of the model were determined by matching the predicted EPID dose images to corresponding measured images for square MLC-defined fields ranging from 1x1 to 20x20 cm². The portal dose image prediction algorithm calculated absolute IMRT fields for prostate and head-and-neck treatment plans, with no material in the beam, within an accuracy of 2% and 3 mm, creating a suitable method for pre-treatment dosimetric verification.

The next step required to predict portal dose images during patients' treatments was a method to accurately incorporate the photon scatter generated in the patient and incident on the EPID. Previous work at CancerCare Manitoba examined the use of a library of Monte Carlo-calculated scatter fluence kernels, dependent on radiological pathlength and

air gap. This patient scatter model was tested with measured, simple open-field fluence profiles to predict EPID dose images, acquired with a variety of phantoms in the beam. The existing patient scatter model, improved and updated with results using newer BEAMnrc simulation software, was integrated with an improved comprehensive fluence model. The fluence model was adapted to include many aspects of the manufacturer's schematics of the MLCs, reducing the overall number of parameters that could be adjusted during the commissioning stage. The entire portal dose image prediction model, including the combination of the comprehensive fluence and patient scatter models was able to predict measured images acquired for a wide range of condition to within +3% and -2%. The conditions included: with slab phantoms in the beam (ranging in thickness from 2-37 cm), over a range of field sizes (1x1 to 20x20 cm²) and over a variety of air gaps (15-50 cm). To minimize the variation among field size, air gap and phantom thickness, a series of calibration factors was determined and used as a look-up table when converting the predicted and measured images to calibrated units. The results of the portal dose image prediction model were then compared to images taken with prostate and head-and-neck IMRT fields delivered to slab phantoms, resulting in successful predictions within 3% and 3 mm.

The development of the full portal dose image prediction model was followed by a study applying the method to dosimetric verification of several IMRT patient treatments. Measured images acquired for each field for most fractions of five prostate and six head-and-neck patients were analyzed. The CT dataset of each patient was converted to an equivalent homogenous phantom to enable the patient scatter calculation. The portal dose

image prediction model was able to accurately predict fields, generally within 3% and 3 mm of the measured images. The largest discrepancies observed in the prostate patient images were determined to be due to variable gas pockets in the rectum and the effect of the support rails on the treatment couch (bed). A common discrepancy discovered in the head-and-neck patients was likely the result of patient weight loss and was most commonly seen at the edge of the fields as an increase in measured dose.

7.2 CONCLUSIONS

In this thesis, a model-based algorithm was developed that was able to calculate the fluence for complex IMRT fields and convert that fluence into a predicted portal dose image prediction. The fluence was used to accurately predict open-field IMRT treatment fields delivered to an a-Si EPID, which can be used for pre-treatment dosimetric verification. The fluence model was then combined with a patient scatter prediction model to enable portal dose image prediction of patient treatments and therefore can be used as a method of *in vivo* dosimetric verification. A rigorous EPID QA program is required to ensure the measured EPID images are of high quality.

This portal dose image prediction model is versatile and can be implemented in any clinic. All that is needed is manufacturer specifications of both a linac and EPID and access to a Monte Carlo simulation software to model both the linac fluence and EPID dose response (i.e. dose kernels). EGSnrc is available on-line and is quite user-friendly. The algorithm can read in exported treatment plans, including CT data, from both Pinnacle and Eclipse, two most common TPSs. Although the work here used a Varian

Clinac iX and an aS1000 EPID, with a 6 MV beam, the portal dose image prediction model can be commissioned for other linacs, EPIDs and energies. All that is required is a measured commissioning dataset similar to that described in Chapter 4 - open, MLC-defined fields ranging from 1x1 cm² to 20x20 cm² delivered to the EPID using the desired energy, and manufacturer schematics of the linac head and EPID.

7.3 FUTURE WORK

A versatile, physics-motivated fluence model has been successfully integrated with an existing patient scatter prediction model to create a portal dose image prediction model that can be utilized to dosimetrically verify patient treatments, *in vivo*. This tool could be used in the clinic to assist in determining whether a patient's treatment was delivered correctly, by calculating the predicted image prior to treatment and using the quick χ -comparison to determine whether the measured and predicted images agree within a specified tolerance. There are some improvements to the model and data acquisition required before large-scale clinical implementation: (1) account for the treatment couch and rail positions, (2) automate the acquisition of the measured images and provide training to the radiation therapists, in order to limit the number of missed images and (3) frequent EPID quality assurance to ensure the obtained patient data is of high quality.

This model can also be easily adapted for verification of treatments that require different photon energies or treatment techniques. Prostate 3D-CRT treatments (which use a photon beam energy of 18 MV) can be easily predicted with the creation of an 18 MV fluence model. This would require an accurate 18 MV Monte Carlo model and measured

18 MV images acquired with the EPID for commissioning. Acquiring 18 MV images may require additional build-up material to be placed on the EPID to ensure charged-particle equilibrium is achieved. Collaborators at the Newcastle Mater Hospital in Newcastle, NSW, Australia have collected 18 MV prostate patient images to test with our model. An undergraduate student is currently establishing an 18 MV fluence model by which to predict the EPID images.

The portal dose image prediction model may also be extended to predicting images from VMAT treatments that are acquired in *cine* acquisition mode, rather than integrated acquisition mode. *Cine* mode, also known as ‘movie’ mode, captures multiple images throughout a treatment and provides time-dependent images of a treatment beam. This is in contrast to the ‘integrated’ image mode which acquires multiple images (or frames, in this case) but averages the frames into a single image for a single beam, thus integrating the entire dose delivered to the imager over the beam’s irradiation. VMAT is a dynamic treatment mode with the gantry moving during beam delivery, so there are no individual fields – simply one, continuous rotating beam. Calculating the predicted image at numerous control points around the patient as a function of gantry angle (or delivered MU) and comparing to images collected in cine mode will allow *in vivo* dosimetric verification of VMAT treatments.

This model may also be used for three-dimensional patient dose reconstruction. The primary focal fluence entering the EPID can be determined from a measured image by removing (from the measured image) the dose contributed by patient scatter, optical

photon glare, backscatter dose and extrafocal dose, as obtained by prediction through the full-forward calculation described in this thesis. This leaves only the measured image due to the focal fluence. The predicted focal fluence (from the forward prediction) is then adjusted pixel-by-pixel to match the measured focal dose image and obtain a measured focal fluence. The focal fluence is then backprojected to a plane above the patient's CT dataset, where the extrafocal fluence (again, from the forward prediction) is reintroduced. Using the combined focal and extrafocal fluence, the three-dimensional dose in the patient is calculated and compared to dose distributions from the TPS. The treatment could then be adapted in subsequent fractions to account for any delivered overdose or underdose. Incorporating cone-beam CTs acquired daily would account for any changes in the patient anatomy that have occurred since the planning CT was obtained and for day-to-day internal organ motion (but not including intra-fraction motion). Taking advantage of deformable registration, one could map daily patient dose onto the patient's CT simulation data set. The resulting patient dose reconstruction then represents an estimate of the actual delivered patient dose.

The modeling developed in this thesis will allow the exciting research projects described here to be realized.

REFERENCES

1. Mackie, T.R., Reckwerdt, P., McNutt, T., Gehring, M., and Sanders, C., *Photon Beam Dose Calculations*, in *Teletherapy: Present and Future*, Mackie, T. R. and Palta, J. R., Editors. 1996, Advanced Medical Publishing: Madison, WI. p. 103-135.

CHAPTER EIGHT: APPENDIX

8.1 HOW TO TAKE IMAGES WITH AN AS1000 EPID

1. Open the “AM Maintenance” software at the console on the OBI (on-board imaging) control computer.
2. Ensure that calibration files (flood-field and dark-field images) for the imager, for “Integrated” mode and for the desired energy and dose rate, have loaded into the software. You should be able to select the “Image” button in the window if the calibration files have loaded – the message below the “Image” button will say “Waiting for beam” if the imager is ready to collect data for an image. Otherwise, “Image” will be greyed out and you cannot select it.

If the calibration files have not loaded:

- a. Press the “Dark field” button to retrieve a dark signal calibration image. The panel is not to be irradiated while obtaining this image.
- b. To collect the flood-field image, move the imager to the height you will be most likely to use it at, press “Flood-field” and irradiate the panel with a field that covers the entire panel but does not irradiate the electronics. For example, if the EPID is at a distance of 150 cm, the magnification factor of $(100/150=1.5)$ indicates that a field of $26.7 \times 20 \text{ cm}^2$ will just cover the $40 \times 30 \text{ cm}^2$ EPID detector area.

c. Save these calibration images by selecting “Save calibration files”.

3. Load the plan and field you wish to deliver to the EPID, press “Image” and turn on the beam. The EPID image will appear when the beam turns off. This image is an average over all the frames collected while the EPID was on. To obtain the total integrated EPID image, multiply the image by the total number of frames (displayed under the “Image” button when the image is finished).

4. If the beam is interrupted during irradiation, the remaining beam irradiation can be collected with a second image. The two images can be combined by adding together the individual total integrated images (i.e. resulting image multiplied by the number of frames), and then divided by the sum of the frames for both images. This step cannot be done within the AM Maintenance software, but can be accomplished with user-created software if it has the ability to read the EPID images. The images are in DICOM format.

8.2 MONTE CARLO SIMULATION

This section is to serve as an addition with more detail on general Monte Carlo modeling than Section 2.1.4 provides. For further detail, please see References 1 and 3.

Monte Carlo simulation is considered the ‘gold standard’ of radiation transport modeling because it is able to accurately model the probabilistic and complex nature of photon interaction and dose deposition [1]. The paths of individual particles are simulated by using pseudo-random numbers to sample probability distributions (e.g. interaction cross-

sections and mass-attenuation coefficients) that describe the physical processes acting on the particles. The random numbers are referred to as pseudo-random because they are computer-generated as opposed to pure random numbers derived from natural processes like radioactive decay. By using a large number of histories (or incident particles), one can calculate accurate, meaningful quantities such as dose deposited, fluence or other dosimetric-related quantities. Monte Carlo simulation also allows the user to calculate quantities that cannot be easily measured or impossible to measure, such as what fraction of photon fluence is due to scatter within the linac treatment head.

In the following sections, the major photon and electron interactions modeled by Monte Carlo simulation will be discussed, as will the basic Monte Carlo algorithm and the accuracy of EGSnrc.

8.2.1 Photon Interactions

The following discussion is based on Chapter 7 of the textbook “Medical Radiation Physics” by F.H. Attix [2].

Photons are a type of indirectly ionizing radiation, meaning that photons do not deposit energy in media but the secondary particles that result from their interactions do. Photons undergo three main interactions by which dose is deposited in the tissue: the Compton effect, the photoelectric effect and pair production. Each type of interaction is dominant for different combinations of photon energy and media atomic number.

At low energies (below 1 MeV), the most common photon interaction is the photoelectric effect. In this process, the photon is absorbed by an atom and a photoelectron is ejected, if the energy of the photon is greater than the binding energy of the electron. Therefore, there is a threshold for this interaction to occur. The mass-attenuation coefficient for the photoelectric effect ($\frac{\tau}{\rho}$) is dependent on photon energy ($h\nu$) and atomic number of the material (Z) it is interacting in, via:

$$(8.1) \quad \frac{\tau}{\rho} \propto \frac{Z^3}{(h\nu)^3}.$$

That means that the photoelectric effect is dominant at both low incident photon energy and in high atomic number material. The ejected photoelectron leaves a vacancy in the atom's electron shell.

With high energy photons (above a few MeV), the pair production effect is much more likely to occur. In pair production, the photon interacts with the nuclear field of the atom, then is absorbed and creates an electron-positron pair. This interaction also creates a vacancy in the electron shell of the atom. Pair production requires a threshold energy in order to occur – the energy for an electron and a positron to be created, or the rest mass of both ($2 \times 0.511 \text{ MeV} = 1.022 \text{ MeV}$). A variation of pair production, triplet production, can occur when a photon interacts with a tightly-bound electron, creating two electrons and a positron. The probability of pair production occurring ($\frac{\kappa}{\rho}$) is also dependent on atomic number of the material:

$$(8.2) \quad \frac{\kappa}{\rho} \propto Z.$$

Therefore, pair production is more prevalent in high atomic number materials and at energies above the threshold energy.

The Compton effect is the most prevalent interaction that occurs in the radiotherapy energy range (approximately 0.1 MeV to 10 MeV for tissue-equivalent materials). In a Compton scattering event (also known as incoherent scatter), a photon interacts with a loosely-bound electron (the binding energy is assumed to be negligible), creating a scattered electron and a scattered photon. The scattered photon is free to interact once again. The likelihood of the Compton effect occurring is independent of atomic number and the mass-attenuation coefficient ($\frac{\sigma}{\rho}$) is defined as:

$$(8.3) \quad \frac{\sigma}{\rho} = \frac{N_A}{A} \cdot Z \cdot \sigma_e,$$

where N_A is Avogadro's number ($6.022 \times 10^{23} \text{ mol}^{-1}$), A is the atomic mass of the material and σ_e is the electron attenuation coefficient, based on the electron density of the material.

When a photon scatters off a bound electron but does not lose energy, the effect is called Rayleigh (or coherent) scattering. This effect is more prominent with low energies as the probability of Rayleigh scattering is inversely proportional to $(h\nu)^2$. Rayleigh scattering will not remove electrons from atomic shells during the interaction and therefore does not contribute to dose deposition.

The mass-attenuation coefficients are related to the differential interaction cross-sections of the photons. Therefore, in rudimentary terms, the probability, $\frac{\mu}{\rho}$, of a photon interacting is the sum of the individual mass-attenuation coefficients (ignoring Rayleigh scattering):

$$(8.4) \quad \frac{\mu}{\rho} = \frac{\sigma}{\rho} + \frac{\tau}{\rho} + \frac{\kappa}{\rho}.$$

The probability, P , of a photon not interacting is then:

$$(8.5) \quad P = 1 - \frac{\mu}{\rho}.$$

Monte Carlo simulations can be based on such a simplification if one wants to calculate a value such as transmission, but Monte Carlo software packages are more detailed and utilize more complicated equations to derive the secondary particles' direction, energy and the interaction probability of the incident photon [3].

8.2.3 Electron Interactions

This section is based on Chapter 8 of the textbook “Medical Radiation Physics” by F.H. Attix [2].

The dose deposition that occurs in radiation transport is caused by the transfer of energy from energetic charged particles (e.g. electrons) to tissue. As energetic electrons travel through matter, they are considered to be continuously losing energy through inelastic collisions with atomic electrons, leaving the atom with a vacancy by transferring energy to an electron that is then ejected (an effect caused by “knock-on” electrons). The atom

can also be left in an excited state. Elastic collisions with nuclei result in no energy loss from the electron, but can change the direction the electron travels.

Electrons also lose energy through interaction with the atomic nucleus, through which a photon is created. This radiative process is referred to as bremsstrahlung and creates a spectrum of photons with the maximum energy being the energy of the interacting electron.

Positrons will annihilate with electrons to create two 'annihilation' photons, each of energy 0.511 MeV if the positron is at rest. If the positron is still energetic, the photons will have a combined energy of 1.022 MeV plus the kinetic energy of the positron.

The vacancies left in the atom by the loss of an electron through any of these interactions can be filled from an electron from a higher shell. There is a net energy difference between the two electron shells, creating a fluorescent x-ray with an energy equal to the net energy difference. The net energy difference can also be transferred to another electron, with the energetic electron being ejected from the atom in the Auger effect. These resultant effects of photon interactions occur until the atom is not in an excited state.

For more details on photon and electron interactions, please refer to Reference 2.

8.2.2 Monte Carlo simulation algorithm and particle transport

The following discussion is based on Chapter 5 of “The Dosimetry of Ionizing Radiation” [1].

8.2.2.a Photon transport

When simulating photon transport in a Monte Carlo algorithm, there are three probability results that need to be determined: 1) the distance to the next photon interaction, 2) what interaction occurs and 3) what is the energy and angle of the result.

If the energy of a tracked photon is greater than the photon cutoff energy (default value for EGSnrc is 0.01 MeV), the photon will not be tracked anymore. That is, the photon’s remaining energy will be deposited in the local voxel. While above the cutoff energy, the energy, location and direction of the photon are all tracked, and the distance to the next photon interaction is calculated by solving the linear attenuation equation for thickness, x :

$$(8.6) \quad x = -\frac{1}{\mu} \cdot \ln(T),$$

where μ is the total linear attenuation coefficient for all photon interactions (dependent on photon energy and material) and T is the transmission (a value between 0 and 1). Replacing T with a random number (also between 0 and 1) generated by the software, the distance to the next interaction is determined. After the distance is determined, a check to ensure that the photon has not left the volume that is being simulated is carried out. If the photon has left the simulation volume, the photon is not tracked anymore.

To illustrate how the type of photon interaction is determined, let us consider a situation where only two photon interactions are possible – Compton scattering and the photoelectric effect. Then:

$$(8.7) \mu = \sigma + \tau$$

is the definition of the total linear attenuation. Another random number is generated by the software and if:

$$(8.8) R \leq \frac{\tau}{\mu},$$

the interaction is due to the photoelectric effect. Otherwise, a Compton scatter occurs.

The last result that needs to be determined is what the energy and direction of the resulting particles are. This is resolved with the generation of random numbers that are input into differential cross-sections for the interacting photon process. The distance to interaction of the resulting photon, if a Compton effect occurs, is then carried out and the process repeats itself until all histories are terminated through the exiting of the volume or with energies below the cutoff energy. The resulting electrons are passed to the electron transport area of the code.

8.2.2.b Electron transport

Electrons undergo a large number of elastic scattering events after being created or knocked out of an atom. Following the scattering of each electron one would drastically increase the total computation time for Monte Carlo simulation. To overcome this obstacle, EGSnrc (and other Monte Carlo codes) use what is called a ‘condensed history’ method. In this technique, large numbers of collision interactions are condensed into a

single step – which is user-defined and represents the fractional energy lost due to the continuous loss of energy (the default value is 0.25) [3]. The effect of the individual interactions is taken into account by sampling the energy and angular deflection of the condensed group from multiple scattering probability distributions.

The electron transport processes determined by random number sampling are: 1) the distance to a discrete electron interaction, 2) the change of direction brought on by multiple scattering, 3) which discrete interaction occurs (knock-on electron or bremsstrahlung photon) and 4) what energy and direction the resultant particle possesses. The electron processes are determined with random numbers, similar to the examples given for photon transport but with different probability distributions to sample against. If the electron leaves the volume or loses energy below the cutoff energy (EGSnrc default value is 0.521 MeV), the electron is not tracked and the history is terminated.

After the multiply scattered photon deflection is calculated, the energy lost along that pathlength is calculated with the collisional stopping power coefficient for the particular electron energy.

8.2.3 EGSnrc accuracy

The following discussion is based on Chapter 5 of “The Dosimetry of Ionizing Radiation” [1].

The accuracy of Monte Carlo results for radiation therapy are typically reported as the statistical uncertainty of the dose results, which decreases with an increase in the number of histories, of the results. However, this estimate of uncertainty does not consider systematic errors. Systematic uncertainties that could be present in the EGSnrc code system can be grouped into four categories: 1) the cross-section data used to determine the probability of interactions, 2) the actual algorithms of the software, 3) creation of the geometry that the Monte Carlo simulation takes place and 4) the analysis and verification of the results.

For energies and media where photoelectric cross-sections dominate (specifically in this thesis, in the phosphor of the EPID dose kernels for low-energy photons), an uncertainty of 3-5% is observed in calculations. As stated previously, radiotherapy applications are dominated by the Compton effect. The Compton scatter cross-sections used in EGSnrc are accurate to within 2-3%, and could be as accurate as 1% for low-Z materials. Pair production cross-sections in EGSnrc is accurate to approximately 5%.

Inelastic electron interaction cross-section data are accurate to within 1-2% for energies above 0.1 MeV. At lower energies, the accuracy ranges from 2-3% for low-Z media and 5-10% for high-Z materials. In EGS4, radiative stopping power cross-sections were accurate to 5% below 2 MeV, and to 2-5% above 2 MeV [1]. With the introduction of EGSnrc and subsequent revisions, the accuracy of the radiative cross-sections have been updated and are more accurate, but to an unreported value [3].

Other uncertainties in the results of the Monte Carlo simulation could be due to systematic errors such as programming errors, modeling inaccuracies in the analytic components of the algorithm and truncation errors.

Statistical uncertainty of simulations can be reduced by increasing the number of histories calculated by the software. The statistical uncertainty is proportional to $N^{-1/2}$, where N is the number of histories simulated [3]. For the use of Monte Carlo simulation in this thesis, all dose uncertainties were $\ll 1\%$ of the maximum dose.

8.3 COMPARISON AND EVALUATION OF DOSE DISTRIBUTIONS

Traditionally, two dose distributions were compared using percentage difference, regardless of whether the distributions consisted of two measured, two calculated or one measured and one calculated dataset. This technique was sufficient when treatments were not modulated and the only steep dose-gradient regions were on the edge of the field in the penumbra areas.

With the introduction of IMRT into the treatment regimen, the standard percentage dose difference method was no longer acceptable to characterize the discrepancies in high dose-gradient regions. Van Dyk *et al.*[4] proposed an approach which separated the dose distributions into low dose-gradient ($<30\%$ /cm) and high dose-gradient ($>30\%$ /cm) regions. The low dose-gradient regions employed the conventional percentage dose difference between the dose distributions while in the high dose-gradient regions, the maximum distance-to-agreement (DTA) between points was measured.

Low *et al.*[5] devised a calculation method to incorporate both percentage dose difference and DTA into a single metric, referred to as the γ -evaluation. An ellipsoid, defined by

$$(8.9) \quad 1 = \sqrt{\frac{\Delta r^2}{\Delta d_M^2} + \frac{\Delta D^2}{\Delta D_M^2}},$$

where ΔD_M is the maximum dose difference and Δd_M is the maximum DTA, is created around each reference point (r_r, D_r) . $\Delta r = |r_r - r_c|$ is the distance and $\Delta D = D_c(r_c) - D_r(r_r)$ is the dose difference between the reference point and comparison point (r_c, D_c) . Each point in the comparison dataset is evaluated to determine if it falls within the “acceptance ellipsoid”, which is defined as:

$$(8.10) \quad \Gamma(r_c, D_c) \equiv \sqrt{\frac{\Delta r^2}{\Delta d_M^2} + \frac{\Delta D^2}{\Delta D_M^2}} \leq 1.$$

$$\gamma = \min(\Gamma(r_c, D_c))$$

If the value of γ is less than 1, then the comparison point agrees with the reference point within the predetermined ΔD_M and Δd_M .

The drawback of the γ -evaluation is the time-consuming nature of evaluating the agreement between each reference point with each comparison point. Bakai *et al.* derived the χ -comparison, a method that is nearly identical to the γ -evaluation, but is more computationally efficient [6]. Instead of discrete “acceptance ellipsoids” around each reference point, a continuous “acceptance tube” is created around each reference dataset. If the comparison points fall within the “acceptance tube”, the comparison agrees with the reference at that point. Mathematically, the χ -comparison uses the dose gradient of

the reference dataset to determine the size of the “acceptance tube” and the dose difference of the whole multi-dimensional dataset, not point-by-point. That is,

$$(8.11) \quad \chi = \frac{D_c(\vec{r}) - D_r(\vec{r})}{\sqrt{\Delta D_M^2 + \Delta d_M^2 \cdot \|\vec{\nabla} D_r\|^2}}$$

If the value of χ is less than one, then the comparison and reference datasets agree for that particular point.

There is an observable difference in the results of the γ -evaluation and χ -comparison. In high dose-gradient regions, the χ -comparison will agree with a greater number of points than the same datasets analyzed with the γ -evaluation. An advantage of the χ -comparison, apart from the increase in efficiency, is that the sign of the dose difference can be determined (e.g. an underprediction or overprediction), unlike the γ -evaluation. A disadvantage of both methods is that noise in the reference dataset can create inaccurate values of γ [7] and χ . The gradient calculation of the χ -comparison is highly susceptible to noise. Therefore, the reference and comparison datasets should be chosen carefully, with the reference dataset defined as the ideal or standard dataset, which will usually be the less noisy dataset. In the comparison of predicted and measured portal dose images, the predicted image is considered the reference as it does not contain image noise or imaging artifacts.

8.4 MODEL PARAMETERS

Below are parameters involved in the models described in both Chapter 4 and Chapter 5.

Where there is a unit for the value of the parameter, it is listed. Otherwise, the parameter is dimensionless. If the value is determined by Monte Carlo, analytical calculation, manufacturer schematics or is not a simple number (e.g. a photon spectrum across 15 energy bins), the value of the parameter is not shown and is replaced by ‘N/A’.

Table 8.1 [Chapter 4 Fluence Parameters]: A list of parameters for the ‘original’ model of Chapter 4.

Parameter	Source of value	Value
Focal FWHM	Variable (manually optimized)	0.25 cm
Extrafocal FWHM	Variable (manually optimized)	1.2 cm
Extrafocal height	Variable (manually optimized)	0.30
Extrafocal tail	Variable (manually optimized)	0.85
Focal and extrafocal CAX spectra	Monte Carlo	N/A
Off-axis softening factor	Variable (manually optimized)	10.0
Incident fluence profile	Variable (manually optimized)	N/A
MLC leaf-tip radius	Variable (manually optimized)	20.0
Interleaf leakage	Variable (manually optimized)	0.04
Tongue-and-groove width	Variable (manually optimized)	0.04 cm
MLC transmission	Variable (manually optimized)	0.02
Jaw transmission	Variable (manually optimized)	0.006

Table 8.2 [Chapter 5 Fluence Parameters]: A list of parameters for the ‘revised’ model of Chapter 5.

Parameter	Source of value	Value
Focal FWHM	Variable (computer-optimized)	0.12 cm
Extrafocal FWHM	Variable (computer-optimized)	1.88 cm
Extrafocal height	Variable (computer-optimized)	0.098
Extrafocal tail	Variable (computer-optimized)	4.96
Focal and extrafocal spectra (CAX and OAX)	Monte Carlo (pre-MLC energy fluence)	N/A
Incident fluence profile	Monte Carlo (pre-MLC energy fluence)	N/A
MLC leaf-tip radius	MLC schematics	N/A
Interleaf leakage	MLC schematics	N/A
Tongue-and-groove width	MLC schematics	N/A
MLC leaf density	Variable (computer-optimized)	18.0 g/cm ³
MLC transmission	Analytical calculation through MLC schematics	N/A
Jaw transmission	Variable	0.002

8.4.1 Optimization of Chapter 5 parameters

The parameters of the fluence model given in Chapter 5 were optimized using ‘fmincon’ from the Optimization Toolbox of MATLAB® (Mathworks Inc., Natwick, MA). Starting at an initial estimate for each parameter, the function ‘fmincon’ attempts to find the minimum of an objective function dependent on several variables that are constrained by upper and lower bounds. This is referred to as a ‘constrained nonlinear optimization problem’ [8].

The function ‘fmincon’ uses the ‘interior point method’ – a linear programming method that optimizes the objective function by iteratively stepping through the interior of the solution space, as opposed to its surface [9].

The objective function (O) is the sum of the absolute difference at central axis for a set of open square fields ranging from $2 \times 2 \text{ cm}^2$ to $20 \times 20 \text{ cm}^2$. That is,:

$$(8.1) \quad O = \left\| CAX_{pred}^{2 \times 2} - CAX_{meas}^{2 \times 2} \right\| + \left\| CAX_{pred}^{5 \times 5} - CAX_{meas}^{5 \times 5} \right\| + \left\| CAX_{pred}^{10 \times 10} - CAX_{meas}^{10 \times 10} \right\| + \left\| CAX_{pred}^{20 \times 20} - CAX_{meas}^{20 \times 20} \right\|$$

where $\left\| CAX_{pred}^{2 \times 2} - CAX_{meas}^{2 \times 2} \right\|$ is the absolute difference between the predicted and measured central axis values for a $2 \times 2 \text{ cm}^2$, with the other terms representing the central axis values for the other field sizes. The predicted central axis values are a function of the parameters in Table 8.2, which are constrained by upper and lower bounds. The parameter values are adjusted iteratively until a minimum is determined.

REFERENCES

1. Rogers, D. W. O. and Bielajew, A. F., *Monte Carlo Techniques of Electron and Photon Transport for Radiation Dosimetry*, in *The Dosimetry of Ionizing Radiation*, K. R. Kase, B. E. Bjarngard, and Frank H. Attix, Editors. 1990, Academic Press.
2. Attix, F. H., *Introduction to Radiological Physics and Radiation Dosimetry*. 1986, New York: John Wiley & Sons, Inc., p. 217-218.
3. Kawarackow, I., Mainegra-Hing, E., Rogers, D. W. O., Tessier, F., and Walters, B. R. B., *The EGSnrc code system: Monte Carlo simulation of electron and photon transport*. 2010, Ionizing Radiation Standards, National Research Council of Canada.
4. Van Dyk, J., Barnett, R. B., Cygler, J. E., and Shragge, P. C., *Commissioning and quality assurance of treatment planning computers*. *Int J Radiat Oncol Biol Phys*, 1993. 26(2): p. 261-73.
5. Low, D. A., Harms, W. B., Mutic, S., and Purdy, J. A., *A technique for the quantitative evaluation of dose distributions*. *Med Phys*, 1998. 25: p. 656-61.
6. Bakai, A., Alber, M., and Nusslin, F., *A revision of the gamma-evaluation concept for the comparison of dose distributions*. *Phys Med Biol*, 2003. 48(21): p. 3543-53.
7. Low, D. A. and Dempsey, J. F., *Evaluation of the gamma dose distribution comparison method*. *Medical Physics*, 2003. 30(9): p. 2455.
8. *MATLAB R2012a Documentation - Optimization Toolbox*, 2012 <http://www.mathworks.com/help/toolbox/optim/ug/fmincon.html>.
9. Wolfram MathWorld, *Interior Point Method*, 2012 <http://www.mathworks.com/help/toolbox/optim/ug/fmincon.html>.

8.5 GLOSSARY

a-Si – Amorphous silicon; The material that the photodiodes for clinical electron portal imaging devices are made from.

Buildup – Generally considered to be the thickness of material required to achieve charge particle equilibrium (CPE), and is equal to the depth of dose maximum. For most dose measuring devices, CPE is a necessary condition to accurately measure dose. At depths larger than dose maximum, charged particle equilibrium exists. The buildup region is the region in the material at depths less than dose maximum.

χ -comparison - Method to analyze two datasets. If the value of the γ -evaluation is less than one, then the datasets agree within the specified percentage difference and DTA criteria. The χ -comparison measure is similar to the γ -evaluation, but is more computationally efficient.

CAX – Central Axis; In the coordinate system of the linear accelerator, it is the centre of the in-plane (y) and cross-plane (x), i.e. the axis about which the collimator of the linear accelerator rotates about.

CPE – Charged particle equilibrium. The number of charged particles entering a medium of a specified volume of an irradiated medium are equal to the number leaving the same volume. Under this condition, the dose delivered to the volume is equal to the collision kerma. In beams of high energy photons, the photons are attenuated while generating secondary charge particles, thus never exactly achieving CPE. However, in this situation, the dose is proportional to the collision kerma and can be related through a constant. This condition is referred to as transient charged particle equilibrium (TCPE).

CT – Computed Tomography; A diagnostic imaging technique which uses projections of low-energy x-rays delivered to a patient over a 360° rotation to reconstruct a three-dimensional X-ray image of the patient’s anatomy.

Commissioning – The full determination of a clinical linac dosimetric quantities and mechanical properties. An example of the quantities measured is the output of the linac through a series of dose profiles in water and PDDs, for a range of field sizes. The entire range of activities employed by a clinical linac need to be tested, including the calibration of the physical quantities of a linac to the fluence model of a TPS. Commissioning can also refer to the validation of any radiation therapy device for use in the clinic (e.g. ionization chambers).

Cross-plane direction – The transverse direction of a two-dimensional field; the ‘x’ direction if the secondary collimator is not rotated.

Dark-field – Two-dimensional EPID image collected prior to EPID irradiation to correct for background signals (i.e. not related to irradiation) of the individual pixels.

Dose build-up effect – This effect occurs at depths shallower than the dose maximum depth. As a beam of radiation particles enters a dense medium (from air), the particles that begin to interact with the medium’s atoms generate secondary charge particles, which themselves can interact with and set in motion additional charge particles. This is a charged particle cascade effect, which causes the quantity of dose to increase as a measurement point is moved from the material surface to the depth of maximum dose. When taking measurements, this effect must be considered, usually by adding a layer of “buildup” material on the detector to bring the dose detecting medium to or beyond the depth of maximum dose.

DQE – Detective Quantum Efficiency; A measure of how efficiently an imaging system makes use of the radiation during image formation. It is a function of signal-to-noise ratio of the signal entering and leaving the system.

DRR – Digitally Reconstructed Radiograph; A “beam’s eye” two-dimensional view of a three-dimensional CT dataset from the same angle the radiation beam is entering the patient. This image is created by the planning system for set-up verification prior to treatment..

DTA – Distance-To-Agreement; A term used in analysis comparing two presumable similar datasets, to describe the physical proximity (in units of length) that is acceptable between two corresponding data points.

Dynamic delivery – An IMRT delivery method that achieves fluence modulation by the continuous motion of the MLC leaves in one direction across the field, with each leaf possible exhibiting a different velocity trajectory. The beam is delivered during MLC movement.

EHP - Equivalent Homogeneous Phantom; A virtual phantom of homogeneous electron density created from the electron density of a phantom or patient derived from a CT dataset). The EHP thickness along each rayline from the linac target spot is based on the water-equivalent thickness of the patient or phantom along that line.

EPID – Electronic Portal Imaging Device; A megavoltage x-ray imaging device that can be used for patient set-up verification with the megavoltage beam prior to a radiation therapy treatment. The current clinical standard for EPID design is the two-dimensional a-Si photodiode array.

Flood-field – A two-dimensional image collected during irradiation of the entire 40x30 cm² EPID area. The image corrects the acquired raw image by creating a uniform field that is advantageous for viewing, but removes dosimetric information inherent in the beam.

Fractionation – This describes a standard radiation therapy technique where the total dose prescribed for a radiation therapy treatment is delivered in smaller doses, or “fractions”. Radiobiological factors, such as allowing time for the normal tissues to repair, ensure this technique reduces radiotherapy complications. For example, a standard treatment regimen delivers 1.8 to 2.0 Gy to the tumour per fraction, once a day, over a period of 5 to 7 weeks.

FWHM – Full-Width at Half-Maximum; the width of a distribution or function at 50% of the maximum value

Gantry – The part of the linac which houses the treatment head where the x-ray radiation is created and collimated into a therapeutic beam for patient treatment. The gantry is able to rotate 360° around the patient.

Gantry angle – Angular direction of the gantry’s central axis, relative to a reference angle. At 0° the gantry’s beam central axis is pointed at the ground (perpendicular to the floor surface), while at 180° the gantry is below the patient with the beam pointing upwards (away from the floor, perpendicular to the floor surface), and at 270° the gantry is on the patient’s right.

Hypofractionated – A radiation therapy regimen that delivers a therapeutic dose in significantly fewer fractions than is considered a clinical standard. Standard fractionation is 1.5 to 2.0 Gy per treatment session over 16-40 fractions, while hypofractionated

courses typically increase the per fraction dose (for radiobiological reasons). An example of a hypofractionated therapy regime is the use of 60 Gy in 20 fractions (3.0 Gy per fraction) for prostate treatment, compared to the normal delivery schedule of 2.0 Gy in 39 fractions achieving a total dose of 78 Gy.

γ -evaluation – Analysis method to quantitatively compare two datasets. If the value of the γ -evaluation is less than one, then the datasets agree within the specified percentage difference and DTA criteria.

IMRT – Intensity Modulated Radiation Therapy; A radiation therapy technique which uses multileaf collimation to deliver complex fluence patterns to the patient, at multiple static gantry angles.

In-plane direction – The direction across the field that is the same direction as the patient lying on the bed, head-to-foot; the ‘y’ direction if the secondary collimator is not rotated.

Linac – Linear accelerator; Refers to a clinical linear accelerator, designed for delivering high-energy x-ray radiation to patients for the purposes of disease treatment.

MTF – Modulation Transfer Function; A measure of spatial resolution of imaging systems. It is dependent on pixel size and noise.

MU – Monitor Unit; A measure of beam-on time for a linac. The linac is calibrated in the TPS to a dose value that is measured with an ion chamber using a standard calibration field delivered to a water tank, at a specific depth for a known amount of delivered monitor units. For example, a typical calibration value is 1 cGy of dose delivered by a 10x10 cm² field on the central-axis at 10 cm depth in water for one monitor-unit of beam-

on time, i.e. 1 cGy/MU is the calibration used in the TPS and calibrates beam-on time to dose calculated using the TPS.

MV- Megavoltage, used to describe the nominal energy of a polyenergetic photon radiation beam, with the energy based on the maximum energy particle contained in the beam. The term describes the effective electric potential that would need to be created in order to generate a beam of photons with that maximum energy (ie. analogous to the use of kV or kilovoltage used to describe the energy of diagnostic photon beams, since they are generated via accelerating electrons through an applied voltage. For example, a 6 MV photon beam consists of photons that range in energy from 0 to 6 MeV. Monoenergetic beams are described in units of MeV. Electron beams are considered reasonably monoenergetic and also use MeV. At imaging energies, kV is the common unit used and also denotes a polyenergetic spectra.

Non-transit image - Image acquired with neither a patient or phantom in the beam. The radiation is delivered directly to the EPID. Also called an open-field image in the literature.

OAR – Organ At Risk; Normal tissue as typically delineated on CT scans in treatment planning software. These organs are to be spared from radiation damage as much as possible.

Open-field image – Image acquired without a patient or phantom in the beam. The radiation is delivered directly to the EPID. Also called a non-transit image in the literature.

PDD – Percentage-Depth Dose; The measurement of dose in a material (usually water) as a function of depth.

Phantom – Attenuating material placed into the beam that is dosimetrically equivalent (or nearly so) to a patient. A phantom can be a simple tank of water or a water-equivalent plastic slab, or made of multiple materials to create an anthropomorphic object that mimics a patient.

PSM – Pixel Sensitivity Matrix; A two-dimensional array that corrects for the individual pixel response of the a-Si EPID. The PSM is required when reintroducing the flood-field into the measured EPID image as the flood-field inherently corrects for pixel sensitivity, but also removes important dosimetric information when correcting the measured image to create a uniform field.

SDD – Source-to-Detector Distance.

SSD – Source-to-Surface Distance.

SNR – Signal-to-Noise Ratio; A measure of the noise (spurious, unwanted signal) in an imaging system.

Step-and-shoot delivery – IMRT delivery method that achieves fluence modulation by dividing the delivery into multiple small fields, or “segments”. The beam is delivered only when the MLC is stationary. Each static gantry angle employs many segments (typically 7-20)

Terma – Total energy released per unit mass in an irradiated medium, specifically by primary x-ray interactions.

TMR – Tissue Maximum Ratio; Ratio of the dose at a particular depth to the dose at depth of dose maximum. A table of TMRs at various depths can be used to calculate dose at multiple depths if a reference dose is known.

TPS – Treatment Planning System; Software employed to customize the radiation treatment for a patient, allowing the creation of a three-dimensional map of the intended radiation dose for the individual patient. TPS software requires a CT dataset of the patient and beam information specific to the linac the patient is to be treated on.

VMAT – Volumetric Modulated Arc Therapy; The most complex form of IMRT currently commercially available. It involves delivery of radiation to the patient while the gantry rotates about the patient, with simultaneous motion of the MLC's and collimator, and variation of the dose rate. This delivery method is known commercially as RapidArc™ (Varian Medical Systems, Palo Alto, CA) or VMAT (Elekta AB, Stockholm, Sweden).

8.6 COPYRIGHTED MATERIAL

The following section is a compilation of the permissions for copyrighted material in this thesis.



American Association of Physicists in Medicine

One Physics Ellipse
College Park, MD 20740-3846
(301) 209-3350
Fax (301) 209-0862
<http://www.aapm.org>

Office of the Executive Director
Angela R. Keyser
Phone: 301-209-3385 Fax: 301-209-0862
E-mail: akeyser@aapm.org

VIA EMAIL

July 19, 2011

Ms. Krista Chytky
PhD Candidate
University of Manitoba
Winnipeg, MB
CANADA

Dear Ms. Chytky:

The American Association of Physicists in Medicine hereby grants permission to Krista Chytky to use the figure indicated below for her PhD thesis:

M. B. Sharpe, D. A. Jaffray, J. J. Battista, and P. Munro, "Extrafocal radiation: A unified approach to the prediction of beam penumbra and output factors for megavoltage x-ray beams." *Med. Phys.* 22(12) 2065-2074 (1995), Figure 1.

Authors seeking permission must also notify the first author of the article from which permission is being sought.

Sincerely,

Angela R. Keyser



RightsLink®

[Home](#)
[Account Info](#)
[Help](#)


Title: Field shaping for three-dimensional conformal radiation therapy and multileaf collimation

Logged in as:
Krista Chytk

[LOGOUT](#)

Author: Radhe Mohan

Publication: Seminars in Radiation Oncology

Publisher: Elsevier

Date: April 1995

Copyright © 1995, Elsevier

Order Completed

Thank you very much for your order.

This is a License Agreement between Krista Chytk ("You") and Elsevier ("Elsevier"). The license consists of your order details, the terms and conditions provided by Elsevier, and the [payment terms and conditions](#).

[Get the printable license.](#)

License Number	2698930031138
License date	Jun 30, 2011
Licensed content publisher	Elsevier
Licensed content publication	Seminars in Radiation Oncology
Licensed content title	Field shaping for three-dimensional conformal radiation therapy and multileaf collimation
Licensed content author	Radhe Mohan
Licensed content date	April 1995
Licensed content volume number	5
Licensed content issue number	2
Number of pages	14
Type of Use	reuse in a thesis/dissertation
Portion	figures/tables/illustrations
Number of figures/tables/illustrations	1
Format	both print and electronic
Are you the author of this Elsevier article?	No
Will you be translating?	No
Order reference number	CHYTYK-2011
Title of your thesis/dissertation	Dosimetric verification of radiation therapy including intensity modulated treatments, using an amorphous-silicon electronic portal imaging device
Expected completion date	Aug 2011
Estimated size (number of pages)	175
Elsevier VAT number	GB 494 6272 12
Permissions price	0.00 USD
VAT/Local Sales Tax	0.0 USD / 0.0 GBP
Total	0.00 USD

[ORDER MORE...](#)
[CLOSE WINDOW](#)

Copyright © 2011 [Copyright Clearance Center, Inc.](#) All Rights Reserved. [Privacy statement.](#)
Comments? We would like to hear from you. E-mail us at customer care@copyright.com



American Association of Physicists in Medicine

One Physics Ellipse
College Park, MD 20740-3846
(301) 209-3350
Fax (301) 209-0862
<http://www.aapm.org>

Office of the Executive Director
Angela R. Keyser
Phone: 301-209-3385 Fax: 301-209-0862
E-mail: akeyser@aapm.org

VIA EMAIL

April 8, 2011

Ms. Krista Chytyk
Ph.D. Student
Division of Medical Physics
CancerCare Manitoba
Winnipeg, Manitoba
CANADA

Dear Ms. Chytyk:

The American Association of Physicists in Medicine hereby grants permission to Krista Chytyk to use the articles indicated below in her Ph.D. thesis:

K. Chytyk and B. M. C. McCurdy, "Investigation of tilted dose kernels for portal dose prediction in *a*-Si electronic portal imagers." *Med. Phys.* 33(9) 3333-3339 (2006).

K. Chytyk and B. M. C. McCurdy, "Comprehensive fluence model for absolute portal dose image prediction," *Med. Phys.* 36(4) 1389-1398 (2009).

Sincerely,

A handwritten signature in black ink that reads "Angela R. Keyser". The signature is written in a cursive, flowing style.

Angela R. Keyser